Федеральное государственное бюджетное учреждение науки
Институт ядерных исследований
Российской академии наук

ТРУДЫ XIII МЕЖДУНАРОДНОГО СЕМИНАРА ПО ЭЛЕКТРОМАГНИТНЫМ ВЗАИМОДЕЙСТВИЯМ ЯДЕР

ЭМИН-2012

Москва, 20-23 сентября 2012 г.

МОСКВА
2013

Institute for Nuclear Research
of the Russian Academy of Sciences

PROCEEDINGS OF THE XIII INTERNATIONAL SEMINAR ON ELECTROMAGNETIC INTERACTIONS OF NUCLEI

EMIN-2012

Moscow, September 20-23, 2012

MOSCOW
2013

УДК 539.17

Труды XIII Международного семинара
по электромагнитным взаимодействиям ядер
ЭМИН-2012
Москва, 20-23 сентября 2012 г.

В сборник включены доклады, представленные
на XIII Международный семинар
по электромагнитным взаимодействиям ядер EMIN-2012
и подготовленные авторами к публикации.

Materials of the XII International Seminar EMIN-2012 (including the talk presentations) one can find at the site http://www.inr.ac.ru/~pnlab/emin2012/Welcome.html

Organizers:

Russian Academy of Sciences,
Institute for Nuclear Research,
Lomonosov Moscow State University,
Russian Foundation for Basic Research

Organizing Committee:

V. G. Nedorezov, vice-chairman, INR RAS, Moscow
B. S. Ishkhanov, vice-chairman, SINP MSU, Moscow
A. L. Polonski, secretary, INR RAS, Moscow
V. Yu. Grishina, INR RAS, Moscow
G. M. Gurevich, INR RAS, Moscow
L. A. Malov, JINR, Dubna
G. V. Solodukhov, INR RAS, Moscow
V. I. Travinsky, SINP MSU, Moscow
B. A. Tulupov, INR RAS, Moscow
M. H. Urin, MEPhI, Moscow
V. A. Ishkanov, SINP MSU, Moscow
V. V. Varlamov, SINP MSU, Moscow

ISBN 978-5-94274-228-7

Contents

SEMINAR PROGRAM

Meson Photoproduction on Free and Bound Nucleons. Barion and Meson Structure

Phil Cole [Idaho StateUniversity]
Barion spectrum and structure with the CLAS detector at JLab.

S.B. Gerasimov [JINR, Dubna]
Towards the inquiring about the non-(q anti-q)- admixture in light meson multiplet structure.

E. Golovach [MSU SINP, Moscow]
Reaction of two pion photoproduction off proton and the structure of nucleon resonances.

P. Pedroni [INFN, Pavia]
Helicity dependent meson photoproduction on ^{3}He in the Δ-resonance region.

V. Polyanskiy [Lebedev PI, Moscow]
On photoproduction of eta-mesic nuclei at the LPI synchrotron.

V. Burov [JINR, Dubna]
Bethe-Salpeter approach and lepton-, hadron-deuteron scattering.

E. Pasyuk [JLAB]
Meson photoproduction and nucleon resonances.

M.I. Levchuk, A.I. L'vov [Stepanov PI, Minsk; Lebedev PI, Moscow]
On extraction of the total photoabsorption cross section on the neutron from data on the deuteron.

Coulomb Dissociation and Fragmentation of Relativistic Nuclei

I.A. Pshenichnov [INR, Moscow]
Electromagnetic fragmentation of nuclei at heavy-ion colliders.

E.V. Karpechev [INR, Moscow]
Emission of neutrons in electromagnetic fragmentation of In and Pb nuclei at the CERN SPS.

K.Z. Mamatkulov [JINR, Dubna]
Fragmentation of relativistic ^{10}C nuclei in nuclear emulsion.

D. Artemenkov [JINR, Dubna]
Study of ^{7}Be relativistic fragmentation in nuclear track emulsion.

Giant Resonances and Nuclear Interactions

N. Goncharova, Iu. Skorodumina [SINP MSU, Moscow]
The structure of giant resonances in calcium and titanium isotopes.

M.H. Urin [MEPhI, Moscow]
Damping of high-energy particle-hole-type nuclear excitations: a semi-microscopic model.
B.A. Tulupov, M.H. Urin [INR, MEPhI, Moscow]
Direct and semidirect neutron radiative capture by medium-heavy mass nuclei: a new version of the semimicroscopic description.

V.N. Orlin [MSU SINP, Moscow]
A combined model of photonuclear reaction.

B.S. Ishkhanov, V.N. Orlin, V.V. Varlamov [MSU SINP, Moscow]
New treatment for neutron multiplicity sorting and partial photoneutron reactions cross sections evaluation.

S. Kamerdhhiev, D. Voitenkov [IPPE, Obninsk]
Transitions between excited states of even-even nuclei within the Theory of Finite Fermi systems.

A.M. Shirokov, J.P. Vary, P, Maris, A.I. Mazur, V.A. Kulikov [MSU SINP, Moscow]
Ab initio theory of light nuclei with inverse scattering NN interaction.

Non Linear QED Interactions.
Multiphoton Exchanges. Exotic resonances

I. Rachek [BINP, Novosibirsk]
Two-photon exchange contribution in elastic electron-proton scattering:
measurements at VEPP-3.

A. Savel'ev [MSU, Moscow]
Gamma-rays and high energy particles production from relativistic laser plasma interaction.

L.V. Fil'kov [Lebedev PI, Moscow]
Search for narrow six-quark states.

New Developments and Perspectives

R. Djilkibaev [INR, Moscow]
Positron source for annihilation spectroscopy.

T. Ohta [RCNP, Osaka]
Development of the polarized hydrogen-deuteride (HD) target for double-polarization experiments at LEPS.

L.Z. Dzhilavyan, S.I. Mishnev, V.G. Nedorezov, D.V. Nikolenko, I.A. Rachek, D.K.Toporkov [INR Moscow, BINP Novosibirsk]
Source of monochromatic photons driven by positron in-flight annihilation using internal target of the storage ring VEPP-3.

To the memory of Prof. Guram Kezerashvili

C. Schaerf [INFN]
Guram: a scientist… a friend.

R. Kezerashvili [Uni, New York]
The interrupted flight – papers that Guram has no opportunity to present.

N.Yu. Muchnoi [BINP, Novosibirsk]
Back scattering of laser radiation on relativistic electrons in transfer magnetic fields: evidence of optical interferences in a MeV scale.

V.G. Nedorezov [INR, Moscow]
New ideas on photo-fission.

Poster session reports

A.V. Andreev [INR, Moscow]
On the possibility of using of electron linac LUE-8 (INR RAS) as the thermal neutrons source.

Phil Cole [Idaho State University]
Photoproduction of phi mesons with line measurements of the atomic number of objects during irradiation with photon beams.

A.A. Kuznetsov [MSU SINP, Moscow]
Photofission of uranium.

A.V. Andreev, Yu.M. Burmistrov, E.S. Konobeevski, M.V. Mordovskoy, S.V Zuev, V.I. Firsov [INR, Moscow]
Low background gamma-spectrometer with cosmic ray anticoincidence shielding.

S. Shulyapov [MSU, Moscow]
Excitation and de-excitation of isomeric nuclear states by femtosecond laser plasma emission.

V. Skorkin [INR, Moscow]
Photoproduction of neutrons in the heavy water irradiation facility at the SL75 linear electron accelerator.

Yu.I. Sorokin [INR, Moscow]
Feynman propagator for particle in homogeneous electromagnetic field.

K.A. Stopani [MSU SINP, Moscow]
Photonuclear reactions on palladium isotopes.

V. Tivkov [INR, Moscow]
On the GRAAL detector calibration procedure.

S.Yu. Troschiev [MSU SINP, Moscow]
Simulation of the gamma-activation experiments.

A. Turinge [INR, Moscow]
Simulation of photonuclear experiment driven by femtosecond laser.

D. Zagorodnyuk [INR, Moscow]
Detector development to measure the interaction products of femtosecond laser with Pb target.

E.S. Konobeevski, M.V. Mordovskoy, I.M. Sharapov, S.V. Zuyev [INR, Moscow]
Neutron-gamma discrimination in organic scintillators using various pulse-shape parameters.

REACTION OF TWO-PION PHOTOPRODUCTION OFF PROTONS AND THE STRUCTURE OF NUCLEON RESONANCES

E.N. Golovach[1], *V.D. Burkert*[2], *R. Gothe*[3], *G.V. Fedotov*[1,3], *B.S. Ishkhanov*[1,4],
E.L. Isupov[1], *V.I. Mokeev*[1,2], *and CLAS collaboration*

[1]Institute of Nuclear Physics, Moscow State University, Moscow, Russia;
[2]Thomas Jefferson National Accelerator Facility, Newport News, USA;
[3]University of South Carolina, Columbia, USA;
[4]Physics Department, Moscow State University, Moscow, Russia.

Physics Motivation

The N^* studies with CLAS (CEBAF Large Acceptance Spectrometer) at JLAB (Thomas Jefferson National Accelerator Facility) are focused on the exploration of the strong interaction in the non-perturbative regime of QCD through studies of transition form factors from the ground state to excited nucleon states. This helps us to determine the relevant degrees of freedom in describing excited nucleons. Another objective of the N^* program is the studies of the N^* spectrum with emphasis on the search for so-called "missing states".[1,2]

The processes $\gamma_{r,v}p \to \pi N$ and $\gamma_{r,v}p \to \pi\pi N$ are two major contributors to the meson photo- and electroproduction in the N^* excitation region, while the two-pion channel has better sensitivity to the high-lying resonances ($M > 1.6$ GeV), since most of them decay preferably into a final state with two pions. Moreover, these channels are strongly coupled by the final state interaction to channels with smaller cross sections and, therefore, may affect other channels, such as ηN, KY, and ωN. Thus, the information on the reactions of single and double pion photo- and electroproduction is important for global multichannel analyses within the framework of coupled channel approaches.[3] Analyses of both channels are needed for the reliable extraction of N^* parameters.

Constituent quark models (CQM) predict more baryon states than have been observed in experiments so far, and different models predict different numbers of states. Recent lattice QCD calculations[4,5] of the N^* spectrum suggest the existence of as many states as are expected in CQM models based on SU(6) spin-flavor symmetry. Therefore, CQM results on the existence of many new baryon states get substantial support from Lattice QCD. It motivates us to search for these new states in experimental data. The two-pion photo- or electroproduction off protons is one of the most suitable reaction channels for this purpose, because CQM calculations[6] predict that "missing" states are weakly coupled to the πN channel, while they should have substantial decays to the final states with two pions. For the first time the signal of a "missing state" candidate was observed[7] in the reaction $\gamma_v p \to \pi^+\pi^- p$ at Q^2 from 0.5 to 1.5 GeV^2. The structure at a CMS energy (W) ≈1.7 GeV could be explained assuming either substantially different $\pi\Delta$ and ρp hadronic decay widths of the conventional $\mathrm{P}_{13}(1720)$ state with respect to the values[8] obtained in experiments with hadronic probes, or implementing a new candidate state $3/2^+(1725)$. In the latter case the parameters of $\mathrm{P}_{13}(1720)$ remained at the values, which reasonably coincide with PDG data. Figure 1 shows the cross section of the $\pi^+\pi^- p$ electroproduction at eight Q^2 values. The bump at $W \approx 1.7$ GeV is clearly seen[7,9] at Q^2 from 0.5 to 5.0 GeV^2. The same reaction with real photons can provide a sensitive check for the existence of this candidate state in a combined analysis of two-pion photo- and electroproduction. The two-pion cross sections should be reproduced in both photo- and electroproduction with the same N^* hadronic decay widths. Furthermore, photoproduction data offer an opportunity to further constrain non-resonant mechanisms.

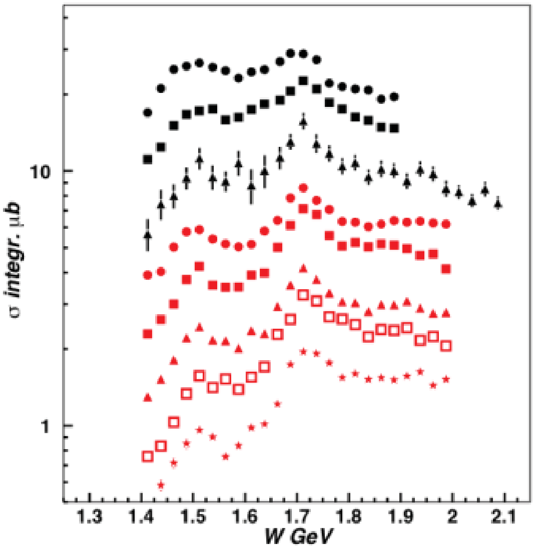

Figure 1: (color online) Integrated cross section for the reaction $\gamma_v p \rightarrow \pi^+\pi^- p$ as a function of W at different Q^2-values. Black symbols[7] correspond to Q^2 = 0.65, 0.95, and 1.3 GeV^2 and preliminary data at Q^2 = 2.3, 2.7, 3.3, 3.9, and 4.6 GeV^2 are shown in red.[9] Increasing Q^2 values correspond to decreasing cross section.

Cross section for $\gamma p \rightarrow \pi^+\pi^- p$ from CLAS data

We analyzed the data of the G11A run period obtained with the CLAS[10] detector in Hall-B at JLAB. CLAS is a superconducting spectrometer with almost 4π-acceptance. The JLAB accelerator delivers continuous electron beam with energies up to ≈6 GeV. The photon tagging system provides tagged photons with 0.5% energy resolution. The unique capability of CLAS to detect multi-particle final hadron states provides an ideal tool for the measurement of the $\gamma p \rightarrow \pi^+\pi^- p$ cross section.

In the G11A run 4 GeV electrons with a current of 60 nA hit the CLAS bremstrahlung target. Tagged photons with energies from 1.6 to 3.8 GeV were directed to a liquid hydrogen target. The CLAS trigger system was set to register events having at least two charged particles. During the run time of 50 days about 7×10^9 triggers were collected.

The large CLAS acceptance and the large number of events made it possible to obtain 1- and 2-fold differential cross sections in narrow W-bins of 25 MeV for the first time. We analysed the sample of events with at least 2 charged particles in the final state. Two-pion events were selected employing a kinematic fitting procedure.[11] Detector efficiency was evaluated in Monte–Carlo approach using the standard CLAS GSIM package. The

$\pi^+\pi^-p$ final state can be fully described with 5 variables. We choose a set of variables comprised of invariant masses of the final particle pairs $M(p\pi^+)$, $M(\pi^+\pi^-)$, CM solid emission angles of a proton ($\theta(p)$, $\phi(p)$) and the rotational angle ($\alpha(p)$) between the plane of the final $\pi^+\pi^-$ pair and the plane of initial and final proton. Our experiment provided nine 1-fold differential cross sections ($d\sigma/dM(i,j)$, $d\sigma/\theta(i)$, $d\sigma/\alpha(i)$, where i and j stand for p, π^+ or π^-) and 21 2-fold differential cross sections in each bin of W. Integration of 5-differential cross section is needed to afford reasonable statistical and systematical accuracy. All cross sections reported in this paper are preliminary.

The cross section integrated over the CLAS acceptance is shown in Fig. 2 as a function of W. The comparison with previously available data[12,13] demonstrates the effect of the limited detector acceptance that has not been taken into account in the JLAB data. CLAS has inactive areas at forward and backward angles.

A special procedure was developed to account for contributions to the cross section from dead zones. For each bin of any 1-fold differential cross section we compute the ratio R: the total amount of contributing 5-D cells over the number of active cells. The corrected cross section was obtained by multiplying the aforementioned cross section by R. We set the uncertainty related to this procedure to be equal to half of the increase in cross section value. Figure 3 shows final hadron CM angular distributions before and after this correction.

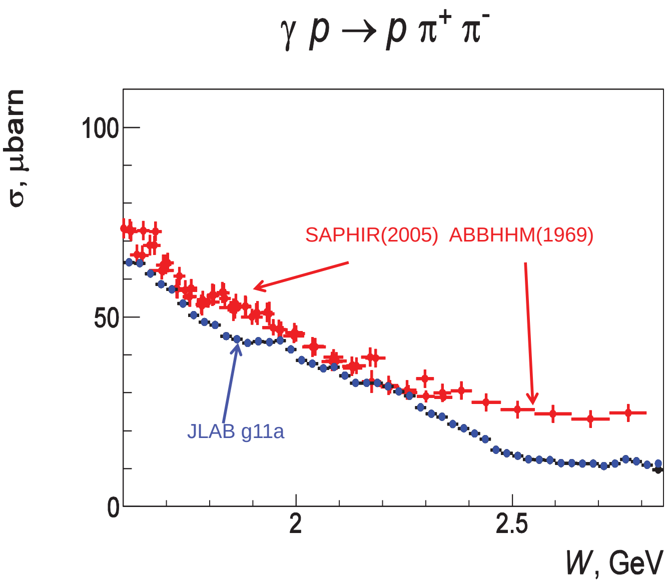

Figure 2: (color online) Integrated $\pi^+\pi^-p$ photoproduction cross section from the CLAS data in comparison with the SAPHIR[12] and ABBHHM[13] data. Only statistical errors are shown for the CLAS cross section.

Integrated cross sections before and after corrections are shown in Fig. 4. Corrected cross sections are systematically larger than world data at $W < 2.4$ GeV while at $W > 2.5$ GeV they become smaller. These discrepancies may be related to the still too naive assumption on the cross section behavior in inefficient areas. In the future we are planning to fit these data within a framework of JM model[14,15] in order to extrapolate the cross

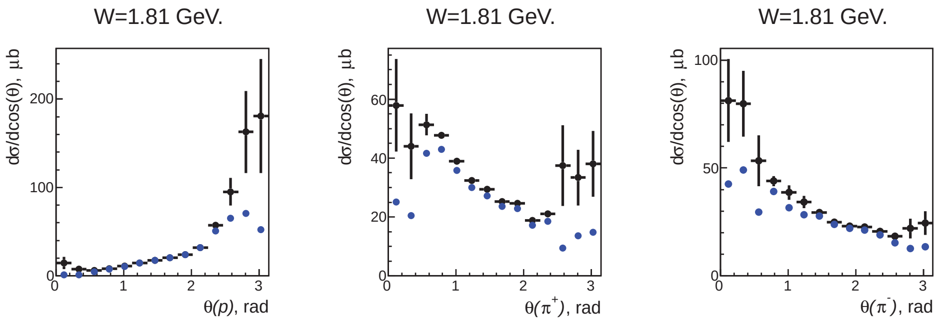

Figure 3: (color online) CM angular distributions of the final hadrons. Blue points correspond to the cross sections inside the CLAS acceptance. Corrected cross sections are shown in black. Uncertainties come mostly from the correction procedure.

section into dead area.

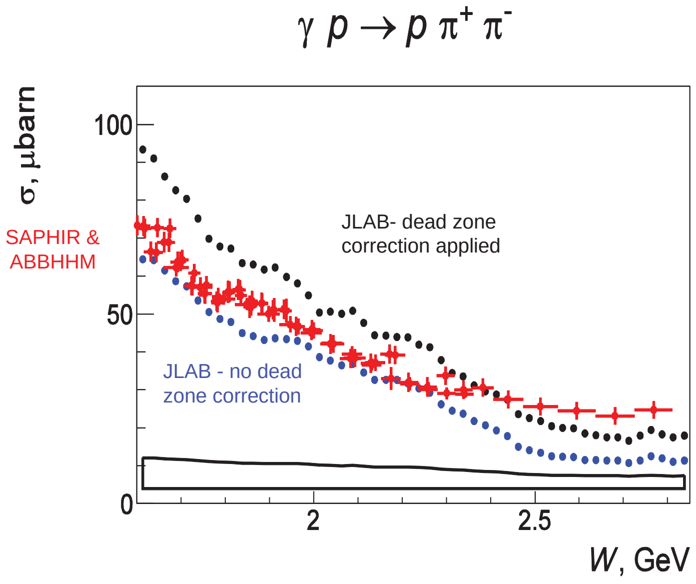

Figure 4: (color online) Integrated $\pi^+\pi^-p$ cross section from the CLAS data in comparison with the SAPHIR[12] and ABBHHM[13] data. Blue points correspond to the cross sections inside the CLAS acceptance. The corrected cross section is shown in black. The error band at the bottom of the plot shows systematical uncertainties related to the correction procedure.

Figure 5 demonstrates examples of the invariant mass distributions. Distributions over the rotational α angles are shown in Fig. 6. Examples of 2-fold differential cross section are presented in Fig. 7.

Summary

For the first time preliminary 1- and 2-fold differential cross sections for the reaction $\gamma p \to \pi^+\pi^-p$ have become available at CM energies from 1.6 to 2.8 GeV. A physics

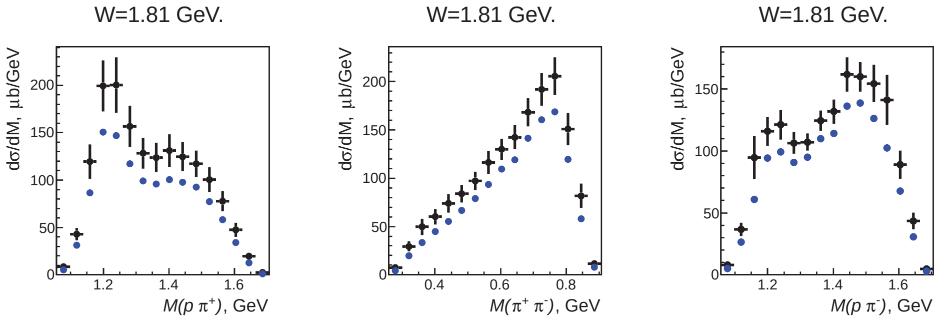

Figure 5: (color online) Invariant mass distributions of the final hadrons. See Fig. 3 for designations.

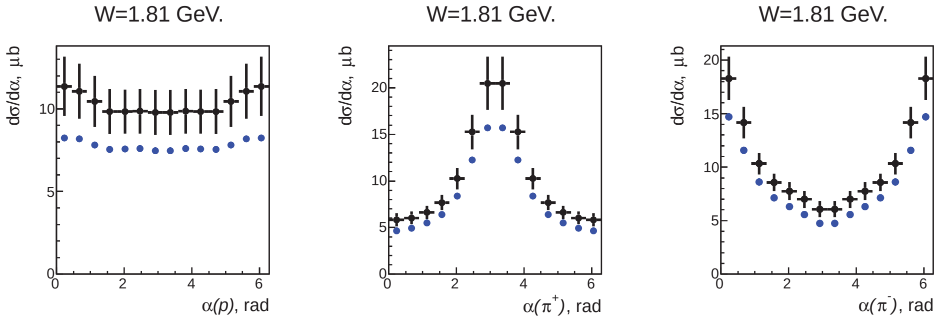

Figure 6: (color online) Rotational α angle distributions. See Fig. 3 for designations.

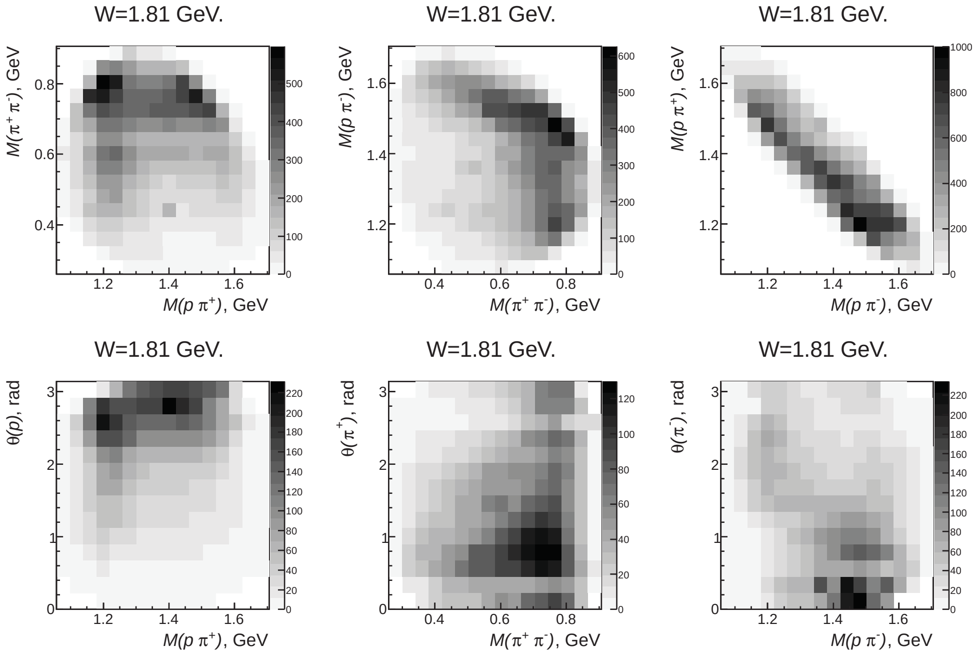

Figure 7: Examples of 2-fold differential cross sections.

analysis of this data within the framework of the reaction model[14, 15] is in progress with the goal to obtain information on resonance photocouplings from this exclusive channel, which is particularly sensitive to high-lying N^*-states with masses above 1.6 GeV. A combined analysis of the $\pi^+\pi^-p$ photo- and electroproduction data off protons looks very promising in order to establish the nature of the structure at $W \approx 1.7$ GeV, which was observed in two-pion electroproduction.

Acknowledgements

This work was supported in part by the US Department of Energy and the National Science Foundation, the Skobeltsyn Institute of Nuclear Physics and Physics Department at Moscow State University. Jefferson Science Associates, LLC operates Lefferson Lab under Contract No. DE-AC05-84ER40150.

References

[1] V. D. Burkert. 12th International Workshop on Meson Production, Properties and Interaction (MESON 2012), Krakov, Poland, 31 May - 5 June 2012. arXiv:1209.2402

[2] V. D. Burkert. 3rd International Conference on Nuclear and Particle Physics with CEBAF at Jefferson Lab. Dubrovnik, Croatia. 3-8 Oct 2010. Fizika B20 (2011) 237.

[3] T.-S. H. Lee. arXiv:1208.5748 (2012).

[4] R. Edwards et al. Phys. Rev. D84 (2011) 074508.

[5] J. J. Dudek, R. G. Edwards. Phys. Rev. D85 (2012) 054016.

[6] S. Capstick, N. Isgur. Phys. Rev. D34 (1986) 2809.

[7] M. Ripani et al, CLAS collaboration. Phys. Rev. Lett. 91 (2003) 022002.

[8] PDG group. Phys. Rev. D86 (2012) 010001.

[9] E. L. Isupov. Private communication. (2012).

[10] B. A. Mecking et al, CLAS collaboration. Nucl.Instrum.Meth. A503 (2003) 513.

[11] M. Williams, C. A. Meyer. CLAS-NOTE 2003-017.

[12] C. Wu et al. Eur. Phys. Journal. A23 (2005) 317.

[13] ABBHHM. Phys. Rev. 175 (1968) 1669.

[14] V. I. Mokeev et al. Phys. Rev. C80 (2009) 045212.

[15] V. I. Mokeev et al, CLAS collaboration. Phys. Rev. C86 (2012) 035203.

HELICITY DEPENDENT MESON PHOTOPRODUCTION ON ^{3}He IN THE Δ-RESONANCE REGION

P.Pedroni[1]

For the CBMAMI and A2 Collaborations

[1] INFN- Sezione di Pavia, via Bassi 6 , 27100, Pavia, Italy

The GDH sum rule

Since the beginning of the 1960s, a central issue of nuclear and particle physics has been the study of the internal structure of the nucleon, in particular of the spin structure, which is not so well understood as other nucleon properties.

For this study, of particular interest are sum rules, which connect information from all energies to fundamental parameters of the present interaction models. The Gerasimov-Drell-Hearn sum rule [1,2] is a good example of these rules. It relates the nucleon anomalous magnetic moment (AMM) κ, the spin S and the mass M of a nucleon to the integral over the weighted helicity difference of the total absorption cross section for circularly polarized photons on a longitudinally polarized nucleon target and it can be written as:

$$I_{GDH} = \int_{\nu_0}^{\infty} \frac{\sigma_P - \sigma_A}{\nu}\, d\nu = \frac{2\pi^2\alpha}{m^2}\kappa^2$$

where ν is the photon energy, α is the fine-structure constant, σ_P and σ_A and denote the total absorption cross section for parallel and antiparallel orientation of photon and particle spins, respectively. The lower limit of the integral, $\nu_{0,}$ corresponds to pion production and photodisintegration threshold for a nucleonic and nuclear target, respectively. Table 1 reports the magnetic moment μ, the AMM κ values and the predicted I_{GDH} values for protons, neutrons, deuterons and ^{3}He nuclei.

Table 1

	p	n	d	^{3}He
μ	2.79	-1.91	0.86	-2.13
κ	1.79	-1.91	-0.14	-8.37
I_{GDH}	204	233	0.65	498

The GDH sum rule is derived from very general fundamental physical principles, in particular from the forward Compton scattering, the optical theorem and the low energy theorems. In the past, there have been several attempts to find causes for a failure of the GDH sum rule. The only ``weak" hypothesis is the assumption that the Compton scattering becomes spin-independent as the energy tends to infinity. Possible explanations for this violation could be the exchange of a_1 – like meson between the photon and the nucleon or the non-pointlike quark structure.

The test of this relation then provides a fundamental check of our knowledge of the γ-nucleon interaction, as well as of the physics of strongly interacting systems; it is also a check of the existing photo-reaction models. In addition, through the helicity dependent partial channels, it will be possible to access new observables and to study the baryonic resonances.

It is possible to estimate the GDH sum rule value for the nucleon by using a combination of multipole analyses of the available single pion photoproduction data (mostly from unpolarized experiments) [3,4] and phenomenological models of multipion and heavy meson photoproduction reactions [5,6,7] up to E_γ~2 GeV. Above this energy, the contribution can be estimated from Regge-type approaches [8]. Table 2 reports the current theoretical estimates of the GDH sum rule values both for the proton and the neutron. Predictions for the $N\pi$ channel are from the SAID [3] and MAID [4] (within brackets) multipole analyses;

Table 2

Proton	I_{GDH} (μb)	Neutron	I_{GDH} (μb)
$\gamma p \rightarrow N\pi$	172 [164]	$\gamma n \rightarrow N\pi$	147 [131]
$\gamma p \rightarrow N\pi\pi$	94	$\gamma n \rightarrow N\pi\pi$	82
$\gamma p \rightarrow N\eta$	-8	$\gamma n \rightarrow N\eta$	-6
$\gamma p \rightarrow K\Lambda\ (\Sigma)$	-4	$\gamma n \rightarrow K\ \Lambda(\Sigma)$	2
$\gamma p \rightarrow N\rho(\omega)$	0	$\gamma n \rightarrow N\rho(\omega)$	2
Regge contrib. (E_γ > 2 Gev)	-14	Regge contrib. (E_γ > 2 Gev)	20
TOTAL	239 [231]	TOTAL	244 [231]
GDH	**205**	**GDH**	**233**

There is a clear discrepancy between these theoretical predictions and the GDH sum rule value for the proton, while the neutron GDH value is roughly reproduced. In addition, it is worth noting that according to the models, I_{GDH} for the proton and the neutron are roughly the same, while this is not the case for the GDH sum rule values. In order to find out the reasons for this discrepancy, a precise measurement of the GDH integral for both the proton and the neutron is needed, as well as a systematic study of the partial channels, in particular of the $N\pi(\pi)$ ones, which give the dominant contribution to the GDH integral.

The first experimental check of the GDH sum rule for the proton was performed by the GDH collaboration jointly at the Mainz and Bonn tagged photon facilities, where the I_{GDH} was experimentally evaluated in the photon energy range between 200 MeV and 2.9 GeV [9,10]. The combination of this result with the theoretical predictions for the unmeasured energy ranges gives an estimated value of the GDH integral of 211± 5 (stat) ± 12 (sys) μb.

The obtained result supports the validity of the GDH sum rule for the proton, at odds with the theoretical estimates given in Table 2. This discrepancy is mainly due to the oscillating photon energy dependence of the GDH integrand, due to the alternating sign of the multipole contributions. In order to have a reliable prediction of the GDH integral, a very high accuracy, that has not been reached yet, is needed for the theoretical models.

The GDH sum rule for the neutron

In the neutron case, the experimental verification of the GDH sum rule is complicated by the lack of free neutron targets. In order to compensate for this lack, deuteron or high pressure ^{3}He targets can be used. In both cases, nuclear structure effects and final state interactions prevent the direct access to the cross section of the ``free nucleon" and the evaluation of the free neutron contribution will be model dependent.

The first experimental measurement carried out using longitudinally polarized deuterons has been performed in the energy region between 0.2 and 1.8 GeV by the GDH collaboration [11,12,13]. In [13] a very rough estimate was derived for the GDH integral value for the neutron from the combination of these data with the ones from the proton. However, the lack of reliable nuclear models describing in a satisfactory manner the helicity dependent γ-d interactions and the presence of a large proton background contribution, prevent at the moment a reliable extraction of the GDH neutron value.

A complementary and more direct access to a free polarized neutron is given by a longitudinally polarized ^{3}He target. While the proton and the neutron inside the deuteron are essentially in s-states of relative motion with aligned spins, ^{3}He is (with ~90% probability) a system consisting of two protons with spins paired off and an active unpaired neutron, in relative s-states. As a result, the contribution of the two protons to the magnetic moment of ^{3}He cancels off and can be approximated with the magnetic moment of the neutron. Therefore, it is expected that the measured GDH integral for ^{3}He above the pion production threshold will be a good approximation of the GDH integral value for the neutron.

In a PWA approach and above the pion production threshold, the following formula can then be used:

$$I_{GDH}[^3He] = p_n \cdot I_{GDH}[neutr] + p_p \cdot I_{GDH}[prot] \qquad (1)$$

where p_p=-0.026 and p_n=0.87 are the are the effective degrees of neutron and proton polarization inside 3He as evaluated by [14]. Since the proton contribution to the measured helicity dependent yields is much smaller for ^{3}He than for the deuteron, it can be clearly seen that the most accurate evaluation of I_{GDH} will come from ^{3}He.

In any case, the comparison between the two different free neutron values extracted from both targets using different nuclear models will play a crucial role in constraining the theoretical analyses and will give a fundamental cross check of the reliability of the free neutron extraction procedures.

Experimental Set-up

The experiment was carried out at the tagged photon facility of the MAMI accelerator in Mainz.

Circularly polarized photons were obtained by bremsstrahlung of longitudinally polarized electrons having an energy of 525 MeV and an average polarization of about 80% .The relative electron polarization was continuously monitored using a Moeller polarimeter and its absolute value was periodically measured using a Mott polarimeter. This parameter was then determined with an absolute accuracy of 3%.

The bremsstrahlung photons were tagged using the Glasgow-Mainz magnetic spectrometer with an energy resolution of about 1 MeV [15,16]. The relative tagging efficiency was monitored throughout the experiment using a ionization chamber which measures the overall photon flux and absolute measurements were regularly made by a total-absorption lead glass counter, which was moved into the beam line at reduced photon intensity. In this way, the intensity of the tagged photon flux was known with an accuracy of 5% [17].

A high-pressure (~4 bar) polarized ^{3}He gas target has for the first time been used with a photon beam line. The polarized gas was contained in a cylindrical cell with a total length of 20 cm and an outer diameter of 6 cm. It is made from quartz glass with two 50 μ thick titanium foils as entry and exit windows for the photon beam. This material was chosen since it provides the necessary gas tightness and give an acceptably long relaxation time (~20) hours of the gas polarization.

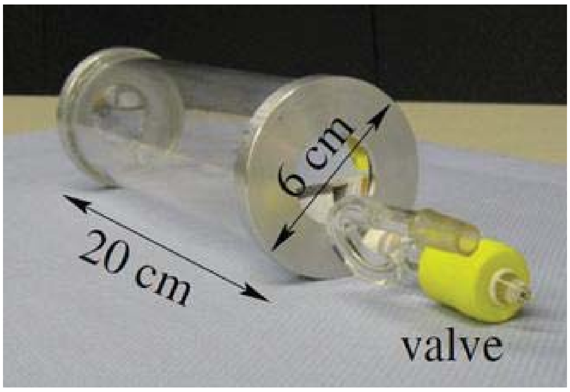

Figure 1

Under these conditions, with a gas pressure of 5 bar, the ^{3}He gas target density is relatively low ($2.5\cdot 10^{21}$ nuclei/cm^2) compared to that of a solid or liquid target (about 100 times less). Despite this, the ^{3}He gas target is pure, so it has a greater fraction of polarized neutron with respect to the deuterated butanol case.

After the polarization process of the gas, performed outside the experimental area using the the Metastability Exchange Optical Pumping (MEOP) method, the target cell was inserted into the detector system. There a solenoid provided a very homogeneous guiding magnetic field to maintain the polarization alignment (see Figure 2). A relative measurement of the polarization was done every hour using NMR techniques. The principles of operation for this target, as well as the complete target setup used in the experiment are detailed in [18]. The ^{3}He nuclei were polarized typically up to about 70% with relaxation times of about 20 hours. The target density and polarization degree were known with an accuracy of 2% and 5% respectively [18].

The reaction products were detected by a detector system, consisting of the Crystal Ball (CB) NaI spectrometer, complemented by the Multi-Wire Proportional Chambers (MWPCs), used to identify and track the charged particles, and the cylindrical Particle Identification Detector (PID), used to distinguish the charged from the neutral particles detected by the CB (see Figure 2). The combined information provided by these three detectors provides accurate energy, angle and particle identification in the azimuthal (ϕ) and polar (θ) angular regions from 0^o to 360^o and from 21^o to 159^o, respectively.

Finally, in order to suppress as much as possible the background originated from electromagnetic reactions inside the target, a threshold Cherenkov detector was installed. The detector was located downstream of the CB detector to cover the polar angular region from 0^o to 18^o, where practically all electromagnetic events occur.

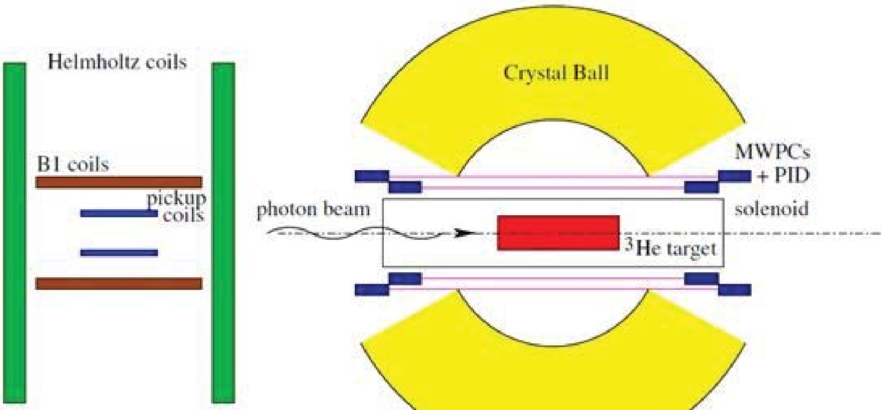

Figure 2

Unpolarized data analysis

a. Total inclusive cross section (σ_{tot})

To avoid large systematic uncertainties arising from the detection of all single partial reaction channels, an inclusive method of data analysis has been developed to directly determine the total photoabsorption cross section (see, for instance, [19]). In this method the identification of individual processes is not required; what is necessary is to observe at least one reaction product of all possible hadronic final states with almost complete acceptance, as far as solid angle and efficiency are concerned. The corrections needed to evaluate the detector efficiencies and the loss of events emitted in the angular/momentum regions not covered by the detector have to be kept as low as possible to minimize model dependent contributions.

Due to the roughly isotropical distributions of the photo-emitted pions and of the protons coming from photodisintegration in the considered photon energy range, the CB detector, with a very large covered solid angle and a detection efficiency greater than about 99% for both charged hadrons and γs coming from neutral meson decays, meets these requirements.

The event selection procedure for the inclusive method was quite simple: at least one cluster (i.e. a group of adjacent hit crystals) was required to be present inside CB. To further reject e.m. background, only clusters which had a total energy of 40 MeV or higher were used in the analysis. Simulations show that, under these conditions, a large fraction of the total inclusive cross section, from ~90% at E_γ=200 MeV to ~ 96% at E_γ=500 MeV can be directly accessed since the minimum pion momenta for the $\pi^\pm$ X channels are above the CB detection threshold due to the dominance of the quasi-free processes on single nucleons. A model dependent extrapolation was evaluated to obtain the remaining part of the total photoabsorption cross section (about 5% of σ_{tot}) which produces events where all charged hadrons and/or γs from π^0 decay are emitted outside the detector acceptance.

The corrections for the $\gamma\ ^3\text{He} \rightarrow \pi$ X reaction were evaluated assuming that only quasi-free processes on the single nucleons are present and using the angular distributions for the γ N $\rightarrow \pi$ N processes predicted by the MAID multipole analysis [4]. The missing contribution from the the $\gamma\ ^3\text{He} \rightarrow$ ppn channel has been evaluated taking into account that the dominant reaction mechanism is the absorption on a correlated (n,p) pair.

The systematic error associated to the simplified models used to evaluate the extrapolation corrections is estimated to be 10% of the calculated correction. The combination of all different sources, gives an overall systematic error of about 6% of σ_{tot}.

In Figure 3 the values of the unpolarized total inclusive cross section σ_{tot} obtained from the present experiment after the subtraction of the empty target spurious contributions are compared to previous results [19]. In this and in all following plots, the error bars are statistical and the hatched band shows the estimated systematic uncertainties.

The good agreement that can be clearly seen with respect to the published data gives confidence in the total inclusive procedure.

b. Partial reaction channels

In order to provide additional experimental information, the particle identification capabilities of the experimental apparatus were used to evaluate the total cross section for the semi-exclusive channels (i) $\gamma\ {}^3He \to \pi^0\ X$, (ii) $\gamma\ {}^3He \to \pi^\pm\ X$ and for the photodisintegration channel (iii) $\gamma\ {}^3He \to ppn$. All these cross sections have not been measured yet.

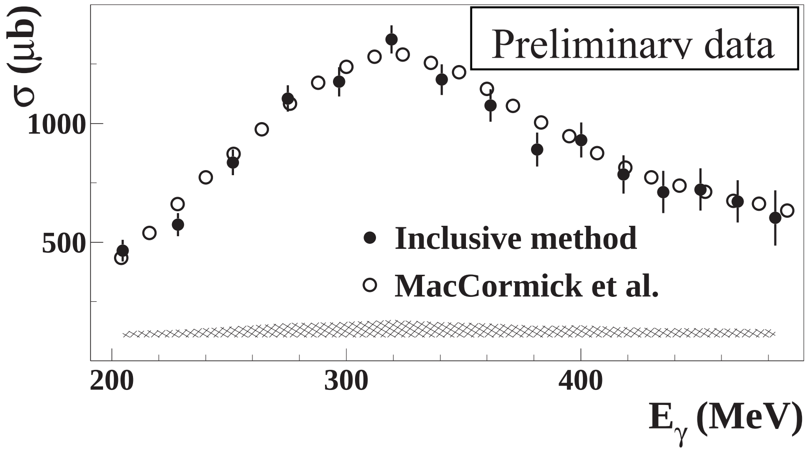

Figure 3

The yield from (i) was evaluated by selecting events having two or three neutral clusters in CB. The π^0 mesons were identified by a standard $\gamma-\gamma$ invariant mass analysis. The main parasitic reactions that can contaminate the data are the $\gamma\ {}^3He \to \pi^0\ \pi^0\ X$ channels. For this reason, the data analysis was limited to $E_\gamma < 450$ MeV. The small contamination present above $E_\gamma = 400$ MeV was evaluated assuming the dominance of the quasi-free $\gamma N \to \pi^0\ \pi^0\ N$ processes and using the measured unpolarized cross section values for these processes.

For this and for the other partial channels, the extrapolation correction have been evaluated as previously explained for the total inclusive method. The systematic error associated to the event selection procedure and to the efficiency corrections was evaluated to be 3% of the measured yield. The addition in quadrature of all the different sources of systematic errors gives an overall systematic error of about 7% of the measured reaction yield.

The obtained results are shown in Fig.4a and compared to the predictions of the Fix-Arenhovel (FA) model (solid line) and of a very simple (VS) model based on the MAID multipole analysis (dashed line). The FA model is a straightforward extension of the work previously done on the deuteron [20]. The elementary production operator $\gamma N \to \pi N$ is taken from the MAID multipole analysis and is afterwards embedded into the wave function to take into account the nuclear effects. Empirical attenuation factors were then applied to take into account the absorption of the photoemitted particles inside the nuclear medium. On the contrary, in our VS model it naively assumed that that all nucleons inside ^{3}He behave as free ones.

As it can be clearly seen from the difference between these two models, the predicted role of the nuclear effects result in damping and broadening the peak corresponding to the Δ resonance excitation.

Proton and charged pions hitting the CB were identified by a standard dE/dX-E analysis, using the energy information from CB, PID and the direction information from MWPCs [17]. In both cases, software cuts on the interaction vertex coordinates of the selected events allowed a suppression of a large fraction of the events originating from the target walls and windows [18]. The trajectory reconstruction efficiency was directly determined from the experimental data since a part of the $\pi^{\pm}$ events can be discriminated using the approximate angular information given by CB alone instead of the one given by MWPCs.

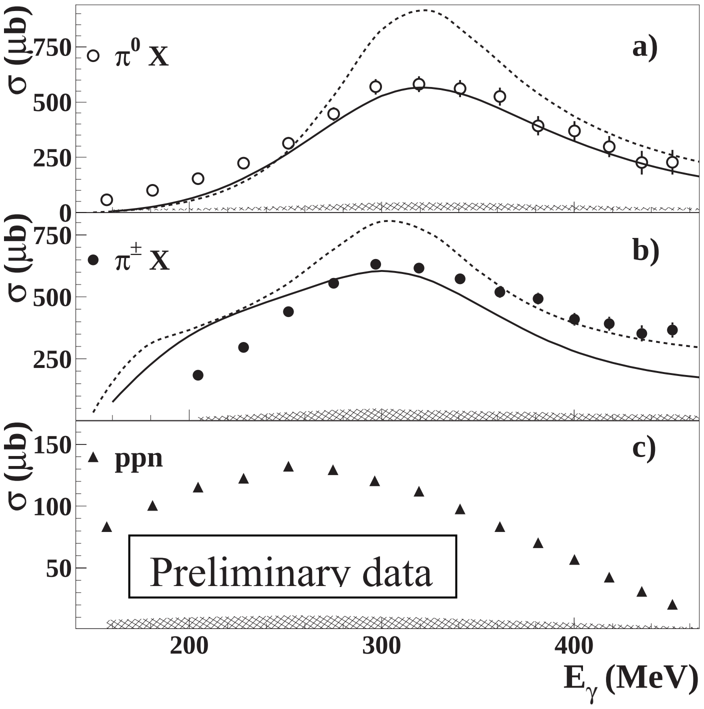

Figure 4

This efficiency was then determined by measuring the fraction of such events that have a reconstructed trajectory using MWPCs information and was found to be about 85% (95%) for $\pi^{\pm}$ (protons) with a smooth dependence on the incident photon energy. An absolute systematic error of 3% has been estimated on this parameter.

Events from reaction (ii) were obtained by requiring one charged pion being identified in CB. In a similar way as before, the data analysis was limited to $E_\gamma < 450$ MeV and the small contamination present above $E_\gamma = 400$ MeV due to the double pion channels was evaluated from the known cross section measured on the single nucleons. The systematic error associated to the event selection procedure and to efficiency corrections was evaluated to 3% of the measured yield. The addition in quadrature of all the different sources of systematic errors gives an overall systematic error of about 7% of the measured reaction yield.

The obtained results are shown in Fig.4b and compared to the predictions of the FA model (continuous line) and of our VS model. In this case the FA model does not well reproduce our data which for to $E_\gamma > 350$ MeV are very close to our simple model.

The yield from reaction (iii) was evaluated by selecting events having one or two protons identified in CB. Since the major competing background is due to the $\gamma\ {}^3He \rightarrow ppn\pi^0$ reaction, the presence of less than two neutral clusters detected inside CB in coincidence with the proton(s) was also required. The residual background was evaluated from the missing mass spectrum $\gamma\ {}^3He \rightarrow p(p)X$ and subtracted accordingly. The addition in quadrature of all the different sources of systematic errors gives an overall systematic error of about 8% of the evaluated reaction cross section.

The resulting total unpolarized cross section is shown in Fig.4c. In this case, since no specific model is available for comparison.

Polarized results and comments

In the analysis of the helicity dependent data, all previously mentioned analysis methods were used to evaluate the difference $\Delta\sigma_{tot} = (\sigma_P - \sigma_A)$. In this case the contributions from all non-polarized materials present in the target cell vanish.

The analysis procedure described above results in the helicity dependent total inclusive cross section $\Delta\sigma_{tot}$ as depicted in Fig.5 in comparison with the predictions of our VS model, where it was again assumed that the nucleons inside ^{3}He behave as free ones. Only the effects on the nucleon spin alignments due to the ^{3}He s' and d-state probabilities have been taken into account according to equation 1.

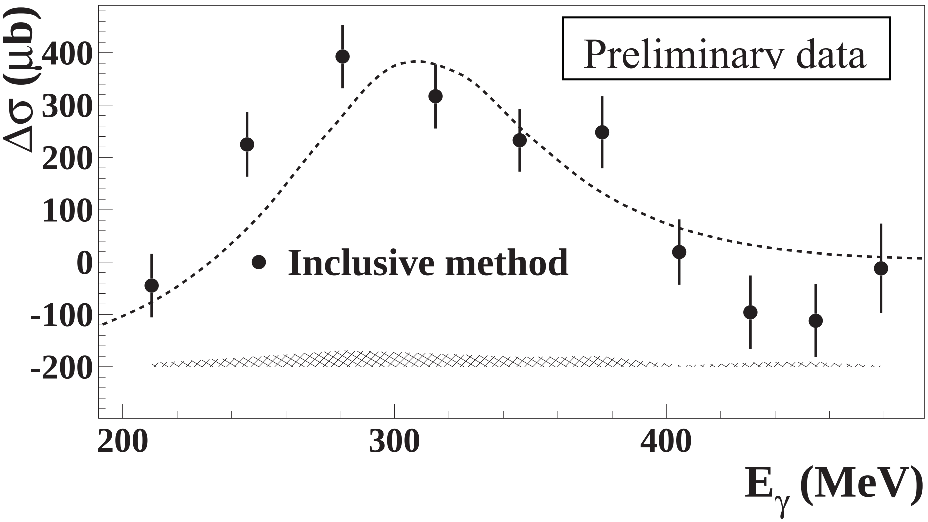

Figure 5

The agreement between our data and the VS model is reasonable, taking into account the non-negligible statistical experimental errors. This is a hint that nuclear effects are less important than in the unpolarized case.

The total helicity dependent cross sections Δσ for the channels (a) $\gamma\ ^3\text{He} \rightarrow \pi^0\ X$, (b) $\gamma\ ^3\text{He} \rightarrow \pi^\pm\ X$ and (c) $\gamma\ ^3\text{He} \rightarrow ppn$ are shown in Fig.6 together with the corresponding predictions of the FA (solid line) and VS (dashed line) model. As in the unpolarized case the FA model fairly well reproduces the) $\gamma\ ^3\text{He} \rightarrow \pi^0\ X$ data only at higher photon energies and it does not reproduces the shape of the $\gamma\ ^3\text{He} \rightarrow \pi^\pm\ X$ data.

Our VS model well reproduces the data at higher photon energies for both reactions. This is a further confirmation that the effects more directly related to the composite nuclear target structure do not have a strong helicity dependence and their net effect is then reduced in the Δσ case.

Conclusions

The helicity dependence of the total inclusive photoabsorption cross section on ^{3}He and both the unpolarized and the helicity dependent cross sections of the partial reaction $\gamma\ ^3\text{He} \rightarrow \pi^0\ X$, $\gamma\ ^3\text{He} \rightarrow \pi^\pm\ X$ and $\gamma\ ^3\text{He} \rightarrow ppn$ have been measured for the first time at MAMI (Mainz) in the energy region 200 MeV< to $E_\gamma < 450$ MeV.

All these new data provide a very powerful tool to further improve the models for the photoreactions on ^{3}He in the Δ resonance region. Available state-of-the-art calculations are not able to describe in a satisfactory manner both the unpolarized and the helicity dependent cross section for the πX channels while no model is at present available for the ppn channel. This fact strongly motivates further theoretical and experimental research in the field.

In order to pin down the origin of these discrepancies the analysis of both the unpolarized and polarized differential cross sections for the $\gamma\, ^3He \to \pi^0\, X$, $\gamma\, ^3He \to \pi^\pm\, X$ is under way.

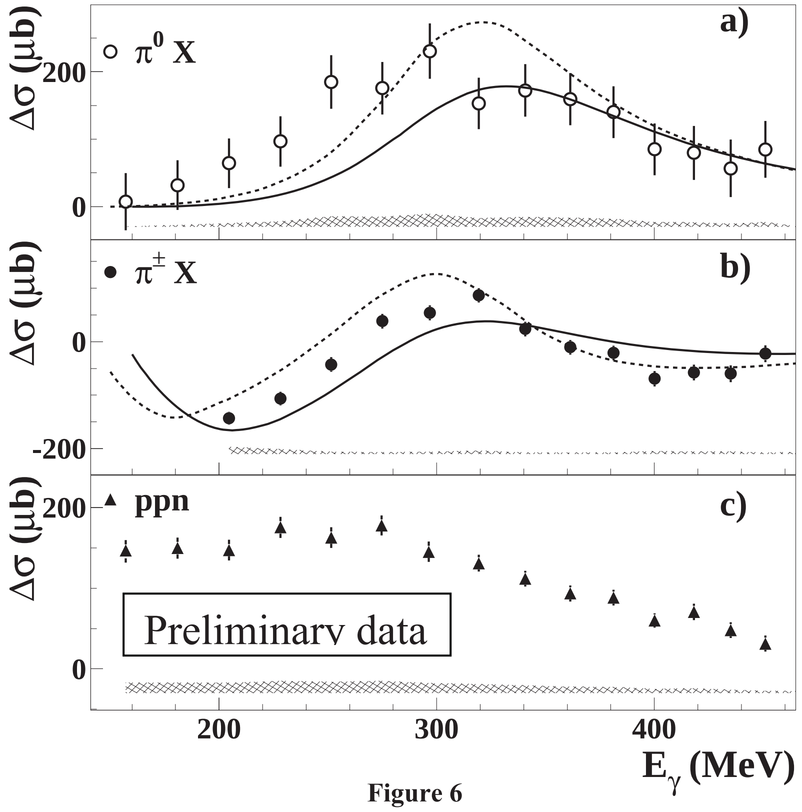

Figure 6

[1] S.B. Gerasimov, Sov. J. Nucl. Phys., 2 (1966) 430.
[2] S.D: Drell and A.C Hearn, 1966 Phys. Rev. 96 (1966) 1428.
[3] R.A. Arndt *et al.,* Phys. Rev. C66 (2002) 055213.
[4] D. Drechsel, S.S. Kamalov and L. Tiator, Eur. Phys. J. A34 (2007) 69.
[5] A. Fix and H.Arenhoevel, Eur. Phys. J. A25 (2005) 115.
[6] S. Sumowigado and T.Mart, Phys. Rev. C60 (1999) 028201.
[7] Q.Zhao , J.S. Al-Khalili and C.Bennhold , Phys. Rev. C65 (2002) 032201.
[8] N.Bianchi and E.Thomas, Phys. Lett. B450 (1999) 439.
[9] J.Ahrens *et al.,* Phys. Rev. Lett . 84 (2000) 5950.
[10] H.Dutz *et al.,* Phys. Rev. Lett. 93 (2004) 032003.
[11] H.Dutz *et al.,* Phys. Rev. Lett. 94 (2005) 162001.
[12] J.Ahrens *et al.,* Phys. Rev. Lett . 97 (2006) 202303.
[13] J.Ahrens *et al.,* Phys. Lett . B672 (2006) 328.
[14] J.L. Friar *et al.,* Phys. Rev. C42 (1990) 2310.
[15] I. Anthony *et al.,* Nucl. Instrum. Methods A301 (1991) 230.
[16] S.J. Hall *et al.,* Nucl. Instrum. Methods A368 (1996) 398.
[17] S. Schumann *et al.,*, Eur. Phys. J. A43 (2010) 269.
[18] J. Krimmer *et al.,* Nucl. Instrum. Methods A648 (2011) 35.
[19] M McCormick *et al.,* Phys. Rev. C53 (1996) 41.
[20] A. Fix and H.Arenhoevel, Phys. Rev. C72 (2005) 064004.

ON PHOTOPRODUCTION OF ETA-MESIC NUCLEI AT THE LPI SYNCHROTRON

V.A. Baskov[1], *A.V. Koltsov*[1], *A.I. L'vov*[1], *A.I. Lebedev*[1], *L.N. Pavlyuchenko*[1],
V.V. Polyanskiy[1*], *E.V. Rzhanov*[1], *S.S. Sidorin*[1], *G.A. Sokol*[1],
S.V. Afanasiev[2], *A.I. Malakhov*[2], *A.S. Ignatov*[3], *V.G. Nedorezov*[3]

[1]P.N. Lebedev Physical Institute of the Russian Academy of Sciences, Moscow, Russia
[2]Joint Institute for Nuclear Research, Dubna, Russia
[3]Institute for Nuclear Research of the Russian Academy of Sciences, Moscow, Russia

A brief review of searches for η-mesic nuclei is presented with emphasis on photoreactions. Results of a new experiment done at the LPI electron synchrotron are reported. They are as follows.

New data on photoproduction of η-mesic nuclei off ^{12}C have been collected at the bremsstrahlung photon beam of $E_{\gamma\,\max} = 850$ MeV. An experimental setup with two plastic time-of flight spectrometers detected correlated $\pi^+ n$ and pn pairs from annihilation of η-mesons stopped in the nuclear matter and measured their velocity distributions. Data analysis was performed using an Intra Nuclear Cascade Model in the GEANT-3 framework in order to take into account properties of the setup and physical background. A separation between charged pions and protons was achieved using information on velocities and ranges of the particles in plastic detectors. The obtained data show, apart from previously observed $\pi^+ n$ pairs from one-nucleon annihilation of etas (via $\eta N \to \pi N$), a presence of emitted correlated pn pairs with velocities corresponding to the kinematics of the near-threshold reaction of two-nucleon absorption of the η-meson in the nucleus ($\eta NN \to NN$). Assuming that such $\pi^+ n$ and pn pairs are mostly produced through formation and decay of quasi-bound states of the η-meson and a nucleus (i.e. η-mesic nuclei $_{\eta}A$), the cross section of η-mesic nuclei formation was estimated as $\sigma(\gamma + {}^{12}\mathrm{C} \to {}_{\eta}A + X) \lesssim 10~\mu$b.

Introduction: η-mesic nuclei

η-mesic nuclei, i.e. nuclear systems $_{\eta}A$ having the η-meson bound in a nuclear orbit by strong interaction with A nucleons, have been predicted long ago [1, 2] — soon after recognizing the attractive character of the ηN interaction at low energies [3]. Observations and investigations of these exotic systems would be very valuable for understanding meson-baryon interactions in free space and in nuclei and for studies of properties of hadrons in the dense nuclear matter.

The η-meson, together with pions and kaons, belongs to the SU(3) octet of pseudoscalar mesons and has, therefore, a similar $q\bar{q}$ space structure. In contrast to the pion, however, the pseudoscalar coupling of η to the nucleon is empirically rather small [4]. Nevertheless the amplitude of ηN s-wave scattering is not as small as that for πN scattering because of the contribution of the s-wave resonance $S_{11}(1535)$ which is actually a chiral partner of the nucleon — the lowest lying baryon with the opposite parity to the nucleon. This resonance has the mass slightly above the ηN threshold, $m_\eta + m_N = 1486$ MeV, and owing to its very strong coupling to the ηN channel [with the branching ratio Br $(S_{11}(1535) \to \eta N) \simeq 55\%$] strongly enhances all interactions in this channel. A nice illustration of this feature is provided by Mainz data [5] on the total cross section of η photoproduction off protons. A huge near-threshold enhancement shown in Fig. 1 is just a manifestation of the $S_{11}(1535)$ resonance excited in the reaction $\gamma p \to S_{11}(1535) \to \eta p$.

---

[*] Email: poly@pluton.lpi.troitsk.ru

The $S_{11}(1535)$ resonance strongly contributes to the low-energy ηN scattering and, in particular, makes the threshold value of the ηN scattering amplitude (i.e. the ηN scattering length $a_{\eta N}$) positive. In the framework of a dynamical resonance model for the coupled channels πN, ηN and $\pi\pi N$, Bhalerao and Liu [3] found

$$a_{\eta N} = 0.28 + i\,0.19 \text{ fm}. \tag{1}$$

The positive value of $\mathrm{Re}\, a_{\eta N}$ means an effective attraction between η and N, so that one can expect that several nucleons could jointly bind η to a nuclear orbit. The first-order static-limit on-shell optical potential of η in the nuclear matter at zero energy $E_\eta^{\rm kin} = 0$ is equal to

$$U(r) = -2\pi\, a_{\eta N}\, \rho(r) \Big(\frac{1}{m_\eta} + \frac{1}{m_N}\Big), \tag{2}$$

what gives [together with Eq. (1)] $U = -34 - i\,23$ MeV at normal nuclear matter density $\rho = \rho_0 = 0.17$ fm^{-3}. The imaginary part of the potential describes a local absorption rate $\Gamma = -2\,\mathrm{Im}\, U$ of η in the nuclear substance.

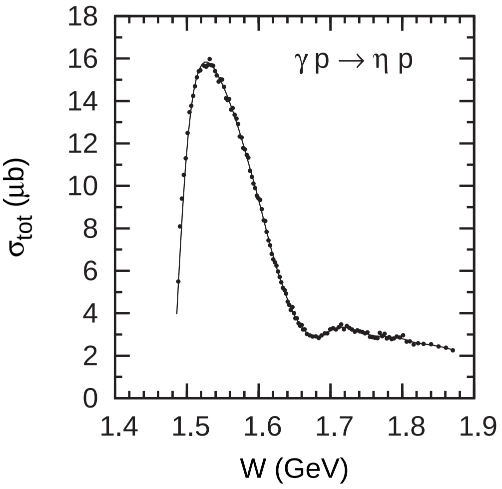

Figure 1: Total cross section of $\gamma p \to \eta p$ [5] as an illustration of the $S_{11}(1535)$ resonance strength in the ηN channel.

With the above strength of the ηA potential, η-mesic nuclei $_\eta A$ are expected to exist for all $A \geq 10$ [6, 7]. Actually, due to a sharp (cusp) energy dependence of the ηN scattering amplitude near threshold, Fermi motion of nucleons and η reduces the optical potential [especially its imaginary part], and this makes η-mesic nuclei to exist only for $A \geq 12$. For binding energies and widths of the lightest η-mesic nuclei Haider and Liu predicted [6, 7]

$$\begin{aligned} E_\eta &= -1.19 \text{ MeV}, & \Gamma_\eta &= 7.34 \text{ MeV} & \text{for } & {}^{12}_{\eta}\mathrm{C}, \\ E_\eta &= -3.45 \text{ MeV}, & \Gamma_\eta &= 10.76 \text{ MeV} & \text{for } & {}^{16}_{\eta}\mathrm{O}, \\ E_\eta &= -6.39 \text{ MeV}, & \Gamma_\eta &= 13.20 \text{ MeV} & \text{for } & {}^{26}_{\eta}\mathrm{Mg}. \end{aligned} \tag{3}$$

Note, however, that a stronger ηN scattering amplitude was inferred in some other analyses. For example, using a K-matrix model for coupled channels πN, ηN, γN and $\pi\pi N$, Green and Wycech [8, 9] found from fit to available data

$$a_{\eta N} = (0.91 \pm 0.06) + i\,(0.27 \pm 0.02) \text{ fm}. \tag{4}$$

With such a big strength of ηN interaction lighter η-mesic nuclei could also exist.

As an example of different predictions for binding energies and widths of η-mesic nuclei we mention very elaborated calculations [10–12], in which a model for meson-baryon interaction with dynamically generated resonances was build using a unitarized chiral perturbation theory for coupled channels πN, ηN, $K\Lambda$, $K\Sigma$ and $\pi\pi N$ and then self-energies of all the particles in the nuclear matter were evaluated consistently. This approach leads to the ηN scattering length $a_{\eta N} = 0.264 + i\,0.245$ fm close to that obtained in Eq. (1). The resulting ηA potential is, however, found stronger owing to nonlinear dressing effects: $U = -54 - i\,29$ MeV at normal nuclear density. Also stronger are η-meson bindings found in [12]:

$$\begin{aligned} E_\eta &= -9.71 \text{ MeV}, & \Gamma_\eta &= 35.0 \text{ MeV} & \text{for } & {}^{12}_{\eta}\mathrm{C}, \\ E_\eta &= -12.57 \text{ MeV}, & \Gamma_\eta &= 33.4 \text{ MeV} & \text{for } & {}^{24}_{\eta}\mathrm{Mg}. \end{aligned} \tag{5}$$

Bindings with equally large widths arise also in calculations [13–15] that use a chiral doublet model and treat ηA and $S_{11}(1535)A$ attraction as a result of partial restoration of chiral symmetry in the dense nuclear matter leading to reduction of the $S_{11}(1535)-N$ mass gap. It is clear that experimental data on energies and widths of η-mesic nuclei are needed to test these and many other models and calculations.

Signature for eta-mesic nuclei produced in photoreactions

A mechanism of η-mesic nuclei formation and decay in the photoreaction

$$\gamma + A \to N' + {}_{\eta}(A-1) \to N' + \pi + N + (A-2) \tag{6}$$

is shown in Fig. 2a. A fast nucleon N' ejected forward at the first stage of the reaction, i.e. in the subprocess

$$\gamma + N' \to N' + \eta_{\text{slow}}, \tag{7}$$

escapes the nucleus, whereas a slow η is captured by remaining $A-1$ nucleons to a bound state. At $E_\gamma \sim 800-900$ MeV, a minimal momentum transfer to η in the reaction (7) is not large (less than 70 MeV$/c$). That is why the total cross section of η-mesic nuclei formation off light nuclei (like carbon or oxygen implied in the following) turns out to be a few μb [16–21], i.e. $\simeq 2-7\%$ of the total cross section $\sigma^{\eta}_{\gamma A}$ of inclusive η photoproduction, with the exact value strongly dependent on the assumed strength of the optical potential U.

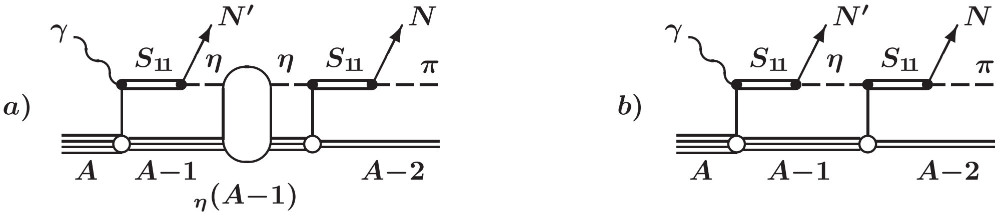

Figure 2: a) η-mesic nuclei formation and decay with the emission of back-to-back πN pairs. b) Background creation of back-to-back πN pairs by unbound η.

Energies $E[{}_{\eta}(A-1)]$ of the produced η-mesic nuclei can, in principle, be determined through missing mass measurements in the reaction (γ, p) using tagged photons γ and a magnetic spectrometer for $N' = p$. Indirectly, the same energy

$$E[{}_{\eta}(A-1)] = E_\eta + E_{A-1} = E_{\pi N} + E_{A-2} \tag{8}$$

can also be found from the observed energy of a correlated back-to-back πN pair produced at the second stage of the reaction (6) where the captured η meson annihilates through the subprocess

$$\eta N \to N\pi. \tag{9}$$

The energy excitation of $(A-2)$ in (8) is not a fixed value. It rather depends on whether an s-shell or p-shell nucleon N is knocked out in the process (9). Therefore a distribution of the experimental observable $E_{\pi N}$ has appropriately a bigger width than the width of the η-mesic nucleus.

Neglecting binding and Fermi motion of nucleons and η, we have the following kinematical characteristics of the ejected correlated πN pairs (as for energies, momenta and velocities):

$$\begin{aligned}
&\sqrt{s} = E_\pi + E_N = m_\eta + m_N = 1486 \text{ MeV}, \\
&E_\pi^{\text{kin}} = 313 \text{ MeV}, \qquad E_N^{\text{kin}} = 94 \text{ MeV}, \qquad p_\pi = p_N = 431 \text{ MeV}/c, \\
&\beta_\pi = 0.95, \qquad \beta_N = 0.42.
\end{aligned} \tag{10}$$

A simple simulation that takes into account the Fermi motion of nucleons and η as well as binding of these particles reveals that fluctuations around these ideal parameters are substantial (see Fig. 3) [specifically, we used in this simulation the η-meson binding energy of 10 MeV with the width 25 MeV; for nucleons, we assumed a Fermi-gas distribution with binding energies distributed between 5 and 30 MeV]. In particular, the angle $\theta_{\pi N}$ between the emitted pion and nucleon may not be so close to 180°, and a subtraction of background events with $\theta_{\pi N} \neq 180^\circ$ used sometimes in practice should be done cautiously. A shift of the peak down to 1486 MeV in the distribution of the total energy $E_{\pi N} = E_\pi + E_N$ seen in Fig. 3 is related with binding of both the η-meson (by 10 MeV) and the nucleon (by 15 MeV).

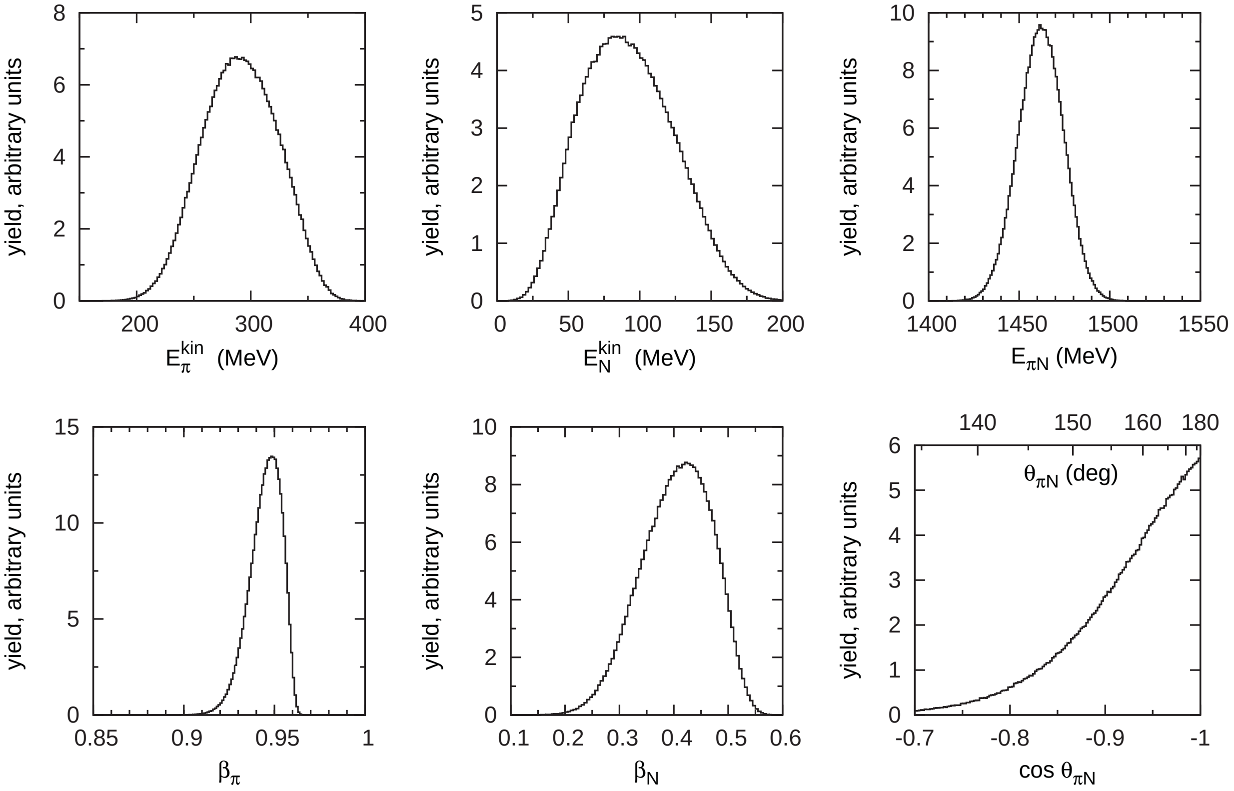

Figure 3: Simulation of πN pairs emitted in η-mesic nuclei decays. Shown are distributions over kinetic energies of the particles, their total energy, velocities, and the πN relative angle.

Notice that πN pairs with the characteristics (10) do not necessary originate from η-mesic nuclei decays. They can also be produced by slow etas in a background nonresonance process shown in Fig. 2b. The resonance and nonresonance processes correspond to a resonance (Breit-Wigner) and nonresonance part of the full propagator [i.e. the Green function $G(\boldsymbol{r}_1, \boldsymbol{r}_2; E_\eta)$] of the η-meson moving in the optical potential $U(r)$. Jointly, these parts generate a complicated spectrum of E_η similar to that obtained in a toy model with a square-well potential [22, 23]. Shown in Fig. 4 is the spectral function in that model,

$$S(E_\eta) = \iint \rho(\boldsymbol{r}_1)\, \rho(\boldsymbol{r}_2)\, |G(\boldsymbol{r}_1, \boldsymbol{r}_2; E_\eta)|^2\, d\boldsymbol{r}_1 d\boldsymbol{r}_2, \tag{11}$$

that characterizes near-threshold energy distribution of the propagated etas as well as the near-threshold energy dependence of the yield of πN pairs produced by these η. Bound states of the η-meson give pronounced peaks in the yield of the πN pairs at subthreshold energies E_η. Generally, observation of a relatively narrow resonance peak in the spectrum of E_η in the region $E_\eta < m_\eta$ is mandatory for claiming an observation of η-mesic nuclei at all. We refer to recent works by Haider and Liu [24, 25] where a deeper and more elaborated consideration is given in relation with a recent experiment.

Since η is isoscalar, the πN pairs produced in the subprocess (9) have isospin $\frac{1}{2}$ and hence the following isotopic contents [for η-mesic nuclei with $A \gg 1$]:

$$\mathrm{Br}\,(\pi N) = \begin{cases} 1/3 & \text{for} \quad \pi^+ n, \\ 1/6 & \text{for} \quad \pi^0 p, \\ 1/6 & \text{for} \quad \pi^0 n, \\ 1/3 & \text{for} \quad \pi^- p. \end{cases} \qquad (12)$$

From these, the channel $\pi^+ n$ was chosen for detection in our experiment.

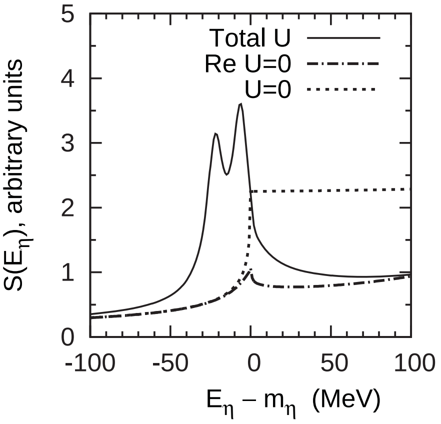

Figure 4: Spectral density of E_η in a model with a rectangular-well attractive optical potential U that approximately simulates the η-mesic nucleus ${}^{12}_{\eta}$C [22]. The chosen potential was so strong that it bounded η both in the s and p-wave states. When the attractive potential is turned on, a pronounced peak (peaks) in the spectral density emerges at subthreshold resonance energy (energies).

Previous searches for η-mesic nuclei

Searches for η-mesic nuclei began very soon after their predictions [1] followed by suggestions [2, 16–18, 26] to seek these novel high-energy nuclear excitations in missing-mass experiments using the inclusive reactions (π^+, p) and (γ, p).

The first two experiments have been done along this line in 1988 at Brookhaven [27] and Los Alamos [28, 29]. In both experiments, a π^+ beam was used and several targets (Li, C, O and Al) were examined. The inclusive (π^+, p) reaction

$$\pi^+ + A \to {}_{\eta}(A-1) + p \qquad (13)$$

was studied in [27] with a magnetic spectrometer, whereas the Los Alamos experiment had also an additional 4π BGO crystal ball for detecting charged paticles ejected in the subprocess (9) of η-mesic nuclei decays to πN pairs in coincidence with the forward proton p.

The Brookhaven experiment did not find a theoretically expected signal [2] — a relatively narrow peak of a predicted strength in the missing mass spectrum. The team working at Los Alamos did report a preliminary evidence for a wanted peak for the ^{16}O target but this report was not confirmed (published) since then.

It was recognized in the following that the above obtained negative or incomplete results do not necessarily mean that the predicted η-mesic nuclei do not exist. It was possible that the binding energies and especially the widths of the η bound states were theoretically underestimated. This point of view was supported by many-body calculations [30] taking into account some effects disregarded in the first theoretical works [1, 2], in particular — dressing, binding and collisional decays of the $S_{11}(1535)$ resonance in the dense nuclear matter. The analysis of [30] was later extended and revised [10–12] (in particular, dressing of mesons was also included) with the main conclusion survived that η-mesic nuclei widths are bigger than those found in [1, 2].

The next experiment has been performed at the Lebedev Physical Institute in Moscow/Troitsk [23, 31] (see also a summary in [32]). It was triggered [33, 34] by a suggestion [35] to seek η-mesic nuclei through observing decay products of η-mesic nuclei, namely two correlated back-to-back particles, a pion and a nucleon, ejected in the process of annihilation of captured η-mesons in the nucleus, Eq. (9). It was hoped that a background for the two very energetic particles (the pion and the nucleon) ejected in decays of η-mesic nuclei transversely to the beam would be lower than that for ejection of forward protons in the inclusive processes. Besides, it was hoped that background conditions in photon-induced reactions would be generally better than those in pion-induced ones.

Studies of the reaction

$$\gamma + {}^{12}\mathrm{C} \to ({}^{11}_{\eta}\mathrm{Be} \;\text{ or }\; {}^{11}_{\eta}\mathrm{C}) + N \to \pi^+ + n + X + N \tag{14}$$

done in the middle of 1990's at the LPI electron synchrotron indeed showed a signal of an enhanced production of the correlated back-to-back $\pi^+ n$ pairs ejected transversely to the photon beam when the photon energy exceeded the η-meson photoproduction threshold. Energy resolution of the experimental setup was, however, not sufficient to resolve a peak similar to that shown in Fig. 4 and to determine whether the observed correlated pairs were produced by bound or unbound intermediate etas.

After the works [23, 31] gaining and using information on the decay products became mandatory for experiment planning and data analysis in all further searches for η-mesic nuclei.

In 2004 an evidence for the η-mesic nucleus ${}^{3}_{\eta}\mathrm{He}$ formed in the reaction

$$\gamma + {}^{3}\mathrm{He} \to {}^{3}_{\eta}\mathrm{He} \to \pi^0 + p + X \tag{15}$$

has been reported from Mainz [36]. A resonance-like structure was observed in a contribution to the cross section from back-to-back $\pi^0 p$ pairs found after a background subtraction. A later study [37] revealed, however, that the background has a rather complicated structure, so that the conclusions of Ref. [36] cannot be confirmed. At the moment their statement is that the existence of the η-mesic nucleus ${}^{3}_{\eta}\mathrm{He}$ is not yet established.

One more attempt to find η-mesic nuclei by detecting their $\pi^- p$ decay products has recently been done at the JINR nuclotron [38]. The reaction studied was

$$d + {}^{12}\mathrm{C} \to ({}^{11}_{\eta}\mathrm{Be} \;\text{ or }\; {}^{11}_{\eta}\mathrm{C}) + N_1 + N_2 \to \pi^- + p + X + N_1 + N_2. \tag{16}$$

The measured effective mass spectra of the correlated back-to-back $\pi^- p$ pairs show a presence of resonance-like peaks lying slightly below the threshold energy $m_\eta + m_N = 1486$ MeV. However, a consistent interpretation of these peaks was not yet obtained.

To date the strongest evidence for the existence of η-mesic nuclei came from the precision COSY-GEM experiment [39]. Following ideas of the work [40] borrowed in turn from previous experience in studying deeply-bound pionic states in nuclei, the reaction

$$p + {}^{27}\mathrm{Al} \to {}^{3}\mathrm{He} + {}^{25}_{\eta}\mathrm{Mg} \to {}^{3}\mathrm{He} + p + \pi^- + X \tag{17}$$

of a recoilless formation of the η-mesic nuclei ${}^{25}_{\eta}\mathrm{Mg}$ was explored and the mass of this η-mesic nucleus was determined through precision missing-mass measurements in $(p, {}^{3}\mathrm{He})$. A clear peak was found in the missing mass spectrum that corresponds to the binding energy -13.13 ± 1.64 MeV and the width 10.22 ± 2.98 MeV of the formed η-mesic nucleus. An upper limit of ≈ 0.5 nb was found for the cross section of the η-mesic nucleus formation.

Recently Haider and Liu argued [24, 25] that the observed peak in (17) is shifted down from the genuine binding energy of η because of interference of the resonance and nonresonance mechanisms of the reaction (similar to those shown in Fig. 2). This very interesting effect signifies that the genuine η binding in ${}^{25}_{\eta}\mathrm{Mg}$ is ≈ -8 MeV with the width ≈ 19 MeV.

On the two-nucleon decay mode of η-mesic nuclei

The main novelty in our present research is exploring a new possibility for searching for η-mesic nuclei, namely through observation of their two-nucleon decay mode arising owing to the two-nucleon absorption of the captured η in the nucleus,

$$\eta NN \to NN, \tag{18}$$

see Fig. 5. Ejected in this process correlated back-to-back nucleons of the NN pairs have very high energies ($E_N^{\rm kin} \simeq \frac{1}{2}m_\eta = 274$ MeV) and momenta ($p_N \simeq 770$ MeV$/c$), so that they are to be visible (especially in coincidence) at the background of other particles emitted in photoreactions at $E_\gamma \sim 800$ MeV and thus should provide a bright signature for the η-mesic nucleus formation.

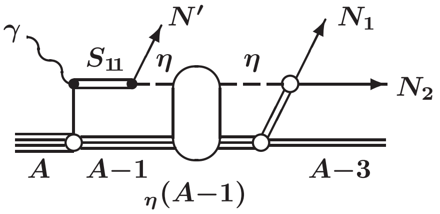

Figure 5: η-mesic nucleus formation and decay with emission of a back-to-back NN pair.

The NN pair production in decays of η in the nuclear matter was considered among other channels by Chiang, Oset and Liu [30] in terms of the self-energy of $S_{11}(1535)$ that includes a contribution of $S_{11}(1535)N \to NN$. A more direct and rather transparent evaluation of this process has been done by Kulpa and Wycech [41] who used available experimental data on the inverse reactions $pp \to pp\eta$, $pn \to pn\eta$ and $pn \to d\eta$ and then converted them into the rate of (18). In terms of the imaginary part W_{NN} of the optical potential U, this rate was found to be proportional to ρ^2, being $W_{NN} = 3.4$ MeV at central nuclear density. This is only about 15% of $W_N \sim 23$ MeV related with the absorption of η by one nucleon. Nevertheless such a small fraction of NN can be quite visible experimentally because of a specific isotopic contents of the πN and NN pairs.

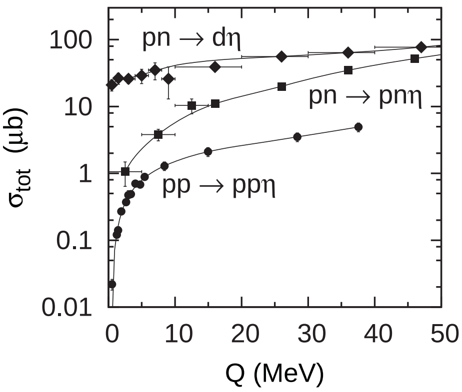

Figure 6: Uppsala-Celsius [42–45] and COSY [46, 47] data (with statistical errors only) on the total cross sections of $pp \to pp\eta$, $pn \to pn\eta$ and $pn \to d\eta$ near threshold vs the excess energy $Q = \sqrt{s} - 2m_N - m_\eta$.

The matter is that $\gtrsim 90\%$ of these NN pairs are proton plus neutron because the cross section of $pp \to pp\eta$ (and $nn \to nn\eta$) is by order or magnitude less than that of $pn \to pn\eta$ (plus $pn \to d\eta$), see Fig. 6 where pertinent Uppsala-Celsius [42–45] and COSY [46, 47] data are shown (and see also, e.g., [48] for theoretical explanations). This difference can be traced to isospin factors and Fermi statistics signs in the dominating pion-exchange mechanism of the reaction $NN \to NN\eta$ shown in Fig. 7. If the experimental setup detects one charged and one neutral particle from the pairs, it detects $\sim 90\%$ of NN and only $\sim 33\%$ of πN. Then count rates of the setup would not be so different for pn and $\pi^+ n$ pairs. That seems to be exactly what we see in our experiment.

Neglecting binding effects and effects of Fermi motion of nucleons and η, we have the following kinematical characteristics of the correlated NN pairs (i.e. energies, momenta, velocities) ejected in η-mesic nuclei decays:

$$E_{N_1}^{\rm kin} = E_{N_2}^{\rm kin} = \frac{1}{2}m_\eta = 274\,\text{MeV}, \qquad p_{N_1} = p_{N_2} = 767\,\text{MeV}/c, \qquad \beta_{N_1} = \beta_{N_2} = 0.63. \tag{19}$$

Actually, the Fermi motion and binding leads to fluctuations around these ideal parameters as a simple simulation reveals, see Fig. 8. Note that the angular correlation in NN pairs is stronger than that in πN pairs — owing to higher momenta of particles in NN.

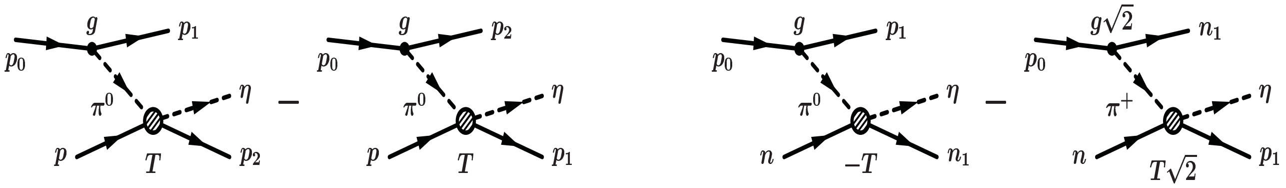

Figure 7: Pion-exchange mechanism of $NN \to NN\eta$. Isospin factors, which accompany the πNN coupling g and the $\pi N \to \eta N$ amplitude T, and the Fermi-statistics signs (both shown in this Figure) jointly determine the big difference between the cross sections of $pp \to pp\eta$ and $pn \to pn\eta$ (plus $pn \to d\eta$). Antisymmetrization of the initial state and initial/final state interactions are not shown.

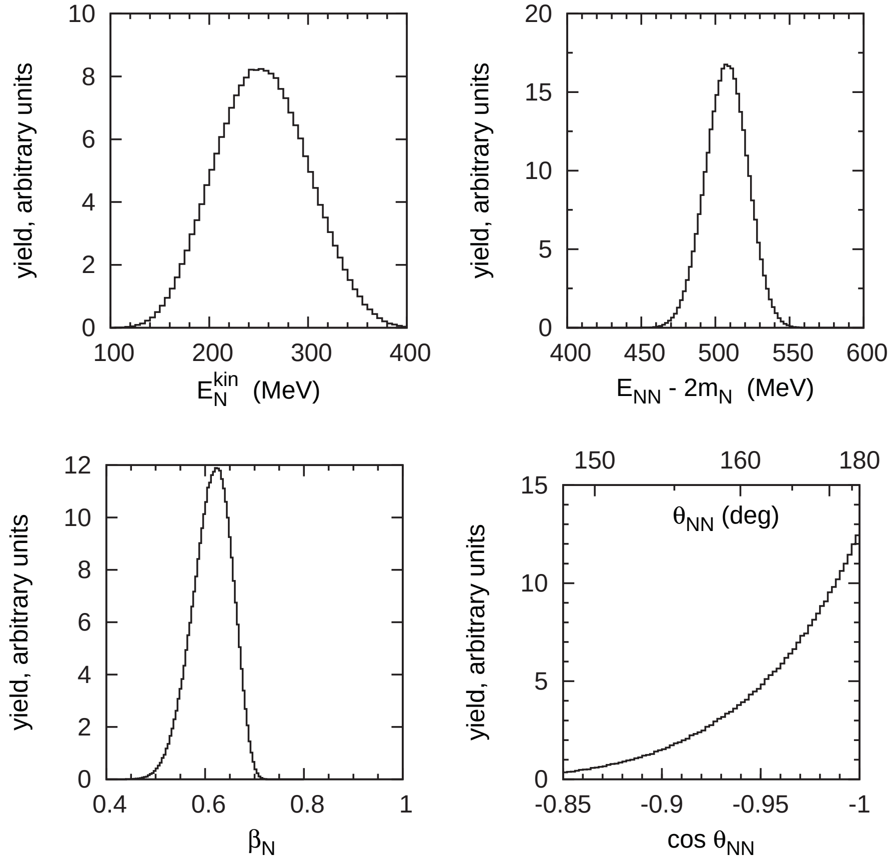

Figure 8: Simulation of NN pairs emitted in decays of η-mesic nuclei. Shown are distributions over the kinetic energy and velocity of one of the nucleons, the total energy of the pair and the relative angle.

The first studies of the photoreaction

$$\gamma + {}^{12}\mathrm{C} \to ({}^{11}_{\eta}\mathrm{Be} \ \text{ or } \ {}^{11}_{\eta}\mathrm{C}) + N \to p + n + X + N \tag{20}$$

have recently been done at the LPI synchrotron and we report below on the obtained results.

Experimental setup at LPI

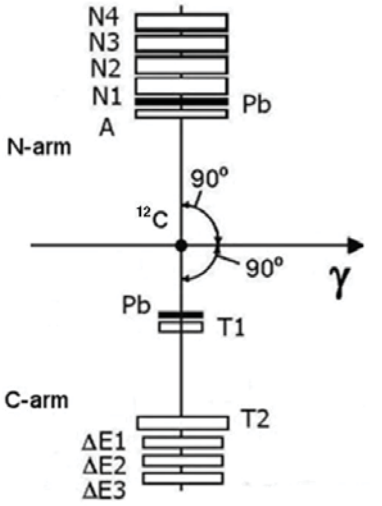

Figure 9: Layout of the experimental setup at LPI.

Our experiment was performed at the bremsstrahlung photon beam of the 1.2-GeV electron synchrotron of the Lebedev Physical Institute. Photons were produced with an electron beam of intensity $I_e \simeq 10^{12}\ \mathrm{s}^{-1}$ and the duty factor $\simeq 10\%$. The energy of the beam was usually $E_e = E_{\gamma\,\max} = 850$ MeV (i.e. above the η photoproduction threshold off free nucleons, $E_{\eta\ \mathrm{thr}} = 708$ MeV); additional measurements of subthreshold backgrounds have been done at $E_e = E_{\gamma\,\max} = 650$ MeV.

The experimental setup included two time-of-flight arms (two scintillation telescopes — C and N arms) for detecting in coincidence charged and neutral particles (back-to-back pairs), see Fig. 9. These arms were both positioned at $90^\circ{-}90^\circ$ with respect to the beam axis in order to minimize background.

The C-arm used for detection of charged particles is a plastic TOF spectrometer for charged pions and protons. It consists of a start detector T1 ($20\times20\times2\ \mathrm{cm}^3$), a stop detector T2 ($50\times50\times5\ \mathrm{cm}^3$) and three energy losses detectors ΔE_1, ΔE_2 and ΔE_3 ($40\times40\times2\ \mathrm{cm}^3$ each). A 4 mm lead (Pb) plate was used in some runs for TOF calibrations with ultrarelativistic electrons/positrons produced in the lead plate with high-energy photons emitted from the target owing to production and decays of neutral pions.

The N-arm is a plastic TOF spectrometer for neutrons. It consists of a veto counter A ($50\times50\times2\ \mathrm{cm}^3$) and four plastic blocks — the neutron detectors N1, N2, N3 and N4 ($50\times50\times10\ \mathrm{cm}^3$ each). Again, a 4 mm lead plate was used in some runs for TOF calibrations. The efficiency of the N-arm for neutrons of energies above 50 MeV was $\approx 30\%$.

In both arms each volume of scintillator counters/blocks was viewed from corners with 4 phototubes. The time-of-flight bases in the C and N arms were 1.4 m and the time resolution was $\simeq 200$ ps (1σ). The target was a carbon cylinder of the 10 cm length along the beam axis. Its diameter was 4 cm, i.e. slightly more than the diameter of the collimated photon beam (3 cm). The distance between the target and the start detector T1 was 0.7 m.

Mostly, the setup was the same as in our previous work [31, 32] but a few useful changes have been made:

- ΔE_i detectors have been placed after the time-of-flight interval T1-T2. This enabled us to have a better $\pi^\pm/p$ separation and time resolution.
- A transverse size of the start detector T1 was cut off according to required geometry. This reduced a background load of the C-arm.
- A thickness of the start detector was also reduced in order to improve time resolution.
- All unnecessary layers of absorbers used previously to suppress radiative backgrounds have been removed from the time-of-flight interval, with the effect of reducing the e^+/e^- background created by photons from π^0 decays.

General tests of the setup, including preliminary time calibrations of the arms, have been done in special runs, in which the quasifree reaction $\gamma p \to \pi^+ n$ inside carbon nuclei was observed. In such runs the two arms of the setup have been moved to the angles $50^\circ{-}50^\circ$ where the high count rate enabled one to do the calibrations quickly. Lead convertors used in these runs provided reliable ultrarelativistic reference points $\beta = 1$ for particle's velocities β_C and β_N measured in the C- and N-arms. A two-dimensional $\beta_C - \beta_N$ plot on Fig. 10 illustrates this procedure.

The calibration done provided a linear scale of velocities in the range $\beta = 0.6 - 1$ with errors of about 3% (1σ). We have checked the linearity of the scale by using cosmic rays and setting different distances between detectors.

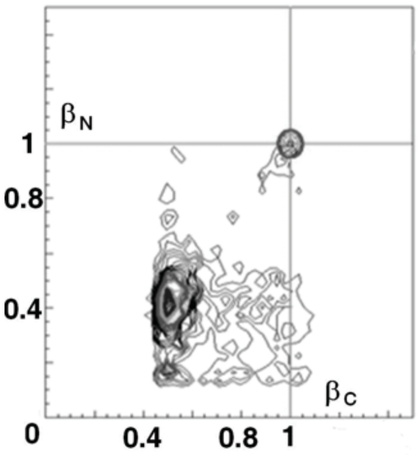

Figure 10: A two-dimensional plot of particle velocities, β_C and β_N, in the C and N arms.

Results and comparison with simulations

Measurement runs have mostly been done in 2009 at two maximal beam energies: $E_{\gamma\,\mathrm{max}} = 650$ MeV and 850 MeV. The on-line trigger was a coincidence of particles in the C- and N-arms within a time gate of 50 ns.

For further off-line analysis events were selected with an additional condition of sufficiently long ranges of the charged particles,

$$\Delta E_i > E_i^{\mathrm{thr}} \quad \text{for } \underline{\text{all}} \; i = 1, 2, 3 \tag{21}$$

with experimentally adjusted thresholds E_i^{thr}. In this way low-energy particles in the C-arm were rejected.

A two-dimensional histogram in the variables $\Delta E - \beta_C$, where ΔE is the minimal energy loss in the ΔE_i detectors,

$$\Delta E = \min_i (\Delta E_i), \tag{22}$$

is shown in Fig. 11 for the beam energy $E_{\gamma\,\mathrm{max}} = 850$ MeV. Results of simulations using the Intra Nuclear Cascade (INC) model [49] in the GEANT-3 framework are shown in Fig. 12 for comparison. The INC model takes into account production of various mesons and baryon resonances, their free propagation in the nuclear matter, and then various $2 \to 2$ collisional reactions including $\eta N \to \pi N$. This model successfully describes many photoreactions in wide kinematical ranges as was demonstrated, beyond [49], in simulations of the GRAAL experiment at energies 500–1500 MeV [50]. Binding effects for η and reactions like $\eta NN \to NN$ were not included into the model, so one can try to find effects arising due to formation and decay of η-mesic nuclei through characteristic deviations of the model predictions from the experimental data.

The simulation shows that the selection (21) of particles with sufficiently long ranges distinguishes very well protons (as particles with $\beta_C \leq 0.7$) and pions (as particles with $\beta_C \geq 0.7$): the overlap is less than 1%.

Considering one-dimensional spectra over β_C of events selected according to the condition (21) of sufficiently long ranges and imposing the additional cut-off $0.3 < \beta_N < 0.7$ for neutron velocities, we find rather interesting structures in the spectra. Shown in Fig. 13 are experimental data together with results of the INC simulation. Separately shown are INC predictions for the number of protons and charged pions in the C-arm. There is a qualitative agreement of the INC simulation with the experimental data for the case of the subthreshold beam energy, $E_e = 650$ MeV. Meanwhile, in the case of $E_e = 850$ MeV there is a clear excess of the experimentally observed events over the simulation results in two velocity regions closely corresponding to the kinematics of η-mesic nuclei decays with emission of πN and NN correlated pairs, Eqs. (10) and (19).

Knowing from the INC simulations that the "normal" (without η-mesic nuclei) dynamics of the considered reaction does not yield a sufficient amount of protons and pions with the velocities of

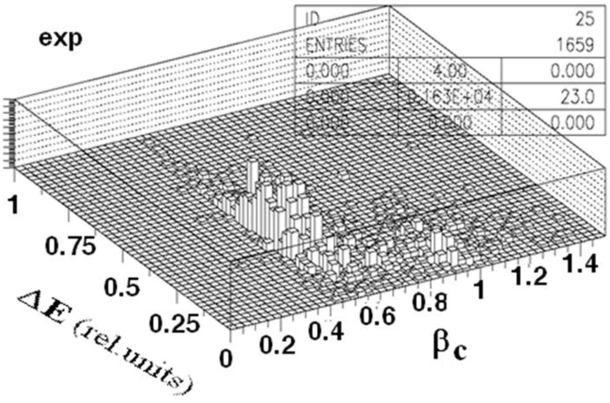

Figure 11: Two-dimensional $\Delta E - \beta_C$ distribution, experiment.

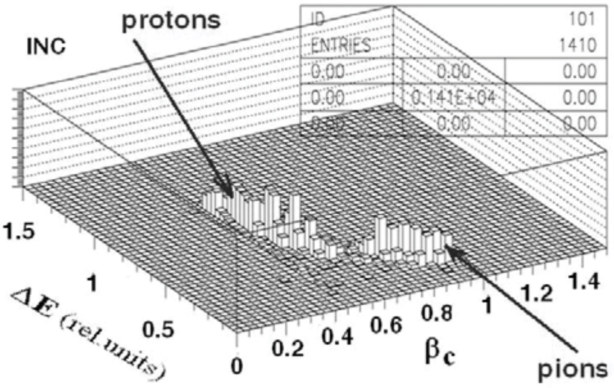

Figure 12: Two-dimensional $\Delta E - \beta_C$ distribution, the INC model.

about $\beta_C \sim 0.7$, we interpret the found anomaly at $\beta_C \sim 0.7$ as a result of production of low-energy η-mesons followed by their two-nucleon annihilation.

The energy resolution of the experimental setup is not sufficient to say whether an essential part of these η-mesons is produced in the bound state, but theoretical arguments discussed in above make such a statement plausible.

Concerning the excess of pions with $\beta_C \simeq 0.95$, this feature is in agreement with our measurements reported earlier [23,31,32]. It can be interpreted as an evidence for one-nucleon annihilation of produced low-energy η-mesons (bound or unbound).

Electron/positron peaks shown in Fig. 13 originate from calibration runs with the lead plate inserted. They were not included into simulations made.

The observed proton peak in the β_C distribution is very unusual because it corresponds to pn pairs with very high kinetic energies $T_p \sim T_n \sim 200-300$ MeV and transverse momenta $p_p \sim p_n \sim 600-800$ MeV/c. One should keep in mind that photons which produce such pairs have quite a modest energy 650 MeV $< E_\gamma <$ 850 MeV. Ordinary photoproduction reactions do not give nucleons with such a high energy and momentum. Creation and annihilation of intermediate low-energy η-mesons seems to be the only explanation to these events.

Assuming that the observed access events are mainly related with formation and isotropic decays of η-mesic nuclei with $A = 11$, we can estimate their photoproduction cross section. The number of photons of the energies $E_\gamma = 650-850$ MeV that hit the carbon target in experimental runs was evaluated via comparison of the total yield of charged pions detected by a single C-arm

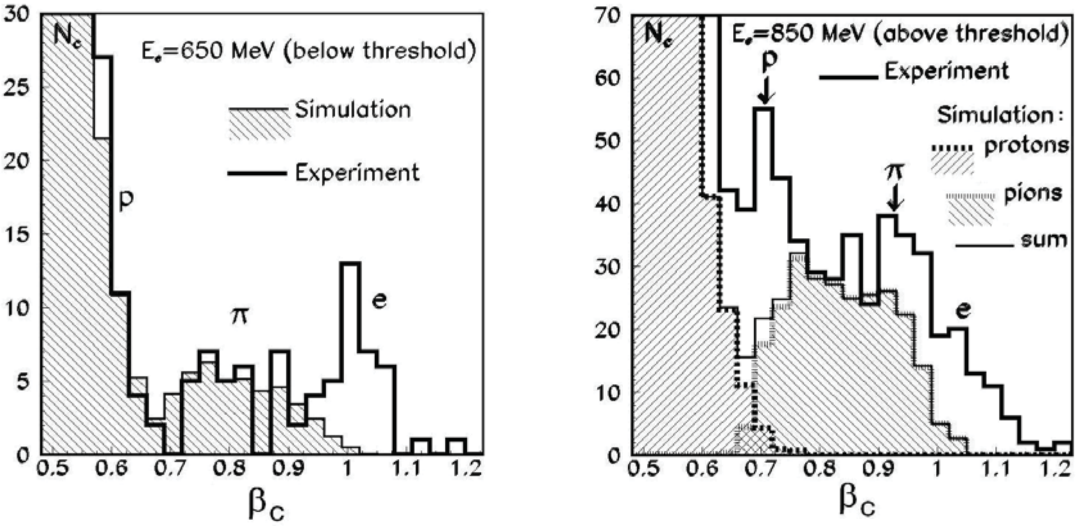

Figure 13: Velocity distribution of charged particles in correlated pairs selected according to the criterion $\Delta E_i > 0$ (for all $i = 1,2,3$) at $E_e = 650$ and 850 MeV. Bold solid line: experimental data. Hatched areas: yields of protons and pions in the INC simulation. A well visible excess of events over the INC simulation is seen at the right panel — in the case of the beam energy exceeding the η-photoproduction threshold — in both velocity regions corresponding to the expected velocities of the πN and NN decay products of η-mesic nuclei.

of the setup with predictions of INC for that yield, thus giving the result $N_\gamma \simeq 1.36 \times 10^{11}$. Taking into account the solid angle of the C-arm telescope ($\Omega_C = 0.027$ sr), efficiencies of detectors, a geometric efficiency of the N-arm of the setup ($\sim 18\%$ as found from theoretically expected angular distributions of particles of the correlated pairs), we arrived at the following cross section of η-mesic nucleus formation:

$$\sigma(\gamma + {}^{12}\mathrm{C} \to {}_{\eta}A + X) \lesssim 10\ \mu\mathrm{b}. \tag{23}$$

We write it as an upper limit because part of the observed events can be related with unbound etas. This number is consistent with available theoretical estimates (typically, a few μb).

Conclusions

The new obtained data confirm the main features of the πN signal of formation and decay of η-mesic nuclei off the carbon target in the photoreaction found in our previous work.

A new signature for formation and decay of η-mesic nuclei, the back-to-back *pn* pairs, was explored. For the first time an experimental evidence was found that the yield of such pairs in the region of $\beta_C \sim 0.6 - 0.7$ is quite large and therefore is also suitable for searching for η–mesic nuclei.

Assuming that the observed excess of events is related with η-mesic nuclei, an estimate of the total cross section of formation of η-nuclei in the photoreaction off carbon have been obtained, see Eq. (23).

We have plans to carry out a more precise experiment, with a better energy resolution, at the deuteron beam of the JINR nuclotron.

Acknowledgments

This work was supported in part by the RFBR grants 08-02-00648-a and 10-02-01433-a. A nice work of the accelerator group of the LPI synchrotron and its leader G.G. Subbotin is highly appreciated.

References

[1] Q. Haider and L.C. Liu. Formation of an eta-mesic nucleus. Phys. Lett. B **172** (1986) 257; Erratum: Ibid. **174** (1986) 465E.

[2] L.C. Liu and Q. Haider. Signature for the existence of eta-mesic nuclei. Phys. Rev. C **34** (1986) 1845.

[3] R.S. Bhalerao and L.C. Liu. Off-shell model for threshold pionic η production on a nucleon and for ηN scattering. Phys. Rev. Lett. **54** (1985) 865.

[4] L. Tiator, C. Bennhold and S.S. Kamalov. The ηNN coupling in eta photoproduction. Nucl. Phys. A **580** (1994) 455.

[5] E.F. McNicoll, S. Prakhov, I.I. Strakovsky et al. Experimental study of the $\gamma p \to \eta p$ reaction with the Crystal Ball detector at the Mainz Microtron (MAMI-C) [data tables are available from the Durham HEPDATA base, `http://durpdg.dur.ac.uk`].

[6] Q. Haider and L.C. Liu. Dependence of calculated binding energies and widths of η-mesic nuclei on treatment of subthreshold η-nucleon interaction. Phys. Rev. C **66** (2002) 045208.

[7] Q. Haider and L.C. Liu. Eta-mesic nucleus: A new form of nuclear matter. Acta Phys. Pol. B Proc. Suppl. **2** (2009) 121.

[8] A.M. Green and S. Wycech. η-nucleon scattering length and effective range. Phys. Rev. C **55** (1997) R2167.

[9] A.M. Green and S. Wycech. η-nucleon scattering length and effective range uncertainties. Phys. Rev. C **71** (2005) 014001.

[10] T. Inoue, E. Oset and M.J. Vicente Vacas Chiral unitary approach to S-wave meson baryon scattering in the strangeness $S = 0$ sector Phys. Rev. C **65** (2002) 035204.

[11] I. Inoue and E. Oset η in the nuclear medium within a chiral unitary approach Nucl. Phys. A **710** (2002) 354.

[12] C. García-Recio, T. Inoue, J. Nieves and E. Oset η bound states in nuclei Phys. Lett. B **550** (2002) 47.

[13] D. Jido, H. Nagahiro and S. Hirenzaki Medium effects to the $N(1535)$ resonance and η mesic nuclei Phys. Rev. C **66** (2002) 045202.

[14] H. Nagahiro, D. Jido and S. Hirenzaki Formation of mesic nuclei by (γ, p) reactions Nucl. Phys. A **761** (2005) 92.

[15] D. Jido, E.E. Kolomeitsev, H. Nagahiro and S. Hirenzaki Level crossing of particle-hole and mesonic modes in eta-mesonic nuclei Nucl. Phys. A **811** (2008) 158.

[16] M. Kohno and H. Tanabe Low energy η production in (π^+,p) and (γ,p) reactions on ^{12}C Phys. Lett. B **231** (1989) 219.

[17] A.I. Lebedev and V.A. Tryasuchev Calcultion of the photoptoduction cross section of η-nuclei Voprosy Atomnoi Nauki i Tekhniki, ser. Yad.-Fiz . Issled. (Kharkov), **8/8** (1989) 97 (in Russian).

[18] A.I. Lebedev and V.A. Tryasuchev Cross section for production of η nuclei by photons J. Phys. G: Nucl. Part. Phys. **17** (1991) 1197.

[19] A.I. Lebedev and V.A. Tryasuchev Study of the photoproduction of eta mesic nuclei on the basis of a complex potential Phys. Atom. Nucl. **58** (1995) 586 [Yad. Fiz . **58** (1995) 642 (in Russian)].

[20] V.A. Tryasuchev Photoproduction of light eta nuclei Phys. Part. Nucl. **30** (1999) 606 [Fiz . Elem. Chast. Atom. Yadra **30** (1999) 1391 (in Russian)].

[21] V.A. Tryasuchev Theoretical analysis of the formation of η mesic nuclei in $\gamma + A \to N + {}_{\eta}A'$ reactions Phys. Atomic Nucl. **64** (2001) 346 [Yad. Fiz . **64** (2001) 396 (in Russian)].

[22] A.I. L'vov Production and decay of eta-mesic nuclei in Proc. of the 7th Int. Conf. 'Mesons and Light Nuclei', Czech Republic, 1998 (Mesons and Light Nuclei '98, World Scientific, Eds. J. Adam, P. Bydžovský, J. Dobeš, R. Mach, J. Mareš and M. Sotona), pp. 469–472; E-print arXiv: nucl-th/9809054.

[23] G.A. Sokol, T.A. Aibergenov, A.V. Kravtsov, A.I. L'vov and L.N. Pavlyuchenko Search for η–mesic nuclei in photoproduction processes Fizika B **8** (1999) 85.

[24] Q. Haider and Lon-Chang Liu Eta-mesic nucleus and COSY-GEM data Acta Phys.Polon. B **41** (2010) 2231.

[25] Q. Haider and Lon-Chang Liu Interference and nuclear medium effects on the eta-mesic nuclear spectrum J. Phys. G: Nucl. Part. Phys. **37** (2010) 125104.

[26] M. Kohno and H. Tanabe Pion-induced η production on nuclei Nucl. Phys. A **519** (1990) 755.

[27] R.E. Chrien, S. Bart, P. Pile et al. Search for bound states of the η meson in light nuclei Phys. Rev. Lett. **60** (1988) 2595.

[28] B.J. Lieb, in Proceedings of International Conference on Nuclear Physics, Sao Paulo, Brazil, 1988.

[29] B.J. Lieb, L.C. Liu, E. Cheung et al. Search for nuclear bound states of the eta meson. Progress at LAMPF, January – December 1988. LA-11670-PR Progress Report, pp. 52-55.

[30] H.C. Chiang, E. Oset and L.C. Liu. Width of bound eta in nuclei. Phys. Rev. C **44** (1991) 738.

[31] G.A. Sokol, T.A. Aibergenov, A.V. Koltsov et al. Discovery of η-mesic nuclei. Part. Nucl. Lett. **102** (2000) 71 [Pisma EChaYa No.5 [102] (2000) 71 (in Russian)].

[32] G.A. Sokol and L.N. Pavlyuchenko. Discovery and investigation of η-mesic nuclei in photoproduction processes. Phys. At. Nucl. **71** (2008) 509 [Yad. Fiz . **71** (2008) 532 (in Russian)].

[33] G.A. Sokol, V.L. Kashevarov, A.I. Lebedev and L.N. Pavlyuchenko. Photoproduction of eta-nuclei. in Proceedings of International Conference on Mesons and Nuclei at Intermediate Energies, Dubna, Russia, 1994 (Eds. M.Kh. Khankhasayev and Zh.B. Kurmanov, World Scientific, Singapore, 1995), p. 651–657; Preprint LPI No. 17 (1994).

[34] A.I. Lebedev and G.A. Sokol. Search for eta-nuclei. Preprint LPI No. 34 (1995).

[35] G.A. Sokol and V.A. Tryasuchev. A possible method of observing eta nuclei. Bull. Lebedev Phys.Inst., No.4 (1991) 21 [Kratk. Soobshch. Fiz . 4 (1991) 23 (in Russian)].

[36] M. Pfeiffer, J. Ahrens, J.R.M. Annand et al. Photoproduction of η-mesic ^{3}He. Phys. Rev. Lett. **92** (2004) 252001; Ibid. **94** (2005) 049102.

[37] F. Pheron, J. Ahrens, J.R.M. Annand et al. Coherent photoproduction of η-mesons off ^{3}He – search for η-mesic nuclei. Phys. Lett. B **709** (2012) 21.

[38] S.V. Afanasiev, A.S. Artiomov, R.N. Bekmirzaev et al. Search results of η-mesic nuclei in the $d+\mathrm{C}$ reaction in JINR. Nucl. Phys. B (Proc. Suppl.) **209-210** (2011) 255.

[39] A. Budzanowski, A. Chatterjee, P. Hawranek et al. Search for η-mesic nuclei in a recoil-free transfer reaction. Phys. Rev. C **79** (2009) 012201(R).

[40] R.S. Hayano, S. Hirenzaki and A. Gillitzer. Formation of η-mesic nuclei using the recoilless $(d,{}^3\mathrm{He})$ reaction. Eur. Phys. J. A **6** (1999) 99.

[41] J. Kulpa and S. Wycech. The absorptive ρ^2 terms in the η optical potential. Acta Phys. Pol. B **29** (1998) 3077.

[42] H. Calén, S. Carius, K. Fransson et al. The $pp \to pp\eta$ reaction near the kinematical threshold. Phys. Lett. B **366** (1996) 39.

[43] H. Calén, J. Dyring, K. Fransson et al. Measument of the quasifree $p+n \to d+\eta$ reaction near threshold. Phys. Rev. Lett. **79** (1997) 2642.

[44] H. Calén, J. Dyring, K. Fransson et al. Threshold structure of the quasifree $p+n \to d+\eta$ reaction. Phys. Rev. Lett. **80** (1998) 2069.

[45] H. Calén, J. Dyring, K. Fransson et al. Measument of the quasifree $pn \to pn\eta$ reaction. Phys. Rev. C **58** (1998) 2667.

[46] J. Smyrski, P. Wünster, J.T. Balewski et al. Near-threshold η meson production in proton-proton collisions. Phys. Lett. B **474** (2000) 182.

[47] P. Moskal, R. Czyżykiewicz, H.-H. Adam et al. Near-threshold production of the η-meson via the quasifree $pn \to pn\eta$ reaction. Phys. Rev. C **79** (2009) 015208.

[48] V. Baru, A.M. Gasparyan, J. Haidenbauer, C. Hanhart, A.E. Kudryavtsev and J. Speth. Production of η mesons in nucleon-nucleon collisions. Phys. Rev. C **67** (2003) 024002.

[49] A.S. Iljinov, I.A. Pschenichnov, N. Bianchi et al. Extension of the intranuclear cascade model for photonuclear reactions at energies up to 10 GeV. Nucl. Phys. A **616** (1997) 575.

[50] A. Ignatov, O. Bartalini, V. Bellini et al. New experimental and simulated results on nuclear media effects in meson photoproduction off nuclei. Prog. Part. Nucl. Phys. **61** (2008) 253.

ON EXTRACTION OF THE TOTAL PHOTOABSORPTION CROSS SECTION ON THE NEUTRON FROM DATA ON THE DEUTERON

M.I. Levchuk[1], *A.I. L'vov*[2]

[1]B.I. Stepanov Institute of Physics of the National Academy of Sciences of Belarus, Minsk
[2]P.N. Lebedev Physical Institute of the Russian Academy of Sciences, Moscow, Russia

An improved procedure is suggested for finding the total photoabsorption cross section on the neutron from data on the deuteron at energies $\lesssim 1.5$ GeV. It includes unfolding of smearing effects caused by Fermi motion of nucleons in the deuteron and also takes into account non-additive contributions to the deuteron cross section due to final-state interactions of particles in single and double pion photoproduction. This procedure is applied to analysis of existing data.

Introduction

This work was motivated by recent preliminary results from the GRAAL experiment on the total photoabsorption cross section off protons and deuterons at photon energies $\omega = 700-1500$ MeV [1–4] and their implications for the neutron. An intriguing feature of the new data is that they indicate an approximately equal and big strength of photoexcitation of the nucleon $F_{15}(1680)$ resonance off both the proton and neutron (as seen, in particular, in Fig. 5 in Ref. [4]). Meanwhile this strength was found small for the neutron in many previous studies (see, e.g., [5, 6]). Particle Data Group [7] quotes the following branching ratios of $N^* = F_{15}(1680)$ to γN:

$$\begin{aligned} \mathrm{Br}(N^* \to \gamma p) &= 0.21-0.32\%, \\ \mathrm{Br}(N^* \to \gamma n) &= 0.021-0.046\%. \end{aligned} \tag{1}$$

Irrespectively on whether the old or new data are correct, it seems timely to (re)consider procedure commonly used to find cross sections off the neutron from the deuteron data.

This procedure was described in detail by the Daresbury group [6] who performed measurements of the total photoabsorption cross sections σ_p [5] and σ_d [6] at energies between 0.265 and 4.215 GeV. In the nucleon resonance energy region they made an Ansats that

$$\sigma_d(\omega) = F(\omega)[\sigma_p(\omega) + \sigma_n(\omega)]. \tag{2}$$

Here the factor of $F(\omega)$ was introduced in order to take into account smearing effects due to Fermi motion of nucleons in the deuteron. This factor was found by numerical integration of the proton cross sections using known momentum distribution of nucleons in the deuteron and then equally applied to the neutron. Finally, the neutron cross section was found, point by point, with the step of 25 MeV, from the corresponding deuteron cross section at the same energy using Eq. (2).

An evident drawback of the Ansatz (2) is that smearing effects are assumed to be the same for the proton and neutron, what cannot be true in case the energy dependencies of $\sigma_p(\omega)$ and $\sigma_n(\omega)$ are different.

The second problem is that smearing of the cross section makes it impossible to relate individual nucleon cross sections $\sigma_N(\omega)$ with $\sigma_d(\omega)$ at the same energy and thus to apply the point-by-point procedure. Instead, some average of $\sigma_N(\omega)$ over a finite energy interval can only be found. In other words, a justified unsmearing procedure should be applied there.

The third point is that non-additive corrections related mostly with final state interactions have been neglected in Eq. (2). Brodsky and Pumplin [8] estimated these corrections at high energies ($\omega \gtrsim 2$ GeV) assuming that high-energy photoproduction on the nucleon is dominated by diffractive photoproduction of vector mesons (ρ, ω, ϕ) which then interact with the second nucleon.

Such corrections have been included in the analysis of high-energy part of the Daresbury data [6] (as well as in studies of photoabsorption off protons and deuterons at energies 20–40 GeV [9]). At lower energies, including energies of GRAAL, the corrections related with vector meson production are small. Nevertheless, other photoproduction channels still might be important. This is indeed the case as explained below. To our knowledge, no estimates of the non-additive corrections to Eq. (2) have been yet done at energies of the GRAAL experiment.

In this work we improve the procedure of [6] in all the above three lines.

Fermi smearing (folding)

We begin with rewriting Eq. (2) more accurately as

$$\sigma_d(\omega) = \hat{F}[\sigma_p(\omega) + \sigma_n(\omega)] + \Delta\sigma_{pn}(\omega). \tag{3}$$

Here $\hat{F}$ is a linear integral operator that smears individual nucleon cross sections in accordance with Fermi motion of nucleons in the deuteron; $\Delta\sigma_{pn}$ is a non-additive correction to be discussed later. The first two terms in Eq. (3) arise from diagrams of impulse approximation (like those in Fig. 1) when interference effects are omitted. We neglect here off-shell effects for intermediate nucleons $\tilde{N}$ because the binding energy of nucleons in the deuteron is rather small (2.2 MeV).

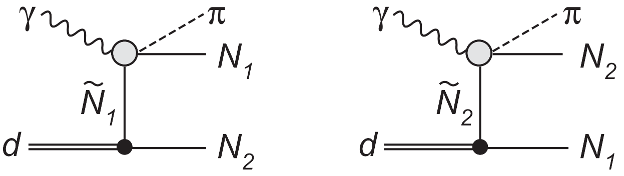

Figure 1: Diagrams of impulse approximation for $\gamma d \to \pi NN$. Antisymmetrization over N_1 and N_2 is not shown.

A simple analysis of diagrams of impulse approximation shows [10] that the smearing operator, in nonrelativistic approximation over nucleons in the deuteron, is reduced to

$$\hat{F}\sigma_N(\omega) = \int W(p_z)\frac{\omega^{\mathrm{eff}}}{\omega}\,\sigma_N(\omega^{\mathrm{eff}})\,dp_z. \tag{4}$$

Here

$$\omega^{\mathrm{eff}} = \omega\left(1 - \frac{p_z}{M}\right) \tag{5}$$

is the effective (Doppler shifted) energy for the moving intermediate nucleon $\tilde{N}$ of the mass M provided its longitudinal (along the photon beam) momentum is equal to p_z. $W(p_z)$ is the longitudinal momentum distribution of nucleons in the deuteron,

$$W(p_z) = \int |\psi(p)|^2 \frac{d^2 p_\perp}{(2\pi)^3}, \tag{6}$$

and the factor $\omega^{\mathrm{eff}}/\omega$ takes into account a change in the photon flux seen by the moving nucleon. As in Ref. [6], we use in the following a simplified deuteron wave function (Hulthén [11]),

$$\psi(r) = \frac{k}{r}(e^{-ar} - e^{-br}), \qquad \int_0^\infty |\psi(r)|^2\, 4\pi r^2 dr = 1, \tag{7}$$

with $a = 45.7$ MeV$/c$, $b = 260$ MeV$/c$ and $k^2 = ab(a+b)/[2\pi(a-b)^2] = 12.588$ MeV$/c$. In the p-space

$$\psi(p) = 4\pi k\Big(\frac{1}{a^2+p^2} - \frac{1}{b^2+p^2}\Big), \tag{8}$$

so that the function $W(p_z)$ is

$$W(p_z) = 2k^2\Big(\frac{1}{A} + \frac{1}{B} - \frac{2\ln(B/A)}{B-A}\Big), \qquad \int W(p_z)\,dp_z = 1, \tag{9}$$

where $A = a^2 + p_z^2$ and $B = b^2 + p_z^2$. This function is shown in Fig. 2 together with a distribution obtained with a realistic (CD-Bonn) wave function [12]. In actual calculations we cut off momenta $|p_z| > p_{\rm cut} = 200$ MeV$/c$ where $W(p_z)$ becomes quite small and the momentum p_z remains nonrelativistic.

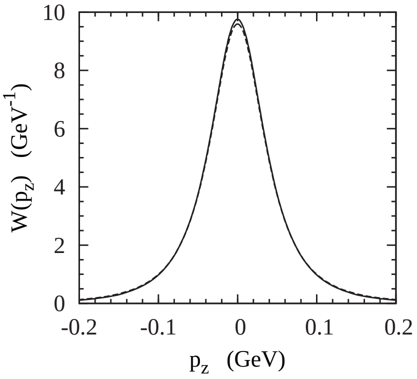

Figure 2: Distribution of the longitudinal momentum in the deuteron. Solid and dashed lines: Hulthén and CD-Bonn wave functions.

The Hulthén distribution for $W(p_z)$ gives the following average longitudinal momentum of nucleons in the deuteron:

$$\langle p_z^2\rangle^{1/2} = 53.9 \text{ MeV}/c \tag{10}$$

(it is 54.9 MeV$/c$ for the CD-Bonn wave function). It also gives the following spread for the effective photon energy seen by the moving nucleon:

$$\Delta\omega^{\rm eff} = \omega\frac{\langle p_z^2\rangle^{1/2}}{M} = 0.057\omega. \tag{11}$$

In other words, this value characterizes the “energy resolution of the deuteron” as a “spectral measuring device” for the neutron. For $\omega \sim 1$ GeV only an average of the nucleon cross section over the range $\sim \pm 60$ MeV can be inferred from the deuteron data. Determination of $\sigma_n(\omega)$ with the step of 25 MeV done in [6] cannot be physically justified.

Unfolding

It is well known that the unfolding problem, i.e. solving the Fredholm integral equation (3) for the unknown “unsmeared deuteron cross section” $\sigma(\omega) = \sigma_p(\omega) + \sigma_n(\omega)$, cannot be solved without further assumptions on properties of the solution $\sigma(\omega)$. In particular, it is not possible to restore fast fluctuations in $\sigma(\omega)$ at the energy scale $\lesssim \Delta\omega^{\rm eff}$. To proceed, we make therefore a physically sound assumption that both the cross sections $\sigma_p(\omega)$ and $\sigma_n(\omega)$ can be approximated with a sum of a few Breit-Wigner resonances (having fixed known standard masses and widths but unknown amplitudes, probably different for p and n) plus a smooth background. Thus we write

$$\sigma(\omega) = \sum_i X_i f_i(\omega) \tag{12}$$

where $f_i(\omega)$ is the basis of the expansion, i.e. either Breit-Wigner distributions or smooth functions of the total energy $\sqrt{s}$. We borrow specific forms of the functions $f_i(\omega)$ from Ref. [6], Eqs. (11) and below. Then unknown coefficients X_i are determined from the fit of $\hat{F}\sigma(\omega)$ to experimental data on $\sigma_d(\omega)$ (at this point we assume that the correction $\Delta\sigma_{pn}$ is already calculated).

A knowledge of X_i, with errorbars δX_i determined in the fit, can be directly converted to the knowledge of $\sigma(\omega)$, also with errorbars. In particular, writing fluctuations in the determined value of $\sigma(\omega)$ as

$$\delta\sigma(\omega) = \sum_i \delta X_i f_i(\omega), \tag{13}$$

we have

$$\delta\sigma^2(\omega) = \sum_{ij} \delta X_i \, \delta X_j \, f_i(\omega) f_j(\omega) \tag{14}$$

and

$$\langle \delta\sigma^2(\omega) \rangle = \sum_{ij} C_{ij} f_i(\omega) f_j(\omega), \tag{15}$$

where

$$C_{ij} = \langle \delta X_i \, \delta X_j \rangle \tag{16}$$

is a standard covariance matrix of errors determined in the fit of X_i.

In this way the extracted unfolded cross section $\sigma(\omega)$ can be shown as a smooth curve (corresponding to the central values of X_i) surrounded with a band of the half-width given by Eq. (15) which represents errors in the cross section.

Nonadditive corrections

The term $\Delta\sigma_{pn}(\omega)$ in Eq. (3) takes into account various effects violating additivity of the photoabsorption cross sections on individual nucleons. Among them:

– interference of diagrams of photoproduction off proton and neutron, Fig. 1, leading to identical final states; the Fermi statistics of the emitted nucleons (antisymmetrization) leading to the so-called Pauli blocking,

– interaction between emitted particles (final state interaction, FSI) including both interaction of unbound nucleons and binding of nucleons (formation of the deuteron in the final state), interaction of pions (or other particles), produced on one nucleon, with the second nucleon in the deuteron,

– absorption of pions (and the presence of processes such as the deuteron photodisintegration, without pions in the final state).

Now we briefly discuss all these effects starting with the reaction of single-pion photoproduction, $\gamma d \to \pi NN$, considered in the model that includes diagrams of impulse approximation (Fig. 1) and the final state NN and πN interaction to one loop (Fig. 3). Formalism and the main building blocks of this model that was previously used in the energy region of the $\Delta(1232)$ resonance can be found elsewhere [13, 14]. Generally, the model works well for the channel $\gamma d \to \pi^- pp$ in the $\Delta(1232)$ region but not so well for $\gamma d \to \pi^0 pn$, see Fig. 4. Reasons for the discrepancy are not clear but other authors get similar results and also cannot describe the data (see, e.g., [17]). We will not use the model for energies too close to the $\Delta(1232)$ region.

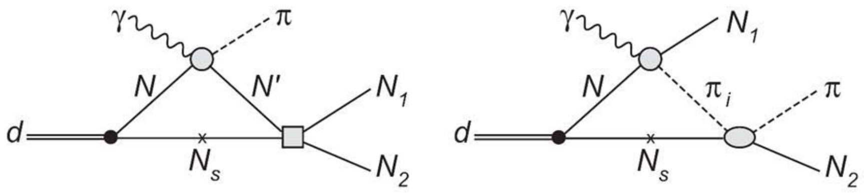

Figure 3: Diagrams with the final state NN and πN interaction (to one loop) for $\gamma d \to \pi NN$.

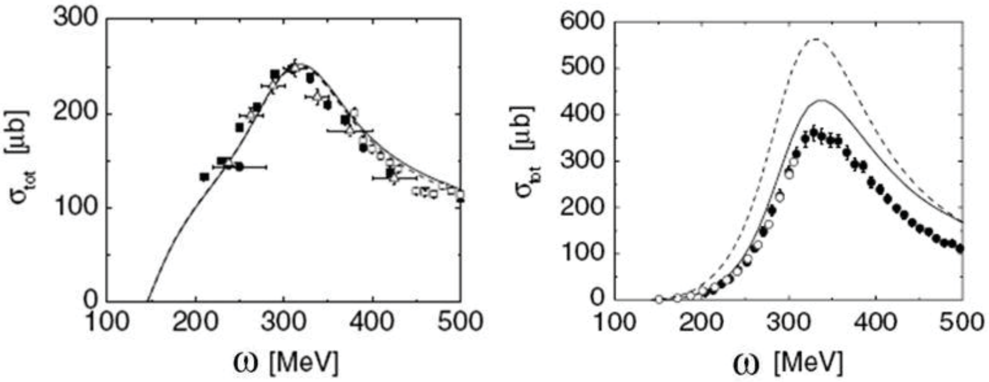

Figure 4: Model [13, 14] predictions for $\gamma d \to \pi^- pp$ (left) and $\gamma d \to \pi^0 pn$ (right) in the region of the $\Delta(1232)$.

In the present calculation that covers higher energies, "elementary" amplitudes of $\gamma N \to \pi N$ are taken from the MAID analysis [15] (with a proper off-shell extrapolation); those for $NN \to NN$ are taken from the analysis of SAID [16] (again with an off-shell extrapolation). In the following plots we show obtained results for $\Delta\sigma_{pn}(\omega)$ in different isotopic channels.

1. Interference contributions from diagrams of impulse approximation for $\gamma d \to \pi NN$

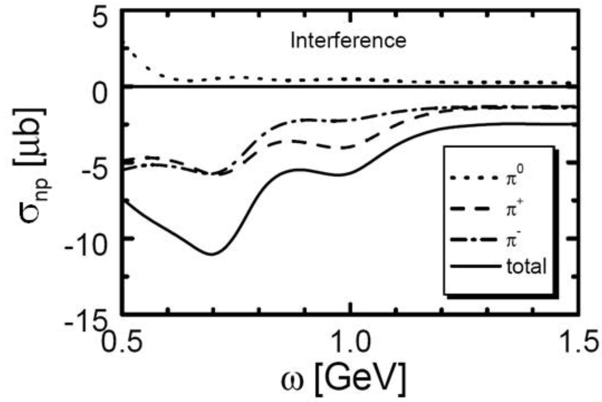

Figure 5: Contribution to $\Delta\sigma_{pn}$ due to interference of diagrams in Fig. 1 of impulse approximation for $\gamma d \to \pi NN$.

2. NN FSI interaction in $\gamma d \to \pi NN$ and $\gamma d \to \pi d$

We put here NN FSI contributions for the continuous and bound states together because there is a tendency for their cancelation that can be traced to the unitarity (closure). The matter is that the NN interaction in the continuous spectrum can be thought as a replacement of the plane NN wave in the reaction amplitude of the plane-wave impulse approximation,

$$T^{\mathrm{PWIA}}(E_{NN}) = \langle NN|T(\gamma N \to \pi N)|d\rangle, \tag{17}$$

with the distorted NN wave in the reaction amplitude of the distorted-wave impulse approximation,

$$T^{\mathrm{DWIA}}(E_{NN}) = \langle \psi^{(-)}(NN)|T(\gamma N \to \pi N)|d\rangle. \tag{18}$$

Here we explicitly indicate the energy of the NN state. Also, the coherent amplitude, with the final bound NN system, is

$$T^{\mathrm{coh}}(E_d) = \langle d|T(\gamma N \to \pi N)|d\rangle. \tag{19}$$

Owing to the closure, i.e. a completeness of eigen states of the free NN Hamiltonian as well as those of a Hamiltonian with NN interaction,

$$1 = \sum_{NN,E_{NN}} |NN\rangle\langle NN| = \sum_{NN,E_{NN}} |\psi^{(-)}(NN)\rangle\langle\psi^{(-)}(NN)| \; + \; \sum_d |d\rangle\langle d|, \tag{20}$$

the square of the PWIA off-shell amplitude integrated over all possible NN states, irrespectively to their energies, exactly coincides with the square of the DWIA off-shell amplitude (also integrated over all possible states) plus the square of the coherent amplitude. In case when a subset of NN states of certain energies is only considered, as in the case of finding cross sections at a certain energy, the coincidence of $|T^{\mathrm{PWIA}}|^2$ with $|T^{\mathrm{DWIA}}|^2 + |T^{\mathrm{coh}}|^2$ is not strictly valid, however a tendency to have a compensation between the coherent contribution to the cross section and a decrease in the DWIA cross section still remains.

An illustration of this general tendency can be found in Fig. 6 where the negative NN-FSI contribution to $\gamma d \to \pi^0 pn$ is close in the magnitude to the positive coherent contribution to $\gamma d \to \pi^0 d$ (see dotted curves).

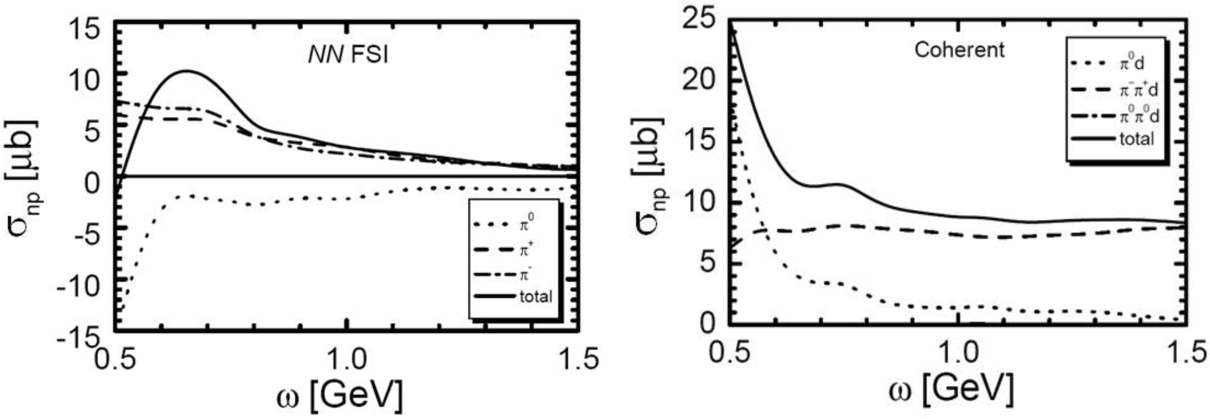

Figure 6: Left: Contribution to $\Delta\sigma_{pn}$ due to final state NN interaction in $\gamma d \to \pi NN$. Right: Contribution to $\Delta\sigma_{pn}$ from $\gamma d \to \pi^0 d$ and $\gamma d \to \pi\pi d$.

3. NN FSI interaction in $\gamma d \to \pi\pi NN$ and $\gamma d \to \pi\pi d$

Consideration of the reactions $\gamma d \to \pi\pi NN$ and $\gamma d \to \pi\pi d$ is similar but more involved owing to a more complicated structure of the elementary $\gamma N \to \pi\pi N$ amplitude. We rely here on results obtained by Fix and Arenhövel [19,20] from which we infer contributions to $\Delta\sigma_{pn}$ shown in Figs. 6 (the right panel) and 7. Again we see an essential partial cancelation between $\gamma d \to \pi^+\pi^- d$ and NN -FSI effects in $\gamma d \to \pi^+\pi^- pn$.

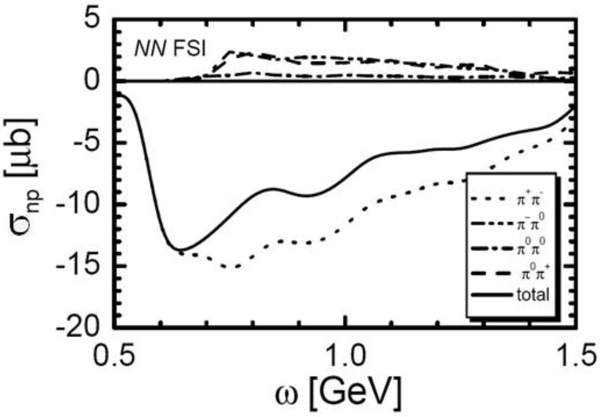

Figure 7: Final state NN interaction in $\gamma d \to \pi\pi NN$.

4. Other small contributions and the net result for $\Delta\sigma_{pn}$

We do not show contributions to $\Delta\sigma_{pn}$ from πN FSI in $\gamma d \to \pi NN$ (found in the described model) and contributions from the deuteron photodisintegration, $\gamma d \to pn$ (it can be directly found from experimental data of CLAS [18]) because they are rather small with the except for energies close to the $\Delta(1232)$ resonance region. We can anticipate that $\Delta\sigma_{pn}$ is not affected by η meson photoproduction because ηN interaction is weaker than that of πN and because effects of NN FSI interaction in the continuum and in the bound state are again nearly canceled.

Taking all contributions together, we arrive at the total value of $\Delta\sigma_{pn}$ shown in Fig. 8 which is the main result of this section. In spite of quite a few pieces of order 10 μb, the sum of all contributions to $\Delta\sigma_{pn}$ is found surprisingly small, so that our improvement to the unfolding procedure is mainly reduced to a refinement in solving the integral equation.

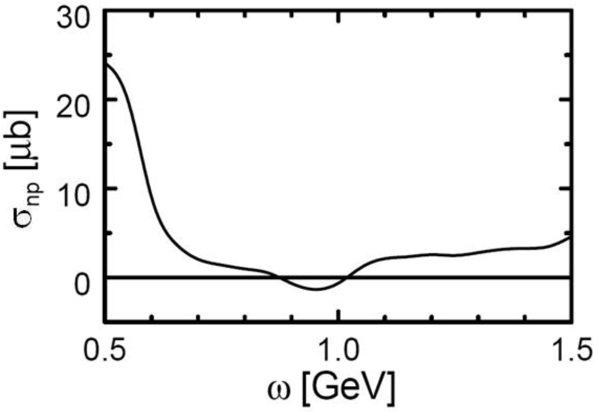

Figure 8: Total value of $\Delta\sigma_{pn}$.

Extraction of the photoabsorption cross section on the neutron

Known now all ingredients of Eq. (3), we can fit experimental data, determine the unsmeared deuteron cross section $\sigma_p + \sigma_n$ and then find the neutron cross section σ_n. We illustrate this procedure using Daresbury data [5, 6] for the proton and the deuteron.

Figure 9 (the left panel) shows a smooth fit (the curve labeled “tot”) with Eq. (12) to the experimental proton data and the result of its smearing with the smearing operator $\hat{F}$. Separately shown is the contribution of resonances (and its smearing) and a smooth background. At the right panel of Fig. 9 a fitting curve is shown that, after smearing and adding $\Delta\sigma_{pn}$, comes through experimental data points (the curve labeled “totF”).

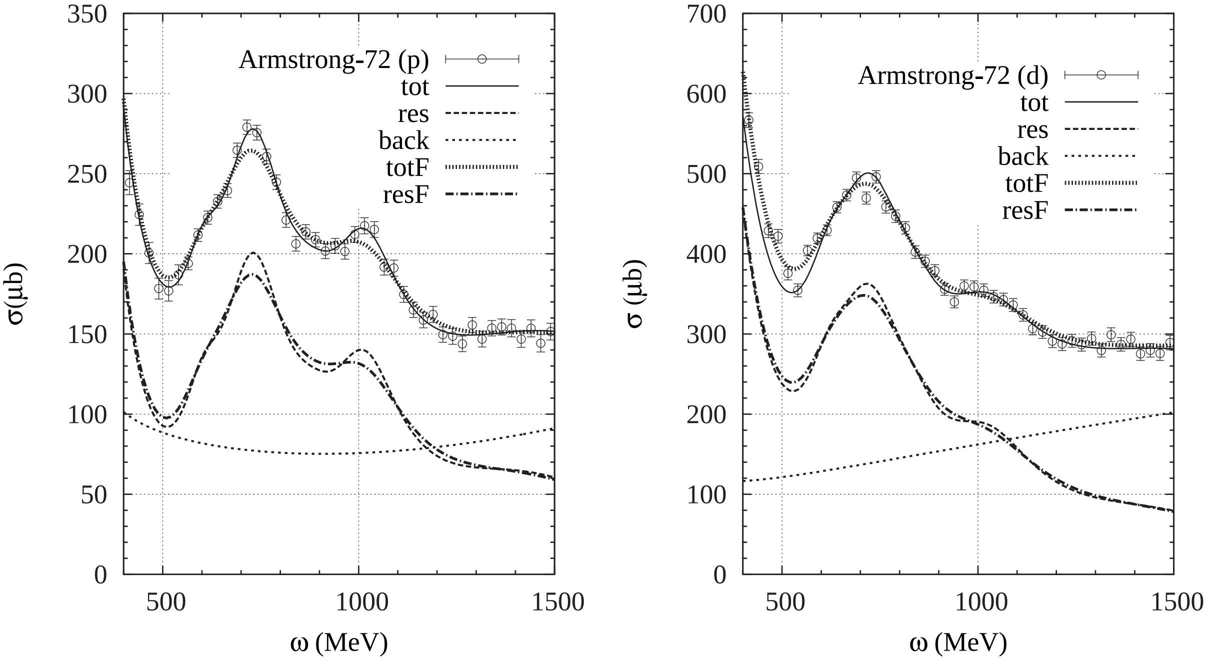

Figure 9: Daresbury data for the proton (left) [5] and the deuteron (right) [6], their fit and smearing.

From this fit the neutron cross section can be found as a difference, see Fig. 10 (the left panel). In a similar way the neutron cross section can be found from Mainz data [21]. Our results are shown in Fig. 10 (the right panel). Bands indicate errors in the found neutron cross sections there.

Conclusions

An improved procedure of extracting the total photoabsorption cross section on the neutron from data on the deuteron is proposed. It involves a more correct treatment of folding/unfolding of the Fermi smearing of individual nucleon contributions.

Non-additive corrections are evaluated at medium energies where VMD does not yet work. They are relatively small in total but they might be more important in analyses of partial channels of photoabsorption.

We hope that the obtained results will be useful for interpretation of the GRAAL data and future experiments.

Acknowledgments

We appreciate very usefull and stimulating discussions with V.G. Nedorezov and A.A. Turinge.

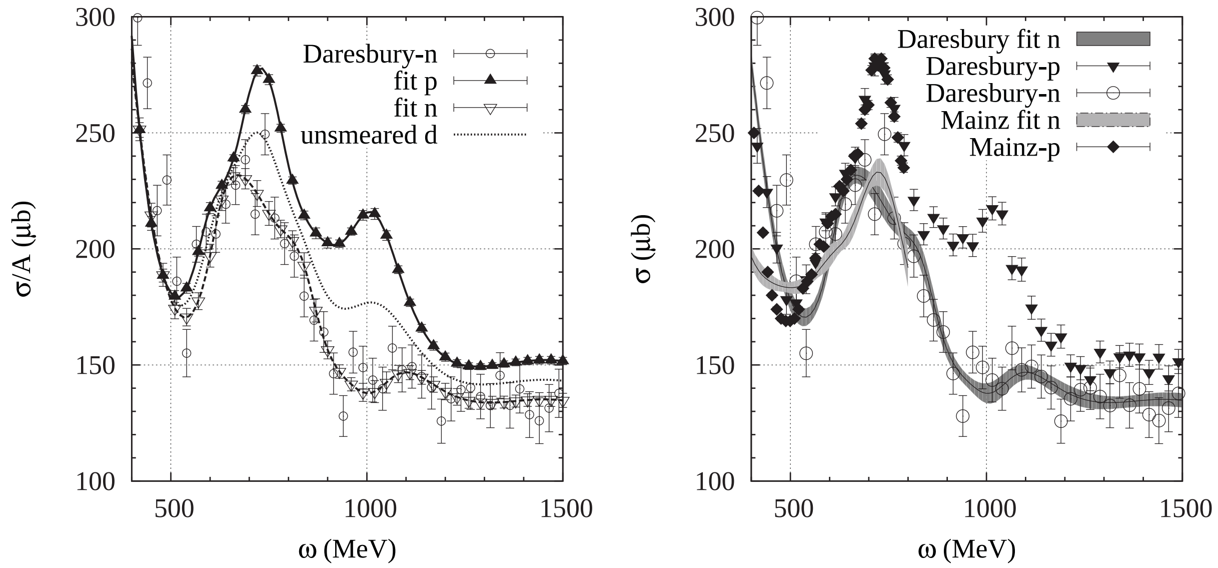

Figure 10: Extraction of the neutron cross section σ_n from the deuteron data (Daresbury [6] and Mainz [21]). Original values of σ_n from the Daresbury experiment are shown with open circles.

References

[1] O. Bartalini, V. Bellini, J.P. Bocquet *et al.*, Yad. Fiz. **71**, 76 (2008) [Phys. Atom. Nucl. **71**, 75 (2008)].

[2] N.V. Rudnev, A.S. Ignatov, A.M. Lapik, A.N. Mushkarenkov, V.G. Nedorezov and A.A. Turinge (for the GRAAL Collaboration), Yad. Fiz. **73**, 1514 (2010) [Phys. Atom. Nucl. **73**, 1469 (2010)].

[3] V.G. Nedorezov, Fiz. Elem. Chast. Atom. Nucl. **43**, 636 (2012) [Phys. Part. Nucl. **43**, 326 (2012)].

[4] A. Turinge, A. Lapik, V. Nedorezov and N. Rudnev for the GRAAL Collaboration, Prog. Part. Nucl. Phys. **67**, 406 (2012).

[5] T.A. Armstrong, W.R. Hogg, G.M. Lewis, A.W. Robertson *et al.*, Phys. Rev. D**5**, 1640 (1972).

[6] T.A. Armstrong, W.R. Hogg, G.M. Lewis, A.W. Robertson *et al.*, Nucl. Phys. B**41**, 445 (1972).

[7] J. Beringer *et al.* (Particle Data Group), Phys. Rev. D**86**, 010001 (2012).

[8] S.J. Brodsky and J. Pumplin, Phys. Rev. **182**, 1794 (1969).

[9] A.S. Belousov, N.P. Budanov, Ya.A. Vazdik, B.B Govorkov, A.I. Lebedev, E.I. Malinovsky, E.V. Minarik, I.V. Mikhailov, V.P. Plaksin, S.V. Rusakov *et al.*, Yad. Fiz. **21**, 556 (1975) [Sov. J. Nucl. Phys. **21**, 289 (1975)].

[10] G.B. West, Ann. of Phys. **74**, 464 (1972).

[11] L. Hulthén and M.Sugawara, in *Handbuch der Physik*, edited by. S. Flugge (Springer-Verlag, Berlin, 1957), Vol. 39, p. 14.

[12] R. Machleidt, Phys. Rev. C **63**, 024001 (2001).

[13] M.I. Levchuk, A.Yu. Loginov, A.A. Sidorov, V.N. Stibunov and M. Schumacher, Phys. Rev. C **74**, 014004 (2006).

[14] M.I. Levchuk, Phys. Rev. C **82**, 044002 (2010).

[15] D. Drechsel, O. Hanstein, S.S. Kamalov and L. Tiator, Nucl. Phys. A **645**, 145 (1999).

[16] R.A. Arndt, W.J. Briscoe, I.I. Strakovsky and R.L. Workman, Phys. Rev. C **66**, 055213 (2002).

[17] M. Schwamb, Phys. Rep. **485**, 109 (2010).

[18] M. Mirazita *et al.*, Phys. Rev. C **70**, 014005 (2004).

[19] A. Fix and H. Arenhövel, Eur. Phys. J. A **25**, 115 (2005).

[20] A. Fix and H. Arenhövel, Phys. Rev. C **72**, 064005 (2005).

[21] M. MacCormick, G. Audit, N. d’Hose, L. Ghedira, V. Isbert, S. Kerhoas, L. Y. Murphy, G. Tamas, P. A. Wallace *et al.*, Phys. Rev. C **53**, 41 (1996).

ELECTROMAGNETIC FRAGMENTATION OF NUCLEI AT HEAVY-ION COLLIDERS

I.A. Pshenichnov

Institute for Nuclear Research, Russian Academy of Sciences, Moscow 117312, Russia

Abstract

Recent experimental and theoretical results on electromagnetic dissociation (EMD) of ultrarelativistic nuclei in ultraperipheral collisions at RHIC and LHC are reviewed. The RELDIS model which was previously successfully validated with experimental data on fragmentation of 30 A GeV lead nuclei on various targets well describes new data on ultraperipheral PbPb collisions at LHC at 1.38+1.38 A GeV. A possibility to study electromagnetic fragmentation of Pb nuclei in pPb collisions at LHC is discussed. RELDIS results for the EMD cross sections in CuAu, AuAu and UU collisions at RHIC and AuAu collisions at NICA are also given.

1. INTRODUCTION

Ultrarelativistic nuclei are forced to collide at the Large Hadron Collider (LHC) at CERN and at the Relativistic Heavy Ion Collider (RHIC) at BNL with the purpose to search for signals of the phase transition between hadronic and quark-gluon phases in hot and dense matter created in such collisions. With this aim it is profitable to study collisions of nuclei with large overlap of their densities. Such collisions typically lead to disintegration of both collision partners and multiple production of secondary hadrons.

The Coulomb fields of colliding nuclei are responsible for their disintegration also in ultraperipheral collisions with large impact parameters $b \geq R_1 + R_2$, where R_1 and R_2 are the nuclear radii. This phenomenon is known as electromagnetic dissociation (EMD) of nuclei [1-3]. An ultrarelativistic nucleus with the Lorentz factor $\gamma_{\mathrm{beam}} >> 1$ representing one of the colliding beams is seen in the laboratory frame as a Lorentz-contracted sheet of nuclear matter. The Coulomb field of such a nucleus is also Lorentz-contracted and therefore highly enhanced, especially when it is observed in the rest frame of the collision partner, where it is characterized by a large effective Lorentz factor $\gamma_{\mathrm{eff}}= 2\gamma^2_{\mathrm{beam}} -1$. For example, $\gamma_{\mathrm{eff}} \sim 4.3 \times 10^6$ for 1.38 + 1.38 A TeV collision energy at LHC. This means that the behavior of nuclear matter under the impact of strong electromagnetic fields can be studied at LHC. The Weizsäcker-Williams method of equivalent photons is frequently used to describe ultraperipheral collisions of nuclei [1-3], which are considered as events with emission and absorption of photons by nuclei with their transition into excited states followed by emission of neutrons. Forward neutrons produced in fragmentation of each of the colliding beams can be detected by Zero Degree Calorimeters (ZDC) installed both at RHIC and LHC [4-6]. EMD events are characterized by few neutrons in ZDC and low (or even zero) multiplicity of particles in central rapidity detectors and thus can be distinguished from hadronic interactions of nuclei.

Apart from the basic scientific interest to study ultraperipheral collisions there are several practical issues related to EMD of nuclei in colliders. Mostly due to large EMD and bound-free e^+e^--pair production cross sections the beam lifetime at RHIC and LHC is restricted [7-9]. As demonstrated [8,9], specific nuclear fragments, in particular ^{206}Pb, produced in EMD events by removal of two neutrons from ^{208}Pb projectile nucleus can provide undesirable heating of LHC components. At the same time it is possible to monitor the collision rate in a heavy-ion collider by detecting neutrons simultaneously emitted in the direction of each of the colliding beams as a result of an ultraperipheral collision [3-6,10].

2. SINGLE AND MUTUAL EMD IN HEAVY-ION COLLIDERS

The electromagnetic dissociation of nuclei is studied at heavy-ion colliders by detecting in ZDCs forward neutrons emitted in the directions of either one or both (denoted as A and C) beams. This makes possible to study single and mutial EMD events. Following Refs. [3,11], a single EMD event is defined as an ultraperipheral collision which is followed by the emission of at least of one neutron by a nucleus from a given beam, e.g. A. At the same time the state of the collision partner from the beam C is not known, as the ZDC for the beam C is not used in detecting single EMD events. In most of such single EMD events the C nucleus which emits photon(s) is not fragmented on the contrary to the fragmenting nucleus A, which emits neutron(s) after its excitation (A-->A*). Single EMD events for the beam C are defined vice versa, when only fragmentation of C beam is detected (C-->C*), while the ZDC for beam A is not involved in measurements. The definitions of single EMD for nuclei A and C are illustrated in Fig.1, where corresponding diagrams are shown. However, more complicated mutual EMD processes can be studied at heavy-ion collider. As discussed in Refs. [3,11], two or more subsequent photon exchanges may take place independently from the primary one in an ultraperipheral collision event, see Fig.1. This means that the set of single EMD events also contains some events with two or more photon exchanges, where the roles of "emitter" and "absorber" were interchanged at the second step, as illustrated by a Venn diagram for these sets of events.

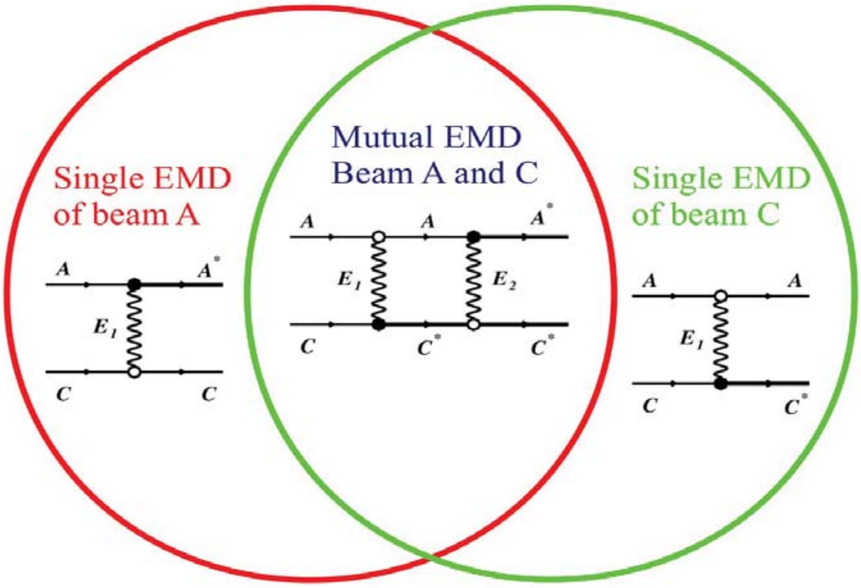

Figure 1: Venn diagram illustrating single and mutual electromagnetic dissociation of nuclei from A and C beams of LHC.

Mutual EMD of both A and C nuclei in a single ultraperipheral event can be detected when the ZDCs detectors are used simultaneously (pairwise), making possible to detect fragmentation of both colliding nuclei. Mutual EMD can only be studied at heavy-ion colliders. This is very different from the experiments performed with accelerated nuclei and fixed targets, where the state of a target nucleus after a collision can not be detected, as emitted neutrons are slow in the laboratory system and easily absorbed in the target material. As considered in Refs. [3,11] and discussed below, more photons can be exchanged with respect to the processes shown in Fig.1 thus leading, e.g., to multiple excitation of giant resonances. In particular, triple excitations of giant resonances can be studied in heavy-ion colliders for the first time [3,11].

3. ELECTROMAGNETIC FRAGMENTATION OF LEAD NUCLEI AT LHC

First measurements of neutron emission in EMD of ^{208}Pb nuclei were performed recently at LHC at 1.38+1.38 A TeV collision energy [12,13]. The cross sections of single and mutual EMD processes were measured and compared to predictions of the RELDIS model, which is described in Refs. [3,11]. As follows from Table 1, which contains selected results from Ref. [13], a very good agreement with RELDIS was found. As one can conclude by comparing the single and mutual EMD cross sections, about 3% of ultraperipheral events of fragmentation of nuclei from beam A are accompanied by fragmentation of nuclei from beam C.

Table 1: Cross sections (barn) of single and mutual EMD of ^{208}Pb nuclei in ultraperipheral collisions at LHC at 1.38+1.38 A TeV collision energy. Only systematical errors are quoted for experimental and theoretical results. From Ref. [13].

Process	Measurements [13]	RELDIS [13]
Single EMD	187.4 ± 13.2	185.2 ± 9.2
Mutual EMD	5.7 ± 0.4	5.5 ± 0.6

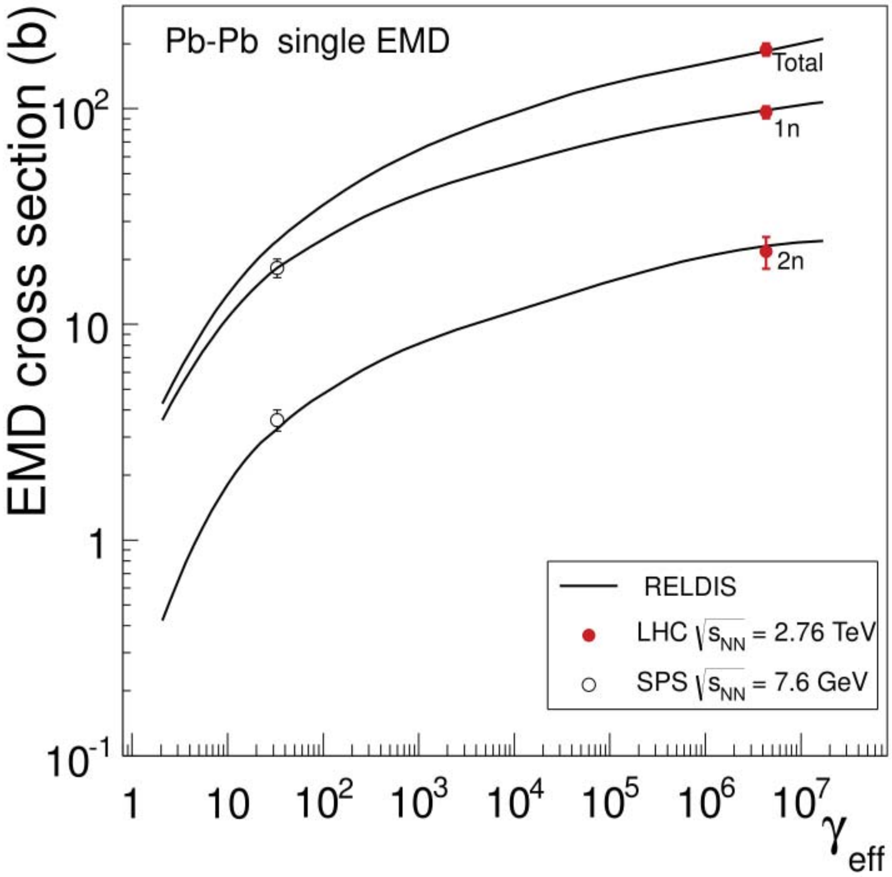

Figure 2: Total, 1n and 2n EMD cross sections as functions of the effective Lorentz factor. Experimental data for EMD in PbPb collisions collected at CERN SPS at 30 A GeV [14] and at LHC at 1.38+1.38 A TeV [13] are shown by open and closed symbols, respectively. RELDIS predictions are shown by solid lines. From Ref. [13].

In addition to the total EMD cross sections, the relative contributions of specific neutron emission channels (1n, 2n or 3n) to true single EMD events where also measured [12,13]. True single EMD events were defined as events with the collision partner certainly left intact, i.e. after subtracting corresponding mutual EMD events. The single 1n and 2n cross sections are presented in Fig. 2 together with the total cross sections. The fractions of 1n, 2n and 3n events in single EMD are listed in Table 2.

Table 2: Relative contributions (in %) of 1n, 2n and 3n events of single EMD after subtracting respective mutual EMD events in ultraperipheral collisions of ^{208}*Pb at 1.38+1.38 A TeV.*

Ratio	Measurements [13]	RELDIS [13]
1n/total	51.5 ± 0.4 stat. ± 0.2 syst.	54.2 ± 2.4
2n/total	11.6 ± 0.3 stat. ± 0.5 syst.	12.7 ± 0.8
3n/total	3.6 ± 0.2 stat. ± 0.2 syst.	5.4 ± 0.7
2n/1n	22.5 ± 0.5 stat. ± 0.9 syst.	23.5 ± 2.5

The measured 1n and 2n single EMD cross sections agree with RELDIS as well as the corresponding fractions of 1n and 2n events. Only the measured 3n fraction is overestimated by RELDIS. This good agreement of 1n and 2n data with RELDIS is not surprising as the model was previously validated with similar neutron yields in ultraperipheral PbPb collisions at CERN SPS at 30 A GeV beam energy [14]. As shown in Fig. 2, the data on EMD of ^{208}Pb nuclei are successfully described by RELDIS within six orders of magnitude of the effective Lorentz-factor γ_{eff}. The 2n/1n ratio measured at LHC (22.5%) is slightly higher compared to the similar ratio (19.7%) reported for 30 A GeV beam energy at SPS. This weak increase, which is well reproduced by the RELDIS model, is explained by additional 2n channels opened at higher collision energy.

Since the RELDIS model is based on Monte Carlo simulations of nuclear reactions induced by equivalent photons, its results should be validated first with the corresponding cross section data on neutron emission due to absorption of real photons by lead nuclei, see e.g. Ref. [15-17]. However, such data have uncertainties related to the separation of 1n and 2n events and normalization of absolute cross section values. This possibly leads to some inaccuracy of the RELDIS model which is tuned to reproduce 2n/1n ratio by adjusting the rate of direct 1n emission from excited lead nucleus at the giant resonance region, as explained in Refs. [3,11]. This typically leads to 5% uncertainties in the total single EMD cross section and to 10% in the mutual one, see Table 1. One can expect that 3n, 4n and 5n EMD yields are calculated by RELDIS even with larger uncertainties, as the corresponding data on absorption of real photons by nuclei are scarce and the model can not be thoroughly validated with respective data. It can be also mentioned that about 3% of single EMD events of lead nuclei are not accompanied by neutron emission. Therefore, the single EMD cross section of neutron emission approaches the total single EMD cross section, but still differs from the it by this small value.

4. ULTRAPERIPHERAL PROTON-LEAD COLLISIONS AT LHC

Fragmentation of lead nuclei in pPb collisions can be also detected at LHC which operated in this mode in 2012. In this accelerator mode 4 TeV protons interact with ^{208}Pb nuclei of 1.577 A TeV. In the rest frame of a lead nucleus a proton is seen with the Lorentz-factor $\gamma_{\rm eff} = 1.4*10^7$. This means that the highest equivalent photon energy exceeds the corresponding energy in PbPb collisions at 1.38+1.38 A TeV. According to RELDIS, the total EMD cross section for ^{208}Pb impacted by proton's Coulomb field is 34 mb, which is ~1% of the total hadronic pPb cross section. As explained above, the relative uncertainty of this cross section is estimated at the level of 5%. The main features of Pb fragmentation in ultraperipheral pPb collisions are quite similar to ones of PbPb collisions. For example, about half of the cross section ~16 mb, is due to 1n emission. Since the main characteristics of EMD of lead nuclei are well known, the rates of forward neutron emission detected by the ZDC installed in the direction of Pb beam can be used to monitor the collider luminosity also in pPb mode.

The photoexcitation of a proton by virtual photons in ultraperipheral pPb collisions is also possible. Only equivalent photons with energies above 140 MeV are important for modeling of such events. According to RELDIS, the total cross section of the photoexcitation of proton amounts to ~400 mb. As some processes of photoproduction of hadrons at high photon energies are neglected in the RELDIS model, this estimation has a larger uncertainty of ~30%. The photoexcitation of beam protons can be experimentally detected with ZDC or other forward detectors installed in the direction of the proton beam. In particular, approximately half of the cross section (~200 mb) is related to the conversion of the beam proton into neutron with emission of charged and neutral mesons. Several such processes can be listed: $\gamma p \text{--->} \pi^+ n$, $\gamma p \text{--->} \pi^+\pi^o n$, $\gamma p \text{--->} \pi^+ 2\pi^o n$, $\gamma p \text{--->} 2\pi^+\pi^- n$ and $\gamma p \text{--->} \rho^+ n$. They all are characterized by production of a neutron which can be detected by ZDC installed in the direction of the proton beam.

5. ULTRAPERIPHERAL COLLISIONS OF URANIUM NUCLEI AT RHIC

Uranium nuclei have the largest charges among nuclear species which were accelerated at heavy-ion colliders. In 2012 RHIC collided 96.5 A GeV uranium nuclei. The total single and mutual EMD cross sections calculated with RELDIS for AuAu and UU collsions at 96.5 + 96.5 A GeV collision energy are listed in Table 3. The EMD cross sections predicted for UU collisions are quite large, about 50% larger than for AuAu at the same collision energy. The mutual EMD cross section for UU collisions approaches the total hadronic cross section for such nuclei, which is estimated as 8.2 b by means of the Glauber model. It is interesting to note that according to RELDIS, ~60% of single EMD events lead to fission of uranium nuclei in addition to neutron emission.

Table 3: Calculated total EMD cross sections (barn) for collisions of gold and uranium nuclei at RHIC.

Process	Collision energy: 96.5 + 96.5 A GeV	
	AuAu	UU
Single EMD	94.15	150.1
Mutual EMD	3.79	7.59

Asymmetric copper-gold collisions were also studied at RHIC in 2012. The RELDIS results for the total EMD cross sections of Cu and Au nuclei are presented in Table 4 for CuAu collisions. These values are compared with the total single EMD cross sections calculated for AuAu collsions at the same energy. Due to a reduced Z^2 factor for Cu nucleus acting as a photon emitter compared to Au, the EMD cross section of Au dissociation in CuAu is reduced compared to AuAu collisions. However, this EMD cross section still remains much larger than the total hadronic AuCu cross section.

Table 4: Calculated total EMD cross sections (barn) for EMD of Cu and Au nuclei collided at RHIC.

	Collision energy:100 + 100 A GeV		
	AuAu	CuAu (copper dissociation)	AuCu (gold dissociation)
Total EMD cross section	95.	22.05	13.37

The difference between the CuAu EMD cross section (copper dissociation) and the AuAu single EMD cross sections can be understood by the following estimate. Due to the Thomas-Reiche-Kuhn (TRK) sum rule written for photon absorption in the giant dipole resonance (GDR) region, the integral of the total photoabsorption cross section is proportional to ZN/A of the absorbing nucleus, with Z and N defined, respectively, as the numbers of protons and neutrons in this nucleus and $A=Z+N$. This factor calculated for the photoabsorption on Cu compared to Au amounts to 0.34 and it controls the relative rates of absorption of equivalent (virtual) photons by such nuclei in the GDR region. When the AuAu EMD cross section is corrected by this factor: 95. b * 0.34 = 32 b, the result turns out to be larger compared to the exact RELDIS result of 22.05 b. There are two reasons which explain the deviation of this estimation from the exact result of the RELDIS model. First, the TRK sum rule is not applicable beyond the GDR region. Second, the maximum energy of equivalent photons $E_{\max}\sim\gamma_{\text{eff}}/R_1+R_2$, see [1-3], depends on the sizes of colliding nuclei.

The cross section of Au dissociation in AuCu collisions follows a simple Z^2-scaling. It can be reliably estimated from the AuAu cross section by applying a factor of $(29/79)^2=0.135$, which then gives 12.8 b, in good agreement with RELDIS.

6. ULTRAPERIPHERAL GOLD-GOLD COLLISIONS AT NICA

The project of Nuclotron-based Ion Collider fAcility NICA/MPD is under development at JINR (Dubna) [18]. It will use a Multi Purpose Detector (MPD) to study heavy-ion collisions at the energy range of few GeV [19]. As MPD will be equipped with ZDCs, the studies of neutron emission in ultraperipheral collisions of heavy nuclei will be also possible. The results of the RELDIS model for the EMD cross sections for ultraperipheral collisions of gold nuclei at 3.5 + 3.5 A GeV are presented in Tables 5 and 6 for single and mutual EMD processes, respectively. The single EMD cross section (~23.9 b) for AuAu collisions is quite large. It is three times as large as the hadronic interaction cross section (~7 b) and essentially affects the beam life-time in NICA. It is estimated that the most probable EMD channel (16.5 b) will be represented by the emission of a single neutron: ^{197}Au --->^{196}Au + n. The emission of two neutrons is also quite probable (3.9 b). We believe that trajectories of Au fragments which are close in mass and charge to beam nuclei have to be thoroughly investigated with respect to their positions in the magnetic field of the accelerator. Such specific fragments can impact some sensitive accelerator components and create undesirable radiation fields and activation. At the same time the detection of mutual EMD events in ultraperipheral collisions at NICA can be used to monitor the collider luminosity.

Table 5: Calculated single EMD cross sections (barn) for AuAu collisions at NICA.

	Collision energy: 3.5 + 3.5 A GeV
Total single EMD	23.9
^{196}Au + n	16.5
^{195}Au + 2n	3.9
^{194}Au + 3n	0.95
^{193}Au + 4n	0.31

Table 6: Calculated mutual EMD cross sections (barn) for AuAu collisions at NICA.

3.5 + 3.5 A GeV	Cross section
Total mutual EMD	1.826
LO	1.374
NLO_{12}+NLO_{21}	0.357
NLO_{22}	0.033
Triple excitations	0.062

Events of mutual EMD of gold nuclei in NICA can be also studied with the aim to detect multiple excitations of giant resonances in such nuclei. NICA provides nuclear beams with energies which are well suited for these studies, as the maximum energy of equivalent photons remains close to the giant resonance region. The mutual EMD cross sections are presented in Table 6 for the leading order and next-to-leading order processes shown in Fig. 3. The cross sections are calculated for ultraperipheral AuAu collisions at NICA at 3.5 + 3.5 A GeV energy. The calculational method is described in Ref. [3,11]. As follows from Table 6, the cross sections of the processes with double photon absorption (NLO_{12}+NLO_{21}+NLO_{22}) approaches ~0.4 b which is about 20% of the total EMD cross section. Even the interactions leading to exotic triple excitations have noticeable cross sections of ~60 mb. Such triple excitations were not yet observed in experiments on absorption of real photons by nuclei. As discussed [3], a relatively large fraction of multiple excitations (~20%) in the set of mutual EMD events compared to single events (~1-2%) can be well understood from that fact that mutual events are characterized by a smaller collision impact parameter on average. As estimated [3], the absorption of equivalent photons by colliding nuclei is more probable in such close collisions. Therefore, the detection of mutual events by using both ZDCs also selects events where multiple excitations of nuclei are quite probable.

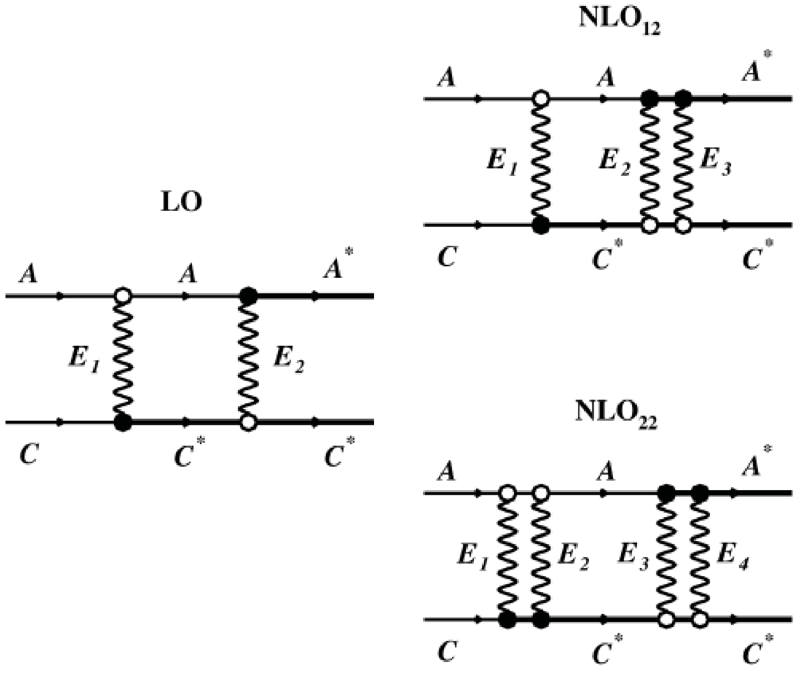

Figure 3: Mutual dissociation of nuclei in the leading (LO) and next-to-leading orders with exchange of three (NLO$_{12}$) and four (NLO$_{22}$) equivalent photons. Photon emission without changing the nuclear state is denoted by the open vertex and photon absorption with nuclear excitation - by the dark one.

7. CONCLUSIONS

Measurements of neutron emission in electromagnetic dissociation (EMD) of nuclei in heavy-ion colliders can be performed with forward detectors, e.g. with ZDC. Single and mutual dissociation events can be disentangled in such studies. Recent data collected at LHC for PbPb collisions are well described by the RELDIS model, which was also successfully used to describe ultraperipheral PbPb collisions at CERN SPS. Basing on this success, reliable predictions for electromagnetic pPb interactions can be also given by means of this model.

The total EMD cross sections for ultraperipheral AuAu, CuAu and UU collisions at RHIC are calculated. As found, about 60% of single EMD events lead to fission of uranium nuclei in addition to neutron emission. These results can be used to estimate the beam lifetime in this accelerator and impact of projectile fragments on accelerator components.

Finally, the results for ultraperipheral AuAu collisions in NICA accelerator indicate the importance of EMD processes even at much lower collisions energies. As expected, a relatively large fraction of mutual EMD events in NICA is related to multiple excitations of giant resonances in colliding Au nuclei.

The author is grateful to Anthony Baltz, Wolfram Fischer and Vladislav Pantuev for discussions of nucleus-nucleus collisions at RHIC.

References

[1] F. Krauss, M. Greiner, and G. Soff, Prog. Part. Nucl. Phys. **39**, 503 (1997).
[2] G. Baur, K. Hencken, and D. Trautmann, J. Phys. G: Nucl. Part. Phys. **24**, 1657 (1998).
[3] I.A. Pshenichnov, Phys. Part. Nucl., **42,** 215 (2011).
[4] C. Adler et al., Nucl. Instrum. Meth. **A499,** 433 (2003).
[5] F. Carminati et al., ALICE collabotation, J. Phys. G: Nucl. Part. Phys. **30,** 1517 (2004).
[6] S.White, Nucl. Instrum. Meth. **A617,** 126 (2010).
[7] A.J. Baltz, M.J. Rhoades-Brown, J. Weneser, Phys. Rev. C **54**, 4233 (1996).
[8] S.R. Klein, Nucl. Instrum. Meth. **A459**, 51 (2001).
[9] R. Bruce et al., Phys. Rev. ST Accel. Beams **12**, 071002 (2009).
[10] A.J. Baltz, C. Chasman and S.N. White, Nucl. Instrum. Meth. **A417**, 1 (1998).
[11] I.A. Pshenichnov, J.P. Bondorf, I.N. Mishustin, A. Ventura, S. Masetti, Phys. Rev. C **64**, 024903 (2001).
[12] C. Oppedisano, J. Phys. G **38**, 124174 (2011); arXiv:1107.1985 [nucl-ex].
[13] B. Abelev et al., ALICE collaboration, arXiv:1203.2436 [nucl-ex]
[14] M.B. Golubeva et al., Phys. Rev. C **71** 024905 (2005).
[15] B.L. Berman, B.L. Fultz, Rev. Mod. Phys. **47**, 713 (1975).
[16] S.S. Dietrich, B.L. Berman, Atomic Data and Nucl. Data Tables **38**, 199 (1988).
[17] B.L. Berman et al., Phys. Rev. C **36**, 1286 (1987).
[18] I.N. Meshkov, Phys. Atomic Nucl. **75**, 594 (2012).
[19] A. Sorin et al., Nucl. Phys. **A855,** 510 (2011).

EMISSION OF NEUTRONS IN ELECTROMAGNETIC FRAGMENTATION OF IN AND PB NUCLEI AT THE CERN SPS

E.V. Karpechev[1]*, T.L. Karavicheva*[1]*, I.A. Pshenichnov*[1]*, A.B. Kurepin*[1]
for the ALICE-lumi experiment (INFN-INR-CERN collaboration)

[1] Institute for Nuclear Research, Russian Academy of Sciences, Moscow 117312, Russia;

Emission of forward neutrons in ultraperipheral collisions of 158A GeV ^{115}In and 30A GeV ^{208}Pb nuclei with Al, Cu, Sn and Pb has been studied at the CERN SPS in the framework of the ALICE-LUMI experiment. In addition to neutron emission cross sections for 30A GeV ^{208}Pb measured earlier, in this work we present new results for 158A GeV ^{115}In projectiles. The measured 1n, 2n and 3n cross sections well agree with results of the RELDIS model for electromagnetic dissociation of In, with the exception of In-Al collisions where the measured cross sections are larger compared to RELDIS. This is attributed to a relatively large contribution of hadronic fragmentation of In in collisions with Al target.

1. INTRODUCTION

Hot and dense nuclear matter can be studied in collisions of ultrarelativistic nuclei at the Super Proton Synchrotron (SPS) and Large Hadron Collider (LHC) at CERN, and at the Relativistic Heavy Ion Collider (RHIC) at BNL. Main efforts are focused on searching for signals of the phase transition between hadronic and quark-gluon phases, which may co-exist in collisions of ultrarelativistic nuclei with large overlap of their nuclear densities. At ultrarelativistic energies a projectile nucleus with the Lorentz factor $\gamma >> 1$ can be thought of as a Lorentz-contracted sheet of nuclear matter. The Coulomb fields of colliding nuclei are also highly Lorentz-contracted. A simple estimate demonstrates that in ultraperipheral collisions of ultrarelativistic nuclei without direct overlap of nuclear densities, at impact parameter $b \geq R_1 + R_2$, where R_1 and R_2 are the nuclear radii, the potential of the Lorentz-boosted Coulomb field is very strong. This potential is estimated as $V_c \sim \alpha\gamma Z/b$ for a nucleus with a charge Z, where b is the collision impact parameter, and α is the fine structure constant. For example, in ultraperipheral collisions of medium-weight or heavy nuclei at the CERN SPS V_c exceeds the effective nucleon-nucleus potential of $\sim$50 MeV which binds the nucleons inside nuclei. Therefore, one or both nuclei may be easily disintegrated by the long-range electromagnetic forces in such ultraperipheral collisions. This phenomenon is well-known under the name of electromagnetic dissociation (EMD) of nuclei [1,2]. It allows to study the behavior of nuclear matter impacted by strong electromagnetic fields.

The Lorentz contraction of electromagnetic fields of nuclei in nucleus-nucleus collisions at the LHC becomes tremendous. As demonstrated by recent measurements [3,4], the total cross section of neutron emission from at least one of the colliding ^{208}Pb nuclei approaches 187 b at 1.38 + 1.38 A TeV collision energy. In this case the nucleus which impacts another nucleus via the action of its electromagnetic field is characterized by a large effective Lorentz factor $\gamma_{\rm eff}= 2\gamma^2_{\rm beam} -1 \sim 4.3 \times 10^6$ which defines the scale of contraction.

As demonstrated in several publications, the EMD process plays a certain role at the LHC. On the one hand, a large EMD cross section imposes restrictions on the beam lifetime at the LHC [5]. Specific nuclear fragments, e.g. ^{206}Pb produced in EMD events can provide undesirable heating of the LHC construction elements [6, 7]. On the other hand, the collider luminosity can be monitored [8] by detecting mutual EMD events characterized by the simultaneous emission of forward neutrons by each of the nuclei in a single ultraperipheral event.

In the present work we study EMD of 30 A GeV ^{208}Pb and 158 A GeV ^{115}In nuclei in their collisions with aluminum, copper, tin and lead targets. The cross sections of forward emission of one, two and three neutrons by these projectiles are measured and compared to results of the RELDIS model [9]. The cross sections of neutron emission in hadronic nucleus-nucleus collisions are calculated by means of a modified version of the abrasion-ablation model [10] and also compared to the experimental data.

Experimental data on fragmentation of indium nuclei are rather scarce. The fragmentation of 158 A GeV ^{115}In in collisions with Si, Ge, Sn, W and Pb was studied in [11] by measuring the cross sections of production of secondary fragments with specific charge, also known as charge-changing cross sections. Since neither fragment masses, nor neutrons emitted from indium nuclei were identified in [11], the measured cross sections represented the sum of hadronic fragmentation cross sections and EMD cross sections. On the contrary, as explained below, mainly the contribution of electromagnetic dissociation was identified in our experiment due to the detection of forward neutrons from indium nuclei. In this sense our data complement the data collected in [11] and provide specific information on EMD of ultrarelativistic ^{115}In nuclei.

Another goal of the present work is to validate the RELDIS model for description of electromagnetic dissociation of ultrarelativistic medium-weight nuclei.

2. THE EXPERIMENTAL SETUP

A general view of our experimental setups is given in Fig. 1. In two independent experiments the beams of 30 A GeV ^{208}Pb and 158 A GeV ^{115}In nuclei were focused on targets which can be moved into and out of the beam by means of a mobile support. Before and after the target two plastic scintillator detectors, S0 and S1, were installed. Both detectors were made of polystyrene with addition of 4 ± 5% of PTP POPOP. They were manufactured as thin plates each 2 mm thick and of 2 cm x 2 cm transverse dimensions. Both detectors provided a good energy resolution. Additional tails observed in signals taken from S1 were related to a lower energy deposition due to nuclear fragments produced in fragmentation of beam nuclei in the target. A small tail was also identified in the signal obtained from the S0 detector due to the presence of nuclear fragments created in interactions of beam nuclei with air on their way to S0.

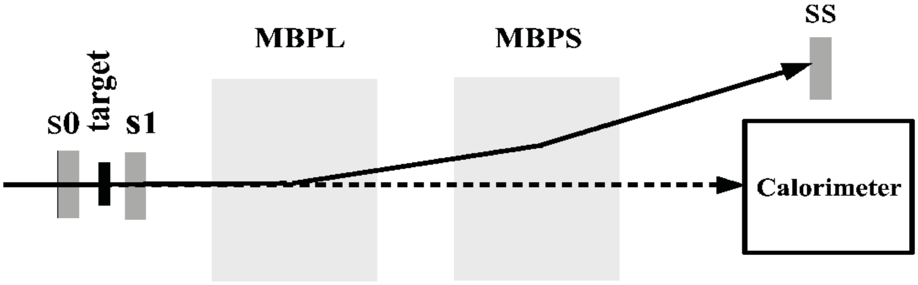

Fig. 1. The experimental setup for registration of forward neutrons from EMD. Vacuum tubes placed between the target and calorimeter are not shown.

Charged particles were deflected out of the neutron calorimeter acceptance by means of two magnets, MBPL and MBPS, with their fields of 3.8 T x m and 1.9 T x m, respectively. These magnets deflected particles in the horizontal plane. Since noninteracting beam nuclei were deflected by these magnets by 7 cm from the primary beam axis, it was possible to place there a plastic scintillator detector SS, also with dimensions of 2 cm x 2 cm, for detecting deflected charged particles. Neutrons from fragmentation of incident ions were not deflected by magnets and therefore hit the neutron calorimeter which was installed after the magnets directly on the axis of the primary beam. S1 was used as a veto detector to suppress the events in neutron calorimeter which were due to charged particles. Vacuum tubes (not shown in Fig.1) were placed between target and neutron calorimeter in order to reduce scattering and absorption of neutrons in air.

The number of primary incident nuclei was defined by counts collected from the S1 detector, while the SS detector was used to tag indium nuclei which were not fragmented neither in air, nor in the target. The neutron calorimeter was placed on a flat platform with its surface aligned parallel to the beam axis. Four materials, aluminum, cooper, tin and lead were used to make targets. Two different lead targets, thick and thin were used in measurements to verify corrections introduced to account for the absorption of beam nuclei and produced forward neutrons. During a separate empty-target run only neutrons produced in the beam line collimators, scintillator plates S0 and S1, and also in air were detected by the neutron calorimeter. This provided us the estimation of the neutron background due to nuclear reactions which take place beyond the target. It was then subtracted from the signal obtained in other runs with installed targets.

3. DATA PROCESSING

The main set of measurements of fragmentation of incident ions was performed with a medium-intensity beam of 5 x10^5 ions per spill. Three different triggers were used in measurements: (1) a random coincidence trigger to estimate the pedestal and noise; (2) a beam trigger only with S0; and (3) a physics trigger for detecting the fragmentation of beam nuclei. The physics trigger included signals from S0, S1 and SS (S0 x S1 x SS) under the condition that the energy registered by the neutron calorimeter exceeds 8 GeV. In addition, some measurements were performed with S0 x SS trigger. The data collected in such measurements were not used for determination of the neutron emission cross sections, but rather helped to estimate the corrections to raw data applied in processing data off-line.

The spectra collected from the S0 and SS detectors were mainly of the Gaussian shape, as can be expected for noninteracting ions or for those nuclei which lost only few neutrons after EMD. However, the tails of the distribution clearly deviated from the Gaussian function. Such deviations were attributed to the interactions of incident ions with air and the windows of the vacuum tubes. The hadronic fragmentation events of beam nuclei were another source of these tails. The energy per nucleon of secondary nuclear fragments created in hadronic interaction can be quite different from the beam energy, on the contrary to the energy of fragments created in the EMD process. The latter process does not change essentially the velocity of a residual nucleus created after the emission of few neutrons from In. Therefore, the rejection of non-Gaussian tails from S0 and SS spectra helped us to disentangle EMD events. Several measurements were performed without target. The obtained spectra were shifted by the pedestal value and corrected according to the signals taken from S0 and SS.

The signal in the neutron calorimeter collected without target was considered as a background attributed to the interactions of beam nuclei with air, the walls of the vacuum tubes and other components of the setup. As the same background existed also in the measurements with target, it was subtracted from the spectra collected in the main run. In this way the signals related only to the interactions of beam nuclei with the target were obtained. Since the spectra obtained in separate runs with and without target corresponded to different numbers of projectile nuclei, these spectra were appropriately weighted before the subtraction. Namely, the spectrum obtained without target was multiplied by the ratio between the number of nuclei crossed the target and number of projectile nuclei in the run without target.

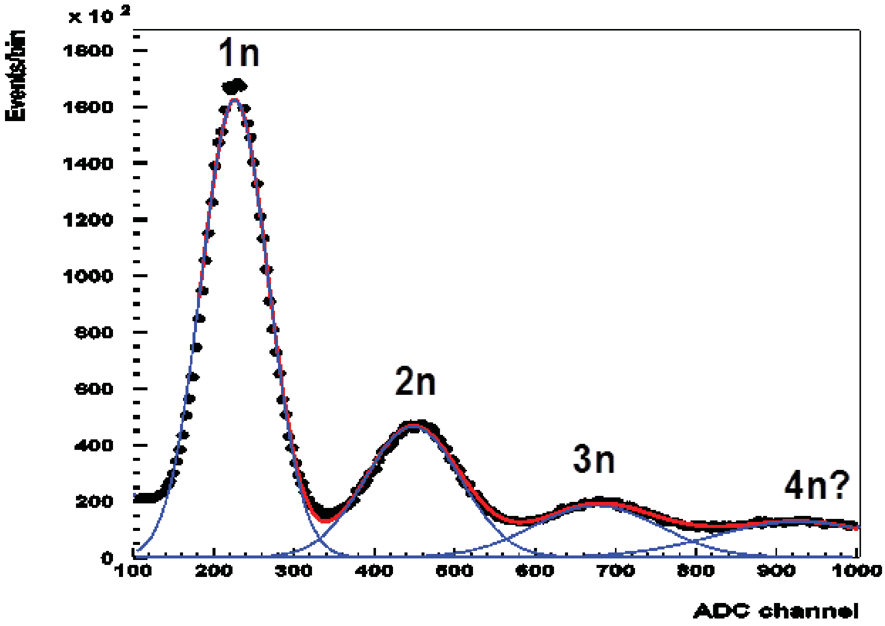

***Fig. 2.** Energy response of the neutron calorimeter to emission of one, two, three and four neutrons by 158A GeV ^{115}In nuclei.*

One of the resulting spectra obtained with ^{115}In beam is shown in Fig. 2. Three distinct peaks corresponding to one, two and three neutrons which hit the calorimeter in a single event are clearly seen. There is also a small contribution from four neutrons.

The resulting spectra for each target were fit by a sum of Gaussians. The average value μ_{1n} and dispersion σ_{1n} for the 1n-peak were introduced as free parameters of the fit. The average values for 2n, 3n and 4n events μ_{2n}, μ_{3n} and μ_{4n}, and the corresponding dispersion values σ_{2n}, σ_{3n} and σ_{4n} were calculated through the values for 1n-peak: $\sigma_{2n} = \sqrt{2}\sigma_{1n}$ and $\mu_{3n} = 3\mu_{1n}$, $\sigma_{3n} = \sqrt{3}\sigma_{1n}$, $\mu_{4n} = 4\mu_{1n}$, $\sigma_{4n} = 2\sigma_{1n}$

Several corrections which take into account the absorption of beam nuclei due to hadronic fragmentation and emitted neutrons due to secondary nuclear reactions have to be applied to these values:

- We took into account the beam attenuation in target due to hadronic fragmentation.
- We corrected results for the misinterpretation of two independent 1n events detected as a single 2n event.
- We corrected results to account for interactions of produced neutrons in target material and air.
- Corrections for 3n events counted as either 2n or 1n events were applied. Then we corrected for 2n events detected as 1n events.

As expected, see e.g. [12], neutrons from EMD are emitted in forward direction and characterized by smaller average transverse momenta compared to neutrons from hadronic fragmentation. Due to the specific design of our experimental setup which is described above mostly EMD neutrons are detected.

4. RESULTS FOR 30 A GEV PB BEAM

We start with presenting our previous experimental results [12]. The cross sections of forward 1n and 2n emission by 30 A GeV ^{208}Pb in collisions with Al, Cu, Sn and Pb are given in Table 1. The measured cross sections are compared with the cross sections calculated with RELDIS, which are also presented in Table 1. The consideration of data collected in two independent experiments both for fragmentation of medium-weight (^{115}In) and heavy (^{208}Pb) projectiles helps in estimating the role of hadronic fragmentation in neutron emission, as it is expected to be different for projectiles with different nuclear charge and mass.

Table 1. *Measured and calculated with RELDIS 1nX and 2nX cross sections (in barns) and their sum for 30 A GeV ^{208}Pb on Al, Cu, Sn and Pb, from Ref. [12]*

Target	σ_{1nX}		σ_{2nX}		$\sigma_{1nX+2nX}$	
	Experiment	**RELDIS**	**Experiment**	**RELDIS**	**Experiment**	**RELDIS**
Al	0.51 ± 0.05	0.55	0.13 ± 0.02	0.09	0.64 ±0.05	0.64
Cu	2.6 ± 0.3	2.58	0.57 ± 0.07	0.45	3.2 ± 0.3	3.03
Sn	8.8 ± 0.9	7.33	2.0 ± 0.2	1.29	10.8 ± 0.9	8.62
Pb	18.3 ± 1.8	18.25	3.6 ± 0.4	3.27	21.9 ± 1.8	21.52

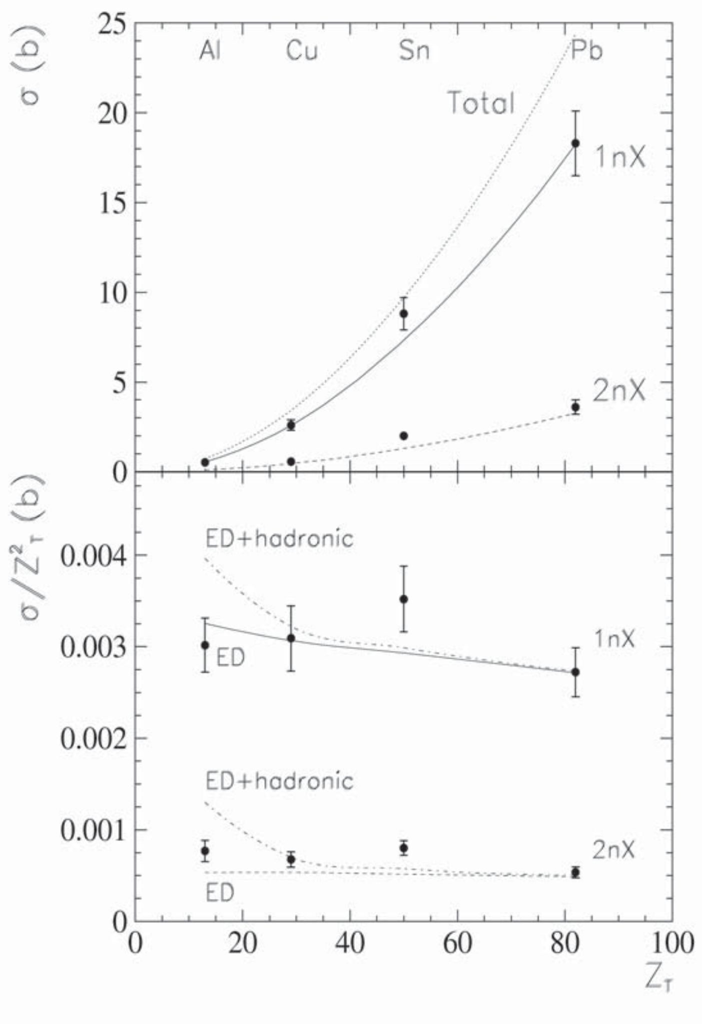

Fig. 3. *(Top) Points show measured cross sections of forward 1n and 2n emission in dissociation of 30A-GeV Pb ions on Al, Cu, Sn, and Pb as a function of the target nucleus charge Z_T. Calculated total, 1nX, and 2nX EMD cross sections are shown by dotted, solid, and dashed lines, respectively. (Bottom) 1nX and 2nX cross sections divided by Z_T^2. The sum of calculated hadronic and EMD cross sections is shown separately for 1n and 2n channels by dash-dotted lines. From Ref.[12].*

The dominance of the electromagnetic interaction in 1n and 2n emission from ^{208}Pb in the forward direction is predicted by theory. Indeed, the hadronic 1n and 2n cross sections estimated [12] by the abrasion-ablation model are typically less than the experimental errors. The exception to this rule is 1n emission in PbAl collisions with its hadronic contribution of ∼25% of the experimental cross section. The 2n emission in PbAl and PbCu collisions due to hadronic interactions is estimated as ∼100% and ∼25%, respectively [12]. However, also in these cases most of neutrons from hadronic fragmentation are emitted beyond the acceptance of the neutron calorimeter. The dependence of the measured 1n and 2n cross sections on the target charge Z_T indicates the electromagnetic nature of forward neutron emission from Pb projectiles, as shown in Fig. 3 [12]. Both the absolute cross sections σ and their values divided by Z_T^2 are plotted. According to the Weizsacker-Williams (WW) method of equivalent photons [1,2], the flux of photons which irradiates a projectile is proportional to Z_T^2. Therefore, a flat dependence of σ/Z_T^2 is expected for electromagnetic dissociation of projectile nuclei. Some deviations of σ/Z_T^2 from a constant value are possible due to an additional Z_T dependence of the maximum photon energy in the spectrum related to the sizes of colliding nuclei, which define the minimum impact parameter in electromagnetic interactions of these nuclei.

The measured 1nX cross sections are in good agreement with those calculated by the RELDIS code. The general trend of the data seen in Fig. 3 clearly indicates the electromagnetic nature of Pb fragmentation. As for the 2nX emission, its dependence on Z_T also clearly reveals the electromagnetic nature of Pb dissociation. However, the experimental values are slightly underestimated by theory. This discrepancy between the calculated and experimental 2nX cross sections can be reduced by neglecting the direct nonstatistical contribution in the GDR decay [12]. The measured sum of 1nX and 2nX cross sections is also presented in Table 1 and compared to the RELDIS results. This sum is in good agreement with theory because the total γPb cross section used in the calculations was measured in experiments with monoenergetic photons [13,14] with reasonable accuracy. Larger uncertainties were typical for the measurements of partial 1n and 2n cross sections, resulting in noticeable disagreement between the results of Saclay [13] and Livermore [14]. Based on the observation that the total photoneutron yields, $\sigma(\gamma,n) + 2\sigma(\gamma,2n) + 3\sigma(\gamma,3n)$, obtained in Livermore and Saclay experiments agree well, an explanation for this disagreement was put forward in [15]. There it was concluded that the neutron multiplicity sorting procedure adopted at Saclay was not correct since some (γ,2n) events were wrongly interpreted as pairs of (γ, n) events.

5. RESULTS FOR 158 A GEV IN BEAM

Table 2 contains the results of our recent measurements of the cross sections of forward 1n, 2n and 3n emission in collisions of 158 A GeV ^{115}In with Al, Cu, Sn and Pb. As seen from Table 2, the measured cross sections agree in general with RELDIS taking into account the uncertainties of measurements listed in the table. However, the data for Al traget for all neutron multiplicities are noticeably larger compared to RELDIS results for this light target nucleus.

***Table 2**. Measured and calculated with RELDIS 1nX, 2nX and 3nX cross sections (in barns) for 158 A GeV ^{115}In on Al, Cu, Sn and Pb.*

Target	σ_{1nX}		σ_{2nX}		σ_{3nX}	
	Experiment	**RELDIS**	**Experiment**	**RELDIS**	**Experiment**	**RELDIS**
Al	0.56 ±0.08	0.40	0.21 ± 0.03	0.09	0.09 ± 0.02	0.03
Cu	2.09 ±0.31	1.91	0.49 ± 0.07	0.45	0.22 ± 0.04	0.13
Sn	5.00 ± 0.75	5.47	1.11 ± 0.17	1.28	0.51 ± 0.10	0.38
Pb	12.32 ±1.85	14.05	2.40 ±0.35	3.32	1.11 ± 0.23	1.03

A convenient presentation of the data and calculations for ^{115}In is given in Fig. 4, where all cross sections are again divided by the square of charge of the target nucleus Z^2, and plotted as a function of Z. As mentioned above, the spectrum of equivalent photons is approximately proportional to Z^2 of the target nuclei (Al, Cu, Sn, or Pb), which emit photons absorbed by ^{115}In. This is illustrated by a flat dependence of RELDIS results divided by Z^2 as a function of Z. There is also a slight increase of σ/Z^2 for lighter targets due to the involvement of nuclear radii in calculations. Despite of the latter peculiarity a flat dependence of σ/Z^2 serves as a clear indication of the electromagnetic nature of interactions. As mentioned above, a similar flat dependence was observed in our studies of the emission of forward neutrons by 30 A GeV Pb nuclei in collisions with Al, Cu, Sn and Pb [12]. Taking into account experimental uncertainties of the present data, σ/Z^2 for Cu, Sn and Pb targets are consistent in general with a flat dependence on Z. However, the cross sections measured with Al target are higher than ones obtained with RELDIS, and also a general descending trend of σ/Z^2 is obvious in Fig. 4, similar to one seen in Fig. 3.

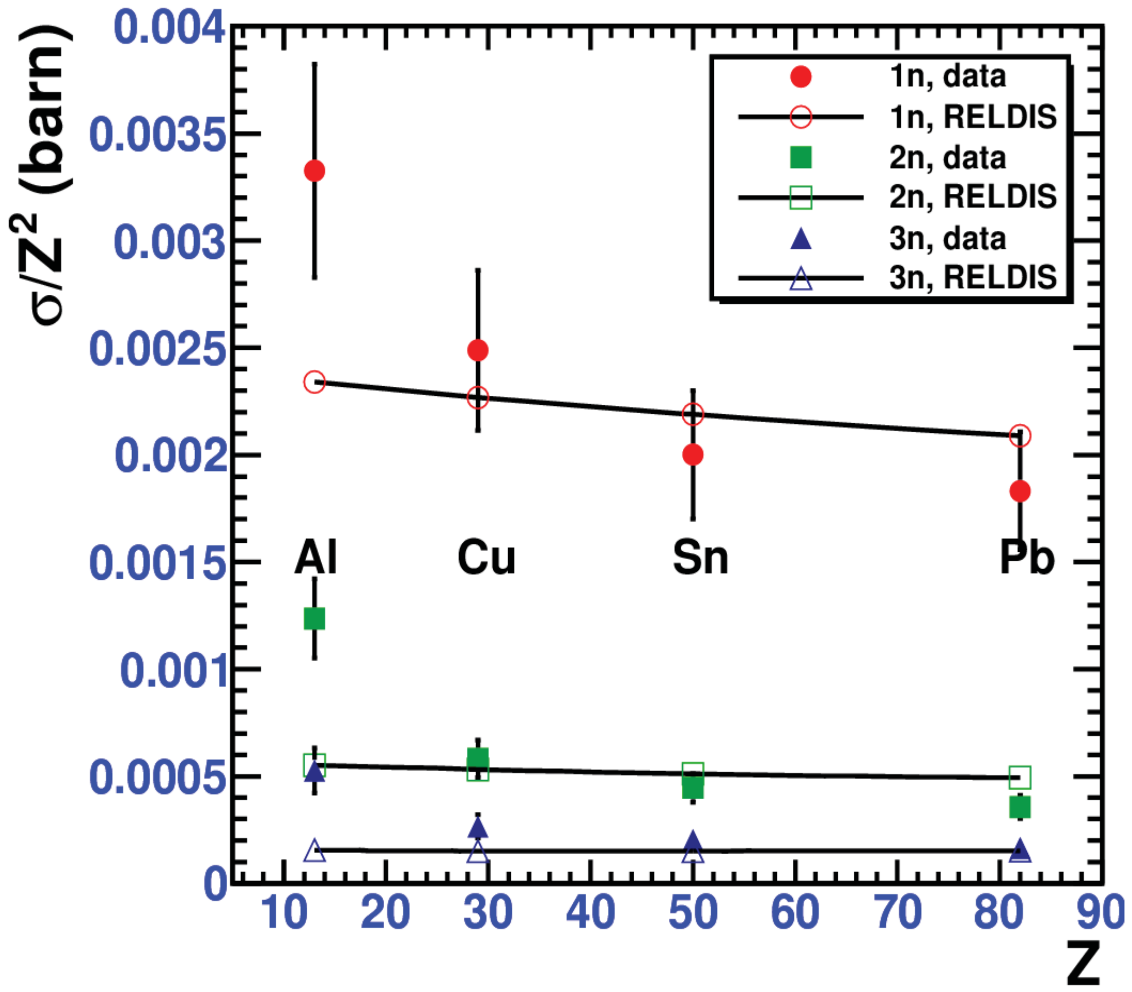

Fig. 4. *Calculated and measured σ/Z^2 for 1n, 2n and 3n emission from 158 A GeV ^{115}In on Al, Cu, Sn and Pb targets*

The relation between the cross sections of 1n, 2n and 3n emission in hadronic and electromagnetic fragmentation of 158 A GeV ^{115}In can be better understood from theoretical results for these cross sections presented in Table 3. The sum of 1nX, 2nX and 3nX channels amounts to 87% of the total EMD cross section, while the same channels of hadronic fragmentation provide only 6-8% of the total hadronic fragmentation cross section. As seen from Table 3, the cross sections of 1n, 2n and 3n emission in hadronic interactions of ^{115}In with Al are comparable to the corresponding EMD cross sections. Therefore, a noticeable contribution of hadronic events to the emission of forward neutrons by ^{115}In in collisions with Al is expected. Apart of the EMD process, one, two and three neutrons are also produced in peripheral grazing hadronic nucleus-nucleus collisions. For a given projectile nucleus the cross section of grazing collisions is proportional to the area of a thin surface rim of the target nucleus: $\sigma \sim Z^{2/3}$. This means that $\sigma/Z^2 \sim 1/Z^{4/3}$, and the descending trend seen in Fig. 4 due the presence of hadronic events is explained.

Table 3. *The cross sections (in barns) calculated with RELDIS and abrasion-ablation models for 1n, 2n and 3n emission from 158A GeV ^{115}In in collisions with Al, Cu, Sn and Pb. The total EMD and hadronic fragmentation cross sections are also given.*

Target nucleus	**Fragmentation channel**	**EMD, RELDIS**	**hadronic fragmentation, abrasion-ablation**
Al	1nX	0.40	0.06
	2nX	0.09	0.08
	3nX	0.03	0.11
	total	0.60	3.34
Cu	1nX	1.91	0.07
	2nX	0.45	0.10
	3nX	0.13	0.12
	total	2.86	4.25
Sn	1nX	5.47	0.08
	2nX	1.28	0.11
	3nX	0.38	0.13
	total	8.19	5.14
Pb	1nX	14.05	0.09
	2nX	3.32	0.12
	3nX	1.03	0.15
	total	21.07	6.18

6. DISCUSSION

Reliable experimental data on absorption of photons by nuclei are very important for further development of theoretical models of EMD. As discussed in Refs. [9,12], the experimental data on the absorption of photons by ^{208}Pb nucleus have uncertainties related to the sorting of neutron emission events into 1n, 2n and 3n channels. The cross sections of these photoabsorption channels measured in different laboratories differ from each other. As the parameters of theoretical models of photoabsorption on nuclei and those of EMD models are tuned by comparison with such data, some uncertainties are inevitably introduced also to calculated 1n and 2n EMD cross sections. This may affect the accuracy of the method proposed in Ref. [8] to monitor the collider luminosity by detecting simultaneous emission of only single neutrons by each of the colliding nuclei in mutual EMD events. As proposed [9,16], the problem of systematic uncertainties of the luminosity measurements can be alleviated by counting together mutual EMD (1nX|1nX), (1nX|2nX), (2nX|1nX) and (2nX|2nX) events. This solution is possible due to a smaller relative uncertainties of 1n+2n cross sections compared to the relative uncertainties of specific 1n and 2n channels.

Similar systematic uncertainties of the cross sections of 1n, 2n and 3n emission measured for photon absorption on ^{115}In may also affect the accuracy of EMD cross sections calculated with RELDIS. Therefore, we first validated RELDIS with existing photonuclear data on ^{115}In [17-20], which are plotted in Fig. 5. As only neutrons were detected in these experiments, (γ,n) and (γ,2n) channels were not clearly separated from (γ,np) and (γ,2np) channels, respectively. Therefore, their sum is presented in Fig. 5 and is referred below as (γ,n) and (γ,2n) for simplicity. The contribution of proton emission from medium-weight and heavy nuclei is expected to be small due to high Coulomb barriers in these nuclei.

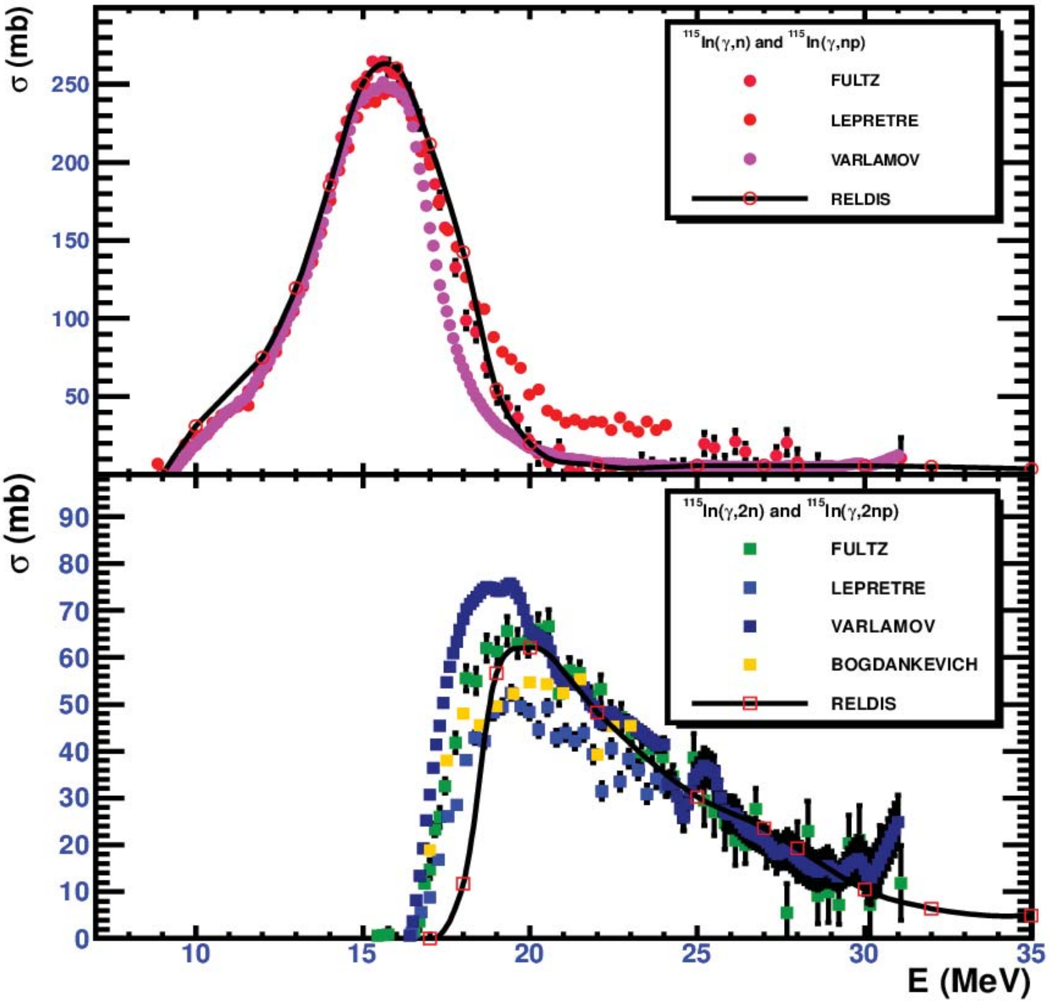

Fig. 5. *Photonuclear data on* ^{115}*In. Measured 1nX (top) and 2nX (bottom) cross sections (points) as functions of photon energy together with RELDIS results (curves). Experimental data [17-20] are shown by various symbols as explained in the legend.*

The experimental data on (γ,n) reaction on ^{115}In collected at the Livermore National Laboratory [18] are well described by RELDIS. However, the threshold of (γ,2n) reaction is overestimated by the model. Nevertheless, the (γ,2n) cross sections calculated with RELDIS still remain closer to Livermore data [18] compared to other measurements [17,19] or evaluations [20]. The recent evaluated data by Varlamov et al., [20] can be considered as the most reliable data on photoabsorption on ^{115}In. The evaluated 1n cross section is well described by RELDIS, except the right-hand side of the GDR peak, where the cross section is overestimated. As result, this leads to the underestimation of 2n cross section seen at the bottom part of Fig. 5 between 16 and 20 MeV where the experiment and theory diverge. This is caused by a less sharp rise of the calculated 2n cross section above the 2n threshold. Above 20 MeV the agreement between RELDIS and the evaluated 1n and 2n cross section data is restored. However, the 1n and 2n EMD cross sections calculated with RELDIS are not very sensitive to such deviations and both agree with our present data, as a much wider range of photon energies is involved in calculations.

Similar to γPb reactions, the main uncertainties in the γIn partial cross sections are related to sorting of 1n and 2n events, with a more accurate determination of their sum. Therefore, in the case if indium nuclei will be accelerated in a heavy-ion collider, the detection of (1nX|1nX), (1nX|2nX), (2nX|1nX) and (2nX|2nX) mutual EMD events together will help to monitor the collider luminosity.

7. CONCLUSIONS

We presented data on emission of one, two and three forward neutrons in collisions of 30 A GeV ^{208}Pb (reported in [12]) and 158A GeV ^{115}In (newly measured) with Al, Cu, Sn and Pb targets. The data are compared to the cross sections of neutron emission in electromagnetic dissociation of these projectiles calculated with the RELDIS model. The measured cross sections agree with the cross sections calculated by RELDIS for ultraperipheral collisions with Cu, Sn and Pb targets within estimated uncertainties of the measurements with the exception of the lightest Al target for which we estimated a relatively large contribution from hadronic fragmentation. The measured cross sections are attributed mainly to the electromagnetic dissociation process, as σ/Z^2 reveals a flat dependence on Z.

Our present results confirm the accuracy of RELDIS in calculating the cross sections of forward neutron emission by ultrarelativistic ^{115}In and ^{208}Pb nuclei. Therefore, the RELDIS model can be used in planning future experiments at the LHC with beams of such nuclei. New experiments on photoabsorption on various nuclei are very desirable, as they help to improve the accuracy of nuclear data used to model EMD.

References

[1] F. Krauss, M. Greiner, and G. Soff, Prog. Part. Nucl. Phys. **39**, 503 (1997).
[2] G. Baur, K. Hencken, and D. Trautmann, J. Phys. G: Nucl. Part. Phys. **24**, 1657 (1998).
[3] C. Oppedisano, J. Phys. G **38**, 124174 (2011) arXiv:1107.1985 [nucl-ex].
[4] B. Abelev et al., ALICE collaboration, arXiv:1203.2436 [nucl-ex], accepted by Phys. Rev. Lett., 2012
[5] A.J. Baltz, M.J. Rhoades-Brown, J. Weneser, Phys. Rev. C **54**, 4233 (1996).
[6] S.R. Klein, Nucl. Instrum. Meth. **A459**, 51 (2001).
[7] R. Bruce, D. Bocian, S. Gilardoni, et al., Phys. Rev. ST Accel. Beams **12**, 071002 (2009).
[8] A.J. Baltz, C. Chasman, S.N. White, Nucl. Instrum. Meth. **A417**, 1 (1998).
[9] I.A. Pshenichnov, J.P. Bondorf, I.N. Mishustin, A. Ventura, S. Masetti, Phys. Rev. C **64**, 024903 (2001).
[10] C. Scheidenberger et al., Phys. Rev. C **70,** 014902 (2004).
[11] U.I. Uggerhoj, I.A Pshenichnov, C. Scheidenberger et al., Phys. Rev. C **72**, 057901 (2005).
[12] M.B. Golubeva et al., Phys. Rev. C **71** 024905 (2005).
[13]. B.L. Berman, B.L. Fultz, Rev. Mod. Phys. **47**, 713 (1975).
[14]. S.S. Dietrich, B.L. Berman, Atomic Data and Nucl. Data Tables **38**, 199 (1988).
[15] B.L. Berman et al., Phys. Rev. C **36**, 1286 (1987).
[16] I.A. Pshenichnov, Phys. Part. Nucl., **42,** 215 (2011).
[17] O.V. Bogdankevich, B.I. Goryachev, V.A. Zapevalov, J. Exp. Theor. Phys. 15 1044 (1962).
[18] S.C. Fultz, B.L. Berman, J.T. Caldwell, R.L. Bramblett, M.A. Kelly, Phys. Rev. **186**, 1255 (1969).
[19] A. Lepretre, H. Beil, R. Bergere, P. Carlos, A. De Miniac, A. Veyssiere, K. Kernbach, Nucl.Phys. **A219,** 39 (1974).
[20] V.V. Varlamov, B.S. Ishkhanov, V.N. Orlin, A.V. Sopov, Preprint SINP MSU 2010-8/864

FRAGMENTATION OF RELATIVISTIC ^{10}C NUCLEI IN NUCLEI EMULSION

K.Z.Mamatkulov[1),2)], D.A.Artemenkov[1)], R.N.Bekmirzaev[2)], V.Bradnova[1)], P.I.Zarubin[1)], I.G.Zarubina[1)], N.V.Kondratieva[1)], N.K.Kornegrutsa[1)], D.O.Krivenkov[1)], R.R.Kattabekov[1),3)], A.I.Malakhov[1)], P.A.Rukoyatkin[1)], V.V.Rusakova[1)]

[1)] Joint Institute for Nuclear Research (JINR), Dubna, Russia
[2)] Jizzah Pedagogical Institute, Uzbekistan
[3)] Physical-Technical Institute, Tashkent, Uzbekistan

ANNOTATION

The features of the fragmentation of relativistic ^{10}C nuclei with energy 1.2 A GeV per nucleon in nuclear emulsion are represented. The structure of the nucleus ^{10}C role foundations play an unstable nucleus ^{8}Be, which appear in the cascade of dissociation of $^{10}C \rightarrow {}^{9}B + p \rightarrow {}^{8}Be + 2p$. Decays of relativistic nuclei $^{8}Be \rightarrow 2\alpha$ via the ground state 0^{+} are identified by excitation energy α-particle pairs ($Q_{2\alpha}$). Events of $^{10}C \rightarrow 2^{4}He+2p$ coherent dissociation are identified.

INTRODUCTION

Dissociation of relativistic nuclei on heavy target nuclei induced in the diffraction of electromagnetic and nuclear interactions. Due to a collimation of fragments of the projectile nucleus, definition of interactions as peripheral is simplified by moving towards to energy from above 1 *A* GeV. In the narrow stream of light nuclei with a total charge, close to the charge of the initial nucleus and the most peripheral of these are not accompanied by the formation of fragments of the target. Events of this type are referred to as the "white" stars, observed in an emulsion with a unique authenticity [1]. Such events occur as a result of electromagnetic and nuclear diffraction on heavy nuclei of emulsion composition (i.e., *Ag* and *Br*). Nuclear emulsion method provides a unique observability with a record spatial resolution (0.5 μm) of multiple systems of relativistic fragments produced by dissociation.

Minimal perturbation of a projectile makes them the most valuable sample for nuclear cluster physics. Excitation energy of a fragment ensemble is estimated as $Q = M^{*}-M$, where M^{*} is the ensemble invariant mass and M – a projectile mass. The value M^{*} is defined as $M^{*2}=(\Sigma P_j)^2=\Sigma(P_i \cdot P_k)$, where $P_{i,k}$ are 4-momenta of the fragments. Assumption of projectile speed conservation by relativistic fragments is sufficient to compensate the lack of momentum measurements. Already it is established that final states of relativistic He fragments effectively correlate with the clustering in the nuclei ^{12}C [8], ^{6}Li [9], and ^{9}Be [4,5]. The described approach is used in the BECQUEREL Project [2] to study the drip line nuclei ^{7}Be, ^{8}B, ^{9}C, ^{10}C, and ^{12}N [1,3-7] by means emulsion stacks exposed to secondary beams of the JINR Nuclotron [6]. The status of the ^{10}C investigation, which entails the production of two α particles and two protons, is presented.

EXPERIMENT AND RESULTS

Nuclear track emulsion is exposed to a mixed beam of ^{12}N, ^{10}C and ^{7}Be nuclei formed by means of primary 1.2 A GeV ^{12}C nucleus beam [6,11]. Search for interactions in emulsion layers was conducted on primary tracks $Z_{pr} > 2$ without sampling. Completely search and charge measurements "white" stars are executed in 12 layers. On total length of viewing of primary tracks, are equal 1088.1 m, was found 7241 inelastic interactions, including 608 "white" stars. The mean free path of nuclei ^{10}C was equal to $\lambda_C = 14.8 \pm 0.9$ sm, which corresponds to the data with the neighboring cluster nuclei in the emulsion, obtained earlier in works [9,10].

From 608 found interaction, so-called "white" stars, were selected events in which the total charge of fragments is equal to the charge of the projectile nucleus $Z_0 = 6$ (186 events). "White" stars are formed in the case of the minimum energy transfer to the fragmenting nucleus, thus in a nuclei collapse intercluster communication and, as a rule, are not affected by intracluster communications because of what they are of special interest for studying cluster structures of nuclei. Fragments of the projectile nucleus in these events are emitted within a narrow anterior cone, the angular cone of a fragmentation amounts to $\theta_{fr} \leq 8^0$.

In table 1 shows distribution on channels dissociation numbers of "white" stars N_{ws} and events with fragments of a target or born mesons N_{tf}, for which the state $Z_{pr} = \Sigma Z_{fr}$ and $\Sigma Z_{fr} = 6$. For a case $\sum Z_{fr} = 6$ such state is checked up in 12 layers at calibration. The most probable channel is represented by 186 events *2He + 2H*, that it is followed expect for an isotope ^{10}C. Channel *He + 4H* has appeared suppressed. Indeed, for peripheral dissociation of ^{10}C requires overcoming of a high threshold of the collapse of α - cluster. In addition, the formation of eight C → 6H “white” stars is noteworthy. In the cases of the isotopes $^{10,11,12}C$, events of this type require a simultaneous breakup of two or three ^4He clusters. Because of very high thresholds, they could hardly proceed without the formation of target fragments. As an example on fig. 5 are given the micrograph of the events of the nuclear fragmentation in the channel $^{10}C \rightarrow 2\alpha + 2p$.

Table 1. Distribution on channels dissociation numbers of "white" stars N_{ws} and events with fragments of a target or born mesons N_{tf}, for which satisfied state $\Sigma Z_{fr} = 6$

Channel (^{10}C)	*2He+2H*	*He+4H*	*3He*	*6H*	*Be+He*	*B+H*	*Li+3H*	^9C+n
N_{ws}=227 (%)	186 (81.9)	12 (5.3)	12 (5.3)	9 (4.0)	6 (2.6)	1 (0.4)	1 (0.4)	-
N_{tf}=627 (%)	361 (57.6)	160 (25.5)	15 (2.4)	30 (4.8)	17 (2.7)	12 (1.9)	2 (0.3)	30 (4.8)

Fig. 1 shows the distribution of the polar emission angle θ of the relativistic fragments with charges $Z_{fr} = 2$ and $Z_{fr} = 1$. The mean value of $<\theta>$ for fragments with $Z_{fr} = 2$ in events $^{10}C \rightarrow {}^9B + p \rightarrow 2\alpha + 2p$ is equal to $<\theta> = (11.07 \pm 1.1) \times 10^{-3}$ rad (RMS = 8.01×10^{-3} rad; where RMS is the root-mean-square deviation) for fragments with $Z_{fr} = 1$ – $<\theta> = (49.3 \pm 7.5) \times 10^{-3}$ rad (RMS = 54.1×10^{-3} rad). The difference in the values of $<\theta>$ for light and heavy fragments reflects the difference of their masses.

Identification for the separation of isotopes of *H* and *He* in emulsion experiments used measurements of the value $p\beta c$, determined by the average angle of multiple coulomb scattering. For determining the $p\beta c$ needs to use traces with length about 2 – 5 sm. This condition does not allow use all of the available statistics interactions. In the fig. 2(a) identified by on value $p\beta c$ of isotopes *H* and *He* for 16 events in channel *2He + 2H*. For comparison presented distribution $p\beta c$ of ^3He fragments from events of fragmentation $^9C \rightarrow 3^3He$ at 1.2 *A* GeV energy. ^3He and ^4He fragments are clearly separated by value $p\beta c$. Thus, in the found statistics of "white" stars *2He + 2H* all nuclei *He* correspond isotope ^4He (α), and *H* – ^1H (p).

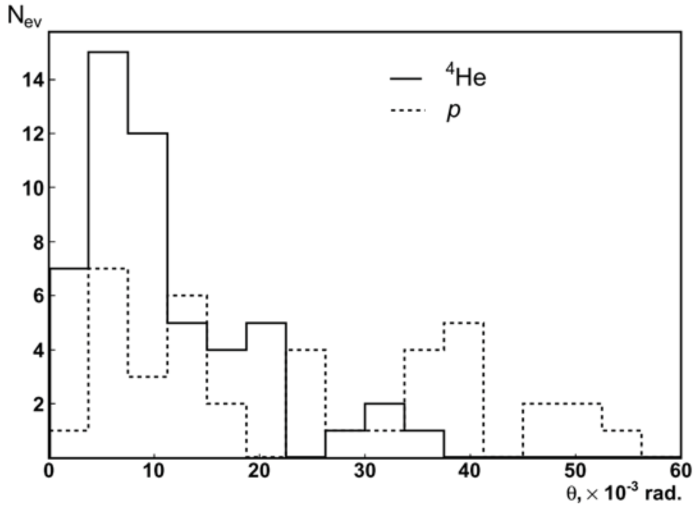

Fig. 1. Distributions with respect to the polar angle θ of relativistic fragments in the $^{10}C \rightarrow {}^{9}B + p \rightarrow 2\alpha + 2p$ “white” stars

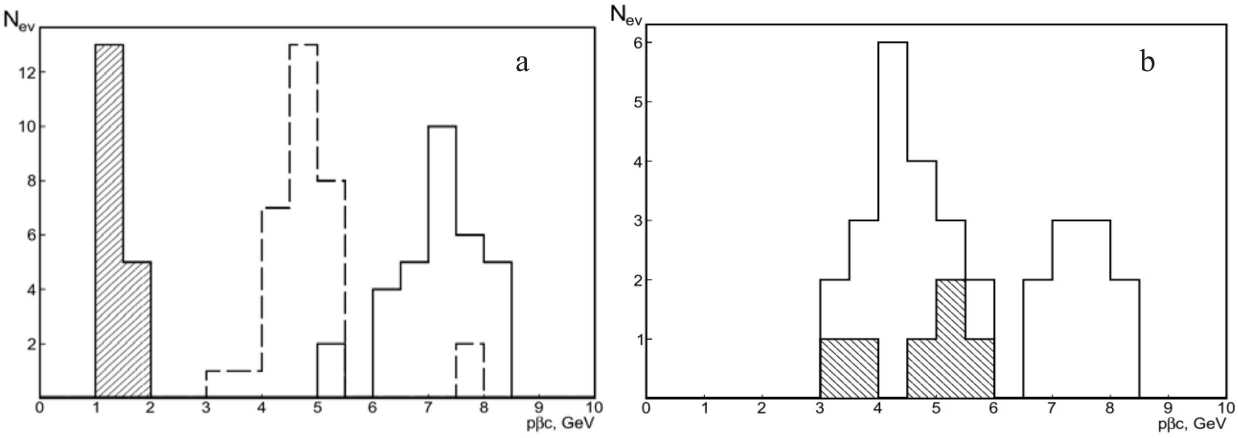

Fig. 2. Distribution of the fragments by value pβc of the "white" stars: (a) – $^{10}C \rightarrow 2He + 2H$ (solid line – *He*; shaded histogram – *H*) and $^{9}C \rightarrow 3^{3}He$ (dotted line); (b) – identified as $^{10}C \rightarrow 2^{3}He + {}^{4}He$ (solid line) and $^{10}C \rightarrow {}^{7}Be + {}^{3}He$ (shaded histogram)

In the structure of the nucleus ^{10}C basic role plays an unstable nucleus ^{8}Be, which should occur in the dissociation of $^{10}C \rightarrow {}^{8}Be$. Decays of relativistic nuclei $^{8}Be \rightarrow 2\alpha$ via the ground state 0^{+} is identified on an accessory α - particle pairs to characteristic area of the least emission angles $\Theta_{2\alpha}$, limited by an impulse 2 *A* GeV/c by a state $\Theta_{2\alpha}$ < 10.5 mrad [4]. The physical meaning has the excitation energy of the α - couples $Q_{2\alpha}=M^{*}_{2\alpha} - M_{2\alpha}$, where $M^{*}_{2\alpha}$ - invariant mass of the fragments $M^{*2} = (\sum P_j)^2 = \sum(P_i{\cdot}P_k)$, and $P_{i,k}$ - 4-momenta of fragments i and k, determined in the approximation of the conservation values of the primary momentum per nucleon; $M_{2\alpha}$ - double the mass of α-particles.

As in the event of $^{9}Be \rightarrow 8Be_{g.s}$, for 68 "white" stars $^{10}C \rightarrow 2\alpha + 2p$ observed in α-partial pair with emission angles do not exceed 10^{-2} rad. Distribution of $Q_{2\alpha}$ (Fig. 3a) suggests that in these events formed the nucleus $^{8}Be_{g.s.}$, that evidenced by the mean value for them $<Q_{2\alpha}>$ = (63 ± 30) keV for 83 keV RMS (in the inset in Fig. 3a). In turn, the distribution of $Q_{2\alpha p}$ (Fig. 3b) indicates that the dissociation of $^{10}C \rightarrow 2\alpha + 2p$ accompanied by formation of an unbound nucleus ^{9}B. The average value of $<Q_{2\alpha p}>$ = (254 ± 18) keV and 96 keV RMS (in the inset in Fig. 3b) are close to value of width and the energy decay of $^{9}B_{g.s.} \rightarrow {}^{8}Be_{g.s.} + p$. A clear correlation between the values of variables $Q_{2\alpha}$ and $Q_{2\alpha p}$ for this group of events points to the cascade character of the process $^{10}C \rightarrow {}^{9}B \rightarrow {}^{8}Be$. It can be concluded that in the cluster structure of the nucleus ^{10}C with a probability about (30 ± 4)% manifested nucleus ^{9}B.

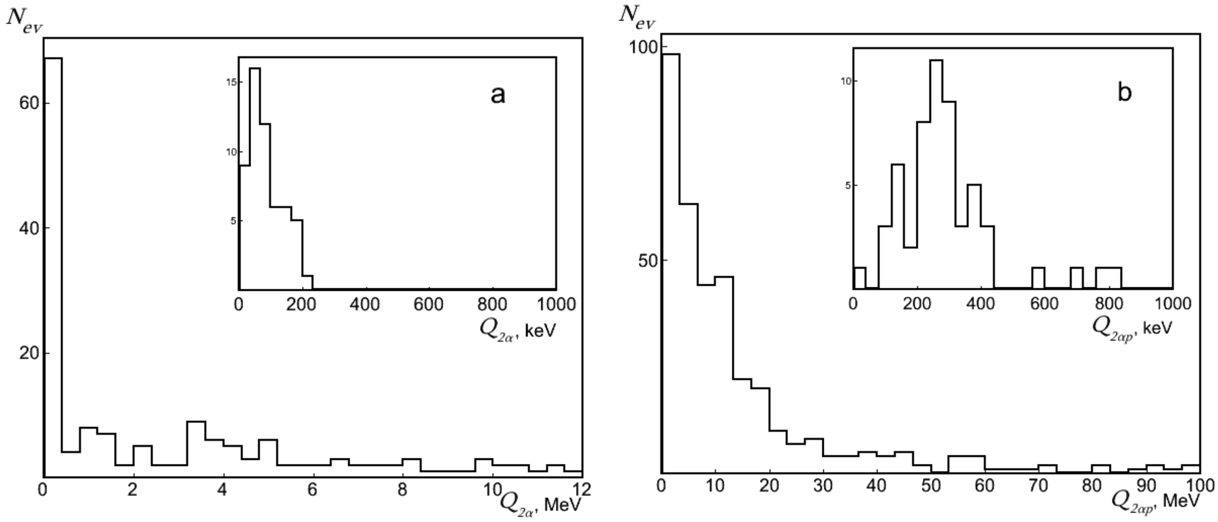

Fig. 3. Distribution of the number of "white" stars N_{ws} of topology $2\alpha + 2p$ on energy of excitation: $Q_{2\alpha}$ pair α-particles; on an insert - zoomed distribution of $Q_{2\alpha}$ (a); $Q_{2\alpha p}$ triples $2\alpha + p$; on an insert - zoomed distribution of $Q_{2\alpha p}$ (b)

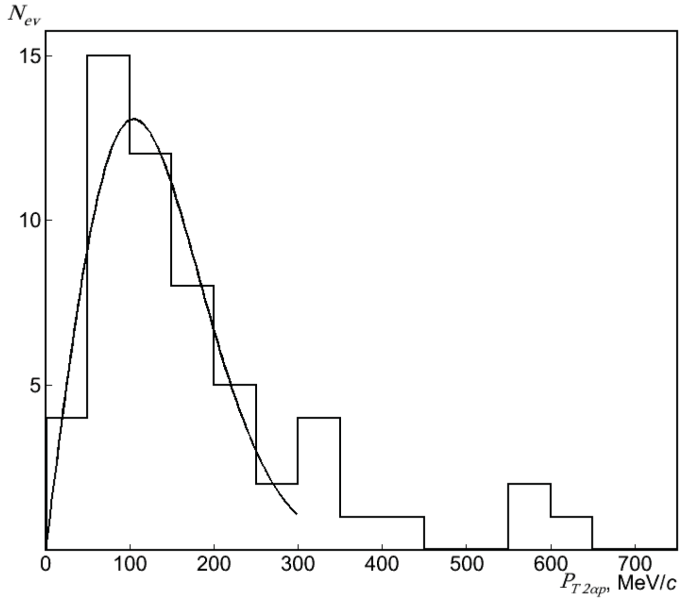

Fig. 4. The distribution of the total transverse momentum $^{9}B \rightarrow 2\alpha + p$.

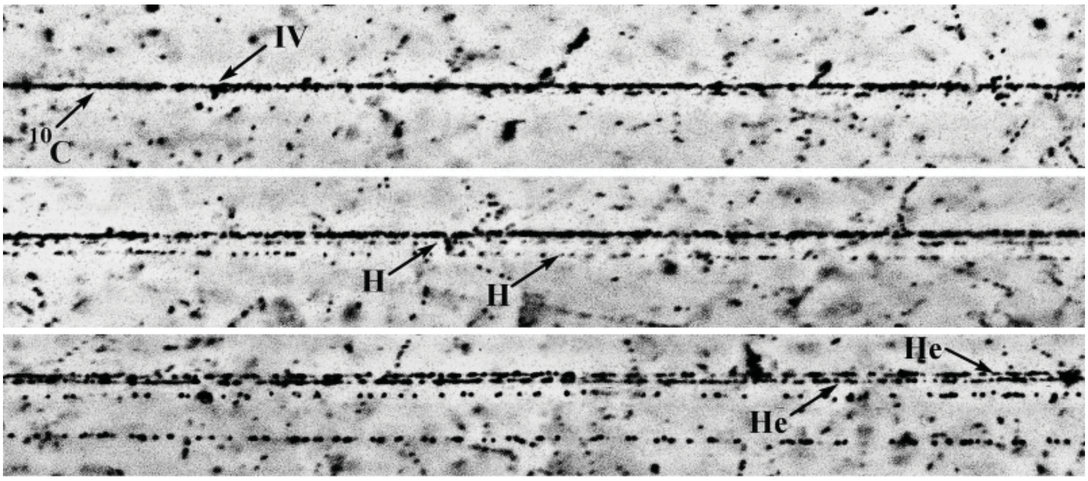

Fig. 5. Microphotograph of a «white» star $^{10}C \rightarrow 2He + 2H$. The interaction vertex is indicated as IV and secondary tracks are as H and He

In favor of this statement evidenced by the distribution of the total transverse momentum of $P_{T2\alpha p}$ triples $2\alpha + p$ from the "white" stars $^{10}C \rightarrow {}^{9}B$ (Fig. 4). For a group of 40 events (73%) a value of $\sigma_{PT}(^{9}B)$ amounts to (92 ± 15) MeV/*c*, which corresponds to value 93 MeV/*c*, expected in the statistical model [12,13]. In this model, the radius of emission region the outside proton from the nucleus ^{10}C is R_p = (2.3 ± 0.4) Fermi, which is consistent with the value extracted from the data on the measurement of inelastic cross sections based model of the geometric overlap [12].

CONCLUSIONS

The report presents the results of research fragmentation of nuclei ^{10}C with energy of 1.2 A GeV, the first derived at the Nuclotron, JINR.

Search and charge measurements of "white" stars are executed in 12 layers. On the total length of viewing of primary tracks of 1088.1 m was found 7241 inelastic interactions, including 608 "white" stars. The mean free path of nuclei ^{10}C was equal to $\lambda_C = 14.8 \pm 0.9$ sm.

Conducted identification on the isotopic composition of the produced fragments *H* and He by value $p\beta c$ for events $2He + 2H$. In the gathered statistics of "white" stars $2He + 2H$ all *He* nuclei correspond to isotope ^{4}He (α), and $H - {}^{1}H$ (p).

Distribution of charge topology indicates the lead role of the channel with a charge configuration $^{10}C \rightarrow 2\alpha + 2p$ (82%)

The process of fragmentation of nuclei $^{10}C \rightarrow 2\alpha + 2p$ in case (≈ 30%) have a cascade character $^{10}C \rightarrow {}^{9}B \rightarrow {}^{8}Be$ by analogy with the nucleus ^{9}Be.

Further analysis of the angular distributions $2\alpha + 2p$ will be directed to the events without formation of nuclei $^{8}Be_{g.s}$ and ^{9}B. In particular, will be performed search the decays of nuclear resonances ^{5}Li and ^{6}Be.

REFERENCES

1. N. P. Andreeva et al., Phys. Atom. Nucl. 68, 455(2005); nucl-ex/0605015.
2. The BECQUEREL Project, http://becquerel.jinr.ru/.
3. N. G. Peresadko et al., Phys. Atom. Nucl. 70, 1266 (2007); nucl-ex/0605014.
4. D. A. Artemenkov et al., Phys. Atom. Nucl. 70, 1226 (2007); nucl-ex/0605018.
5. R. Stanoeva et al., Phys. of At. Nucl. 72, 690 (2009); arXiv: 0906.4220.
6. P. A. Rukoyatkin et al.: Secondary nuclear fragment beams for investigations of relativistic fragmentation of light radioactive nuclei using nuclear photoemulsion at Nuclotron. Eur. Phys. J. ST 162, 267 (2008)
7. T. V. Shchedrina et al., Phys. Atom. Nucl. 70, 1230 (2007); arXiv: nucl-ex/0605022.
8. V. V. Belaga et al., Phys. Atom. Nucl. 58, 1905(1995).
9. M. I. Adamovich et all., Phys. Atom. Nucl. 62, 1378 (1999).
10. M. I. Adamovich et all., J. Phys. G 30, 1479 (2004).
11. R.R.Kattabekov, K.Z.Mamatkulov, D.A.Artemenkov et al.: Exposure of nuclear track emulsion to a mixed beam of relativistic ^{12}N, ^{10}C, and ^{7}Be nuclei. Phys. At. Nucl. 73, (2010)
12. H. Feshbach and K. Huang, Phys. Lett. 47B, 300 (1973).
13. A. S. Goldhaber, Phys. Lett. 53B, 306 (1974).

THE STRUCTURE OF GIANT RESONANCES IN CALCIUM AND TITANIUM ISOTOPES

N.G.Goncharova, *Iu.A.Skorodumina*

Skobelzyn Institute of Nuclear Physics, Moscow State University,Moscow,Russia

n.g.goncharova@gmail.com

The experimental investigation of nuclear interaction with various projectiles provides a wealth of quantitative information on nuclear excited states. The main features dominating in the nuclear response to excitations in the continuum region are giant multipole resonances (MR); their structures and widths depend on nuclear quantum numbers and momentum transferred to target nucleus. Microscopic description of MR characteristics in light and medium nuclei is usually based on shell model (SM) calculations. In the multiparticle shell model (MSM) resonances in nuclear excitations are considered as complicated collective states built on a number of so-called doorway configurations. For the nuclei with closed shells or subshells doorway configurations usually constructed as a set of particle-hole pairs. This approach was successful in understanding the positions of mean energies of resonances but not in interpretation their complicated structure. The origins of the MR' complicated structure were discussed and investigated this last decades. As main sources of the observed fragmentation should be mentioned the deviation of target nucleus from closed shell, dynamic deformations of excited nucleus and the interaction of doorway states with collective vibrations. The deviation of target nucleus from closed shells or subshells takes place as well in so-called magic nuclei as a result of ground state correlation. The interplay of all these effects leads to the splitting of MR' cross sections. The properties of resonances are highly influenced as well by isospins of target and daughters nuclei under consideration.

Some advance in the interpretation of MR could be achieved in particle – core coupling version of shell model (PCC SM) [1]. In PCC SM in the calculations of MR' distributions and probabilities the energy spreading of final nuclei states is taken into account. The wave functions of MR in PCC SM are constructed by a coupling a nucleon in a free orbit to low-lying states of residual nucleus (A-1):

$$\left|J_f T_f\right\rangle = \sum \alpha_f^{J'T',j} \left|(J'E'T')_{(A-1)} \times (n_f l_f j_f) : J_f T_f\right\rangle \tag{1}$$

In (1) all states of residual nuclei with noticeable fractional parentage coefficients C of ground state $\left|J_i T_i\right\rangle$ should be included into calculations:

$$\left|J_i T_i\right\rangle = \sum C_i^{J'T',j} \left|(J'E'T')_{(A-1)} \times (n_i l_i j_i) : J_i T_i\right\rangle \tag{2}$$

Fractional parentage coefficients C_i could be extracted from wave functions for ground states of target nuclei. If the reliable wave function of the nuclear ground s tate could be found, its expanding helps to get needed information on the coefficients C_i (see [2] and references there). This procedure was successfully performed for resonances in 1p-shell nuclei and SM has shown good agreement with experimental data for nuclei with A from 7 up to 15. The same approach to more heavy nuclei strike against the lack of reliable wave functions for nuclear ground states. The alternative way to estimate the fractional parentage properties of these nuclei is to use the spectroscopy of direct pick-up reactions [3]. Then C_i could be evaluated as

$$C_i = \sqrt{\frac{S_i}{\sum_i S_i}}\ , \qquad (3)$$

where S_i are spectroscopic factors of the pick-up reaction that leads to the excitation of $(J'E'T')$ level of (A-1) final nucleus.

Here would be discussed the results of PCC SM approach to the dipole resonances in even-even isotopes of titanium and calcium.

Matrix elements of the operators in the space of basic configurations could be represented as sums of one-particle transitions multiplied on spectroscopic amplitudes Z:

$$\left\langle J_f T_f M_T \left\| \widehat{B}^J_{TM_T} \right\| J_i T_i M_T \right\rangle = \sum_{i, j_i, j_f} < j_f \left\| \widehat{O}^J_{TM_T} \right\| j_i > \sqrt{2}\sqrt{2J_i+1} \cdot Z^J_{TM_T}(j_f j_i);$$

$$Z^J_{TM_T}(j_f j_i) = \sum_{J'T'} C_i^{JT, j_i} \alpha_f^{J'T', j_f} \times f(J_i, J_f, j_i, j_f, T_{i,} T_f). \qquad (4)$$

The information on the structure of final and initial states of nucleus is embedded in spectroscopic amplitudes Z. The matrix elements of PCC Hamiltonian involve the excitation energies of final nuclei levels:

$$\widehat{H}_{ij} = (E' + \varepsilon_j + E_c)\delta_{ij} + \widehat{V}_{ij}. \qquad (5)$$

The interactions $\widehat{V}_{ij}$ between doorway states could be calculated as

$$\left\langle (J''T''E''), j_2 : J_f T_f \left| \widehat{V}_{\text{int}} \right| (J'T'E'), j_1 : J_f T_f \right\rangle = \sum_{J,T} \times \sum_{j,j'} \left\langle J'T'E' \left| J_i T_i, j^{-1} \right.\right\rangle \left\langle J_i T_i, j'^{-1} \left| J''T''E'' \right.\right\rangle \times$$

$$(2J+1)(2T+1)\sqrt{(2J'+1)(2T'+1)(2J''+1)}\sqrt{(2T''+1)} \cdot W(J_i j J_f j_1; J'J) W(J_i j' J_f j_2; J''J) \times \qquad (5')$$

$$W(T_i \tfrac{1}{2} T_f \tfrac{1}{2}; T'T) W(T_i \tfrac{1}{2} T_f \tfrac{1}{2}; T''T) \left\langle j^{-1} j_1 : JT \left| V_{\text{int}} \right| j'^{-1} j_2 : JT \right\rangle.$$

Diagonalization of the Hamiltonian (5) on the set of basic configurations Produces energies and wave functions for excited states. The ε_j -single particle energies of nucleons removed via $1\hbar\omega$ transitions were found in Saxon-Woods potential well.

In the sets of basic configurations for the E1excitation were included all the States of (A-1) nuclei which have noticeable spectroscopic factors of direct reaction for neutron pick-up. For isotopes ^{46}Ti, ^{48}Ti and ^{50}Ti these S factors were obtained from the results of (p,d) reactions [4]. For ^{40}Ca and for ^{48}Ca the S factors were extracted from [5] and [6], respectively. The numbers of E1 basic configurations for these 5 nuclei are listed in the Table 1. It should be mentioned that S<0.02 were omitted.

The number of basic configurations

Table 1

^{40}Ca	^{46}Ti		^{48}Ti		^{50}Ti		^{48}Ca	
T	$T_<$	$T_>$	$T_<$	$T_>$	$T_>$	$T_>$	$T_<$	$T_>$
1	1	2	2	3	4	3	4	5
58	35	11	36	37	11	8	31	11

Wave functions for 1^- $T_<$ and for 1^- $T_>$ states in Ca and Ti even-even isotopes were used to calculate E1 form factors $F_{E1}(q)$ at photopoint.

Calculations of form factors and partial cross sections for the nuclei' photodisintegration were based on specially built computer program provided for diagonalization of the full Hamiltonian matrices and estimations of the peaks' partial widths.

The PCC SM calculations for the dipole resonance energy distribution in the Ca and Ti even-even isotopes show that E1 strength is highly fragmented due to energy distribution of final nuclei states. The structure of isovector dipole states in ^{46}Ti, ^{48}Ti, ^{50}T and ^{48}Ca nuclei is influenced as well by isospin splitting of $T_<$ and $T_>$ states. An example of isospin factors working upon excitation and decay of isovector resonance is shown in the fig.1 for ^{46}Ti.

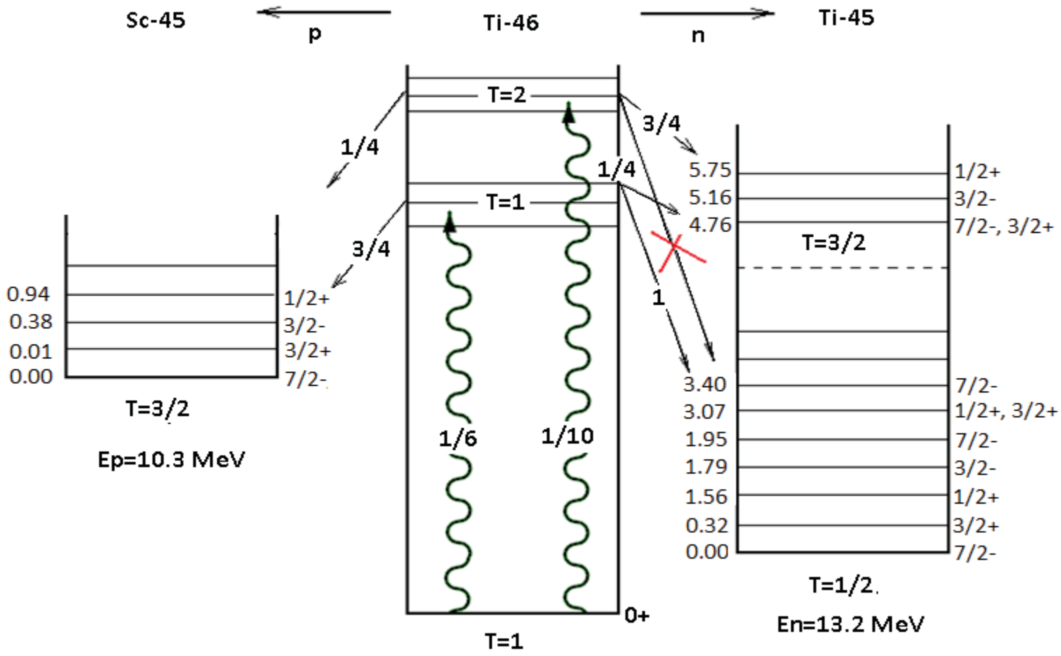

Fig.1. Squared isospin coefficients for excitation and decay ^{46}Ti.

The results of PCC SM calculations for the (γ, n) reactions on titanium isotopes are shown in the Figs 2-4 together with experimental data (right axis in the figures). The solid lines show the results of calculations of summed probabilities based on the estimations of peaks' widths.

Since photodisintegration probabilities depend on the wave function structure and isospin of final nuclei states, the relation of photoproton and photoneutron channels changes form peak to peak.

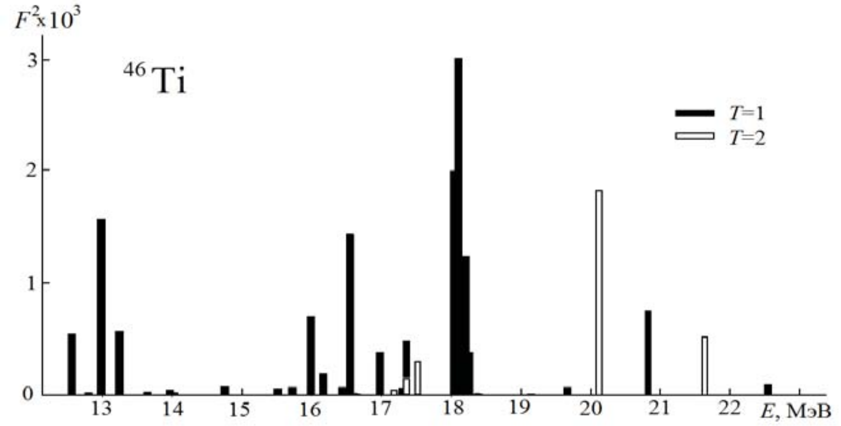

Fig.2a. E1 form factors distribution for ^{46}*Ti.*

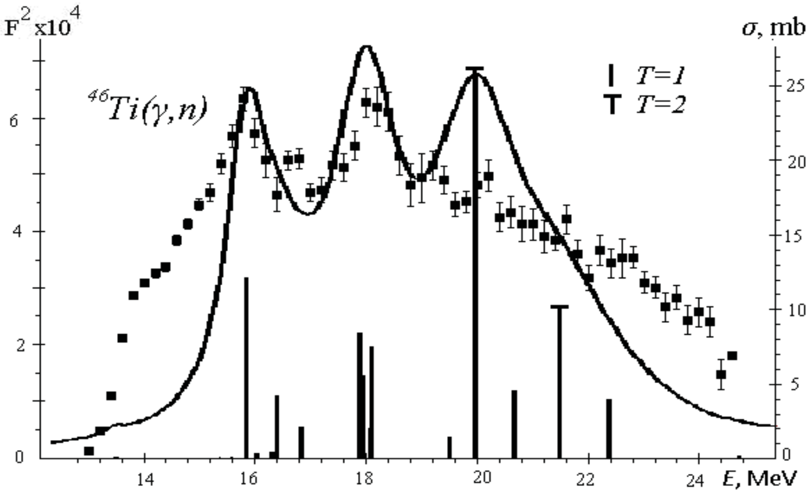

Fig.2b. E1 peaks distribution for $^{46}Ti(\gamma,n)$*. Experiment [7]*

In the Fig.2a are shown calculated form factors for photoexcitation of ^{46}Ti. The differences in the structure of 1^- peaks lead to various probabilities of nucleon decay channels. For example, the peaks at about E=18 MeV (T=1) are built mostly on the T=3/2 state of final nuclei with A=45. As a consequence, they would decay mainly through proton emitting. For the T=2 peaks at 20 and 21.6 MeV, on the contrary, (γ,n) channel is about 3 times more probable than (γ,p).

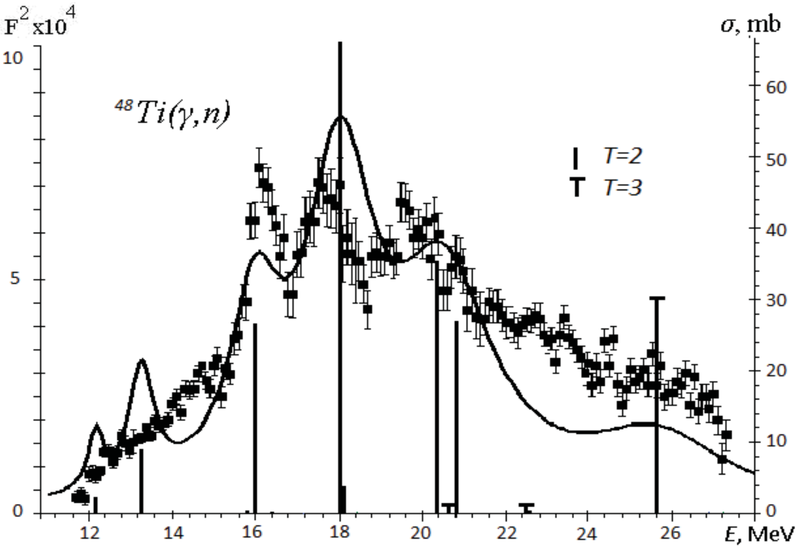

Fig.3. E1 for $^{48}Ti(\gamma,n)$*. Experiment [8]*

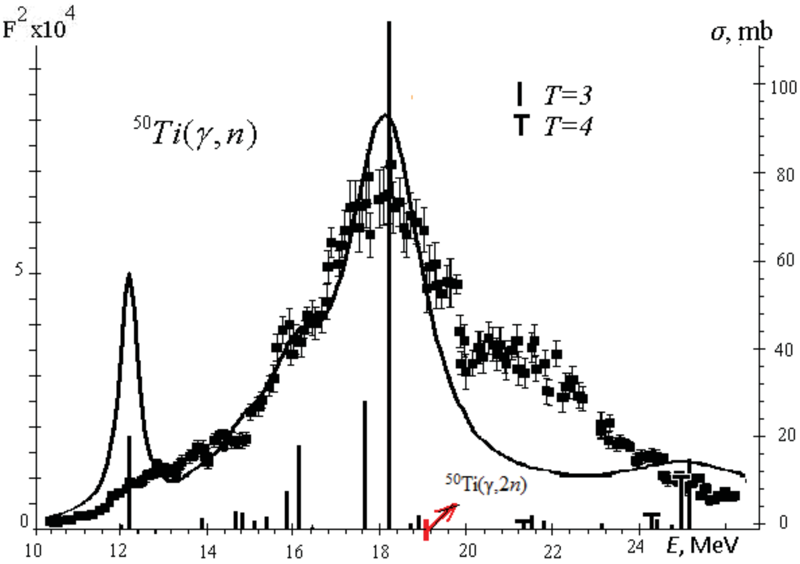

Fig.4. E1 distribution for $^{50}Ti(\gamma,n)$*. Experimental data [9] for* $^{50}Ti(\gamma,n)+{}^{50}Ti(\gamma,2n)$*.*

The giant dipole resonance in the double magic ^{40}Ca belongs to the most detailed investigated ones. In the Fig.4a.,4b would be shown the PCC SM calculation results together with distribution of spectroscopic factors for the pick-up reaction [12]. Experimental data for ^{40}Ca (γ,n) [11]. According to wave functions structure in PCC SM approach, the bump in^{40}Ca (γ,n) at E_γ=23-25 MeV correspond to contributions of basic configurations built on $5/2^+$ states of final nucleus with A=39. The wide energy distribution of these states leads to spreading of E1 resonance.

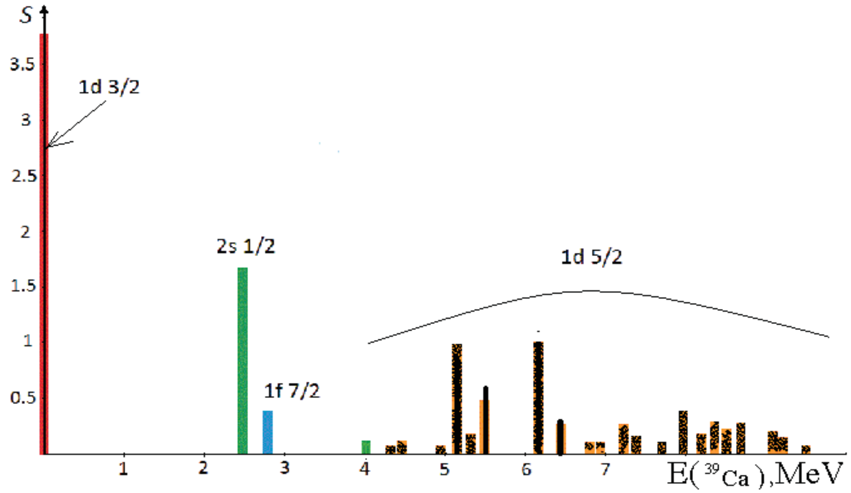

Fig. 4a. Distribution of spectroscopic factors from ^{40}*Ca(d,t) reaction received with* E_d *=52 MeV [5].*

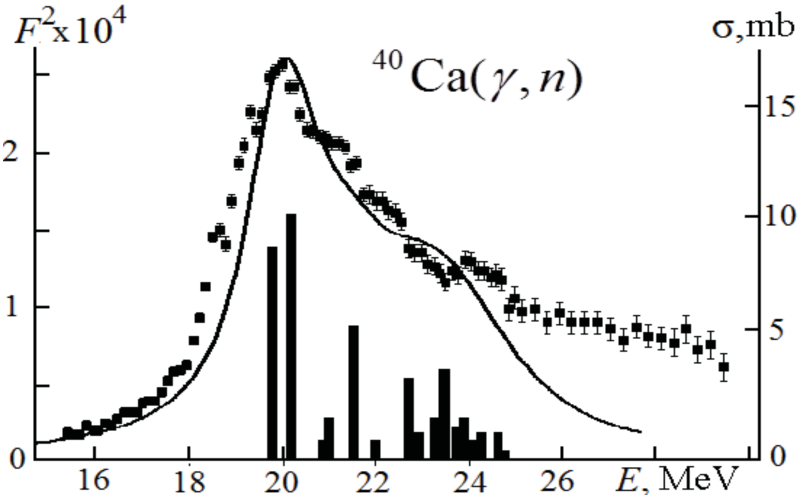

Fig.4b. Calculated results for ^{40}*Ca (γ,n) and experiment [11]*

The PCC SM results for E1 resonance in ^{48}Ca are shown in the Fig.5. The spectroscopic factors used in the calculation are taken from ^{48}Ca(d,t), ^{48}Ca(p,d) reactions [6], where the energies of projectile were not higher than 40 MeV. The comparison of two direct experiments [5] and [6] shows that if the energy of projectile is low, the sum of spectroscopic factors for subshell would be quenched (Table 2). Therefore the calculation of E1 distribution in ^{48}Ca was performed with corrected occupation numbers for $d_{5/2}$.

Table 2

Occupation numbers for neutrons from pick-up reactions on ^{40}Ca and ^{48}Ca

Nucleus	E_{max}	$2p_{3/2}$	$1f_{7/2}$	$1d_{3/2}$	$2s_{1/2}$	$1d_{5/2}$
^{40}Ca, [5]	52	0	0.36	3.74	1.74	5.41
^{48}Ca, [6]	40	0.02	6.8	3.78	1.9	0.95

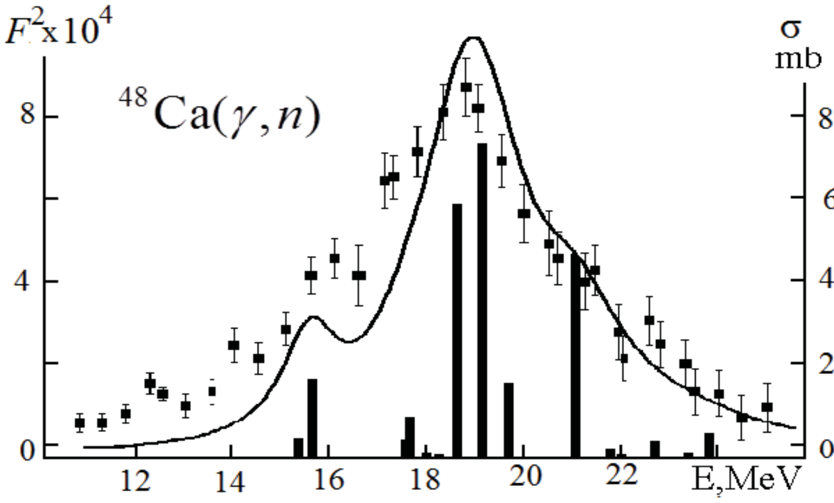

Fig. 5. *E1 distribution for ^{48}Ca (γ,n) and data [12]*

The analysis of the isospin branches in non-self conjugated titanium Isotopes and ^{48}Ca reproduced in the Table 3 shows that calculated mean distance between $T_<$ and $T_>$ states is in the frame of estimations [13].

Table3

Mean weighted energies for $T_<$ and $T_>$ branches and isospin splitting

	^{46}Ti, T_0=1	^{48}Ti, T_0=2	^{50}Ti, T_0=3	^{48}Ca, T_0=4
$E_{cp}(T_<)$, MeV	17.7	18.1	18.7	20.5
$E_{cp}(T_>)$, MeV	20.0	23.6	25	26.8
ΔE, MeV	2.3	5.5	6.3	6.3
$\Delta E=60(T_0+1)/A$, MeV	2.6	3.75	4.8	6.25
$\Delta E=100(T_0+1)/A$, MeV	4.3	6.25	8	10.4

SUMMARY

1. The deviation of (A) nucleus from closed shells or subshells reveals in a wide range of energy distribution for ”hole” among the (A-1) nuclei states. In the PCC version of SM these distributions are taken into account in microscopic description of multipole resonances.
2. The connection between direct and resonance reactions revealed in the distributions of spectroscopy factors for pick-up processes makes possible to calculate matrix elements for multipole transitions in nuclei.
3. The calculations of the E1 strengths in calcium and titanium isotopes have shown that one of the main origin of resonances’ fragmentation is the energy spread of final nuclei states.
4. The obtaining of probabilities for final nuclei states excitations from hadrons pick-up processes run into a problem of differences in electromagnetic and strong reactions mechanisms. For the realistic description of the nuclei disintegration due to interactions with electromagnetic fields spectroscopic information on direct reactions should be obtained with energy of projectiles at least on 10 MeVhigher than the maximum energy of the photon.

References

1. N.G.Goncharova, N.P.Yudin, Phys. Lett.**B29**, (1969) 272;
2. N.G. Goncharova -" – Proc. XII Int. Seminar on Electromagn. Int.of Nuclei, Moscow, Sept 2009, I.N.R. RAS, 2010, p.86-93
3. N.G.Goncharova, A.Dzhioev, Nucl.Phys.**A690** (2001) 247**c**
4. P.J.Plauger, E.Kashy, Nucl.Phys.**A152**(1970)609
5. P. Doll, G.J. Wagner, K.T. Knopfle, Nucl.Phys. **A263**(1976)210
6. P. Martin, M. Buenerd *et al*, Nucl. Phys **A185**(1972)465
7. R.Sutton, M.N. Thompson *et al*, Nucl.Phys. **A339**(1980)125
8. R. E. Pywell, M.N. Thompson, Nucl. Phys.**A318**(1979) 461
9. R. E. Pywell, M.N. Thompson, R.A.Hicks, Nucl. Phys.**A325**(1979)116
10. R.Sutton, M.N. Thompson *et al,* Nucl.Phys. A398 (1983)415
11. A.Veyssiere *et al*., Nucl. Phys.**A227**(1972)513
12. G.J O'Keefe., M.N Thompson. *et al*, Nucl.Phys. **A469**(1987)239
13. A.M. Lane, Nucl.Phys**.35(**1962)676.

DAMPING OF HIGH-ENERGY PARTICLE-HOLE-TYPE NUCLEAR EXCITATIONS: A SEMIMICROSCOPIC DESCRIPTION

M.H.Urin

National Research Nuclear University "MEPhI", Moscow, Russia

Abstract

A semi-microscopic model (particle-hole dispersive optical model) is formulated to describe the main relaxation modes of high-energy particle-hole-type excitations in medium-heavy mass nuclei. Within this model Landau damping and the single-particle continuum are considered microscopically, while the spreading effect is treated phenomenologically with taking a statistical assumption into account. Description of direct-nucleon-decay properties of the above-mentioned excitations (including giant resonances) is a unique feature of the proposed model, which in applying to closed-shell nuclei is arranged for practical implementations.

1 Introduction

A great variety of high-energy particle-hole-type excitations, including giant resonances (GRs), is characterized by three main relaxation modes. They are: (i) the particle-hole (p-h) strength distribution, or Landau damping, which is a result of the shell structure of nuclei; (ii) coupling of (p-h)-type states to the single-particle (s. p.) continuum that leads to direct nucleon decay and related phenomena; (iii) coupling of (p-h)-type states to many-quasi-particle configurations, or chaotic states, that leads to the spreading effect. Actually, the interplay of these relaxation modes is being changed with increasing the excitation energy. Giant resonances correspond to collective (p-h)-type excitations.

As applied to description of GR damping, we developed a semi-microscopic approach based on the continuum-RPA (cRPA) versions of the Migdal's finite Fermi-system theory [1]. Within this approach Landau damping and coupling to the s. p. continuum are described microscopically, using a mean field and p-h interaction, while the spreading effect is phenomenologically taken into account directly in the cRPA equations for energy-averaged quantities in terms of an effective s. p. optical-model potential. Such a method allows one to realize the statistical assumption: after energy averaging different (p-h)-type states, having the same angular momentum and parity, "decay" into chaotic states independently of one another. In implementations of the approach to description of GR main properties a phenomenological mean field and the Landau-Migdal p-h interaction bound by some self-consistency conditions are used. The imaginary part of the effective s. p. optical-model potential determines contribution of the spreading effect to the GR main characteristics together with the corresponding real part found from a proper dispersive relationship. The intensity of the imaginary part, which is parametrized as a universal function, exhibiting the saturation-like energy dependence, is adjusted to describe the experimental GR strength distribution. In applying to such a description the semi-microscopic approach is intermediate between "fully microscopic" (chaotic states are substituted by a limited number of 2p-2h configurations) and semi-classical (the shell structure of nuclei is ignored) approaches. The unique feature of the semi-microscopic approach is a possibility to describe direct-nucleon-decay properties of GRs without the use of specific adjustable parameters. Formulation and a diversity of implementations of the semi-microscopic approach, which is valid in the "pole" approximation (i.e., at the close range of the GR energy), are reviewed in [2, 3].

To extend the above-described approach on arbitrary (but high enough) excitation energies and also to verify validity of this approach in the energy region of a given GR, we formulate the new semi-microscopic model without using additional model parameters. We call this model as the particle-hole dispersive optical model (PHDOM) in view of a methodical similarity with formulation of the well-known single-quasiparticle dispersive optical model [4]. In particular, the starting point in formulations of both models is the equation for the corresponding many-body Green function (GF). Preliminary considerations of the PHDOM are given in [5, 3].

2 Extension of the cRPA standard version

Within the PHDOM the standard and non-standard versions of the cRPA are extended to take the spreading effect phenomenologically into account. The cRPA standard version is formulated in terms of the local p-h GF $A(x, x_1; \omega)$ (x is the set of s. p. coordinates, including the spin and isospin variables; ω is the excitation energy) [6]. The free p-h GF $A_0(x, x_1; \omega)$, which is determined by a mean field (via the s. p. energies ε_λ, wave functions $\phi_\lambda(x)$, GFs $g(x, x'; \varepsilon)$) and the ground-state s. p. occupation numbers n_λ, and also a p-h interaction $F(x, x_1)$ are the input quantities for calculating $A(x, x_1; \omega)$ from the Bethe-Goldstone-type equation. The alternative (and fully equivalent) effective-field method, which is used within the cRPA version of the Migdal's finite Fermi-system theory [1], is actually based on the relationship: $[A(\omega)V_0] = [A_0(\omega)V(\omega)]$. Here, $V(x, \omega)$ is the effective field, corresponding to an external s. p. field $V_0(x)$ of a given spin-angular and isospin symmetry; the brackets $[\dots]$ mean integration over one set of s. p. coordinates. The equation for V, which follows from the equation for A, is widely used [1]. The basic quantities A and/or V determine within the cRPA standard version the integral characteristics of (p-h)-type excitations: the strength distribution and transition density.

To take the above-mentioned statistical assumption into account, we start formulation of the PHDOM with choosing the non-local p-h GF $\mathcal{A}(x, x'; x_1, x'_1; \omega)$ as the basic quantity [5, 3]. In accordance with its spectral expansion [1, 3], this GF carries information on (p-h)-type excitations. In particular, it determines the strength function $S_{\mathcal{V}_0}(\omega) = -(1/\pi)\mathrm{Im}[..[\mathcal{V}_0^+ \mathcal{A}(\omega)\mathcal{V}_0]..]$, corresponding to a non-local external field $\mathcal{V}_0(x, x')$ (possibly, $\mathcal{V}_0(x, x') = V_0(x)\delta(x - x')$), and the transition density matrix $\rho(x, x'; \omega)$. Being considered only in the continuum region, this quantity determines the strength function, as $S_{\mathcal{V}_0}(\omega) = |[[\rho(\omega)\mathcal{V}_0]]|^2$. Accordingly to their spectral expansions, the free GFs A_0 and $\mathcal{A}_0$ are determined by the same input quantities. However, contrary to the free transition densities (appeared in the expansion for A_0), the different transition density matrices $\rho^0_{\lambda\mu}(x, x') = (1 - n_\lambda)n_\mu\phi^*_\lambda(x)\phi_\mu(x')$ are orthogonal.

The Bethe-Goldstone-type equation for $\mathcal{A}$

$$\mathcal{A}(\omega) = \mathcal{A}_0(\omega) + [..\,[\mathcal{A}_0(\omega)\mathcal{F}(\omega)\mathcal{A}(\omega)]\,..] \tag{1}$$

contains the p-h interaction $\mathcal{F}(\omega) = \mathcal{F}_{l\text{-}r} + \mathcal{F}_{spr}(\omega)$. The interaction

$$\mathcal{F}_{l\text{-}r}(x, x'; x_1, x'_1) = F(x, x_1)\delta(x - x_1)\delta(x_1 - x'_1)$$

leads to long-range correlations, including formation of GRs. The interaction $\mathcal{F}_{spr}(\omega) = \mathcal{P}(\omega) - \mathcal{P}(0)$ appears due to coupling of (p-h)-type states to many-quasi-particle configurations. The fragmentation scattering amplitude, or polarization operator, $\mathcal{P}$ is described by a full set of diagrams irreducible in the p-h channel and, therefore, it takes into account the interference of spreading particles and holes. Because 2p-2h configurations are the doorway states for spreading of (p-h)-type states, the quantity $\mathcal{P}(x, x'; x_1, x'_1)$ is a convolution of the 2p-2h (local) GF $B(x_1, x_2, x_3, x_4; \omega)$ with a "residual" pair interaction $H'(x, x_1)$: $\mathcal{P} = [[H'B(\omega)H']]$. The spectral expansion of $\mathcal{P}(\omega)$ follows from that for the GF $B(\omega)$ and exhibits a high density of poles, corresponding to chaotic states [3]. The p-h interaction $\bar{\mathcal{F}}_{spr}(\omega)$ cannot be obviously calculated microscopically. Only the energy-averaged quantity $\bar{\mathcal{F}}_{spr}(\omega)$, having an imaginary part, can be reasonably parametrized:

$$\bar{\mathcal{F}}_{spr}(x,x';x_1,x_1';\omega)=\big(-i\mathcal{W}(x,x';\omega)+\mathcal{P}(x,x';\omega)\big)\times\delta(x-x_1)\delta(x'-x_1'). \tag{2}$$

Supposing the same coordinate dependence of $\mathcal{W}$ and $\mathcal{P}$, i.e. $\mathcal{W}(x,x';\omega)=W(\omega)f(x,x')$ and $\mathcal{P}(x,x';\omega)=P(\omega)\cdot f(x,x')$, one can get from the spectral expansion of $\mathcal{T}(\omega)$ a dispersive relationship for $P(\omega)$ as the functional of $W(\omega)$. Within the semi-microscopic approach to description of GR damping an universal function $W(\omega)$, having a saturation-like energy dependence, is used [2, 3]. The corresponding expression for $P(\omega)$ is obtained in [7]. To ensure validity of the statistical assumption, the form-factor $f(x,x')$ should be taken as a constant in the nuclear volume (in implementations of the PHDOM we take $f(x,x')=f_{\mathrm{W}S}(x)\cdot f_{\mathrm{W}S}(x')$ or $f(x,x')=f_{\mathrm{W}S}(x)$, where $f_{\mathrm{W}S}(x)$ is the Woods-Saxon function). Being related to free p-h states $|\lambda\mu\rangle$, the statistical assumption is then realized, as follows:

$$\langle\lambda'\mu'|\bar{\mathcal{F}}_{spr}(\omega)|\lambda\mu\rangle=(-iW(\omega)+P(\omega))[[\rho^{0*}_{\lambda'\mu'}f\rho^{0}_{\lambda\mu}]]\simeq(-iW(\omega)+P(\omega))f_\lambda f_\mu\delta_{\lambda\lambda'}\delta_{\mu\mu'}, \tag{3}$$

where $f_\lambda=[\phi^*_\lambda f_{\mathrm{W}S}\phi_\lambda]$.

The solution of the energy-averaged basic equation (1) can be sought after the following identical transformation:

$$\bar{\mathcal{A}}(\omega)=\bar{\mathcal{A}}_0(\omega)+\left[..\left[\bar{\mathcal{A}}_0(\omega)\mathcal{F}_{l\text{-}r}\bar{\mathcal{A}}(\omega))\right]..\right], \tag{4}$$

where the auxiliary quantity $\bar{\mathcal{A}}_0(\omega)$ satisfies the equation:

$$\bar{\mathcal{A}}_0(\omega)=\mathcal{A}_0(\omega)+\left[..\left[\mathcal{A}_0(\omega)\bar{\mathcal{F}}_{spr}\bar{\mathcal{A}}_0(\omega)\right]..\right]. \tag{5}$$

In view of (3) this equation, corresponding to the model non-interacting damping quasiparticles, can be solved and the result is given below:

$$\begin{aligned}\bar{\mathcal{A}}_0(x,x';x_1,x_1';\omega)&=\sum_{\lambda\mu}\bar{A}_{\lambda\mu}(\omega)\phi_\lambda(x)\phi^*_\mu(x')\phi_\mu(x_1')\phi^*_\lambda(x_1),\\ \bar{A}_{\lambda\mu}(\omega)&=\frac{(n_\lambda-n_\mu)}{(\varepsilon_\lambda-\varepsilon_\mu-\omega+(n_\lambda-n_\mu)(iW(\omega)-P(\omega))f_\lambda f_\mu)}.\end{aligned} \tag{6}$$

After transition to the local limit in Eqs. (4), (6), i.e., $x'\to x$; $x_1'\to x_1$, we get the equation for the energy-averaged local p-h GF $\bar{A}(x,x_1;\omega)$:

$$\bar{A}(\omega)=\bar{A}_0(\omega)+\left[\left[\bar{A}_0(\omega)F\bar{A}(\omega)\right]\right]. \tag{7}$$

Starting from Eq. (6), one can present the GF $\bar{A}_0$ in the form, allowing to take approximately the s. p. continuum into account, using the s. p. optical-model GFs $\bar{g}(x,x';\varepsilon_\lambda\pm\omega)$. This rather cumbersome expression for $\bar{A}_0$ (explicitly given in [3]) together with Eq. (7) for $\bar{A}$, or with the equivalent equation for the energy-averaged effective field $\bar{V}$ (defined by the relationship $[\bar{A}(\omega)V_0]=[\bar{A}_0(\omega)\bar{V}(\omega)]$) presents extension of the cRPA standard version on taking the spreading effect into account. In, particular, the GF $\bar{A}$ determines the $\overline{\text{energy-averaged}}$ strength functions in the continuum region: $\bar{S}_{V_0}(\omega)=\overline{|[\rho(\omega)V_0]|^2}$, where $\overline{(\rho^*(x,\omega)\rho(x',\omega))}=-(1/\pi)\mathrm{Im}\bar{A}(x,x';\omega)$.

In conclusion of this Section we note that the "pole" approximation exploited within the semi-microscopic approach to the description of GR damping corresponds to using the basic quantity $\bar{A}^{(pole)}_{\lambda\mu}(\omega)$, which is following after substitution $(n_\lambda-n_\mu)\to-1$ in the numerator of the second expression in Eq. (6). In other words, $\bar{A}^{(pole)}_0(\omega)=A_0(\omega\to\omega+iW(\omega)-P(\omega))$ [2, 3].

3 Extension of the cRPA non-standard version

Being developed to describe direct-decay properties of various GRs, the cRPA non-standard version was formulated within the effective-field method in terms of the amplitudes of "direct + semi-direct" (DSD) reactions induced by an external field $V_0(x)$ and related to population of one-hole state μ^{-1} of the product nucleus: $M_{V_0,c}(\omega) = [\Psi_{c,0}^{(+)} V(\omega)]$ [2, 3]. Here $V(x,\omega)$ is the corresponding effective field, $\Psi_{c,0}^{(+)}(x) = n_\mu \phi_{\varepsilon_c}^{+}(x)\phi_\mu(x)$ is the free (local) reaction-channel wave function (w.f.) with $\phi_{\varepsilon_c}^{(+)}(x)$ being the nucleon continuum-state w.f. ($\varepsilon_c = \omega + \varepsilon_\mu$), "c" is the set of reaction-channel quantum numbers [2, 3].

To describe phenomenologically the spreading effect on direct-decay properties of (p-h)-type states at arbitrary energies with taking the statistical assumption into account, we consider the non-local quantities $\psi_{c,0}^{(+)}(x,x')$, $\mathcal{V}(x,x';\omega)$, $\mathcal{M}_{V_0,c}(\omega) = [[\psi_{c,0}^{(+)}\mathcal{V}(\omega)]] = [[\psi_c^{(+)}(\omega)\mathcal{V}_0]]$. Here, the effective (non-local) reaction-channel w.f. $\psi_c^{(+)}(x,x';\omega)$ satisfies the equation similar to Eq. (1) for $\mathcal{A}(\omega)$, so that the solution for the corresponding energy-averaged quantity can be sought in a similar way:

$$\bar\psi_c^{(+)}(\omega) = \bar\psi_{c,0}^{(+)}(\omega) + \left[\left[\bar{\mathcal{A}}_0(\omega)\mathcal{F}_{l\text{-}r}\bar\psi_c^{(+)}(\omega)\right]\right] \tag{8}$$

(compare with Eq. (4)), where $\bar\psi_{c,0}^{(+)}(x,x';\omega)$ satisfies the auxiliary equation

$$\bar\psi_{c,0}^{(+)}(\omega) = \psi_{c,0}^{(+)}(\omega) + \left[\left[\mathcal{A}_0(\omega)\bar{\mathcal{F}}_{spr}(\omega)\bar\psi_{c,0}^{(+)}(\omega)\right]\right] \tag{9}$$

(compare with Eq. (5)). The solution of this equation can be sought in the form $\bar\psi_{c,0}^{(+)}(x,x';\omega) = n_\mu\bar\phi_{\varepsilon_c}^{(+)}(x)\phi_\mu(x')$ with taking the statistical assumption into account. The result consists in the integral equation for the s. p. OM continuum-state wave function, which is satisfies the equivalent differential equation:

$$\left\{H_0(x) - (\varepsilon_c + (iW(\omega) - P(\omega))\, f_\mu f_{WS}(x))\right\}\bar\phi_{\varepsilon_c}^{(+)} = 0 \tag{10}$$

Going to the local limit within the expression $\bar{\mathcal{M}}_{\mathcal{V}_0,c} = [[\bar\psi_c^{(+)}(\omega)\mathcal{V}_0]]$, we get the corresponding expression for the energy-averaged DSD-reaction amplitude $\bar M_{V_0,c}(\omega) =[\bar\Psi_c^{(+)}(\omega)V_0]$, which can be further transformed: $\bar M_{V_0,c}(\omega) = [\bar\Psi_{c,0}^{(+)}\bar V(\omega)]$. Here, the energy-averaged effective field satisfies the equation

$$\bar V(\omega) = V_0 + \left[\left[F\bar A_0(\omega)\bar V(\omega)\right]\right], \tag{11}$$

which is first mentioned in Sect. 2.

Apart from the energy-averaged DSD-reaction cross sections, the squared reaction amplitudes determine the partial branching ratios $b_c(\delta)$ for nucleon decay of (p-h)-type states in the channel "c" from an excitation energy interval δ:

$$b_c(\delta) = \int_\delta \bar S_{V_0,c}(\omega)d\omega \Big/ \int_\delta \bar S_{V_0}(\omega)d\omega. \tag{12}$$

Here, $\bar S_{V_0,c}(\omega) = |\bar M_{V_0,c}(\omega)|^2$ is the energy-averaged decay-channel strength function (the fluctuating part of the energy-averaged DSD-reaction cross section is neglected), $\bar S_{V_0}(\omega)$ is the ordinary strength function discussed in Sect. 2. In view of the spreading effect, the total branching ratio $b_{tot}(\delta) = \sum_c b_c(\delta)$ is less than unity. Therefore, the difference $1 - b_{tot}$, which is proportional to $W(\omega)$, can be considered as the branching ratio for statistical (mainly neutron) decay.

4 Conclusive remarks

The equations of the PHDOM for the basic quantities $\bar{A}_0(x,x';\omega)$, $\bar{\psi}^{(+)}_{c,0}(x,\omega)$ and $\bar{A}(x,x';\omega)$, $\bar{V}(x,\omega)$, $\bar{M}_{V_0,c}(\omega)$ are given above in a rather schematic form. In practice, it is necessary to separate in these equations the spin-angular and isobaric variables. This straightforward procedure used within the semi-microscopic approach to description of GR damping for closed-shell nuclei is described, e. g. in [3]. As a result, one can get the corresponding PHDOM radial equations having as the same structure as the schematic equations have. First implementations of the PHDOM are given in [8], as applied to neutron radiative capture accompanied by excitation of the isovector giant dipole and quadrupole resonances.

Here we show only one example concerned with calculations of the isoscalar monopole strength functions $\bar{S}_{V_0}(\omega)$ and $\bar{S}^{(pole)}_{V_0}$ ($V_0 = r^2Y_{00}$) in a vicinity of the isoscalar monopole GR in ^{208}Pb. (Fig.1, the solid and dotted lines, respectively).

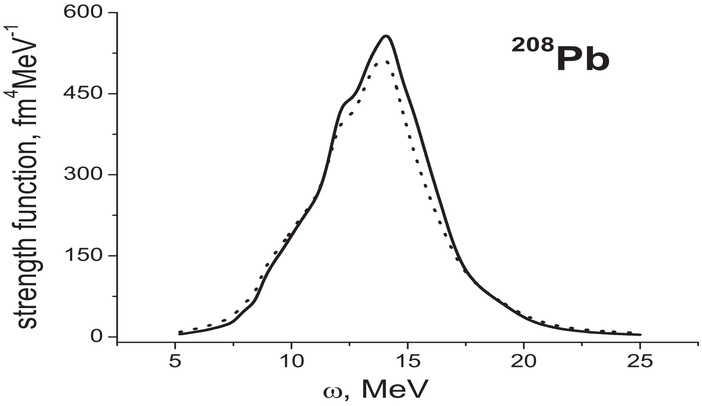

Fig 1. The isoscalar monopole strength functions calculated for ^{208}Pb

The ratio $R(\omega) = 2(\bar{S}_{V_0}(\omega) - \bar{S}^{(pole)}_{V_0}(\omega))/(\bar{S}_{V_0}(\omega) + \bar{S}^{(pole)}_{V_0}(\omega))$ illustrates the difference of the results obtained within the PHDOM and semi-microscopic approach to the description of GR damping (Fig.2). As expected, the relative difference $R(\omega)$ is noticeable at the GR "tails" where the considered strength functions are relatively small.

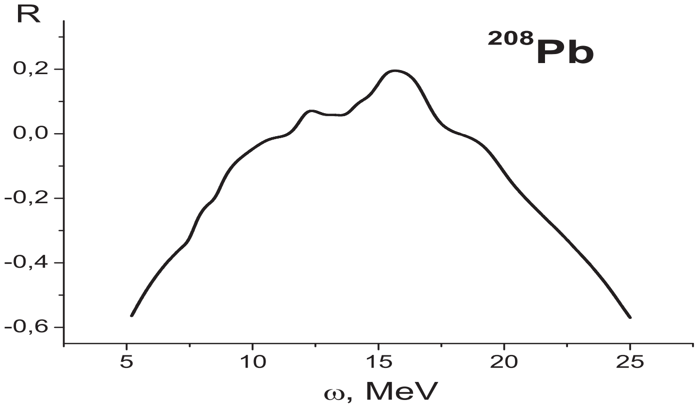

Fig 2. The relative difference of the isoscalar monopole strength functions calculated for ^{208}Pb within the PHDOM and semimicroscopic approach to the description of GR damping.

In conclusion, in the present work we formulate a new semi-microscopic model (particle-hole dispersive optical model) to describe the main relaxation modes of high-energy particle-hole-type excitations in medium-heavy nuclei. Within this model, which is the extension and verification of the early developed semi-microscopic approach to the description of giant resonance damping, Landau damping and the single-particle continuum are considered microscopically, while the spreading effect is treated phenomenologically with taking the statistical assumption into account. The model is valid at arbitrary (but high enough) excitation energies. The description of direct-nucleon-decay properties of above-mentioned excitations (including giant resonances) is a unique feature of the proposed model, which in applying to closed-shell nuclei is arranged for practical implementations.

The main results of the presented work are published in the Proceedings of the International Conference "Nuclear Structure and Related Topics (NSRT12)", Dubna, July 2-7, 2012 [9].

This work is partially supported by the Russian Foundation for Basic Research (project no. 12-02-01303-a).

References

[1] A.B. Migdal, *Theory of Finite Fermi Systems and Applications to Atomic Nuclei* (Nauka, Moscow, 1983, 2nd ed.; Intersci., New York, 1967).

[2] M.H. Urin, Nucl. Phys. A **8**11, 107 (2008).

[3] M.G. Urin, Phys. At. Nucl. **7**4, 1189 (2011).

[4] C. Mahaux and S. Sartor, Adv. Nucl. Phys. **2**0, 1 (1991).

[5] M.G. Urin, Phys. At. Nucl. **7**3, 1384 (2010); M.H. Urin, arXiv: 1005.2349v1 [nucl-th].

[6] S. Shlomo and G. Bertsch, Nucl. Phys. A **2**43, 507 (1975).

[7] B.A. Tulupov and M.G. Urin, Phys. At. Nucl. **7**2, 737 (2009).

[8] B.A. Tulupov and M.H. Urin, EPJ Web of Conferences **38**, 17010 (2012) (www.epj-conferences.org).

[9] M.H. Urin, EPJ Web of Conferences **38**, 02002 (2012) (www.epj-conferences.org).

DIRECT AND SEMIDIRECT NEUTRON RADIATIVE CAPTURE BY MEDIUM-HEAVY MASS NUCLEI: A NEW VERSION OF THE SEMIMICRISCOPIC DESCRIPTION

B.A.Tulupov[1], *M.H.Urin*[2]

[1]Institute for Nuclear Research RAS, Moscow, Russia
[2]National Research Nuclear University "MEPhI", Moscow, Russia

Abstract

The new version of the semimicroscopic model (particle-hole dispersive optical model) recently developed for describing high-energy particle-hole-type excitations in medium-heavy mass nuclei is applied for the description of the simplest photonuclear reactions accompanied by excitation of the isovector giant dipole and quadrupole resonances. The calculated reaction cross sections and their derivatives are compared with corresponding experimental data and also with the similar results obtained within the previously used semimicroscopic approach.

1 Introduction

The simplest photonuclear reactions (photoabsorption, direct and semidirect (DSD) photonucleon and inverse reactions) many years were a powerful tool of experimental studies of the isovector giant dipole and quadrupole resonances (IVGDR and IVGQR, respectively) (see, e.g. [1]). Theoretical description of the above mentioned reactions is most adequate within microscopic and semimicroscopic approaches, allowing to take into account the main relaxation modes of giant resonances (GRs). In case of GRs in medium-heavy mass 'hard' spherical nuclei (in particular, in singly- and doubly-closed-shell nuclei) these modes are: (i) particle-hole (p-h) strength distribution, or Landau damping, which is a result of shell structure of nuclei; (ii) coupling of the (p-h)-type states, forming a given GR, to the single-particle (s. p.) continuum, that leads to GR direct-nucleon decay, or to the DSD reactions with one nucleon in the continuum; (iii) coupling of the mentioned (p-h)-type states to many-quasiparticle configurations (chaotic states), that leads to the spreading effect. These relaxation modes are taken into account within the semimicroscopic approach to the description of GRs (SMAGR) based on the versions of the continuum-Random-Phase-Approximation (cRPA) [2, 3]. Within this approach Landau damping and coupling to the s. p. continuum are considered microscopically, using the cRPA, while the spreading effect is described in a phenomenological way in terms of the energy-dependent imaginary part $W(\omega)$ of the effective s. p. optical-model potential directly used in the cRPA equations. In implementations of the SMAGR a phenomenological mean field and the Landau-Migdal (momentum-independent) p-h interaction connected by some self-consistency conditions are used, as the input quantities. The above mentioned imaginary part is parameterized by an universal function, having the saturation-like energy dependence, with intensity $\alpha(\text{MeV}^{-1})$ chosen to describe the experimental total width of a given GR. Being appeared due to the spreading effect, the real part of the effective s. p. optical-model potential $P(\omega)$ is determined by the imaginary part via the proper dispersive relationship [4]. The unique feature of the SMAGR is its ability to describe direct-nucleon-decay properties of various GRs without the use of specific adjustable parameters. (A number of implementations of the approach are briefly reviewed in [2, 3]). As applied to the description of photoabsorption within the above described approach, it was found the necessity to take the isovector momentum-dependent forces into account to reproduce in partially self-consistent cRPA calculations the observed IVGDR energy and the excess of the experimental integral photo-absorption cross section over the Thomas-Reich-Kuhn sum rule. To formulate the cRPA equations in a closed form, these forces are taken as separable p-h dipole-dipole and quadrupole-quadrupole isovector velocity-dependent interactions (with the dimensionless intensities $k'_L, L = 1, 2$). This extended version of the SMAGR is used in our recent paper [5], where reasonable description of the photoabsorption and partial DSD $(\gamma, n)-$ and $(n, \gamma)-$reaction cross sections is obtained for a number of medium-heavy mass spherical nuclei. In particular, the asymmetry (with respect to 90°) of the partial differential $(\gamma, n)-$ and $(n, \gamma)-$reaction cross sections was also described. Being determined by interference of the E1- and E2-reaction amplitudes (the latter is due to the p-h interaction), this asymmetry exhibits a nonmonotonic energy dependence in a vicinity of the IVGQR and is the most suitable object for the study of this resonance properties.

Within the SMAGR phenomenological treatment of the spreading effect consists in the substitution $\omega \to \omega + iW(\omega) - P(\omega)$ in cRPA equations and, therefore, was expected to be valid in the 'pole' approximation (i.e., in the energy region of a given GR) [2, 3]. In some cases it is necessary to know properties of (p-h)-type excitations at energies far from the corresponding GR energy. For example, the above discussed asymmetry is determined, in particular, by the E1-reaction amplitude taken in the energy region of the IVGQR [5]. Recently, a semimicroscopic model (the p-h dispersive optical model (PHDOM)) is developed to describe properties of (p-h)-type excitations at arbitrary (but high enough) energies [3, 6]. Within the PHDOM and SMAGR the same input quantities and model parameters are used. In other words, the PHDOM is the verification and extension of the SMAGR. Moreover, in the energy region of a given GR the results obtained within both models are expected to be close. The distinctions might appear outside the GR region. In the 'pole' approximation the energy-averaged 'free' p-h Green function is taken as:

$$\overline{A}_0^{pole}(\omega) = A_0^{cRPA}(\omega \to \omega + iW(\omega) - P(\omega))\,. \tag{1}$$

The main new point in formulation of the PHDOM is the corresponding expression for the energy-averaged 'free' p-h radial Green function $\overline{A}_0(\omega)$ which is different from that used within the SMAGR. The easiest way to see the distinction between these quantities is the use of $\lambda-$representation ('λ' is a set of single-quasiparticle quantum numbers). In this case the quantity $A_0(\omega)$, used in the calculation of $A_0^{cRPA}(\omega)$, is well known [7]:

$$(A_0^{PRA})_{\lambda\lambda'}(\omega) = \frac{n_\lambda - n_{\lambda'}}{\varepsilon_\lambda - \varepsilon_{\lambda'} - \omega}\,, \tag{2}$$

whereas $(\overline{A}_0)_{\lambda\lambda'}(\omega)$ has the form [3, 6]:

$$(\overline{A}_0)_{\lambda\lambda'}(\omega) = \frac{n_\lambda - n_{\lambda'}}{\varepsilon_\lambda - \varepsilon_{\lambda'} - \omega + (n_\lambda - n_{\lambda'})(iW(\omega) - P(\omega))f_\lambda f_{\lambda'}}\,. \tag{3}$$

The meaning of the quantities, introduced in (3), is determined in [3, 6]. In the present work some calculation results obtained within the PHDOM for the photoabsorption and

$(n,\gamma)-$reaction are shown and compared with the results obtained within the SMAGR [5] and also with the corresponding experimental data.

2 Calculation results

Basic relationships for description within the cRPA of the simplest photonuclear reactions, namely, the strength functions, the total photoabsorption cross sections, the partial differential cross sections of $(n,\gamma)-$reaction, the anisotropy parameter a_2 and the asymmetry are given in [5]. Modifications of these relationships made for taking the spreading effect into account within the SMAGR and PHDOM are discussed above. Following [5], we employ in calculations the partially self-consistent phenomenological mean field, described in [8]. Due to the isovector self-consistency condition, the (dimensionless) intensity f' of the isovector spinless part of the Landau-Migdal p-h interaction is found from description of the symmetry potential. Therefore, only two above-mentioned adjustable parameters α and k_1', determining, respectively, the total width and energy of the IVGDR, are used to reproduce in calculations within the SMAGR and PHDOM the experimental photoabsorption cross section. The adjusted parameters are listed in Table 1.

Table 1. The adjustable parameters used in the studies of the simplest photonuclear reactions in the IVGDR energy region.

Nucleus	α, Mev^{-1}		k_1'	
	SMAGR	PHDOM	SMAGR	PHDOM
^{89}Y	0.125	0.13	0.3	0.3
^{140}Ce	0.105	0.115	0.3	0.3
^{208}Pb	0.10	0.105	0.4	0.35

Quality of such description of the IVGDR one can see from Figs. 1, 2, where the corresponding data are shown for ^{208}Pb, ^{140}Ce and ^{89}Y target nuclei.

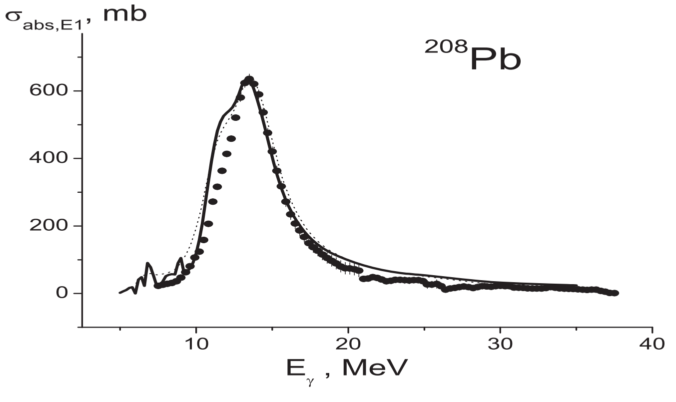

Fig 1. Calculated E1 total photoabsorption cross section for ^{208}Pb in comparison with the experimental data [10]. Hereafter the solid and dotted lines correspond to the results obtained within the PHDOM and SMAGR, respectively.

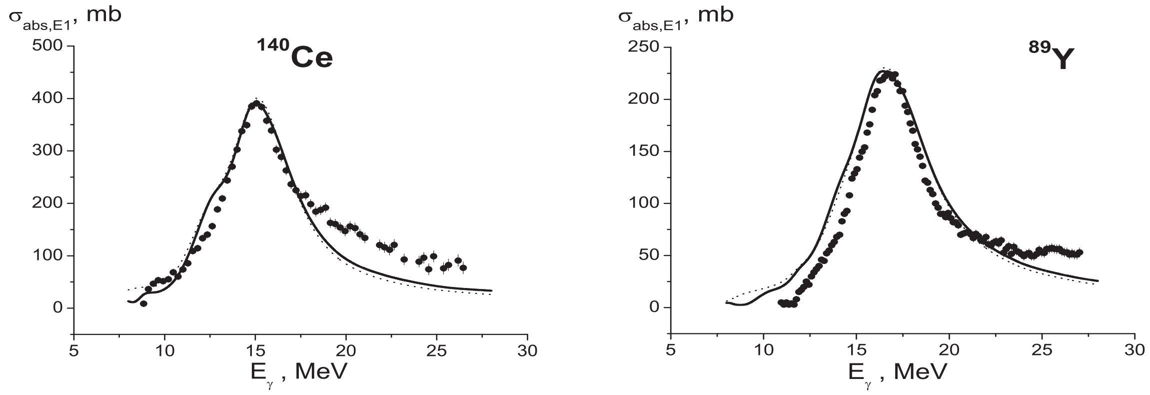

Fig 2. Calculated E1 total photoabsorption cross sections for ^{140}Ce (left-side panel) and for ^{89}Y (right-side panel) in comparison with the experimental data [10].

The partial DSD $(n,\gamma)-$reaction cross sections are calculated without use of additional adjusted parameters. The calculated cross sections at 90° are shown in Figs. 3, 4 in comparison with the corresponding experimental data.

Also the calculated anisotropy parameter a_2 for some partial $^{208}\mathrm{Pb}(n,\gamma)$ reactions is shown in Fig. 5. In the presented calculation results the experimental spectroscopic factors for s. p. states populated in the radiative capture process are taken from Ref. [9].

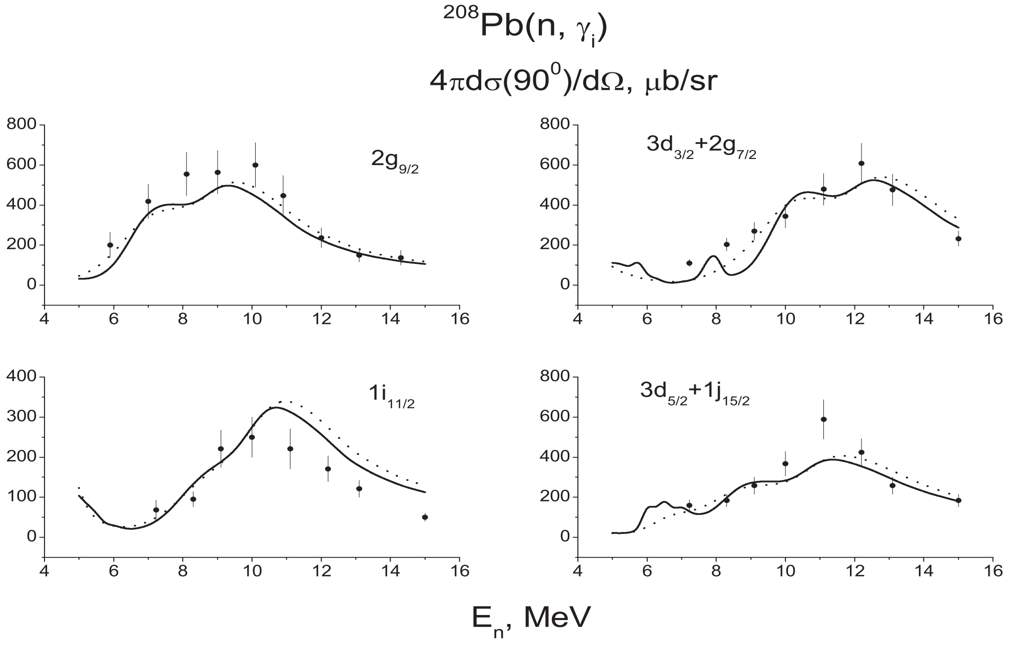

Fig 3. Calculated $(n,\gamma)-$reaction partial cross sections for ^{208}Pb. The experimental data are from Ref. [11].

As it has been noted above, to study the properties of the IVGQR it is reasonable to research, in particular, the asymmetry of the $(n,\gamma)-$reaction partial cross sections in this energy region. To this aim it needs to introduce one more adjustable parameter k_2'. As the examples the calculated values of this asymmetry for ^{208}Pb and ^{209}Bi are shown in Figs. 6 and 7, respectively, in comparison with the corresponding experimental data. These results are obtained for $k_2' = 0.1$. The IVGQR energy and its other characteristics, evaluated with this value of k_2', happened to be consistent with the systematic of Ref. [1].

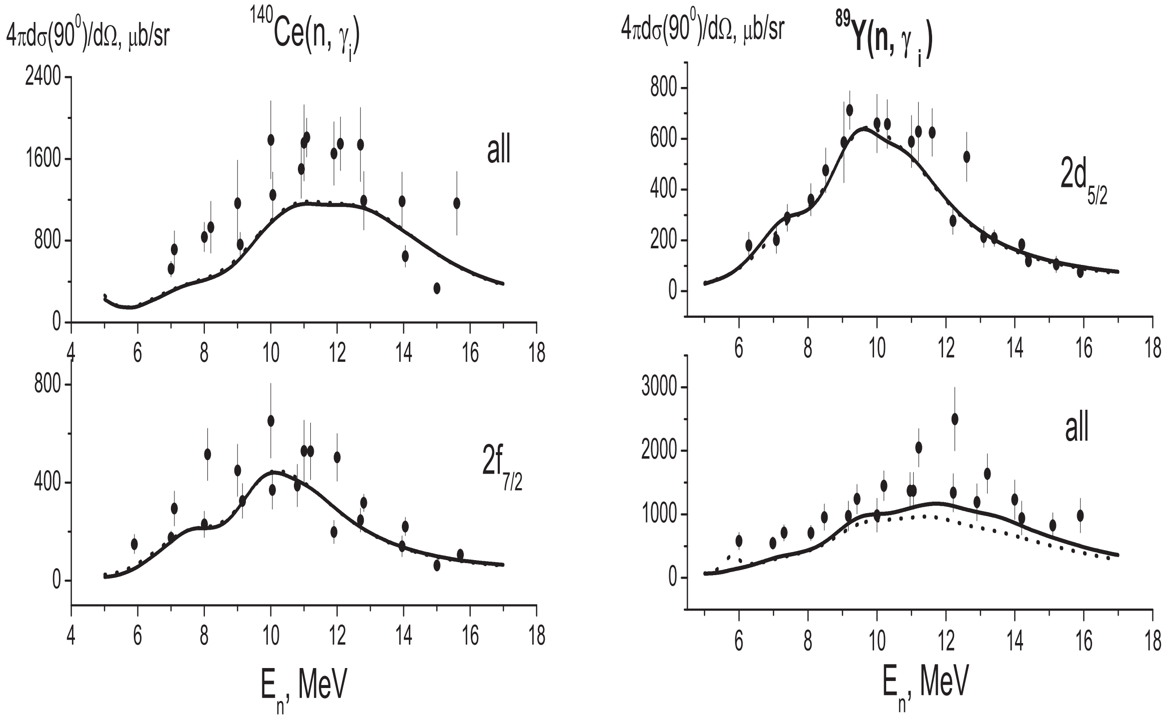

Fig 4. Calculated $(n, \gamma)-$reaction partial cross sections for ^{140}Ce (left-side panel) and for ^{89}Y (right-side panel) . The experimental data are from Ref. [12].

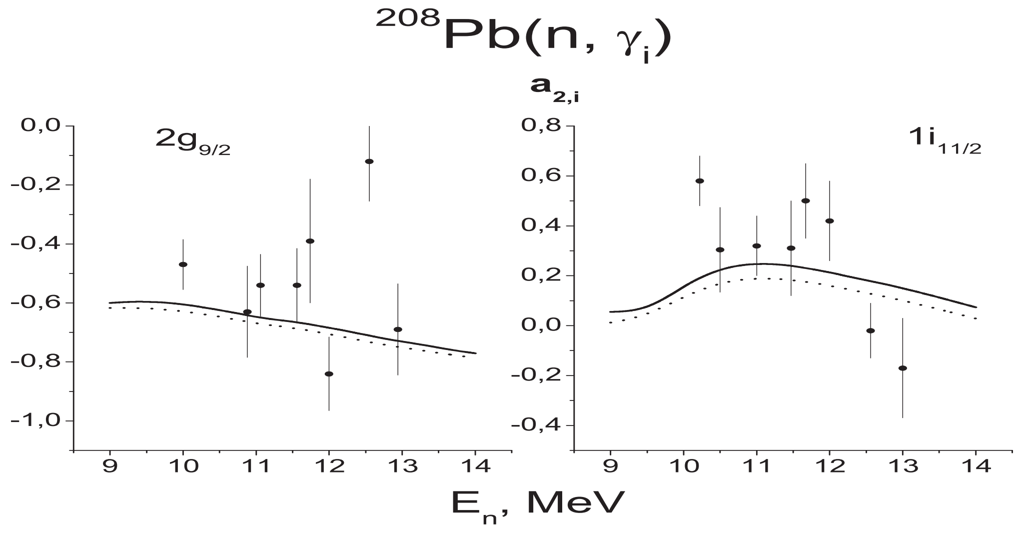

Fig 5. Calculated anisotropy parameter a_2 for some partial ^{208}Pb(n, γ) reactions. The experimental data are taken from Ref. [11].

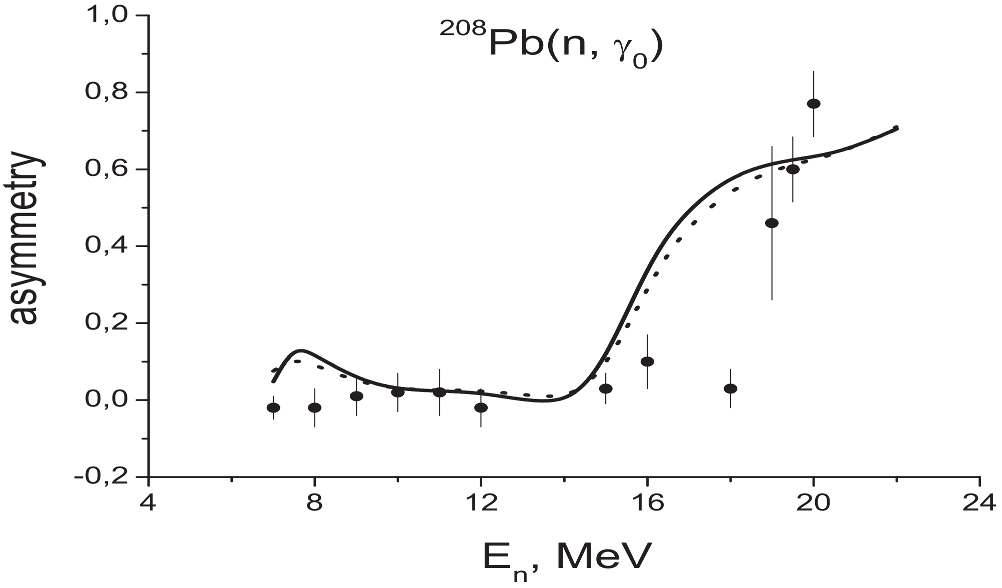

Fig 6. Calculated asymmetry of (n, γ_0)−reaction partial cross section for ^{208}Pb in comparison with the experimental data [13].

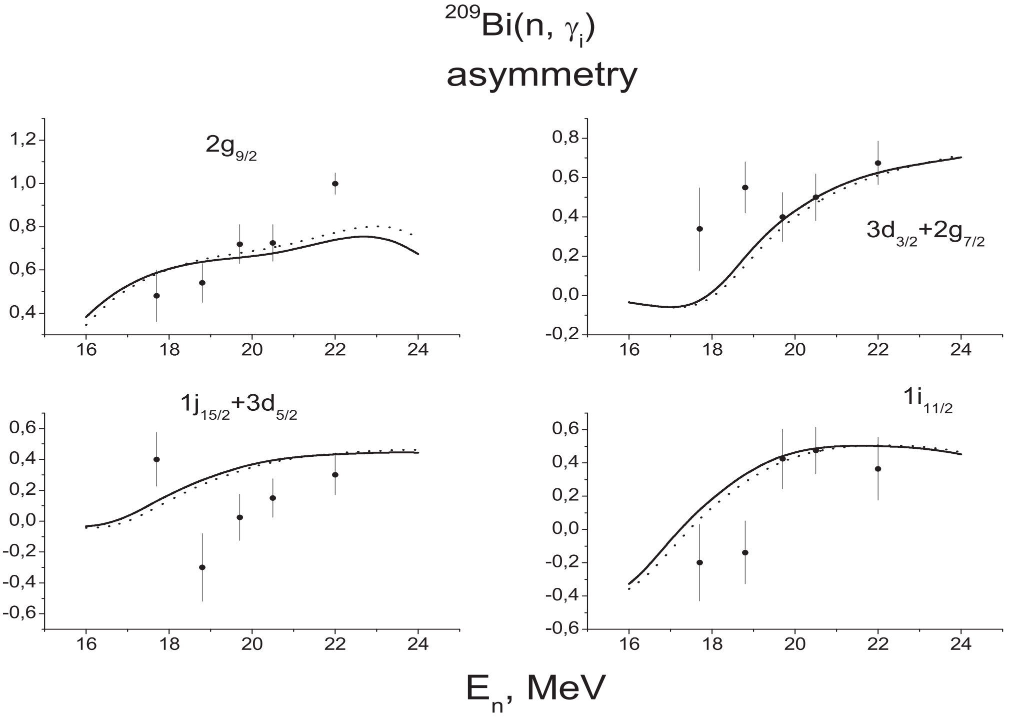

Fig 7. Calculated asymmetry of (n, γ_i)−reaction partial cross sections for ^{209}Bi in comparison with the experimental data [14].

3 Conclusion

In this work first implementations of the new semimicroscopic model, p-h dispersive optical model, are realized. Satisfactory description of the neutron radiative capture accompanied by excitation of the isovector giant dipole and quadrupole resonances in a few medium-heavy mass nuclei is obtained without the use of specific adjustable parameters. Within the mentioned model the verification and extension (on arbitrary, but high enough excitation energies) of the semimicroscopic approach to description of giant resonances (including direct-nucleon-decay properties) are achieved. New implementations of the model to describe the simplest photonuclear reactions are in progress.

The main results of the presented work are published in the Proceedings of the International Conference "Nuclear Structure and Related Topics (NSRT12)", Dubna, July 2-7, 2012 [15].

This work was supported in part by the Russian Foundation for Basic Research (project no. 12-02-01303-a).

References

[1] M.N. Harakeh and A. van der Woude, *Giant resonances: Fundamental High-Frequency Modes of Nuclear Excitations* (Oxford, University Press, New York, 2001).

[2] M.H. Urin, Nucl. Phys. A **811**, 107 (2008).

[3] M.H. Urin, Phys. At. Nucl. **74**, 1189 (2011).

[4] B.A. Tulupov and M.G. Urin, Phys. At. Nucl. **72**, 737 (2009).

[5] B.A. Tulupov and M.G. Urin, Phys. At. Nucl. **75**, 1041 (2012).

[6] M.H. Urin, EPJ Web of Conferences **38**, 02002 (2012) (www.epj-conferences.org).

[7] A.B. Migdal, *Theory of Finite Fermi Systems and Applications to Atomic Nuclei* (Interscience, New York, 1967)

[8] S.Yu. Igashov and M.G. Urin, Bull. RAS. Phys. **70**, 212 (2006).

[9] A. Likar and T. Vidmar, Nucl. Phys. A **591**, 458 (1995).

[10] A. Vessière *et al.*, Nucl. Phys. A **159**, 561 (1970); I.N. Boboshin *et al*, CDFE nuclear data bases, http://depni.npi.msu.su/cdfe.

[11] I. Bergqvist, D. M. Drake and D. K. McDaniels, Nucl. Phys. A **191**, 641 (1972).

[12] I. Bergqvist *et al.*, Nucl. Phys. A **295**, 256 (1978).

[13] D.M.Drake, S.Joly *et al.*, Phys. Rev. Lett. **47**, 1581 (1981).

[14] A. Hakansson, J. Blomgren *et al.*, Nucl. Phys. A **512**, 399 (1990).

[15] B.A. Tulupov and M.G. Urin, EPJ Web of Conferences **38**,17010 (2012) (www.epj-conferences.org).

NEW TREATMENT FOR NEUTRON MULTIPLICITY SORTING AND PARTIAL PHOTONEUTRON REACTIONS CROSS SECTIONS EVALUATION

B.S.Ishkhanov, V.N.Orlin, V.V.Varlamov

Lomonosov Moscow State University, Skobeltsyn Institute of Nuclear Physics,
119991 Moscow, Russia

Introduction

The problem of significant discrepancies between partial photoneutron reactions cross sections obtained in different experiments is as old and well-known as modern and very important. Data on reactions with formation of various numbers of neutrons, primarily (γ,n), (γ,2n), and (γ,3n), were obtained as a rule many years ago and were included into various reviews [1], Atlases [2,3] and databases [4]. They are used in many basic and applied research such as traditional (Giant Dipole Resonance (GDR) main features, GDR configurational and isospin splitting, competition between statistical and direct processes in GDR decay channels, sum rule exhaustion etc.) investigations as in actual new onces [for example, for monitoring of the beam luminosity in ultra-relativistic heavy-ion colliders [5, 6] by measuring neutron emission rates in mutual electromagnetic dissociation of colliding nuclei – neutron emission (primarily (γ,n) and (γ,2n) rates in nuclei mutual electromagnetic dissociation).

The majority of such kind data has been obtained using quasimonoenergetic γ-quanta produced by annihilation in flight of relativistic positrons at two laboratories - Livermore (USA) and Saclay (France) [1, 2]. At both laboratories the neutron multiplicity was obtained using their kinetic energy measurements but experimental methods were different. Those arrangement differences mean that cross section obtaining conditions are different and as result there are many complicated, curious, dramatic systematic discrepancies between partial photoneutron reaction cross sections obtained at Livermore and Saclay. Briefly without details – all (γ,n) reaction cross sections are larger at Saclay but all (γ,2n) ones - vise versa at Livermore. Those disagreements were the subject of special investigations during many years.

Because data of both laboratories agree as to total number of neutrons detected, the differences in their reaction cross sections $\sigma(\gamma,n)$ and $\sigma(\gamma,2n)$ were proposed [8] to arise from the separation of counts into 1n and 2n events (neutron multiplicity sorting). In [8] the results obtained using neutron multiplicity sorting were compared with those obtained using alternative method of induced activity in which concrete partial reactions are identified using detection of not outgoing neutrons but of formatting final nucleus. That was shown that results of measurements for ^{181}Ta of σ(e,xn) and σ(e,n) reaction cross sections (measured directly by activation method for 98.3 keV γ-ray line from decay of final nucleus $^{180}\mathrm{Ta} \rightarrow {}^{180}\mathrm{Hf}$) recalculated using virtual photon spectra into correspondent σ(γ,xn) and σ(γ,n) reaction cross sections lead to agreement with Livermore data but not with Saclay data: Saclay $\sigma(\gamma,2n)$ data are significantly underestimated and therefore $\sigma(\gamma,n)$ data – correspondingly overestimated because some events from (γ,2n) reaction at Saclay were interpreted as two (γ,n) events.

This point of view give to one possibility for simple, clear and direct way for correction the situation and evaluation of "correct" $\sigma(\gamma,2n)$ obtained at Saclay $\sigma^{2n}{}_{S}{}^{*}$ which must put into agreement with "corrected" (multiplied by $R = \sigma^{int}{}_{S}(\gamma,xn)/\sigma^{int}{}_{L}(\gamma,xn)$) data obtained at Livermore $R\sigma^{2n}{}_{L}$ – extra neutrons must be removed from σ(γ,n) and put into $\sigma(\gamma,2n)$:

$$\sigma^{2n}{}_{S}{}^{*} = \sigma^{2n}{}_{S} + \tfrac{1}{2}(\sigma^{n}{}_{S} - R\sigma^{n}{}_{L}) = R\sigma^{2n}{}_{L}. \quad (1)$$

Such approach was used in [8] for evaluation of corrected data for 12 nuclei (^{89}Y, ^{115}In, ^{117,118,120,124}Sn, ^{133}Cs, ^{159}Tb, ^{165}Ho, ^{181}Ta, ^{197}Au, ^{208}Pb) and later in [7] for their reevaluation and new evaluations for additional 7 nuclei (^{51}V, ^{75}As, ^{90}Zr ^{116}Sn, ^{127}I, ^{232}Th, ^{238}U). Conclusions are:

– Photoneutron multiplicity sorting was correct at Livermore but not at Saclay;

– $\sigma(\gamma,2n)$ obtained at Saclay are significantly underestimated and but $\sigma(\gamma,n)$ – overestimated;

– "Correct" Livermore data could be used after simple renormalization ($R\sigma^{2n}_{L}$) but for "incorrect" Saclay data the serious recalculation (1) must be used.

So the old well-known problem of systematic disagreements under discussion seemed to be solved. But after more detailed investigations the new problem appeared.

1. Transitional neutron multiplicity functions as objective criteria of data reliability

Because very strange behaviour of some $\sigma(\gamma,n)$ obtained at Livermore in their vanishing above (γ,2n) reaction threshold $B2n$ the new problem of reliability and authenticity of "correct" Livermore data appeared. One typical example of ^{116}Sn(γ,n)^{115}Sn cross section obtained at Livermore [9] behaviour is presented in the top of Fig. 1.

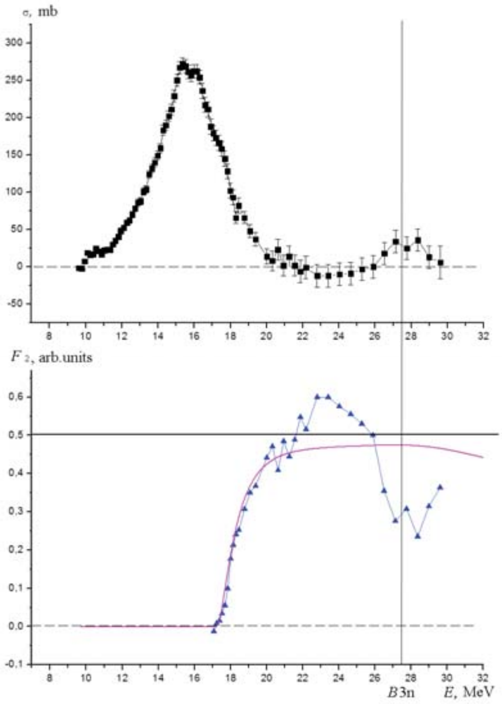

Fig. 1. Non-physical behaviour of ^{116}Sn(γ,n)^{115}Sn reaction cross section [9] -top and of correspondent multiplicity functions F_2^{exp} [10] - bottom (triangles) and F_2^{theor} [11, 12] (line).

One can see that above the GDR maximum $\sigma(\gamma,n)$ falls rapidly going into the region of negative values, than goes again to positive values showing clear positive maximum. This is not natural for typical resonance behaviour of photonuclear reaction cross section.

In the bottom of Fig. 1 there are presented experimental and theoretical data for the specially proposed [10] transition multiplicity function F_2 which is an objective very simple, clear, direct and absolute criterion of data reliability and authenticity of three reaction cross sections - $\sigma(\gamma,n)$, $\sigma(\gamma,2n)$ and $\sigma(\gamma,3n)$ - at the same time:

$$F_2 = \sigma(\gamma,2n)/\sigma(\gamma,xn) = = \sigma(\gamma,2n)/\sigma[(\gamma,n) + 2(\gamma,2n) + 3(\gamma,3n) + ...]. \quad (2)$$

The point is that follow its definition (2) without $\sigma(\gamma,n)$ and $\sigma(\gamma,3n)$ contributions into $\sigma(\gamma,xn)$ F_2 = const = 0.50. Deviation from the line "const = 0.50" at low energies is due to presence of high-energy tail of $\sigma(\gamma,n)$, at high energies – due to presence of the front of $\sigma(\gamma,3n)$. From (2) it is absolutely clear that "$F_2 > 0.50$" means that multiplicity sorting has been done incorrectly.

Fig. 1 shows that that is in fact for $^{116}Sn(\gamma,2n)^{114}Sn$ reaction cross section [9] in the energy region E = 21.5 – 26.0 MeV where "$F_2^{exp} > 0.50$" strongly correlates with $\sigma(\gamma,n)$ strange non-physical negative values.

Additionally in Fig. 1 (bottom) results of theoretical calculations of F_2^{theor} in the frame of modern pre-equilibrium model of photonuclear reactions [11, 12] based on the Fermi-gas densities equations and taking into account the effects of nuclear deformation and GDR isospin splitting are presented. One can see that behaviour of F_2^{theor} differ from that of F_2^{exp} is pure physical:

– Below $B2n$ only (γ,n) is possible and $F_2 = 0$;

– Above $B2n$ (γ,2n) reaction is open, F_2^{theor} increases (in accordance with competition between decreasing $\sigma(\gamma,n)$ and increasing $\sigma(\gamma,2n)$), going to "0.50" top boundary, nowhere reaching it because of $\sigma(\gamma,n)$ tail presence;

– Above threshold $B3n$ (γ,3n) reaction is open, F_2^{theor} decreases because of $3\sigma(\gamma,3n)$ contribution appearance.

In systematic research carried out [10, 13-15] that have been found out that analogous behaviour of $\sigma(\gamma,n)$ and F_2^{theor} is typical for many data obtained at Livermore (^{90,91,94}Zr, ^{115}In, ^{112,114,116,117,118,119,120,122,124}Sn, ^{127}I, ^{159}Tb, ^{165}Ho, ^{181}Ta, ^{188,189}Os, ^{197}Au, ^{208}Pb). Several examples of main features of that research are presented in Table 1.

Table 1.

Parameters of $\sigma(\gamma,n)$ and F_2^{theor} non-physical behaviour.

Nucleus [Ref.]	Negative $\sigma(\gamma,n)$ values energy range, MeV	F_2^{exp}-max value
^{91}Zr [16]	23.0 – 30.0	0.80
^{94}Zr [16]	21.5 - 27.0	0.70
^{115}In [9]	20.5 – 31.0	0.60
^{116}Sn [9]	21.5 – 26.0	0.62
^{159}Tb [17]	18.5 – 22.0 26.0 - 30.0	0.60 2.00
^{181}Ta [18]	17.0 - 22.5 22.5 – 24.0	0.55 0.75
^{180}Os [19]	18.0 – 21.0	0.60
^{208}Pb [20]	17.5 – 26.5	0.65

Because such non-physical behaviour of $\sigma(\gamma,n)$ and F_2^{theor} is typical for many nuclei investigated at Livermore there are many serious doubts that "correct" Livermore data for $\sigma(\gamma,n)$ and therefore for $\sigma(\gamma,2n)$ also are really correct. In addition to conclusions concern "incorrect" Saclay data have been made before [7, 8] that means that practically we have no reliable data. That forced us to investigate data reliability and authenticity in details using objective criteria. It is evident that in addition to criterion $F_2 < 0.50$ mentioned above the criteria $F_1 < 1.00$, $F_3 < 0.33$, $F_4 < 0.25$, $F_5 < 0.20$, etc. could be proposed [13].

Fig. 2 presents $F_{1,2,3}$ criteria for ^{208}Pb.

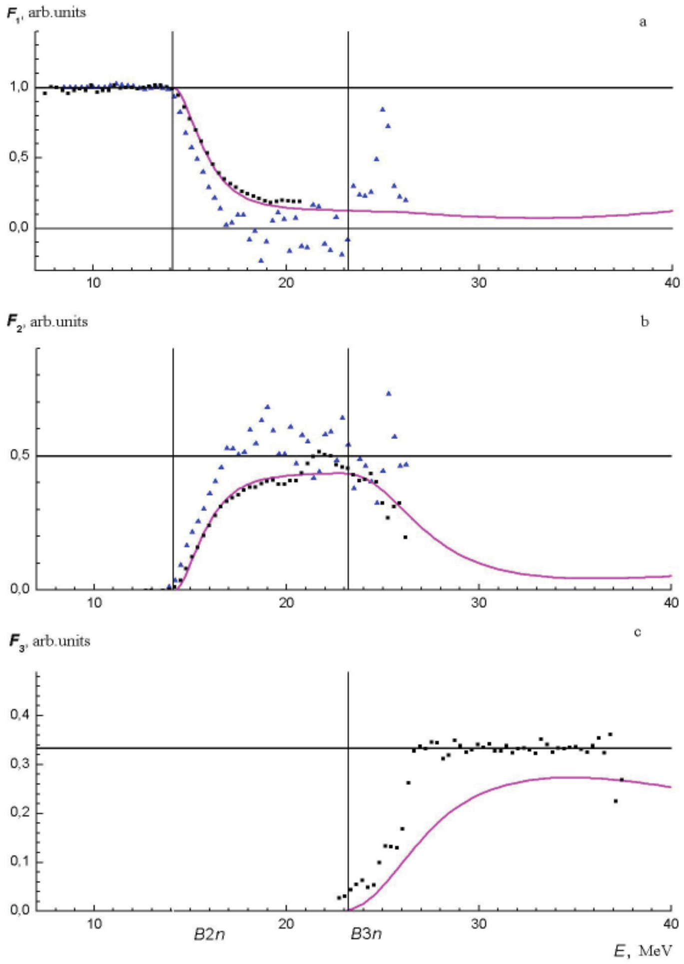

Fig. 2. Experimental Livermore ([20], triangles) and Saclay ([21], squares) $F_{1,2,3}^{\text{exp}}$ data for ^{208}Pb in comparison with theoretical results ([11, 12], line).

One can see that neutron multiplicity sorting has been done incorrectly:

– In the energy range ~ 17.5 – 23.0 MeV F_1^{exp} has negative values;

– In the same energy range ~ 17.5 – 23.0 MeV F_2^{exp} has values larger 0.50;

– At E > 26 MeVF_3^{exp} values are close to 0.33, that means that there are no absolutely the neutrons with multiplicity 1 and 2 (all such neutrons were erroneously attributed to $\sigma(\gamma,3n)$).

That is very important to point out that for ^{208}Pb in contradictory to mentioned above conclusions and recommendations have been made before [7, 8], the results of our previous systematic research [10, 13-15], and absolutely unexpected Saclay data for both $\sigma(\gamma,n)$ and $\sigma(\gamma,2n)$ are reliably agree with theoretical results (although for $\sigma(\gamma,3n)$ Saclay data disagree significantly). That strongly complicates the problem of data reliability – that means that all known data should be reanalyzed individually.

2. New experimentally-theoretical method for reliable data evaluation

In systematic investigations [10, 13-15] of well-known data on partial photoneutron reaction cross sections that was found out that there are many such kind data which reliability and authenticity are very doubtful – there are many energy regions in which cross sections have non-physical negative values and/or objective criteria $F_{2,3}^{\mathrm{exp}}$ have values larger than physically permitted boundaries – correspondingly 0.50 and 0.33. Therefore using such unreliable data in various applications could lead to doubtful conclusions. So the problem of development of the method for reliable data evaluation is very actual and important. Because the main reason of data disagreements and unreliability under discussion are connected with shortcomings of experimental methods of neutron multiplicity sorting the new so-called "experimentally-theoretical" approach for data evaluation free from such methods shortcomings has been proposed [10, 13-15].

The new approach uses as initial experimental data only that for total neutron yield reaction cross section $\sigma(\gamma,\mathrm{xn}) = \sigma[(\gamma,\mathrm{n}) + 2(\gamma,2\mathrm{n}) + 3(\gamma,3\mathrm{n}) + ...]$ and for separation of that into partial reaction cross sections - transition multiplicity functions $F_{1,2,3}^{\mathrm{theor}}$ calculated in the frame of modern exciton pre-equilibrium photonuclear reaction model [11, 12] based on Fermi-gas densities and taking into account the effects of nucleus deformation and GDR isospin splitting. So the reliable reaction cross section is evaluated by the way

$$\sigma^{\mathrm{eval}}(\gamma,\mathrm{in}) = F_{\mathrm{i}}^{\mathrm{theor}}(\gamma,\mathrm{in}) \cdot \sigma^{\mathrm{exp}}(\gamma,\mathrm{xn}). \quad (3)$$

Such way of new reliable data evaluation means that competition of partial reactions is in accordance with equations of model and the sum of evaluated cross sections is equal to the experimental data for total neutron yield cross section.

Fig. 3 illustrates the deviations of valuated cross sections from experimental ones for three partial reactions on ^{159}Tb.

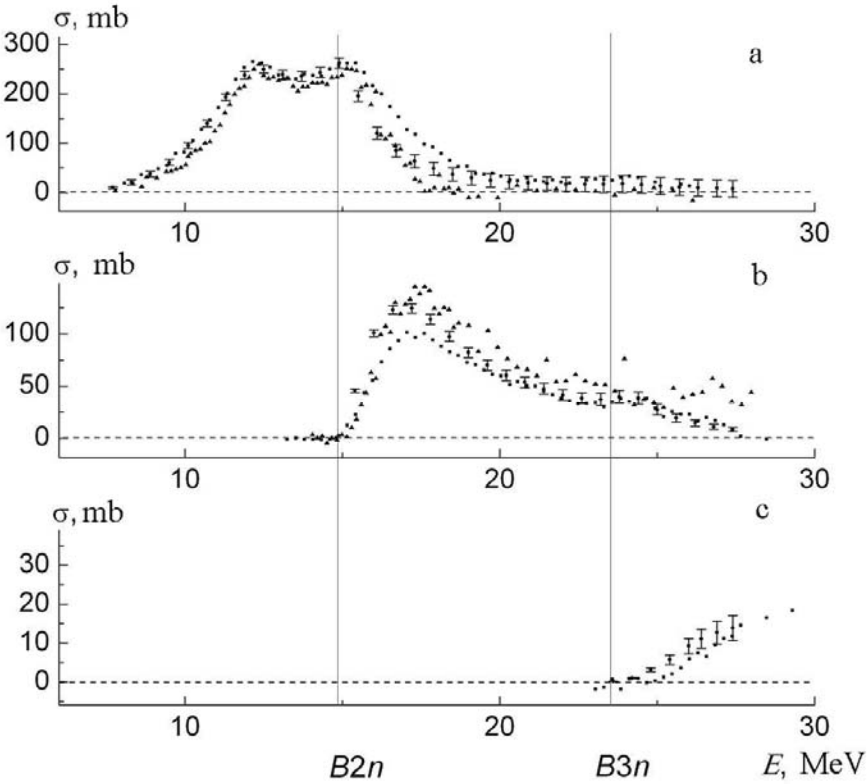

Fig. 3. Evaluated ([15], dots) and experimental (Livermore [17], triangles and Saclay [22], squares) photonuclear reaction cross sections for ^{159}Tb: a) - $\sigma(\gamma,\mathrm{n})$, b) - $\sigma(\gamma,2\mathrm{n})$, c - $\sigma(\gamma,3\mathrm{n})$.

That is important to underline that data evaluated for conditions free from experimental neutron multiplicity sorting methods shortcomings deviate from experimental cross sections significantly. Table 2 presents ratios of correspondent integrated cross sections for $\sigma(\gamma,n)$ and $\sigma(\gamma,2n)$ for ^{159}Tb.

One can see that evaluated $\sigma(\gamma,n)$ is 19 % smaller than Saclay data but 18% larger than Livermore ones. At the same time $\sigma(\gamma,2n)$ is 15% larger than Saclay data but 22% smaller than Livermore once. So the ratio $\sigma^{int}(\gamma,2n)/\sigma^{int}(\gamma,n)$ that is very important for many physical processes probabilities estimation increased in 27% compare to Saclay data and decreased in 30% compare to Livermore ones. That force one to reevaluate many physical effects, for example, competition between statistical and direct processes probabilities in various GDR decay channels.

Table 2.

Ratios of evaluated [15] integrated cross sections and experimental (Saclay [22] and Livermore [17]) ones for ^{159}Tb.

Reaction	$\sigma^{int}_{eval}/\sigma^{int}_{S}$, % (MeV·mb)	$\sigma^{int}_{eval}/\sigma^{int}_{L}$, % (MeV·mb)
(γ,n)	-19 (1642/1950)	+18 (1642/1390)
$(\gamma,2n)$	+15 (715/610)	-22 (715/870)
$(\gamma,3n)$	+16 (26/16)	no data

To understand the real reasons of deviations of experimental cross section from evaluated once the correlations between such deviations and behaviour of $F_{1,2,3}^{exp}$ were investigated in details. Fig. 4 presents comparison of differences $[\sigma^{exp}(\gamma,n) - \sigma^{eval}(\gamma,n)]$ and $[\sigma^{eval}(\gamma,2n) - \sigma^{exp}(\gamma,2n)]$ and $[\sigma^{exp}(\gamma,2n) - \sigma^{eval}(\gamma,2n)]$ and $[\sigma^{eval}(\gamma,3n) - \sigma^{exp}(\gamma,3n)]$ calculated [14] for data obtained at Livermore [9] for ^{115}In.

One can see that the correlation is absolutely clear – if some number of neutrons is added to $\sigma(\gamma,n)$ the same number of those is subtracted from $\sigma(\gamma,2n)$ and vise versa. That is very important to underline that in energy range ~ 20 – 26 MeV function F_2^{exp} has (Table 2) physically unreliable values larger than 0.50 and correspondingly $\sigma(\gamma,n)$ has physically unreliable negative values. That must be pointed out that mistakes in experimentally obtained neutron multiplicities depends on energy of incident photons and correspondingly of that of outgoing neutrons – at energies smaller ~20 MeV $\sigma^{exp}(\gamma,n) > \sigma^{eval}(\gamma,n)$ but at energies higher ~20 MeV vise versa $\sigma^{eval}(\gamma,n) > \sigma^{exp}(\gamma,n)$ and for $\sigma(\gamma,2n)$ the situation is quite inverse.

Absolutely analogous is the situation for differences $[\sigma^{exp}(\gamma,2n) - \sigma^{eval}(\gamma,2n)]$ and $[\sigma^{eval}(\gamma,3n) - \sigma^{exp}(\gamma,3n)]$ in energy range ~ 26 – 32 MeV: some number of neutrons is subtracted from “3n” channel (and therefore $\sigma(\gamma,3n)$ decreases and falls into the region of non-physical negative values) and corresponding number of neutrons is added to “2n” channel (and therefore F_2^{exp} increases and goes to the region of non-physical values larger 0.50).

3. Evaluated and experimental data disagreements – possible reasons

3.1. Different methods of neutron kinetic energy measurement

Both at Saclay and Livermore neutron multiplicity was obtained from neutron kinetic energy on the base of hypothesis that both neutrons from “2n”-channel have energy smaller than one neutron from “1n”-channel. But as that was shown above the number of neutrons with small energy (“from (γ,2n) reaction”) as a rule is underestimated at Saclay but overestimated at Livermore and vise versa the number of neutrons with large energy (“from (γ,n) reaction” vise versa is overestimated at Saclay and underestimated at Livermore. Therefore one should to a conclusion that such disagreements could be connected with the neutron registration method.

At Saclay for neutron energy measurement the large-volume Gd-loaded liquid scintillator was used. Because of formation of two neutrons in reaction (γ,2n) is realized at short nuclear time at poor time resolution of detection system there is definite opportunity for small pulses pile-up that certainly could lead to increasing the number of neutrons in "1n" channel in comparison to that of "2n" channel.

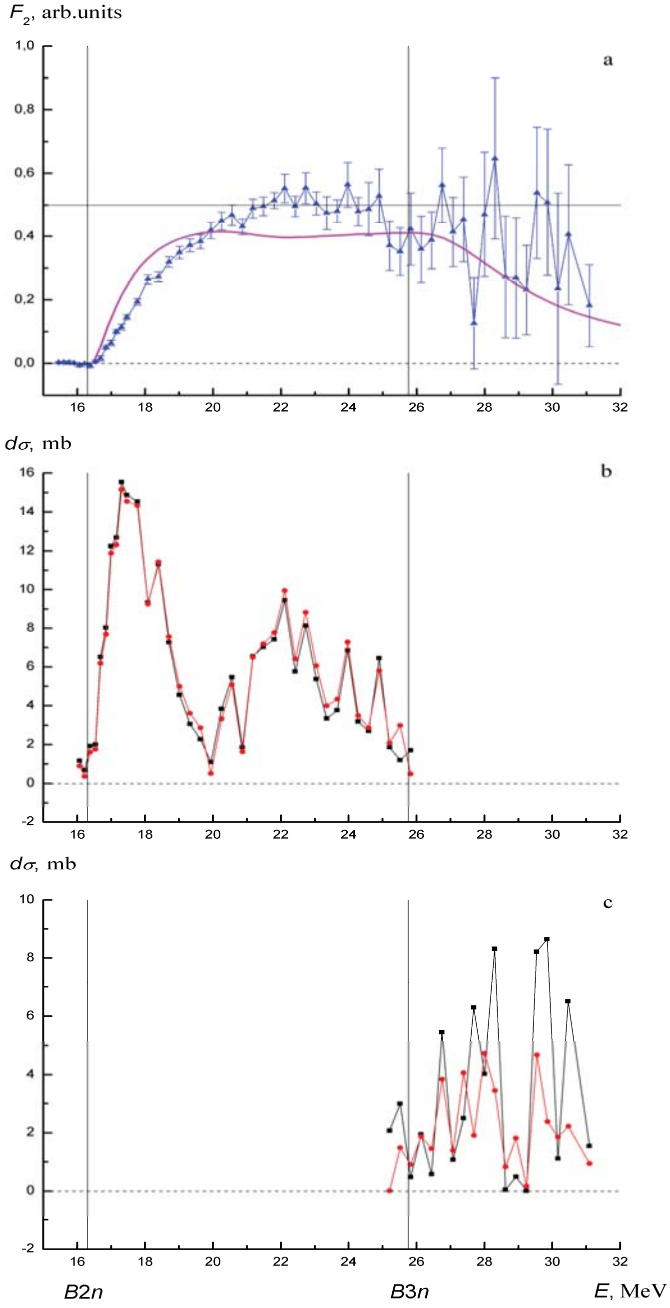

Fig. 4. Differences between experimental data of Livermore [9] and evaluated data [14] and for ^{115}In: a) – F_2 behaviour; [$\sigma^{exp}(\gamma,n)$ - $\sigma^{eval}(\gamma,n)$] – circles and [$\sigma^{exp}(\gamma,2n)$ - $\sigma^{eval}(\gamma,2n)$] – squares; b) - [$\sigma^{exp}(\gamma,2n)$ - $\sigma^{eval}(\gamma,2n)$] – circles and [$\sigma^{eval}(\gamma,3n)$ - $\sigma^{exp}(\gamma,3n)$] – squares.

At Livermore so-called "ring-ratio" method was used: neutron counters were putted into paraffin moderator by concentric rings around the target. Low-energy neutrons (as have been supposed, from reaction (γ,2n)) should have enough time for moderation in the way from target to inner ring but high-energy neutrons (as supposed from reaction (γ,n)) should go to the outer ring passing inner ring. But because of multiple scattering the neutron way certainly should not be as straight line – there is definite opportunity that neutron will go back to inner ring. That could certainly increase the number of neutrons in "2n" channel in comparison to correspondent number of neutrons in "1n" channel.

3.2. Neutron multiplicity and kinetic energy complex connection

Both at Saclay and Livermore neutron multiplicity determination methods were based on the supposition that one unique neutron from (γ,n) reaction has energy more than both neutrons from reaction (γ,2n). But as that was shown above degree of discrepancies between Saclay and Livermore data and between both of them and new evaluated cross sections in "1n, "2n", and "3n" channels depends on energy of photons and therefore on energy of neutrons. So degree of disagreements in neutron multiplicities obtained depends on individual features of neutron spectra. That means that neutron "energy – multiplicity" connection could be really not so simple and direct as has been supposed. In special investigation [23] that was shown that mean energy of the 1-st neutron from the reaction ^{181}Ta(γ,2n)^{179}Ta is much larger than that of 2-nd neutron (for example, at photon energy 25 MeV 1-st neutron has energy 4.0 MeV, but 2-nd one – 1.4 MeV). So both Saclay and Livermore methods of neutron kinetic energy measurement could be mistaken generally: if the energy of first chance neutron from reaction (γ,2n) is "enough small" the correspondent event could be correctly and reliably attributed to "2n" channel, but if its energy is "enough large" the event could be erroneously and unreliably attributed to "1n" channel.

Additionally that must be pointed out that really situation could be more complicated because in reaction (γ,n) after escape of one unique neutron and in reactions (γ,2n) and (γ,3n) after escape of first chance neutron the same nucleus is formed. Moreover the same nucleus is formed in reactions (γ,np), (γ,2np),...Therefore the possible reason of disagreements between unreliable experimental and reliable evaluated reaction cross sections could be not direct and very complex connection between neutron kinetic energy and its multiplicity.

4. Reliability of new evaluated data testing

That was mentioned above that there is alternative to neutron multiplicity sorting method of partial reaction investigation. That is the method of induced activity in which the concrete reaction is identified using detection of not outgoing neutrons but final nucleus. Because the final nuclei in reactions (γ,n), (γ,2n), and (γ,3n) are different the method of induced activity is direct for partial reaction cross section determination and there are no problems of their separation.

With the aim of testing of reliability and authenticity of photoneutron partial reaction cross sections evaluated in the frame of proposed new experimentally-theoretical approach special measurements were carried out [23] on the γ-quanta beam of new generation electron accelerator – race-track microtron with the maximal electron energy 65 MeV. Using high-quality HpGe detector the yields of (γ,n), (γ,2n), (γ,3n), (γ,4n), (γ,5n), (γ,6n), and (γ,7n) reactions on ^{181}Ta were measured [23] at one experiment. Correspondent such kind data for (γ,n), (γ,2n), and (γ,3n) reactions are compared in the Table 3.

Data presented show clear that in comparison to the induced activity results experimental data for σ(γ,2n) obtained at Saclay are definitely underestimated (0.24 vs 0.34), those obtained at Livermore – definitely underestimated (0.42 vs 0.34). That is important to underline that our new data evaluated in the frame of proposed experimentally-theoretical approach agree with induced activity data well (0.33 vs 0.34). That confirms that data evaluated in the frame of proposed new experimentally-theoretical approach are enough reliable and authentic.

Table 3.

Comparison of ratios of cross sections σ and yields Y for ^{181}Ta and reactions (γ,2n)/(γ,n) and (γ,3n)/(γ,n) obtained for experimental and evaluated data.

Ratio	Experiments			Evaluation
	Saclay [22]	Livermore [18]	Activity [23]	Our data [24]
$\sigma(\gamma,2n)/\sigma(\gamma,n)$	0.36 (797/2190)	0.67 (887/1316)		0.49 (958/1956)
$Y(\gamma,2n)/Y(\gamma,n)$	0.24	0.42	0.34 (7)	0.33
$Y(\gamma,3n)/Y(\gamma,n)$	0.02		0.023 (2)	0.018

But that produces one more serious problem should be analyzed specially. The point is that as follow from Table 4 data for $\sigma(\gamma,2n)/\sigma(\gamma,n)$ ratio obtained at Livermore [18] for ^{181}Ta are overestimated, although in special experiment has been carried many years before [8] and has used both neutron multiplicity sorting and induced activity also that was shown that $\sigma(\gamma,2n)$ obtained at Livermore is quiet reliable. Therefore that was supposed (only supposed because experimental data for $\sigma(\gamma,n)$ using induced activity data have not been obtained) that $\sigma(\gamma,n)$ for ^{181}Ta also is reliable. From the first point of view there is clear contradiction with results of our investigations using objective criteria of data reliability. To solve that contradiction the detailed evaluation has been carried out for ^{181}Ta [23] using our new experimentally-theoretical approach. The results (Table 4) were very interesting and unexpected. They show clear that as larger is the partial reaction ^{181}Ta(γ,n)^{180}Ta contribution into the total reactions (^{181}Ta(γ,xn) and ^{181}Ta(γ,sn), (γ,sn) = [(γ,n) + (γ,2n) + (γ,3n) + ...] larger is deviation of that total reaction cross section from correspondent evaluated one (1.24 → 1.30). For pure ^{181}Ta(γ,n)^{180}Ta reaction cross section its deviation from correspondent evaluated one is significantly larger – 1.46!

Table 4.

Total and partial reactions integrated cross section ratios comparison for experimental and evaluated data for ^{181}Ta.

Reaction	$\sigma^{int}_{eval}/\sigma^{int}_{S}$, arb.units (MeV·mb)	$\sigma^{int}_{eval}/\sigma^{int}_{L}$, arb.units (MeV·mb)
(γ,xn)	1	1.24 (3814/3068)
(γ,sn)	0.96 (2867/2998)	1.30 (2867/2199)
(γ,n)	0.88 (1922/2190)	1.46 (1922/1316)
(γ,2n)	1.16 (929/798)	1.05 (929/887)

That means that overestimation (Table 4) of ratios $\sigma(\gamma,2n)/\sigma(\gamma,n)$ and $Y(\gamma,2n)/Y(\gamma,n)$ for ^{181}Ta is not because $\sigma(\gamma,2n)$ namely is overestimated (moreover data of Table 5 show that in this case we have slightly (5%) underestimation!) but because $\sigma(\gamma,n)$ is significantly (46%!) underestimated. The reason for so significant underestimation of $\sigma(\gamma,n)$ is absolutely misunderstood but for ^{181}Ta that is in case really and also is directly reflected in significant underestimation (Table 5 – 24%) of total neutron yield reaction cross section $\sigma(\gamma,xn)$ for this nucleus in comparison with not only evaluated and experimental Saclay ones but with other results of analogous cross sections obtained using bremsstrahlung [24]. That is useful to point out that in accordance with results of systematic investigations [3, 25, 26] of discrepancies of $\sigma(\gamma,xn)$ reaction integrated cross section ratios obtained at various laboratories the mean ratio for such discrepancies was estimated to be equal to only 12%.

Conclusions

Using new objective criteria of data reliability and new experimentally-theoretical approach to partial reaction cross section evaluation many experimental data for (γ,n), (γ,2n) reactions (and if it was possible - for (γ,3n) reaction) have been analyzed for 15 nuclei ^{90}Zr, ^{115}In, ^{112,114,116,117,118,119,120,122,124}Sn, ^{159}Tb, ^{181}Ta, ^{197}Au, and ^{208}Pb. That has been found out that:

- At Saclay for all nuclei mentioned above with exception of ^{208}Pb in accordance with F_{i} behaviour σ(γ,n) are over- but σ(γ,2n) – underestimated; for ^{208}Pb competition of both reaction cross sections is reliable;
- At Livermore for all nuclei mentioned with exception ^{181}Ta in accordance with F_{i} behaviour vise versa σ(γ,2n) are under- but σ(γ,n) – overestimated; for ^{181}Ta σ(γ,2n) small (5%) underestimation is correlated with significant (46%) σ(γ,n) underestimation;
- For ^{181}Ta data evaluated using new experimentally-theoretical approach proposed disagree with unreliable data obtained using neutron multiplicity sorting between “1n” and “2n” channels, but agree with data obtained using alternative method of induced activity.

So the main conclusions of new treatment using are the following:

- Practically all investigations show that neutron multiplicity sorting experiments were carried out incorrectly and data obtained are not reliable;
- The main reason of that is complex and not direct connection between neutron kinetic energy measured and its multiplicity obtained;
- Systematic disagreements of data obtained using various neutron multiplicity sorting methods appear from the neutron kinetic energy measurement shortcomings;
- Experimental data on partial photoneutron reaction cross sections should be reanalyzed and reevaluated individually for nuclei investigated before;
- For reliable determination of partial photoneutron reaction cross sections the methods of direct reaction identification – detection of final nucleus activity or outgoing neutrons in coincidences – should be used;
- Proposed experimentally-theoretical approach for partial photoneutron reaction cross section evaluation based on joint using of experimental data only for neutron total yield reaction cross section σ(γ,xn) and equations of modern model of photonuclear reactions give results that contradict to the results obtained using neutron multiplicity sorting but agree to those obtained using the method of induced activity.

The work was supported by Russia BFR Grant 09-02-00368, Scientific Schools grant 02.120.21.485-SS and Contract 02.740.11.0242. Authors acknowledge very much Drs. M.A.Makarov, N.N.Peskov, T.S.Polevich, and M.E.Stepanov for help in data obtaining and presentation.

References

1. B.L.Berman, S.S.Fultz, Rev. Mod. Phys. 47 (1975)713
2. S.S.Dietrich, B.L.Berman, Atom. Data and Nucl. Data Tables 38 (1988) 199
3. A.V.Varlamov, V.V.Varlamov, D.S.Rudenko, M.E.Stepanov, INDC(NDS)-394, IAEA NDS, Vienna, Austria, 1999
4. Nuclear Reaction Database (EXFOR), URL: http://cdfe.sinp.msu.ru/exfor/index.php
5. CSISRS and EXFOR Nuclear reaction experimental data (database),
6. URL: http://www.nndc.bnl.gov/exfor/exfor00.htm
7. V.V.Varlamov, B.S.Ishkhanov, N.N.Peskov, M.E.Stepanov, I.A.Pshenichnov, Phys. Atom. Nucl. 67 (2004) 2122
8. U.I.Uggerhoj, I.A.Pshenichnov, et al, Phys. Rev. C72 (2005) 057901

9. V.V.Varlamov, N.N.Peskov, D.S.Rudenko, M.E. Stepanov, INDC(CCP)-440, IAEA NDC, Vienna, Austria, 2004
10. E.Wolynec, M.N.Martins, Rev. Bras. Fis. 17 (1987) 56
11. S.C.Fultz, B.L.Berman, J.T.Caldwell, et al, Phys. Rev. 186 (1969) 1255
12. V.V.Varlamov, B.S.Ishkhanov, V.N.Orlin, V.A.Chetvertkova, Bull. Rus. Acad. Sci. 74 (2010) 883
13. B.S.Ishkhanov, V.N.Orlin, Phys. Part. Nucl. 38 (2007) 232
14. B.S.Ishkhanov, V.N.Orlin, Phys. Atom. Nucl. 71 (2008) 493
15. V.V.Varlamov, B.S.Ishkhanov, V.N.Orlin, S.Yu.Troshchiev, Bull. Rus. Acad. Sci., 74 (2010) 842
16. V.V.Varlamov, B.S.Ishkhanov, V.N.Orlin, A.V.Sopov, MSU SIMP Preprint-8/864, 2010
17. V.V.Varlamov, B.S.Ishkhanov, V.N.Orlin, Phys. Atom. Nucl. 75 (2012) 1339.
18. S.C.Fultz, B.L.Berman, J.T. Caldwell, et al, Phys. Rev. 186 (1969) 1255
19. R.L.Bramblett, J.T.Caldwell, et al, Phys. Rev. 133 (1964) B869
20. R.L.Bramblett, J.T.Caldwell, G.F.Auchampaugh, et al, Phys. Rev. 129 (1963) 2723
21. B.L.Berman, D.D.Faul, R.A.Alvarez, et al, Phys. Rev. C19 (1979) 1205
22. R.R.Harvey, J.T.Caldwell, R.L.Bramblett, et al, Phys. Rev. 136 (1964) B126
23. A.Veyssiere, H.Beil, R.Bergere, et al, Nucl. Phys. A159 (1970) 561
24. R.Bergere, H.Beil, A.Veyssiere, et al, Nucl. Phys. A121 (1968) 463
25. B.S.Ishkhanov, V.N.Orlin, S.Yu.Troshchiev, Phys. Atom. Nucl. 75 (2012) 253
26. V.V.Varlamov, V.N.Orlin, N.N.Peskov, T.S.Polevich, MSU SIMP Preprint-1/879, 2012
27. V.V.Varlamov, B.S.Ishkhanov, INDC(NDS)-432, IAEA NDS, Vienna, Austria, 2002.
28. V.V.Varlamov, B.S.Ishkhanov, Phys. Part. Nucl. 35 (2004) 459.

AB INITIO THEORY OF LIGHT NUCLEI WITH INVERSE SCATTERING *NN* INTERACTION

A. M. Shirokov[1], *J. P. Vary*[2], *P. Maris*[2], *A. I. Mazur*[3], *V. A. Kulikov*[1]

[1]Skobeltsyn Institute of Nuclear Physics, Moscow State University, Moscow, Russia
[2]Department of Physics and Astronomy, Iowa State University, Ames IA, USA
[3]Pacific National University, Khabarovsk, Russia

We discuss the studies of light nuclei in *ab initio* No-core Full Configuration approach based on extrapolations to the infinite model space of large-scale No-core Shell Model calculations on supercomputers. The convergence at the end of *p* shell and beginning of the *sd* shell can be achieved if only reasonable soft enough *NN* interactions are used. In particular, good predictions are obtained with a realistic JISP16 *NN* interaction obtained in *J*-matrix inverse scattering approach and fitted to reproduce light nuclei observables without three-nucleon forces. We discuss the current status of this *NN* interaction and its recent development.

1. INTRODUCTION

One of the mainstreams of modern nuclear theory is an *ab initio* description of nuclei, i. e. model-free calculations of many-nucleon systems using supercomputers. A rapid development of *ab initio* methods for solving finite nuclei has opened a range of nuclear phenomena that can be evaluated to high precision using realistic nucleon-nucleon interactions. Nowadays, due to increased computing power and novel techniques, *ab initio* approaches like the No-core Shell Model (NCSM) [1], the Green's function Monte Carlo [2] and the Coupled-Cluster Theory [3] are able to reproduce properties of a large number of atomic nuclei with mass up to $A = 16$ and can be extended for heavier nuclei. Recently a new *ab initio* method, the No-Core Full Configuration (NCFC) approach [4], was introduced. NCFC is based on extrapolation of the NCSM results in successive basis spaces to the infinite basis space limit. This makes it possible to obtain basis space independent predictions for binding energies and to evaluate their numerical uncertainties. We concentrate the discussion here on the NCFC approach and on some new results obtained with it. In particular, we discuss the predictions [5] for the binding energy and spectrum of the extreme proton-excess nucleus ^{14}F confirmed by the first experimental observation of this isotope reported recently [6].

The *ab initio* methods require a reliable realistic strong interaction providing an accurate description of *NN* scattering data and high-quality predictions for binding energies, spectra and other observables in light nuclei. A number of meson-exchange potentials sometimes supplemented with phenomenological terms to achieve high accuracy in fitting *NN* data (CD-Bonn [7], Nijmegen [8], Argonne [9]) have been developed that should be used together with modern *NNN* forces (Urbana [10,11], Illinois [12], Tucson–Melbourne [13–15]) to reproduce properties of many-body nuclear systems. On the other hand, one sees the emergence of realistic *NN* and *NNN* interactions with ties to QCD [16–19].

Three-nucleon forces require a significant increase of computational resources needed to diagonalize a many-body Hamiltonian matrix since the *NNN* interaction increases the number of non-zero matrix elements approximately by a factor of 30 in the case of *p*-shell nuclei. As a result, one needs to restrict the basis space in many-body calculations when *NNN* forces are involved that makes the predictions less reliable. *Ab initio* many-body studies benefit from the use of recently developed purely two-nucleon interactions of INOY (Inside Nonlocal Outside Yukawa) [20,21] and JISP (*J*-matrix Inverse Scattering Potential) [22–25] types fitted not only to the *NN* data but also to binding energies of $A = 3$ and heavier nuclei. At the fundamental level, these *NN* interactions are supported by the work of Polyzou and Glöckle [26] who demonstrated that a realistic *NN* interaction is equivalent at the $A = 3$ level to some *NN* + *NNN* interaction where the new *NN* force is related to the initial one through a phase-equivalent transformation (PET). It seems reasonable then to exploit this freedom and work to minimize the need for the explicit introduction of three- and higher-body forces. Endeavors along these lines have resulted in the design of INOY and JISP strong interaction models.

The JISP *NN* interaction provides a fast convergence of NCSM calculations, it is fitted in NCSM and NCFC studies to the properties of light nuclei and is developing together with the progress in these *ab initio* approaches. We discuss here the progress in developing of the JISP *NN* interaction in line with related progress of NCSM and NCFC studies of light nuclei.

2. JISP16 *NN* INTERACTION AND NCFC APPROACH

The *J*-matrix inverse scattering approach was suggested in Ref. [27]. It was further developed and used to design a high-quality JISP *NN* interaction in Ref. [22]. A nonlocal interaction obtained in this approach is in the form of a matrix in the oscillator basis in each of *NN* partial waves. To reproduce scattering data in a wider energy range, one needs to increase the size of the potential matrix and/or the $\hbar\Omega$ parameter of the oscillator basis. From the point of view of shell model applications, it is desirable however to reduce the size of potential matrices and to use $\hbar\Omega$ values in the range of few tens of MeV. A compromise solution is to use $\hbar\Omega = 40$ MeV with $N_{\max} = 9$ truncation of potential matrices [22], i. e., the JISP *NN* interaction matrices include all relative *NN* motion oscillator states with excitation quanta $N_{\max}$ up to 8 or 9 depending on parity. In other words, we use potential matrices of the rank *r* = 5 in s and p NN partial waves, *r* = 4 matrices in d and f partial waves, etc.; in the case of coupled waves, the rank of the potential matrix is a sum of the respective ranks, e. g., the rank of the coupled sd wave matrix is *r* = 5 + 4 = 9. The $N_{\max} = 9$ truncated JISP interaction with $\hbar\Omega = 40$ MeV provides an excellent description of *NN* scattering data with χ^2/datum = 1.03 for the 1992 np data base (2514 data), and 1.05 for the 1999 np data base (3058 data) [28].

PETs originating from unitary transformations of the oscillator basis proposed in Refs. [29,30], give rise to ambiguity of the interaction obtained in the *J*-matrix inverse scattering approach. This ambiguity is eliminated at the first stage by postulating the simplest tridiagonal form of the *NN* interaction in uncoupled and quasi-tridiagonal form in coupled *NN* partial waves [22]. At the next stage, PETs are used to fit the JISP interaction to various nuclear properties. First of all, the *sd* component of the *NN* interaction is modified with the help of PETs to reproduce the deuteron quadrupole moment *Q* and rms radius without violating the excellent description of scattering data. It is worth noting here that the deuteron binding energy E_d and asymptotic normalization constants are used as an input in the inverse scattering approach and are not affected by PETs.

After that we employ PETs in other *NN* partial waves attempting to improve the description of binding energies and spectra of light nuclei in NCSM calculations. Following this *ab exitu* route, the JISP6 *NN* interaction fitted to properties of nuclei with masses $A \leq 6$, was proposed in Refs. [23,24]. It was found out later that JISP6 strongly overbinds nuclei with $A \geq 10$. Therefore a new fit of PET parameters was performed that resulted in the JISP16 *NN* interaction [25,31] fitted to nuclei with masses up through $A \leq 16$.

The JISP16 *NN* interaction provides a good description of binding energies, spectra and other properties of *s* and *p* shell nuclei. It was used in a number of papers of various groups [4,5,25,32–

44] and was shown to be one of the best if not the best as compared to other modern models of the realistic strong interaction from the point of view of description of observables in light nuclei. It is worth noting that JISP16 provides better convergence of *ab initio* calculations than other realistic *NN* interactions and avoids the need to use three-nucleon forces. As a result, the JISP16 predictions for light nuclei are more reliable than that of other realistic models of *NN* interactions. With modern supercomputer facilities, we can obtain converged or nearly converged energies of nuclei with mass $A \leq 6$. For calculations of heavier nuclear systems, we proposed recently a NCFC approach [4].

It was found [4] that binding energies of many light nuclei represent an exponential convergence pattern in the excitation oscillator quanta $N_{\max}$ characterizing the basis space of the NCSM. Therefore, we fit the set of ground state energies obtained with each fixed $\hbar\Omega$ value using the relation

$$E_{gs}(N_{\max}) = a\exp(-cN_{\max}) + E_{gs}(\infty), \tag{1}$$

where fitting parameters a and c depend on the $\hbar\Omega$ value and $E_{gs}(\infty)$ is the extrapolated ground state energy in the infinite basis space. The exponential convergence patterns and fits by Eq. (1) are illustrated by Fig. 1. Within the NCFC approach, we use two extrapolation methods: a global extrapolation based on the results obtained in four successive basis spaces with five $\hbar\Omega$ values from a 10 MeV interval (extrapolation A); and extrapolation B based on the results obtained at various fixed $\hbar\Omega$ values in three successive basis spaces and defining the most reliable $\hbar\Omega$ value for the extrapolation. These extrapolations provide consistent results and were carefully tested in a number of light nuclei where a complete convergence can be achieved [4].

An exciting recent result obtained with JISP16 *NN* interaction and NCFC method, is an *ab initio* prediction [5] of properties of the exotic extreme proton-excess nucleus ^{14}F. The first experimental results regarding this isotope became available recently from Cyclotron Institute at Texas A&M University [6]. The largest calculations were performed in the $N_{\max}\hbar\Omega$ basis space with $N_{\max} = 8,$ which for this nucleus contains 1 990 061 078 basis states with natural parity (negative). The determination of the lowest ten to fifteen eigenstates of the sparse Hamiltonian matrix, for each oscillator parameter $\hbar\Omega$, requires 2 to 3 hours on 30 504 quad-core compute nodes at the Jaguar supercomputer at ORNL.

Table 1. NCFC predictions for the ground state energies (in MeV) of ^{13}O, ^{14}B and ^{14}F based on NCSM calculations with JISP16 in up to $N_{\max} = 8$ basis spaces [5]. Estimates of the accuracy of the extrapolations are shown in parentheses. Experimental data for ^{13}O and ^{14}B are taken from Ref. [45] and from Ref. [6] for ^{14}F.

Nucleus	Extrapolation A	Extrapolation B	Experiment
^{13}O	–75.7(2.2)	–77.6(3.0)	–75.556
^{14}B	–84.4(3.2)	–86.6(3.8)	–85.423
^{14}F	–70.9(3.6)	–73.1(3.7)	–74.00

We present in Table 1 the results of NCFC calculations [5] of the ^{14}F ground state energy. Combining the extrapolations A and B predictions suggests a binding energy of 72 ± 4 MeV for ^{14}F nicely confirmed by a later experiment [6] where a value of 74.00 MeV was reported. We performed similar calculations for the mirror nucleus ^{14}B with a known binding energy of 85.423 MeV [45]. This value agrees with our prediction from combination of extrapolations A and B of 86 ± 4 MeV. We also performed NCFC calculations of the neighboring nucleus ^{13}O using basis spaces up to $N_{\max} = 8.$ The calculated binding energy of 77 ± 3 MeV also agrees with the experimental value of 75.556 MeV [45].

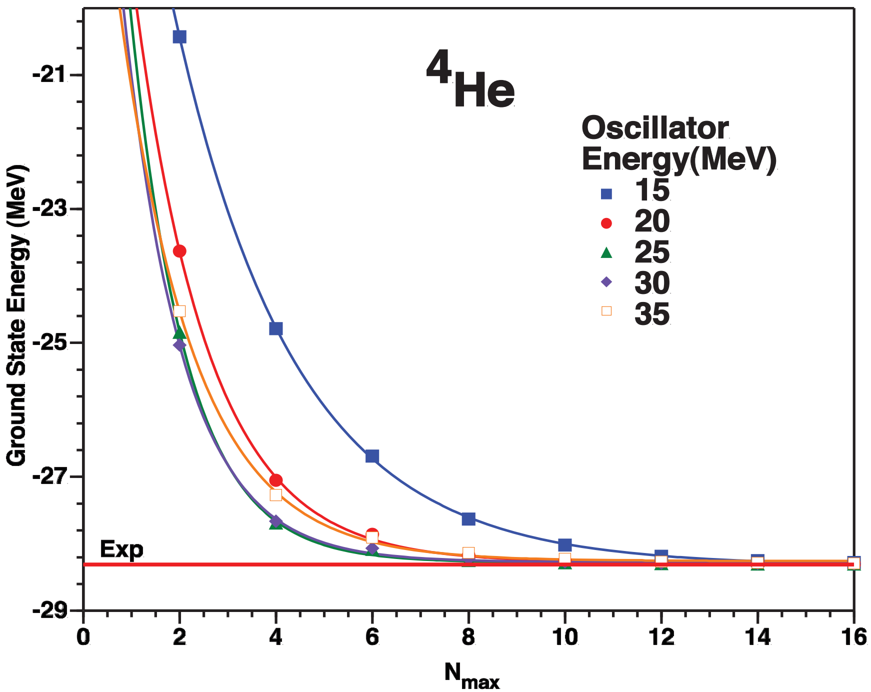

Figure 1. Ground state energies of ^{4}He obtained with different $N_{\max}$ and $\hbar\Omega$ values. Each set of points at fixed $\hbar\Omega$ is fitted by Eq. (1) (solid curves). Horizontal line shows the experimental binding energy

We note that a good description of both ^{14}F and ^{13}O in the same approach is important to ensure consistency of the theory and experiment in which ^{14}F was produced in the $^{13}\mathrm{O}+p$ reaction. In this respect it is interesting to note that although the energies of the extrapolations A and B differ by about 2 MeV, the differences between the ground state energies of these three nuclei are almost independent of the extrapolation method. The numerical uncertainty in these differences is unclear, but expected to be significantly smaller than the uncertainty in the total energies.

In calculations of the ^{14}F excitation spectrum [5], we performed independent separate extrapolation fits for total energies of all states. The differences between the extrapolated total energies and the ground state energy is our prediction for the excitation energies. This approach was carefully tested in Ref. [5] in calculations of the ^{6}Li spectrum where a good convergence can be achieved. Evaluated uncertainties of extrapolated total energies of excited states are of the same order as that of the ground state; nevertheless, as discussed above, we expect the uncertainties of energy differences, i. e., of excitation energies, to be significantly smaller. The obtained spectrum is rather dense and includes many states, however, we expect the five lowest excited states only to have small enough widths (see Ref. [5] for a detailed discussion).

Several excited states in ^{14}F were observed experimentally [6]. They are compared with our predictions [5] in Fig. 2. The experiment [6] is seen to confirm our predictions for the ^{14}F spectrum [5] obtained before the first observation of this nucleus. These results provide a strong support to our *ab initio* approach based on NCSM calculations, NCFC extrapolations and the use of realistic JISP16 *NN* interaction. The *ab initio* results are seen from Fig. 2 to reproduce the experiment much better than conventional shell model calculations with an inert core and phenomenological effective interactions WPB and MK.

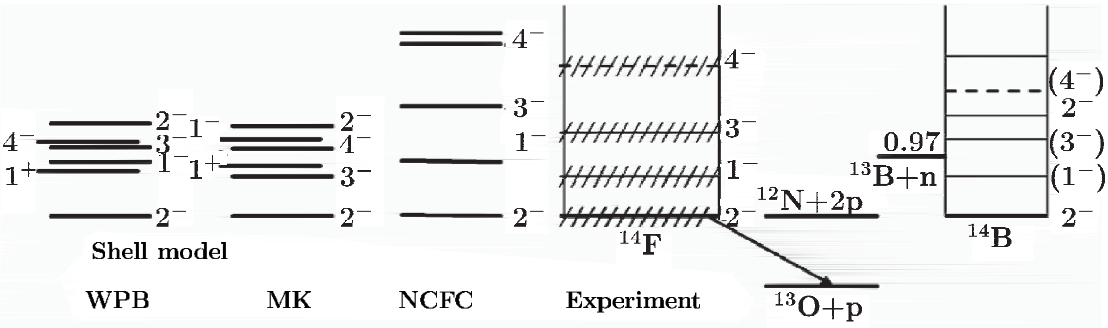

Figure 2. The ^{14}F spectrum: shell model calculations with WPB and MK interactions [6] and our predictions [5] (NCFC) in comparison with experimental data reported in Ref. [6] (experiment) and that of the mirror ^{14}B nucleus [45]

3. REFINED JISP16$_{2010}$ INTERACTION

The new NCFC approach provides much more reliable *ab initio* predictions for bindings than an earlier pure NCSM approach. The NCFC extrapolation technique revealed some drawbacks of the JISP16 *NN* interaction that was fitted to nuclear observables before this technique was developed. In particular, it was found that the JISP16 interaction overbinds essentially nuclei with mass $A \geq 14$ and $N \approx Z$.

These deficiencies of the *NN* interaction can be addressed by a new fit in the NCFC calculations of the PET parameters defining JISP interaction. We refer to as JISP16$_{2010}$ the revised *NN* interaction obtained in this fit. The JISP16 and JISP16$_{2010}$ describe *NN* scattering data with the same accuracy; the same PET defines both these interactions in the *sd* partial wave, hence they predict the same deuteron properties. However PET parameters in other *NN* partial waves differ between JISP16$_{2010}$ and JISP16. We note also that JISP16 was defined only in the *NN* partial waves with momenta $J \leq 4$ while the JISP16$_{2010}$ is extended to all $J \leq 8$.

We compare binding energies of some nuclei obtained with JISP16 and JISP16$_{2010}$ interactions in Table 2. It is seen that the new interaction essentially improves the description of the *p* shell nuclei. In particular, JISP16$_{2010}$ provides nearly exact binding energies of nuclei with $10 \leq A \leq 16$ and only slightly underbinds some of lighter nuclei listed in Table 2.

Table 2. Binding energies (in MeV) of some nuclei obtained with JISP16 and JISP16$_{2010}$ *NN* interactions in the NCFC approach and uncertainties of extrapolations; the $N_{\max}$ columns show the largest NCSM basis space used for the extrapolations.

		JISP16			JISP16$_{2010}$		
Nucleus	Experim.	Extrap. A	Extrap. B	$N_{\max}$	Extrap. A	Extrap. B	$N_{\max}$
^{3}H	8.482	8.369 ± 0.001	8.3695 ± 0.0025	18	8.369 ± 0.010	$8.367^{+0.012}_{-0.007}$	14
^{3}He	7.718	7.665 ± 0.001	7.668 ± 0.005	18	7.664 ± 0.011	7.663 ± 0.008	14
^{4}He	28.296	28.299 ± 0.001	28.299 ± 0.001	18	28.294 ± 0.002	$28.294^{+0.002}_{-0.001}$	14
^{8}He	31.408	29.69 ± 0.69	29.29 ± 0.96	10	30.30 ± 0.46	$29.99^{+1.31}_{-1.06}$	10
^{6}Li	31.995	31.47 ± 0.09	31.48 ± 0.03	16	31.33 ± 0.16	31.34 ± 0.07	14
^{10}B	64.751	63.1 ± 1.2	63.7 ± 1.1	8	62.6 ± 1.4	63.4 ± 1.5	8
^{12}C	92.162	93.9 ± 1.1	95.1 ± 2.7	8	91.1 ± 1.3	92.3 ± 2.9	8
^{14}C	105.284	112.1 ± 2.1	114.3 ± 6.0	8	102.5 ± 1.6	104.8 ± 3.6	8
^{14}N	104.659	114.2 ± 1.9	115.8 ± 5.5	8	102.7 ± 1.5	104.7 ± 3.1	8
^{16}O	127.619	143.5 ± 1.0	150 ± 14	8	126.7 ± 3.1	129.6 ± 6.1	8

We plan to explore the properties of the refined realistic nonlocal *NN* interaction JISP16_{2010} in systematic large-scale calculations of other light nuclei including the ones with $A > 16$ and away from $N \sim Z$, and to carefully study its predictions not only for the binding energies but also for the spectra, electromagnetic transitions and other observables. Our plan is also to tune the interaction to the description of phenomenological nuclear matter properties.

An additional possibility for further improvement of the JISP-type *NN* interaction provides DET-PET, a new type of phase-equivalent transformations suggested recently [46,47]. Contrary to conventional PETs resulting in modification of bound-state and scattering wave functions, DET-PET guarantees that the transformed interaction generates not only the same scattering phase shifts and two-body binding energy (or, more generally, bound state energies) but also the same bound state (deuteron) wave function as the initial untransformed interaction. Clearly, DET-PET has the advantage of preserving the deuteron ground-state observables. The DET-PET theory can be easily reformulated to preserve scattering wave functions at a given energy instead of the bound state wave function. On the other hand, DET-PET, as well as any PET, modifies a two-body interaction off-shell, and hence manifests itself in many-body systems. It would be interesting to utilize DET-PET preserving *NN* correlations of the initial realistic *NN* interaction in modifications of this interaction aimed to fit the description of light nuclei.

This work was supported in part by the Ministry of Education and Science of the Russian Federation through the contract 14.V37.21.1297, by the Russian Foundation of Basic Research and by US DOE Grants DE-FC02-09ER41582 and DE-FG02-87ER40371. Computational resources were provided by DOE (supercomputer HOPPER) through the National Energy Research Scientific Computing Center (NERSC) and by Moscow State University (supercomputer Lomonosov).

[1] P. Navrátil, J. P. Vary, B. R. Barrett. Phys. Rev. Lett. 84 (2000) 5728; Phys. Rev. C62 (2000) 054311.

[2] S. Pieper, R. B. Wiringa. Annu. Rev. Nucl. Part. Sci. 51 (2001) 53.

[3] K. Kowalski, D. J. Dean, M. Hjorth-Jensen, T. Papenbrock, P. Piecuch. Phys. Rev. Lett. 92 (2004) 132501.

[4] P. Maris, J. P. Vary, A. M. Shirokov. Phys. Rev. C79 (2009) 014308.

[5] P. Maris, A. M. Shirokov, J. P. Vary. Phys. Rev. C81 (2010) 021301(R).

[6] V. Z. Goldberg, B. T. Roeder, G. V. Rogachev, G. G. Chubarian, E. D. Johnson, C. Fu, A. A. Alharbi, M. L. Avila, A. Banu, M. McCleskey, J. P. Mitchell, E. Simmons, G. Tabacaru, L. Trache, R. E. Tribble. Phys. Lett. B692 (2010) 307.

[7] R. Machleidt. Phys. Rev. C63 (2001) 024001.

[8] V. G. J. Stoks, R. A. M. Klomp, C.P.F. Terheggen, J. J. de Swart. Phys. Rev. C49. (1994) 2950.

[9] R. B. Wiringa, V. G. J. Stoks, R. Schiavilla. Phys. Rev. C51 (1995) 38.

[10] J. Carlson, V. R. Pandharipande, R. B. Wiringa. Nucl. Phys. A401 (1983) 59.

[11] B. S. Pudliner, V. R. Pandharipande, J. Carlson, S. C. Pieper, R. B. Wiringa. Phys. Rev. C56 (1997) 1720.

[12] S. C. Pieper, Pandharipande V. R., Wiringa R. B., Carlson J. // Phys. Rev. C. 2001. V. 64. 014001.

[13] S. A. Coon, M. D. Scadron, P. C. McNamee, B. R. Barrett, D. W. E. Blatt, B. H. J. McKellar. Nucl. Phys. A317 (1979) 242.

[14] J. L. Friar, D. Hüber, U. van Kolck. Phys. Rev. C59 (1999) 53.

[15] D. Hüber, J. L. Friar, A. Nogga, H. Witala, U. van Kolck. Few-Body Syst. 30 (2001) 95.

[16] P. F. Bedaque, H.-W. Hammer, U. van Kolck. Phys. Rev. Lett. 82 (1999) 463.

[17] E. Epelbaum, A. Nogga, W. Glöckle, H. Kamada, Ulf-G. Meißner, H. Witala. Phys. Rev. C66 (2002) 064001.

[18] D. R. Entem, R. Machleidt. Phys. Lett. B524 (2002) 93; Phys. Rev. C68 (2003) 041001(R).

[19] P. Navrátil, V. G. Gueorguiev, J. P. Vary, A. Nogga, W. E. Ormand. Phys. Rev. Lett. 99 (2007) 042501.

[20] P. Doleschall. Phys. Rev. C69 (2004) 054001.

[21] P. Doleschall, I. Borbély, Z. Papp, W. Plessas. Phys. Rev. C67 (2003) 064005.

[22] A. M. Shirokov, A. I. Mazur, S. A. Zaytsev, J. P. Vary, T. A. Weber. Phys. Rev. C70 (2004) 044005.

[23] A. M. Shirokov, J. P. Vary, A. I. Mazur, S. A. Zaytsev, T. A. Weber. Phys. Lett. B621 (2005) 96.

[24] A. M. Shirokov, J. P. Vary, A. I. Mazur, S. A. Zaytsev, T. A. Weber. J. Phys. G31 (2005) S1283.

[25] A. M. Shirokov, J. P. Vary, A. I. Mazur, T. A. Weber. Phys. Lett. B644 (2007) 33.

[26] W. N. Polyzou, W. Glöckle. Few-Body Syst. 9 (1990) 97.

[27] S. A. Zaytsev. Theor. Math. Phys. 115 (1998) P. 575.

[28] R. Machleidt. Private communication (2006).

[29] Yu. A. Lurie, A. M. Shirokov. Bull. Rus. Acad. Sci., Phys. Ser. 61 (1997) 1665.

[30] Yu. A. Lurie, A. M. Shirokov. Ann. Phys. (N.Y.) 312 (2004) 284.

[31] A Fortran code generating the JISP16 interaction matrix elements is available at http://nuclear.physics.iastate.edu.

[32] N. Barnea, W. Leidemann, G. Orlandini. Phys. Rev. C74 (2006) 034003.

[33] W. Leidemann. Nucl. Phys. A790 (2007) 24.

[34] G. Orlandini, S. Bacca, N. Barnea, W. Leidemann. Nucl. Phys. A790 (2007) 368.

[35] I. Šlaus. Nucl. Phys. A790 (2007) 199.

[36] A. M. Shirokov, J. P. Vary, A. I. Mazur, T. A. Weber. Yad. Fiz. 71 (2008) 1260 [Phys. At. Nucl. 71 (2008) 1232].

[37] A. M. Shirokov, J. P. Vary, P. Maris. In *Proc. 27th Int. Workshop Nuclear Theory, Rila Mountains, Bulgaria, 23–28 June, 2008* (Ed. S. Dimitrova). Bulgarian Academy of Science, Sofia, 2008, p. 205; arXiv:0810.1014 [nucl-th] (2008).

[38] J. P. Vary, P. Maris, A. Shirokov. Int. J. Mod. Phys. E17, Suppl. 1 (2008) 109.

[39] S. Vaintraub, N. Barnea, D. Gazit. Phys. Rev. C79 (2009) 065501.

[40] A. M. Shirokov, V. A. Kulikov, P. Maris, A. I. Mazur, E. A. Mazur, J. P. Vary. EPJ Web of Conf. 3 (2010) 05015.

[41] A. M. Shirokov, V. A. Kulikov, P. Maris, A. I. Mazur, E. A. Mazur, J. P. Vary. In *Proc. 3rd Int. Conf. Current Problems in Nucl. Phys. and At. Energy (NPAE-Kyiv2010), June 7–12, 2010, Kyiv, Ukraine.* Kyiv, 2011, Part I, p. 321; arXiv:1009.2993 [nucl-th] (2010).

[42] N. Barnea, W. Leidemann, G. Orlandini. Phys. Rev. C81 (2010) 064001.

[43] G. Orlandini, N. Barnea, W. Leidemann. J. Phys. Conf. Ser. 312 (2011) 092049.

[44] A. M. Shirokov, J. P. Vary, V. A. Kulikov, P. Maris, A. I. Mazur, E. A. Mazur. Izv. Ross. Akad. Nauk, Ser. Fiz. 75 (2011) 499 [Bul. Rus. Acad. Sci.: Phys. 75 (2011) 463].

[45] F. Ajzenberg-Selove. Nucl. Phys. A523 (1991) 1.

[46] A. M. Shirokov, V. A. Kulikov, A. I. Mazur, J. P. Vary, P. Maris. Phys. Rev. C85 (2012) 034004.

[47] A. M. Shirokov, V. A. Kulikov, A. I. Mazur, J. P. Vary, P. Maris. Izv. Ross. Akad. Nauk, Ser. Fiz. 76 (2012) 554 [Bul. Rus. Acad. Sci.: Phys. 76 (2012) 496].

TWO-PHOTON EXCHANGE CONTRIBUTION IN ELASTIC ELECTRON-PROTON SCATTERING : MEASUREMENTS AT VEPP-3

I.A.Rachek,[1] *J. Arrington,*[2] *L.M. Barkov,*[1] *V.F. Dmitriev,*[1,3] *V.V. Gauzshtein,*[4]
R.A. Golovin,[1,3] *A.V. Gramolin,*[1] *R.J. Holt,*[2] *V.V. Kaminsky,*[1,5]
B.A. Lazarenko,[1] *S.I. Mishnev,*[1] *N.Yu. Muchnoi,*[1] *V.V. Neufeld,*[1]
D.M. Nikolenko,[1] *R.Sh. Sadykov,*[1] *Yu.V. Shestakov,*[1] *V.N. Stibunov,*[4]
D.K. Toporkov,[1,3] *H.de Vries,*[6] *S.A. Zevakov*[1] *and V.N. Zhilich*[1]

[1]Budker Institute of Nuclear Physics, 630090 Novosibirsk, Russia
[2]Argonne National Laboratory, Argonne, IL 60439, USA
[3]Novosibirsk State University, 630090 Novosibirsk, Russia
[4]Nuclear Physics Institute at Tomsk Polytechnical University, 634050 Tomsk, Russia
[5]Novosibirsk State Technical University, 630092 Novosibirsk, Russia
[6]NIKHEF, P.O.Box 41882, 1009 DB Amsterdam, The Netherland

I. INTRODUCTION

The electro-magnetic form factors are essential ingredients of our knowledge of the nucleon structure and this justifies the big efforts devoted to their experimental determination.

In the standard one-photon exchange (Born) approximation, the proton electromagnetic current operator is parametrized in terms of two form factors:

$$\Gamma^{\mu}(q) = \gamma^{\mu} F_1(q^2) + \frac{i\sigma^{\mu\nu} q_{\nu}}{2M} F_2(q^2)$$

where F_1 - non spin-flip Dirac form factor and F_2 - spin-flip Pauli form factor.

Experimentalists prefer other two functions which are linear combinations of F_1 and F_2 - the Sachs form factors. Those are Electric form factor G_E and Magnetic form factor G_M. In non-relativistic limit these two functions of Q^2 describe the distribution of charge and magnetism of the proton. We know that at least at small transferred momentum G_E and G_M follow the dipole approximation. We hope that in the foreseeable future precise calculations in terms of quarks and gluons will become available using lattice QCD techniques.

Electromagnetic Form Factors puzzle

The experimental study of proton form factors is performed with elastic electron-proton scattering. There are two basic approaches to this task. First is the Rosenbluth or Longitudinal-Transverse separation. It is based on the Rosenbluth formula [1] for the differential cross section:

$$\frac{d\sigma}{d\Omega} = \left(\frac{d\sigma}{d\Omega}\right)_{Mott} \times \frac{\tau}{\epsilon(1+\tau)} \times \left[\ \frac{\epsilon}{\tau} G_E^2 + G_M^2\ \right] \qquad (1)$$

where $\tau = Q^2/4M^2$ and $\epsilon = \left[1 + 2(1+\tau)\tan^2(\theta/2)\right]^{-1}$ – virtual photon polarization. So in this method one measures the unpolarized (ep)-elastic cross section at constant Q^2, varying beam energy and scattering angle.

In the second method polarized beams and targets or recoil polarimeters are used. In 1968 Akhieser and Recalo [2] have first shown that in elastic scattering of polarized electron

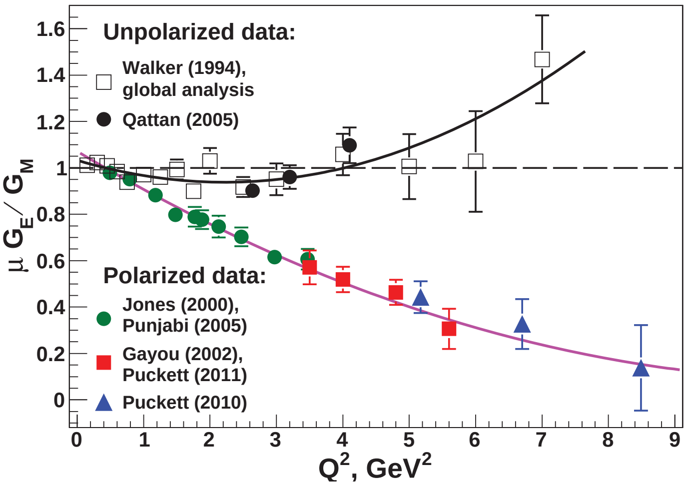

FIG. 1: The observed inconsistency between two approaches to the measurement of the proton form factor ratio.

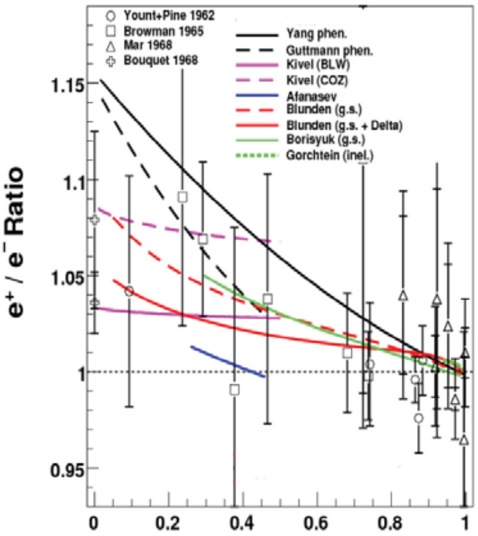

FIG. 2: Data and some theoretical calculations for the ratio of positron-proton to electron-proton elastic scattering cross-section – circa 2007

on proton the ratio of form factors can be directly related to the ratio of components of the recoil polarization:

$$\frac{G_E}{G_M} = \frac{P_T}{P_L} \times K,$$

where P_T and P_L are transverse and longitudinal polarization components of proton, $K = -\sqrt{\tau(1+\epsilon)/2\epsilon}$ – is a kinematic factor.

The Rosenbluth technique was used starting from 1950th with gradual increase of momentum transfer range. The double-polarization approach becomes feasible only about 15 years ago with experiments at MIT Bates and a series of measurements at TJNAF. And unexpectedly a clear discrepancy between results of two methods was observed, see Fig. 1. It is seen that the deviation between the two methods starts around 2 GeV^2 and increases with Q^2. This discrepancy is a serious problem as it generates confusion and doubt about the whole methodology of lepton scattering experiments.

It was suggested that it is radiative corrections, in particular, a short-range Two-Photon Exchange (TPE) is a likely origin of the discrepancy. But this is not connected with the standard radiative corrections, which deal with soft photons (both real and virtual). The effect of standard radiative corrections is well under control. Their dominant (infra-red) part can be factorized in the observables and is believed to be accounted for precisely enough.

$$\begin{aligned}\sigma(e^{\pm}p) = {} & |\mathcal{M}_{\text{Born}}|^2 \pm 2\,\mathcal{R}\text{e}\left(\mathcal{M}^{\dagger}_{\text{Born}}\mathcal{M}_{2\gamma}\right) + \\ & + 2\,\mathcal{R}\text{e}\left(\mathcal{M}^{\dagger}_{\text{Born}}\mathcal{M}_{\text{vac}}\right) + 2\,\mathcal{R}\text{e}\left(\mathcal{M}^{\dagger}_{\text{Born}}\mathcal{M}^{e}_{\text{vert}}\right) + 2\,\mathcal{R}\text{e}\left(\mathcal{M}^{\dagger}_{\text{Born}}\mathcal{M}^{p}_{\text{vert}}\right) + \ldots \\ & + |\mathcal{M}^{e}_{\text{brem}}|^2 + |\mathcal{M}^{p}_{\text{brem}}|^2 \pm 2\,\mathcal{R}\text{e}\left(\mathcal{M}^{e\dagger}_{\text{brem}}\mathcal{M}^{p}_{\text{brem}}\right) + \ldots\end{aligned} \tag{2}$$

But one has to consider the exchange of hard photons between the lepton and the hadron. However the evaluation of the box and cross-box diagrams is difficult because an integral over all off-shell proton intermediate state contributions must be made. It is not known how

TABLE I: Feynman diagrams for standard radiative corrections.

“Elastic” scattering ($e^{\pm}p \to e^{\pm}p$):

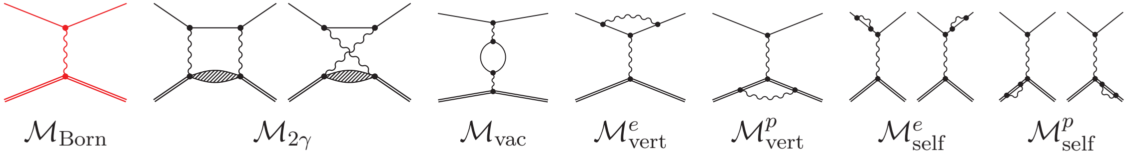

Bremsstrahlung ($e^{\pm}p \to e^{\pm}p\,\gamma$):

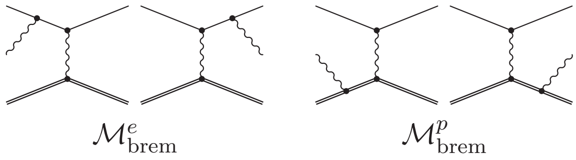

to perform this calculation in a model independent way. Various models and approximations are used, that means experimental verification is mandatory. One can readily see how such measurements can be done. The leading TPE effect comes from the interference of the one- and two-photon exchange amplitudes. And in contrast to the Born term this term is *charge-odd*, and therefore it can be singled out by measuring the ratio **R** of *positron*-proton and *electron*-proton cross-sections for the identical kinematics:

$$R \equiv \frac{\sigma(e^{+}p)}{\sigma(e^{-}p)} \approx 1 + 4\frac{\mathcal{R}\text{e}\left(\mathcal{M}^{\dagger}_{\text{Born}}\mathcal{M}_{2\gamma}\right)}{|\mathcal{M}_{\text{Born}}|^{2}},$$

Figure 2 demonstrates a status of this observable circa 2007: experimental data - from 1960th; many theoretical/phenomenological approaches exist, they predict different results not constrained by data. Clearly new precise data, especially for small ϵ are required to verify the models. That is why we at Novosibirsk have joined this activity.

II. EXPERIMENT AT VEPP–3

A. Milestones of the Novosibirsk TPE experiment

The proposal for VEPP-3 utilizing available positron/electron beams and internal gas target facility was published in 2004 [3]. The idea was suggested by John Arrington from ANL. So after that we basically were waiting for beam time at VEPP-3. We had an engineering run in 2007. In 2009 there was the first 4-month production run at a 1.6 GeV beams energy. The second longest run at a 1 GeV beams energy between September 2011 and March 2012, followed by a short third run at 600 MeV beams energy. Some preliminary results of the first run were reported at several Conferences and published in their proceedings. We don’t plan any more data taking. Now the analysis is underway and we are going to publish the final results shortly.

B. Kinematics

Kinematic settings of the three Runs are shown in the Table II. Run-I has three angular ranges, Run-II and Run-III have 2 angular ranges. but in all three setting the smallest angular range was used for luminosity monitoring only. That is because it is generally believed that for small Q^2 and for $\epsilon \approx 1$ the TPE is negligible and ratio is very close to one.

TABLE II: Kinematic settings of three Runs of the Novosibirsk TPE experiment

Parameter	Run I			Run II		Run III	
	LA	MA	SA	LA	MA	LA	MA
E_{beam}, GeV	1.6			1.0		0.6	
$\theta_{e\pm}$	55°÷75°	15°÷25°	8°÷15°	65°÷105°	15°÷25°	75°÷110°	25°÷35°
Q^2, GeV^2	1.26÷ ÷1.68	0.16÷ ÷0.41	0.05÷ ÷0.16	0.71÷ ÷1.08	0.07÷ ÷0.17	0.36÷ ÷0.52	0.06÷ ÷0.12
ε	0.37÷ ÷0.58	0.90÷ ÷0.97	0.97÷ ÷0.99	0.18÷ ÷0.51	0.91÷ ÷0.97	0.18÷ ÷0.44	0.83÷ ÷0.91
$\int I_{\text{beam}}dt$, kC	54			100		3	
$\Delta R/R$, stat.	1.1%	0.1%	—	0.3%	—	0.8%	—

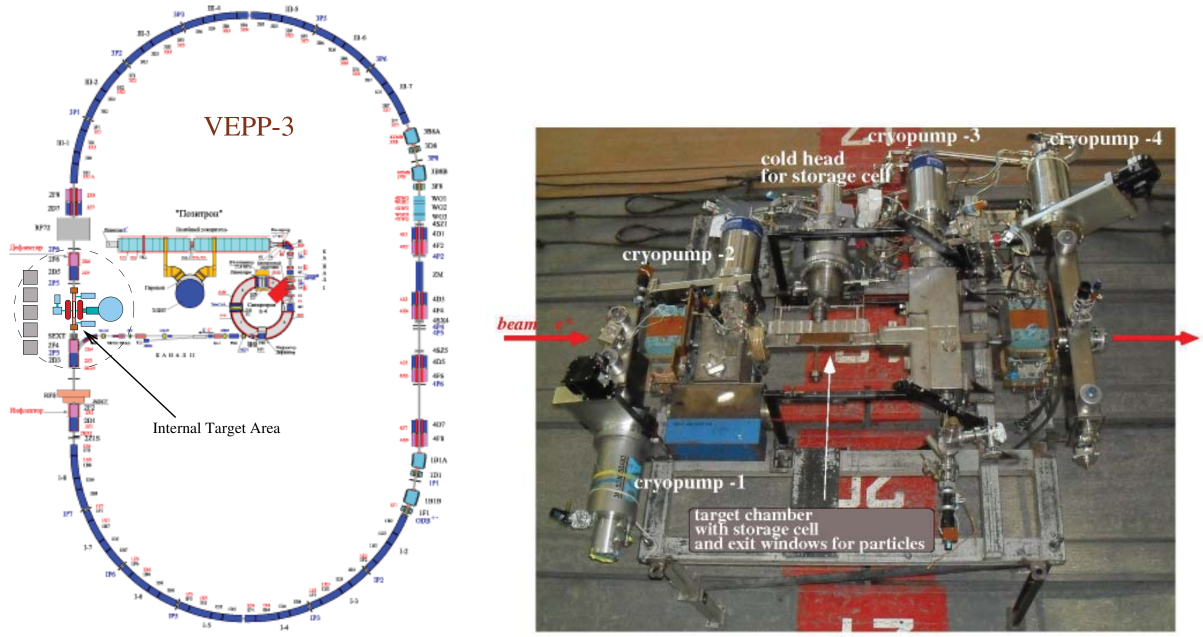

FIG. 3: Left – a scheme of the VEPP-3 storage ring. Right – view at the VEPP-3 Internal Target section.

C. Instrumentation

1. *VEPP-3*

VEPP-3 is the electron/positron storage ring with maximal beam energy 2 GeV. Largest available positron beam current is about 60 mA. The Internal Target Area is located inside one of the straight section of the ring occupying slightly more than 2 meter long segment, see Fig. 3.

2. *Internal hydrogen target*

The Internal Target Section, ready to be moved and installed at VEPP-3, is shown in Fig. 3. The central part contains a storage cell and windows for outgoing particles. The 40cm long open-ended storage cell is cooled down by a cold head. Four powerful cryopumps serve

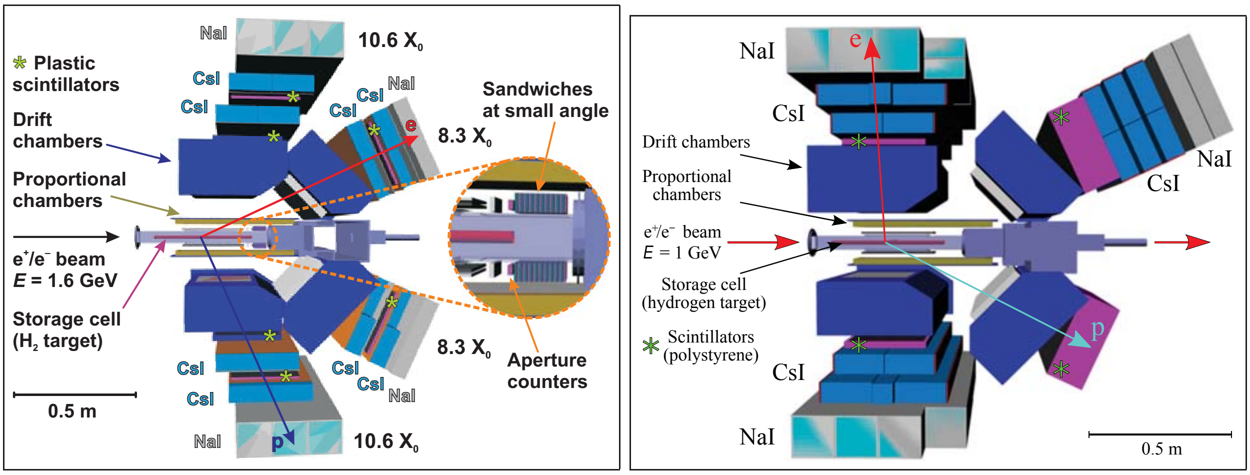

FIG. 4: Schematic view of the detector package. Left – for the Run-I, right – for the Run-II and Run-III.

to remove the hydrogen gas leaking from the storage cell to the VEPP-3 vacuum chamber. We worked at the target thickness of about $(1-2)\times 10^{15}$ atoms/cm^2.

3. *Particle Detector*

The detector package for the first run contained 3 pairs of arms providing 3 ranges of scattering angle, Fig. 4. Each of four main arms consists of wire chambers for tracking, plastic scintillators for triggering and TOF and multilayer segmented electro-magnetic calorimeter comprised of CsI and NaI crystals. So our detector is a wide-aperture non-magnetic apparatus. Moreover, we also removed a magnetic field from the target area to ensure the identical detector acceptance for electrons and positrons. (Such a magnetic field was usually applied to deflect low-energy electrons knocked-out from hydrogen, which, otherwise, hit the wire chambers and produce the background.) Instead, a carefully chosen material has been placed in front of wire chambers to suppress such a background.

Similar detector package was used in the Runs II and III, see Fig. 4, just the small-angle electron arms were removed, while the large-angle arms were moved at more backward angles.

D. Data Analysis

1. *Selection of the elastic scattering events*

The data analysis of the elastic scattering data is relatively simple. To select signal events we used:

- correlations characteristic for two-body final state:
  – correlation between polar angles ($\theta_{e^\pm}$ vs. θ_p);
  – correlation between azimuthal angles ($\phi_{e^\pm}$ vs. ϕ_p);
  – correlation between lepton scattering angle and proton energy ($\theta_{e^\pm}$ vs. E_p);
  – correlation between lepton scattering angle and electron energy ($\theta_{e^\pm}$ vs. $E_{e^\pm}$);

- particle ID:
  – *Time-Of-Flight analysis* for low-energy protons;

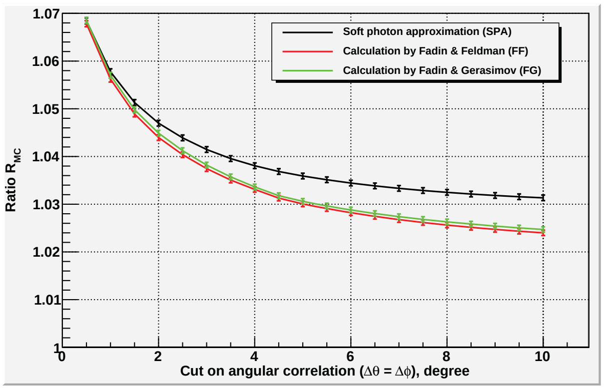

FIG. 5: Comparison of the approaches to the calculations of standard radiative corrections, see text for details.

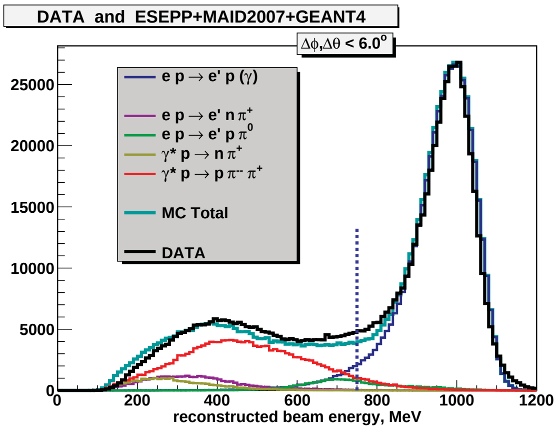

FIG. 6: Beam energy, reconstructed using measured energy and flight direction of a particle assumed to be an electron.

– ΔE–E *analysis* for middle-energy protons;
– cut on *Energy deposition* in EM-calorimeter for electrons/positrons

2. Simulation of the standard radiative corrections

A precise account for standard radiative corrections is a crucial task for the analysis. Let us remind that several terms in standard radiative corrections (Eq. 2) are also charge-dependent and will contribute to the ratio of cross sections. And the size of this contribution is comparable with the effect under study. For a wide-acceptance non-magnetic detector that we use the standard prescriptions with soft-photon peaking approximation could not be applied. A detailed Monte-Carlo simulation with a dedicated event generator is mandatory. Such a job was carried out by our Ph.D. student A.Gramolin. With a help of our theorists, Professor V.S.Fadin and his students, he developed an event generator ESEPP [4]. In ESEPP the evaluation of bremsstrahlung process, provided by Fadin&Feldman, is done without simplifications used in the soft-photon approach. Besides, Fadin&Gerasimov evaluated the diagram describing the bremsstrahlung with Δ-isobar excitation.

The Figure 5 demonstrates a comparison between the approaches. Shown is a ratio of positron-proton to electron-proton elastic cross sections versus the value of angular correlation cut. One can see that the soft-photon calculation differs considerably from the more sophisticated ones while further accounting for Δ-isobar in bremsstrahlung gives a negligible deviation.

3. Simulation of background processes

An extensive Monte Carlo simulation of background processes was carried out to define how many inelastic events remain in the final data set after all cuts applied. The main background obviously consists of events from pion-production reactions. We develop a generator for such events based on MAID2007 and 2-PION-MAID models [5]. Above mentioned ESEPP generator was used to generate bremsstrahlung events. Figure 6 demonstrates the results of the simulation. In this figure it is shown a spectrum of beam energy, reconstructed from measured energy and direction of a particle detected in the Large-Angle arm, assuming this is an elastic scattered electron. For pure elastic events and for ideal detector we would get a narrow peak at 1 GeV, that is the actual beam energy. In reality we have wider peak due to finite calorimeter energy resolution and a tail due to inelastic processes. For illustration this picture is obtained applying loose angular cuts, so the inelastic tail is quite large. One can see that data and Monte Carlo Total are consistent. It is clear that optimal cut for this parameter is around 750 MeV. So we found that when all proper cuts applied the background contribution does not exceed 1%.

E. Suppression of systematic errors

For such an experiment, where an asymmetry of order of few per cent is measured a careful control and suppression of systematics is very important.

a. Slow drift of parameters. In our measurements the data collection with electron and positron beams was altered regularly. This allows us to suppress effects related to slow drift in time of target thickness, detection efficiency and so on. We had one cycle of positron and electron beams per approximately 1 hour. There were several thousand such cycles in the whole data taking run. The systematic error from slow drift of experimental parameters is estimated to not exceed 0.2%.

b. Beams position. Variation of beam position on the target for electrons and positrons could be a source of false asymmetry. We used the VEPP-3 beam orbit stabilization system and measured the beam position in the target area by several methods to use it for corrections during the data analysis. Uncertainty in the cross section ratio from this source is estimated to be below 0.2%.

c. Beams energy. Another possible source of false asymmetry is unequal energy of electron and positron beams. Switching from electrons to positrons requires swapping polarities of multiple magnets and of corresponding power supplies of VEPP-3 ring. Fortunately at Budker Institute we have well developed methods of precise measurement of beam energy in storage rings. Especially effective is a method based on reconstruction of beam energy from the energy of laser photons back-scattered on beam particles [1]. Such a setup was successfully assembled and commissioned at VEPP-3 for our experiment. And this allow us to tune the VEPP-3 operation regimes and to monitor beams energy during the experiments to ensure that the contribution to systematic error from this source is below 0.1%.

Total systematic uncertainty should not exceed **0.3%**.

III. COMPARISON WITH OTHER CURRENT EXPERIMENTS

Currently there are two more experiments aimed at precise measurement of the ratio R. The first one is carried out by the CLAS collaboration at TJNAF [6], the second one is performed by the OLYMPUS collaboration at DESY [7]. Figure 7 shows the kinematic coverage of three experiments, plotted versus two variables : ϵ and Q^2. If the beam energy is fixed than it results in a smooth curve on this plot. One can see 3 curves for the VEPP-3 Runs and a curve for the OLYMPUS measurement at 2 GeV beams energy. Lowest-Q^2 and largest-ϵ regions are for luminosity monitoring. The CLAS TPE experiment has a wide spectrum of energy of electrons/positrons, therefore this experiment covers not a line, but an area on this plot.

---

[1] Guram Kezerashvili is a founder of this very fruitful method at Budker Institute

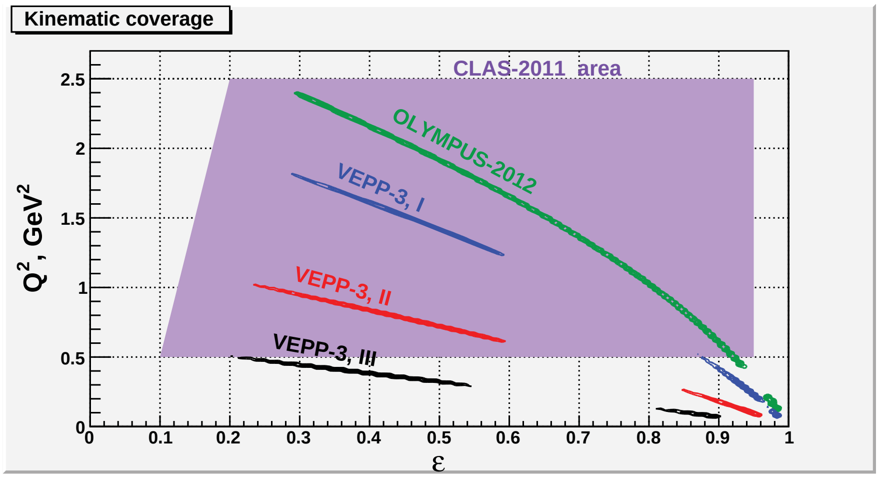

FIG. 7: Comparison of the kinematics of three TPE experiments.

TABLE III: Comparison of main features of the three TPE experiments. The items that may be considered as an advantage of the setup are shown in boldface font.

	VEPP-3 Novosibirsk	OLYMPUS DESY	EG5 CLAS JLab
Beam energy	3 fixed	1(+1?) fixed	*wide spectrum*
equality of $e^{\pm}$ beam energy	**measured precisely**	assumed (*measured?*)	reconstructed
e^{+}/e^{-} swapping frequency	half-hour	8 hours	**simultaneously**
e^{+}/e^{-} lumi monitor	**elastic low-Q^2**	**elastic low-Q^2, Möller/Bhabha**	from simulation
energy of scattered $e^{\pm}$	EM-calorimeter	**mag. analysis**	**mag. analysis**
proton PID	$\Delta E/E$, TOF	**mag. analysis, TOF**	**mag. analysis, TOF**
e^{+}/e^{-} detector acceptance	**identical**	big difference	big difference
luminosity	1.0×10^{32}	$\mathbf{2.0 \times 10^{33}}$	2.5×10^{32}
systematic error	$<$ **0.3%**	1%	1%

CLAS TPE experiment. For the TPE experiment at Hall B, TJNAF the existing secondary photon source was complemented by a pair production convertor and a magnetic system to guide the lepton beams to the liquid hydrogen target, while dumping the remaining photons. CLAS detector is used to detect elastic events. Data taking is completed in February 2011. The analysis is in progress, no any preliminary results are presented so far.

OLYMPUS TPE experiment. The OLYMPUS collaboration has arranged an internal target setup at DORIS storage ring in DESY, Hamburg. Elements of BLAST detector from MIT Bates as well as some newly developed sub-detectors are used. The first one-month-long run at beams energy of 2 GeV was done in February this year. Another 2 months or running is expected in October-December.

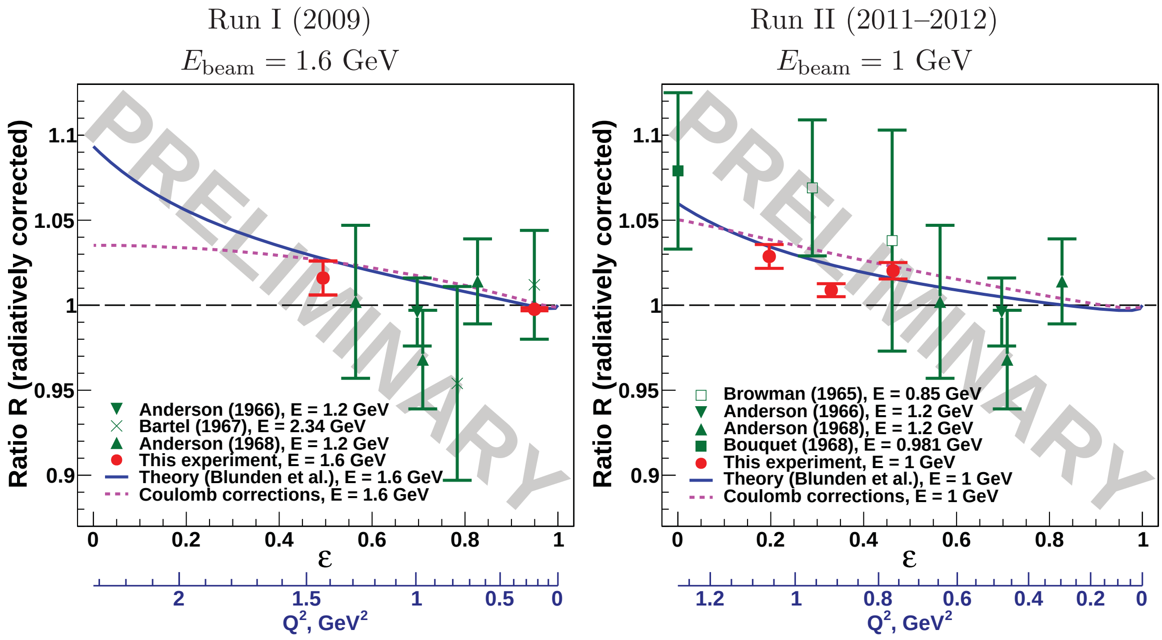

FIG. 8: Preliminary results of the VEPP–3 TPE experiment (full circles). Left panel: Run-I at 1.6 GeV beams energy. Right panel: Run-II at 1.0 GeV beams energy. Old data obtained with beams of close energy are also shown. Theoretical curves: Coulomb corrections [8] (dash), hadronic TPE calculations [9] (solid).

Table III compares main features of the three experiments. Summing up, one should note that:

- Novosibirsk experiment is inferior to the other two in experimental luminosity and in quality of particle ID;
- However, the detector performance is quite sufficient for reliable identification of elastic scattering events.
- At the same time our non-magnetic detector, measurement of beams energy, frequent swapping of electron/positron beams allow *lowest systematic error*.
- The three experiments are complementary, but VEPP-3 experiment is the very first to provide results on precise measurement of the positron-proton to electron-proton elastic scattering cross-section ratio.

IV. PRELIMINARY RESULTS

The preliminary results for Run-I and Run-II of the Novosibirsk TPE experiment are shown in Figure 8. Only statistical errors are included. The standard radiative corrections are taken into account. Some corrections are not yet applied, so these results are still preliminary. Two theoretical predictions are shown: calculation of Coulomb correction by Arrington and Sick [8], and the hadronic TPE calculation by Blunden, Melnitchouk and Tjon [9].

Looks like our data are consistent with calculation [9], however have a tendency to be slightly overestimated by the theory.

Note that in [10] it is shown that if the TPE correction calculated in [9] is applied for the analysis of the electron-proton elastic scattering data, than the discrepancy between unpolarized and polarized measurements of G_E^p/G_M^p form factors ratio is resolved.

V. CONCLUSION

- The first precision measurement of the ratio $R = \sigma(e^+p)/\sigma(e^-p)$ has been performed. Data taking has been completed, analysis is in progress.
- Systematic errors in the VEPP-3 experiment is expected to be lower than those at OLYMPUS and CLAS TPE experiments.
- It is very important to carefully consider the standard radiative corrections. Procedure of account for RC has been developed (ESEPP event generator + Geant4 detector simulation).
- Preliminary results are presented. They are consistent with the theoretical predictions by Blunden *et al* [9], which, apparently, resolve the inconsistensy of two approaches to the measurement of proton form factors.
- Final results of the experiment are expected in 2013.

This work was supported by Ministry of Education and Science of the Russian Federation; by RFBR, grants: 08-02-00624-a, 08-02-01155-a; by Russian Federal Agency for Education, State Contract P522; by Russian Federal Agency for Science and Innovation, Contract 02.740.11.0245.1; by US DOE, grant DE-AC02-06CH11357; by US NSF, grant PHY-03-54871.

[1] M.N. Rosenbluth, Phys. Rev. **79** (1950) 615.
[2] A.I. Akhiezer and M.P. Rekalo, Sov. J. Part. Nucl. **4** (1974) 277.
[3] J. Arrington *et al.*, arXiv:nucl-ex/0408020.
[4] `http://www.inp.nsk.su/~gramolin/esepp.html`
[5] `http://wwwkph.kph.uni-mainz.de/MAID/`
[6] `http://www.jlab.org/exp_prog/CEBAF_EXP/E04116.html`
[7] `http://web.mit.edu/OLYMPUS/`
[8] J. Arrington and I. Sick, Phys. Rev. **C70** (2004) 028203.
[9] P.G. Blunden, W. Melnitchouk and J.A. Tjon, Phys. Rev. **C72** (2005) 034612.
[10] J. Arrington, P.G. Blunden and W. Melnitchouk, Prog. Part. Nucl. Phys. **66** (2011) 782.

SEARCH FOR NARROW SIX-QUARK STATES IN THE REACTIONS $\gamma d \to \pi\gamma NN$

L.V. Fil'kov[1], *V.L.Kashevarov*[1,2], *M.Ostrick*[2]

[1]Lebedev Physical Institute, Moscow, Russia
[2]Institut für Kernphysik, University of Mainz, Germany

Abstract

We study the reactions $\gamma d \to \pi\gamma NN$ with the aim to search for six-quark states, the decay of which into two nucleons is forbidden by the Pauli exclusion principle. These states with the masses $M < 2m_N + m_\pi$ should mainly decay by emitting a photon. This is a new class of metastable six-quark states with the decay widths << 1keV. The recent experiment at Proton Linear Accelerator of INR (Moscow) suggests a possibility of the existence of such states with masses 1904, 1926, and 1942 MeV. The proposed experiment at MAMI-C could provide an unique opportunity to observe such dibaryon states in mass region up to 2000 MeV and determine their masses and quantum numbers.

1 Introduction

The possibility of the existence of multiquark states was predicted by QCD inspired models [1, 2]. These works initiated a lot of experimental searches for six-quark states (dibaryons). Usually authors of these works looked for dibaryons in the NN channel (see for review ref. [3]). Such dibaryons have decay widths from a few up to hundred MeV. Their relative contributions are small enough and the background contribution is big and uncertain as a rule. It often leads to contradictory results.

We consider six-quark states, a decay of which into two nucleons is forbidden by the Pauli exclusion principle. Such states satisfy the following condition:

$$(-1)^{T+S}P = +1 \tag{1}$$

where T is the isospin, S is the spin of the nucleon pair inside a six-quark state, and P is the dibaryon parity. In the NN channel, these six-quark states would correspond to the following forbidden states: even singlets and odd triplets with the isotopic spin $T = 0$ as well as odd singlets and even triplets with $T = 1$. Such six-quark states with the masses $M < 2m_N + m_\pi$ ($m_N(m_\pi)$ is the nucleon (pion) mass) could mainly decay by emission of a photon. This is a new class of metastable six-quark states with the decay widths << 1keV [4, 5]. Such states were called "supernarrow dibaryons" (SND).

The experimental discovery of the SNDs would have important consequences for particle and nuclear physics and astrophysics. This would lead to a deeper understanding of the evolution of compact stars and the new possibility of quark-gluon plasma production in their interior. In nuclear physics there would be a new concept: SND-nuclei.

In the framework of the MIT bag model, Mulders et al. [2] calculated the masses of different dibaryons, in particular, NN-decoupled dibaryons. They predicted dibaryons $D(T = 0; J^P = 0^-, 1^-, 2^-; M = 2.11\text{ GeV})$ and $D(1; 1^-; 2.2\text{ GeV})$ corresponding to the forbidden states $^{13}P_J$ and $^{31}P_1$ in the NN channel. However, the dibaryon masses obtained by them exceed the pion production threshold. Therefore, these dibaryons preferentially decay into the πNN channel and their decay widths are larger than 1 MeV.

Using the chiral soliton model, Kopeliovich [6] predicted that the masses of $D(1, 1^+)$ and $D(0, 2^+)$ SNDs could exceeded the two nucleon mass by 60 and 90 MeV, respectively. These values are lower than the pion production threshold.

In the framework of the canonically quantized biskyrmion model, Krupnovnickas *et al.* [7] obtained an indication on possibility of the existence of one dibaryon with J=T=0 and two dibaryons with J=T=1 with masses smaller than $2m_N + m_\pi$.

Unfortunately, all predicted values of the dibaryon masses are strongly model dependent. Therefore, only an experiment could answer the question about the existence of SNDs and determine their masses.

For the first time, SNDs have been observed in the reactions $pd \to p{+}pX_1$ and $pd \to p{+}dX_2$ [8–11]. The experiment was carried out at the Proton Linear Accelerator of INR with 305 MeV proton beam using the two-arm mass spectrometer TAMS.

Several software cuts have been applied to the mass spectra in these works. In particular, the authors limited themselves by the consideration of an interval of the proton energy from the decay of the pX_1 states and its narrow angle cone of the with respect to the direction of the dibaryon motion, which were determined by the kinematics of the SND decay into γNN channel. Such cuts are very important as they provide a possibility to suppress the contribution from the background reactions and random coincidences essentially.

As a result, three narrow peaks in missing mass spectra were observed (Fig. 1a) at $M_{pX_1} =$ 1904±2, 1926±2, and 1942±2 MeV with widths equal to the experimental resolution (~ 5 MeV) and with numbers of standard deviations (SD) of 6.0, 7.0, and 6.3, respectively. It should be noted that the dibaryon peaks at $M = 1904$ and 1926 MeV had been observed earlier by same authors in ref. [8–10] under different kinematical conditions. On the other hand, no noticeable signal of the dibaryons were observed in the missing mass M_{dX_2} spectra of the reaction $pd \to p{+}dX_2$. The analysis of the angular distributions of the protons from the decay of pX_1 states and the suppression observed of the SND decay into γd showed that the peaks found can be explained as a manifestation of isovector SNDs, the decay of which into two nucleons is forbidden by the Pauli exclusion principle.

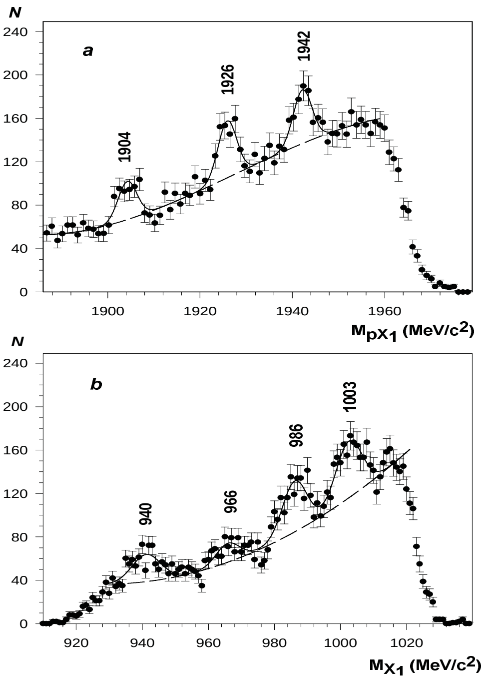

Figure 1: The missing mass M_{pX_1} (a) and M_{X_1} (b) spectra of the reaction $pd \to p + pX_1$ The dashed and solid curves are results of interpolation by polynomials (for the background) and Gaussian (for the peaks), respectively.

Additional information about the nature of the observed states was obtained by studying the missing mass M_{X_1} spectrum of the reaction $pd \to p + pX_1$. If the state found is a dibaryon decaying mainly into two nucleons then X_1 is the neutron and the mass M_{X_1} is equal to the neutron mass m_n. If the value of M_{X_1}, obtained from the experiment, differs essentially from m_n, then $X_1 = \gamma + n$ and we have the additional indication that the observed dibaryon is SND.

In the experimental missing mass M_{X_1} spectrum besides the peak at the neutron mass caused by the process $pd \to p{+}pn$, a resonance-like behavior of the spectrum were observed at 966 ± 2, 986 ± 2, and 1003 ± 2 MeV [11]. These values of M_{X_1} coincide with the ones obtained by the simulation. Hence, for all states under study, we have $X_1 = \gamma + n$ in support of the statement that the dibaryons found are SNDs.

On the other hand, the peak at $M_{X_1} = 1003 \pm 2$ MeV corresponds to the peak found in ref. [12] and was attributed to an exotic baryon state N^* below the πN threshold. In that work the authors investigated the reaction $pp \to \pi^+ pX$ and found altogether three such states with masses 1004, 1044, and 1094 MeV. Therefore, if the exotic baryons with anomalously small masses really exist, the observed peaks at 966, 986, and 1003 MeV might be a manifestation of such states. The existence of such exotic states, if established, would fundamentally change our understanding of the quark structure of hadrons [13, 14]. However, the experiments on single nucleons have not observed any significant structure [15–17]. Therefore, the question about a nature of peaks observed in [11, 12] is open still.

In ref. [18] dibaryons with exotic quantum numbers were searched for in the process $pp \to pp\gamma\gamma$. The experiment was performed with a proton beam from the JINR Phasotron at an energy of about 216 MeV. The energy spectrum of the photons emitted at 90° was measured. As a result, two peaks were observed in this spectrum. This behavior of the photon energy spectrum was interpreted as a signature of the exotic dibaryon resonance d_1 with a mass of about 1956 MeV and possible isospin $T = 2$.

On the other hand, an analysis [19] of the Uppsala proton-proton bremsstrahlung data looking for the presence of a dibaryon in the mass range from 1900 to 1960 MeV only gave upper limits of 10 and 3 nb for the dibaryon production cross section at proton beam energies of 200 and 310 MeV, respectively. This result agrees with the estimates of the cross section obtained at the conditions of this experiment in the framework of the dibaryon production model suggested in ref. [10].

The reactions $pd \to ppX$ and $pd \to pdX$ were studied also in the Research Center for Nuclear Physics at the proton energy 295 MeV over a mass range of 1898 to 1953 MeV [20]. They did not observe any narrow structure and determined upper limits of the production cross sections below 1μb/sr. These results are in contradiction to the observation at INR and with the investigation of Tatischeff *et al.* [12].

In order to argue more convincingly that the states found are really SNDs, an additional experimental investigation of the dibaryon production is needed.

In ref. [21] narrow dibaryon resonances were searched for in the reaction $\gamma d \to \pi^0 X$ in the photon energy region 140–300 MeV. No significant structure was observed. Upper limits for the production of narrow dibaryons in the range 2–5 μb averaged over the 0.8 MeV resolution were established. However, the expected values of the SND photoproduction cross section are bellow 5nb. Significantly larger cross sections are expected in charged pion photoproduction.

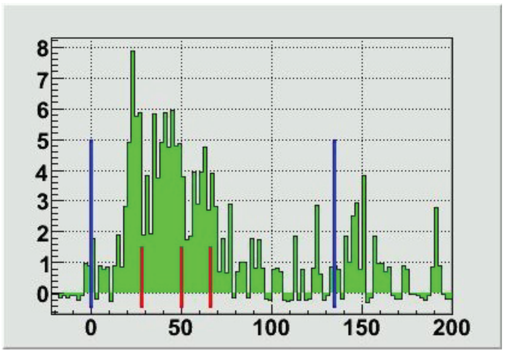

Figure 2: The missing mass ($MM(\gamma, \pi^0) - m_d$) (MeV) spectra of the reaction $\gamma d \to \pi^0 \gamma pn$

In ref. [22] a search for SNDs in the processes of pions photoproduction by the linearly polarized photon was proposed. It was shown a large variation between the differential cross sections of pions emitted in the plane parallel to the incident photon polarization and pions emitted in the plane perpendicular to the polarization.

Such an experiment was performed using LEGS facility at Brookhaven National Laboratory [23]. They analyzed the reaction $d(\vec{\gamma}, \pi^+ n\gamma')n$ in the photon energy range 210 − 340 MeV. The average linear polarization of incident photons was ≥ 80%. As a result, they observed three peaks in missing mass spectrum when the π^+ was emitted in the plane parallel to the polarization of the incident $\vec{\gamma}$. The values of the mass found are very close to the values obtained in INR [10, 11]. This result supports the SND existence. However, these data were limited by the resolution of the pion detection. So, they cannot be considered to be conclusive proof.

The preliminary analysis of the missing mass distributions of the available data on the process $\gamma d \to \pi^0 \gamma pn$, obtained at MAMI [24], demonstrates three peaks (Fig. 2), which good enough correspond to the values of the SND masses found in INR [10, 11] (red lines). Unfortunately, the statistic was very poor in this case.

We propose to search for the SNDs by studying the reactions $\gamma d \to \pi^+ \gamma nn$, $\gamma d \to \pi^- \gamma pp$, and $\gamma d \to \pi^0 \gamma pn$ in the photon energy region 250–800 MeV at MAMI-C using the tagged photon beam, the Crystal Ball/TAPS spectrometer, a multi-wire proportional chamber (MWPC), and PID. The mass of SNDs will be reconstructed by the measurement of the photon and two nucleons and will be compared with the missing mass spectrum analysis obtained by the pion detection. The use of the photon beam with the energies of 300–800 MeV and the Crystal Ball/TAPS spectrometer, MWPC, and PID will give a possibility to suppress essentially background and to investigate a wide mass spectrum and, particular, check the possibility of the existence of the SNDs at $M_{pX_1} = 1956$ [18] and 1982 MeV. The latter one was predicted in [11, 25]. This experiment can also help to understand nature of the peaks in the M_{X_1} mass spectra and clarify a possibility of existence of exotic baryons with small masses.

2 Supernarrow dibaryons

We will consider the following SNDs: $D(T = 1, J^P = 1^+, S = 1)$ and $D(1, 1^-, 0)$. It is worth noting that the state $(T = 1, J^P = 1^-)$ corresponds to the states $^{31}P_1$ and $^{33}P_1$ in the NN channel. The former is forbidden and the latter is allowed for a two-nucleon state. In our work we will study the dibaryon $D(1, 1^-, 0)$, a decay of which into two nucleons is forbidden by the Pauli principle (i.e. $^{31}P_1$ state).

In the process $\gamma d \to \pi D$, SNDs can be produced only if the nucleons in the deuteron overlap sufficiently that a 6-quark state with deuteron quantum numbers can be formed. In this case, an interaction of a photon or a meson with this state can change its quantum numbers so that a metastable state is formed. Therefore, the probability of the production of such dibaryons is proportional to the probability η of the 6-quark state existing in the deuteron.

The magnitude of η can be estimated by using the discrepancy between the theoretical and experimental values of the deuteron magnetic moment [26, 27]. This method gave $\eta \le 0.03$ [27]. In ref. [25] the magnitude of η was estimated by an analysis of the mass formula for SNDs using the experimental value of the cross section of the SND production in the process $pd \to p + pX_1$ obtained in [11, 20]. As a result, $\eta \approx 10^{-4}$ was obtained.

Since the energy of nucleons, produced in the decay of the SNDs under study with $M < 2m_N + m_\pi$, is small, it may be expected that the main contribution to a two nucleon system should come from the $^{31}S_0$ (virtual singlet) state. The results of calculations of the decay widths of the dibaryons into γNN on the basis of such assumptions at $\eta = 0.01$ are listed in Table 1.

Table 1: Decay widths of the dibaryons $D(1, 1^+, 1)$ and $D(1, 1^-, 0)$ at various dibaryon masses M. $\Gamma_t \approx \Gamma_{\gamma NN}$

M(GeV)	1.90	1.91	1.93	1.96	1.98	2.00	2.013
$\Gamma_t(1, 1^+)$ (eV)	0.51	1.57	6.7	25.6	48	81	109
$\Gamma_t(1, 1^-)$ (eV)	0.13	0.39	1.67	6.4	12	20	27

As a result of the SND decay through $^{31}S_0$ in the intermediate state, the probability distribution of such decays over the emitted photon energy ω should be characterized by a narrow peak at the photon energy close to the maximum value. Note that the interval of the photon energy from ω_m to $\omega_m - 1$ MeV contains about 75% of the contribution to the width of the decay $D(1, 1^{\pm}) \to \gamma NN$. This leads to a very small relative energy of the nucleons from the SND decay so these nucleons will be emitted into a narrow angle cone with respect to the direction of the SND momentum.

Such dibaryons could be produced in the processes under consideration if a pion is only emitted from the 6-quark state of the deuteron. Therefore the vertexes of $d \to \pi D$ can be written as

$$\Gamma_{d\to\pi D(1,1^-,0)} = \frac{g_1}{M}\sqrt{\eta}\Phi_{\mu\nu}G^{\mu\nu}, \tag{2}$$

$$\Gamma_{d\to\pi D(1,1^+,1)} = \frac{g_2}{M}\sqrt{\eta}\varepsilon_{\mu\nu\lambda\sigma}\Phi^{\mu\nu}G^{\lambda\sigma}, \tag{3}$$

where $\Phi_{\mu\nu} = r_\mu w_\nu - w_\mu r_\nu$, $G_{\mu\nu} = p_{1\mu}v_\nu - v_\mu p_{1\nu}$, w and v are 4-vectors of the dibaryon and deuteron polarization, respectively; and r and p_1 are the dibaryon and deuteron 4-momenta.

The constants $g_1^2/4\pi$, $g_2^2/4\pi$, and η are unknown. However, the products of these coupling constants and η can be estimated from the results of work [23] where the SNDs were searched for in the process $\overrightarrow{\gamma}d \to \pi^+ D \to \gamma'\pi^+ nn$.

As a result, we have

$$\eta\frac{g_1^2}{4\pi} = 1.4\times10^{-4}, \qquad \eta\frac{g_2^2}{4\pi} = 3\times10^{-4}. \tag{4}$$

The cross section of the SND photoproduction by linear polarized photons in the reaction $\overrightarrow{\gamma}d \to \pi D$ can be written as:

$$\frac{d\sigma}{d\Omega} = A + \frac{q^2}{2}\sin^2\theta_\pi\, B(1 - P\,\cos 2\alpha) \tag{5}$$

where α is the angle of the photon polarization relative to the reaction plane. The result of the calculation of the expected asymmetry $R = \frac{(\sigma(\alpha=90^o)-\sigma(\alpha=0^o))}{(\sigma(\alpha=90^o)+\sigma(\alpha=0^o))}$ for the process $\vec{\gamma}d \to \pi^+ D$ is shown in Fig. 3 as the function of the polarization degree P for SNDs $D(1,1^-)$ (for any mass), $D(1,1^+, M = 1904)$, and $D(1,1^+, M = 1926)$. The largest asymmetry is expected for $D(1,1^-)$. The asymmetry at MAMI could be about $R \approx 0.7$ for $D(1,1^-)$.

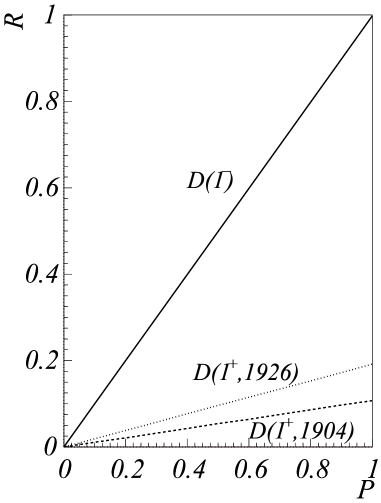

Figure 3: The asymmetry $R = (\sigma(\alpha = 90^o) - \sigma(\alpha = 0^o))/(\sigma(\alpha = 90^o) + \sigma(\alpha = 0^o))$ for the process $\vec{\gamma}d \to \pi^+ D$ as a function of the degree of photon polarization P.

3 Kinematics of SND Photoproduction

We consider SNDs with the masses M in the region 1900–2000 MeV and calculated the total and differential cross sections of the $D(1,1^-)$ and $D(1,1^+)$ production in the processes of the charged and neutral pion photoproduction from the deuteron.

The total cross sections for the $D(1,1^-)$ photoproduction in the reaction with the π^+ meson formation (Fig. 4) change from 10 nb up to 32 nb in the photon energy interval under consideration. The main contribution to the differential cross sections is given by pions emitted in the angular region $0^\circ \div 100^\circ$ with maximum at $10^\circ - 30^\circ$. The total cross sections for the $D(1,1^+)$ photoproduction in this reaction are equal to ~ 10 nb (Fig. 5).

In the case of the π^- meson photoproduction, the total cross sections for the $D(1,1^-)$ and $D(1,1^+)$ production are greater and reach for $M = 1904$ MeV 45 nb and 22 nb, respectively (Fig. 6).

The values for the total cross sections of the $D(1, 1^{\pm})$ production in the reaction $\gamma d \to \pi^0 D$ are significantly less. However, the detection efficiency of the π^0 meson photoproduction by the Crystal Ball Spectrometer and TAPS is higher than it is for the charged pions and, therefore, the good yields are expected in this case.

So, the comparison of the SND photoproduction cross sections in the reactions with the production of π^+, π^-, and π^0 mesons allows the quantum numbers of SND to be determined.

Distributions of kinematical variables for the reaction under study are presented in Figs. 7– 9 for the SND masses 1904, 1926, 1942, and 1982 MeV.

Fig. 7 illustrates the expected distributions of the nucleons over the energy and the emission angle. The nucleon energy is usually smaller than 100 MeV. Therefore, we will limit ourselves by a consideration of the nucleon with such an energy. It will permit us to suppress the background essentially. The distribution over $\cos\theta_n$ in Fig. 7 shows that nucleons will be emitted primarily between $0^\circ - 75^\circ$.

Distributions over the angle between final nucleons and the relative difference of the energies of these nucleons $|E_{N1} - E_{N_2}|/(E_{N1} + E_{N2})$ are presented in Fig. 8. As can be seen from these figures, the angle between the two nucleons is below 15° and the relative difference of their energies should be below 10%.

Fig. 9 demonstrates distributions over the energy of the photon from the SND decay and over $\cos\theta_\gamma$ for different masses of SND (blac – $M = 1904$, red – 1926, green – 1942, blue – 1982 MeV). As seen from these the distributions for the energy of the final photon, the SND productions should be characterized by narrow peaks.

4 Background

The charged and neutral particles CB/TAPS detector combined with the Glasgow-Mainz tagging facility is a very advantageous instrument to search for and investigate the narrow six-quark states in the pion photoproduction reactions. For this experimental setup an optimal way to recognize the narrow six-quark states is a reconstruction of the invariant mass for three particles detected: photon and two nucleons. To suppress a background contribution to this spectrum it is necessary to detect additionally the pion and to determine the missing mass spectrum.

The major anticipated background reactions are

$$\begin{aligned} \gamma + d &\to \pi^0 + \pi^+ + n + n \\ \gamma + d &\to \pi^0 + \pi^- + p + p \\ \gamma + d &\to \pi^0 + \pi^0 + p + n \end{aligned} \tag{6}$$

$$\gamma + d \to \pi + \gamma + N + N \tag{7}$$

We will limit ourselves by the consideration of SNDs with the masses $M < 2m_N + m_\pi$. So, the reactions (6) could be considered when only one of the photons from the π^0 decay is detected. But the π^0 detection efficiency for CB/TAPS detector is over 85% and so few such events are expected.

The process (7) has a total cross section similar to those of the process being investigated. However, this background will be distributed over full missing mass region, whereas the processes of interest give contributions in narrow regions about the six-quark state masses.

In order to suppress the background more strongly, we will take into account the following conditions:

- the energy of the nucleons from the SND decay $T_N \lesssim 100\,\mathrm{MeV}$;
- the relative difference between the nucleon energies should be $\lesssim$10%;
- the angle between the nucleons should be $\Delta\theta_{NN} \approx 15^\circ$;
- there should be narrow peaks in the final photon energy spectrum.

M (MeV)	$\gamma d \to \pi^+ D(1,1^-)$		$\gamma d \to \pi^- D(1,1^-)$		$\gamma d \to \pi^0 D(1,1^+)$	
	yields	σ_M	yields	σ_M	yields	σ_M
1904	170	4.0	2000	4.0	620	3.8
1926	210	4.6	2360	4.6	650	4.4
1942	200	5.7	2180	5.5	650	5.6
1982	240	6.9	2100	7.0	530	6.9

Table 2: Expected yields of the SNDs and the mass resolutions (σ_M (MeV))

5 GEANT simulation

To estimate expected yields for the SND formation we performed Monte-Carlo simulation based on GEANT3 code [28], in which all relevant properties of the setup were taken into account. Initial distributions for event generator included differential cross sections of the SND production calculated according to the expressions obtained by us. The distribution of the decay photons also is taken into account. In addition, the following beam conditions were used:

- Incoming electron beam energy: 855 MeV.
- Tagged photon energy range: 250 – 800 MeV.
- Maximal count rate in the tagger: 6×10^5 1/sec.
- Tagging efficiency: 50%.

The results of the GEANT simulation of the invariant γNN mass spectra for the production of the isovector SNDs with masses 1904, 1926, 1942, and 1982 MeV for the processes of the pion photoproduction from the deuteron are presented in Fig. 10 for 500 hours of the beam time. The productions of $D(1,1^-)$ in the reactions $\gamma d \to \pi^+\gamma nn$ and $\gamma d \to \pi^-\gamma pp$ are shown in Fig. 10a and 10b, respectively. Fig. 10c shows the invariant γpn mass spectrum for the $D(1,1^+)$ in the process of π^0 meson photoproduction from the deuteron. As seen from Fig. 10, it is expected that SNDs can be easy extracted from the data with the number of standard deviations more than 10.

If SNDs really exist then, besides the peaks in γNN spectra, we must also observe the corresponding peaks in γp and γn mass spectra which connected with the dynamic of the SNDs decay. Such spectra, obtained in the GEANT simulation, are represented in Fig. 11 for the process $\gamma d \to \pi^0 D(1,1^+)$, $D(1,1^+) \to \gamma pn$.

The expected yields of SND as a result of the simulation of the isovector SND production in the processes of the π^+, π^-, and π^0-meson photoproduction from the deuteron at the Mainz microtron MAMI-C in the photon energy region 250–800 MeV for the beam time of 500 hours are listed in Table 2 for the different masses of SNDs. The expected mass resolution σ_M are presented here too.

6 Summary

- A search for narrow six-quark states in the reactions $\gamma d \to \pi^+\gamma nn$, $\gamma d \to \pi^-\gamma pp$, and $\gamma d \to \pi^0\gamma pn$ at MAMI-C in the photon energy region 250–800 MeV is proposed.
- The masses of SNDs will be reconstructed by the measurement of the photon and two nucleon and will be compared with the missing mass spectrum analysis obtained by the pion detection.

- Using of the Crystal Ball/TAPS spectrometer, MWPC, and PID allows one to detect γ, p and n with good enough accuracy and suppress essentially the background.
- This experiment provides an unique opportunity to observe the SNDs in the mass region from 1880 up to 2000 MeV with good precision.
- A comparison of the results obtained for the reactions under study will allow the quantum numbers of the SNDs (T, J^P) to be determined.
- The beam time of 500 hours will allow one to determine SNDs with the standard deviation number more than 10.
- Study of the γp and γn mass spectra will give an additional information about the nature of the observed dibaryon states and a possibility of existence of exotic baryons with small masses.
- Since the large beam asymmetry is expected at photoproduction of SNDs by linear polarized photons off the deuteron, we propose first to carry out such an experiment, which will, in particular, allow the result obtained at LEGS [23] to be checked.

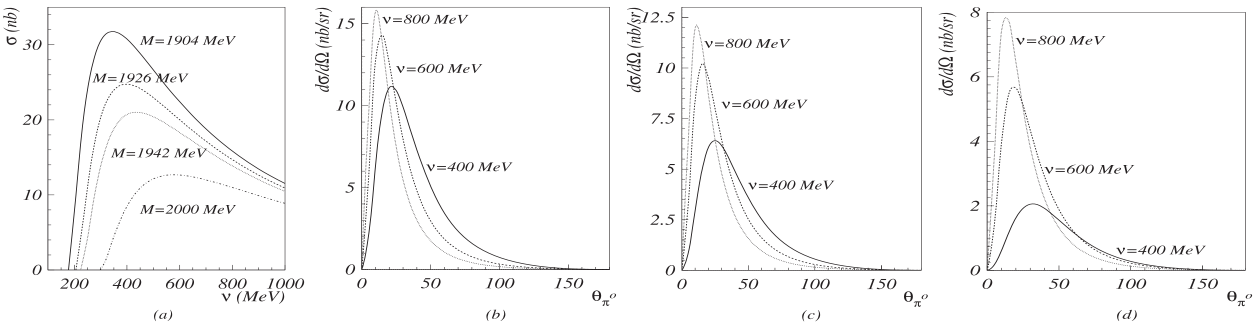

Figure 4: The cross sections of the SND $D(1, 1^-, 0)$ production in the reaction $\gamma d \to \pi^+ D$; (a) –the total cross sections; (b,c,d) – the differential cross sections for M = 1904, 1942,, and 2000 MeV, respectively.

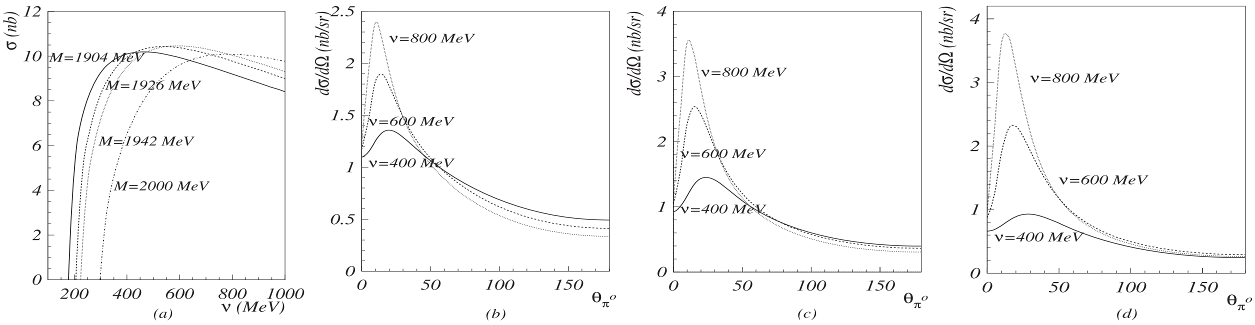

Figure 5: The cross sections of the SND $D(1, 1^+, 1)$ production in the reaction $\gamma d \to \pi^+ D$.

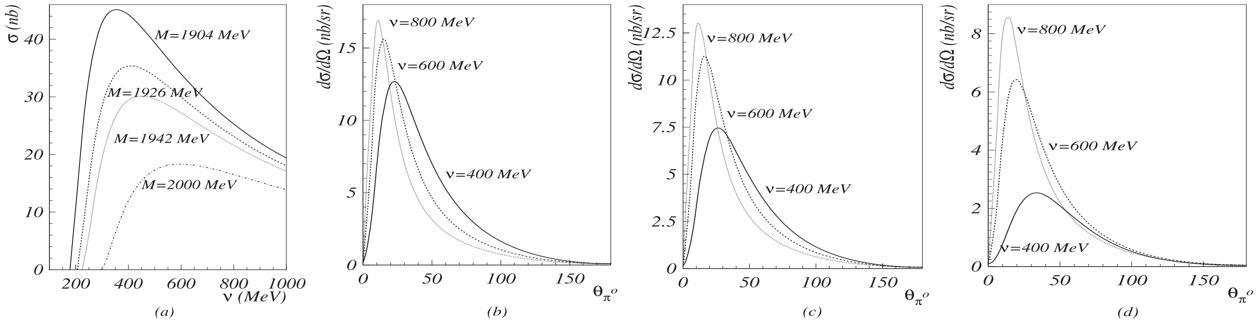

Figure 6: The cross sections of the SND $D(1, 1^-, 0)$ production in the reaction $\gamma d \to \pi^- D$.

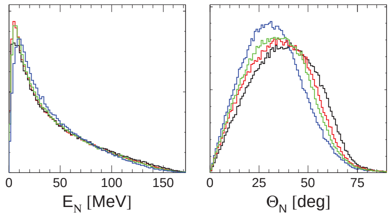

Figure 7: The energy and angular distributions of the nucleons from the decays of the dibaryons with different masses: (blac) – M = 1900, (red) – 1926, (green) – 1942, (blue) – 1982 MeV

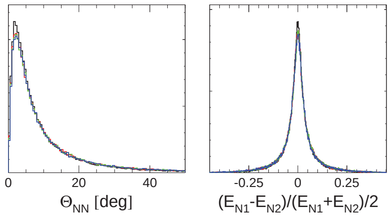

Figure 8: The distributions over the angle between the final nucleons and over the relative difference of the energies of these nuclons.

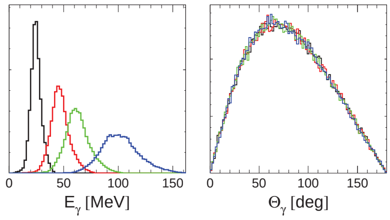

Figure 9: The energy and angular distributions of the photons from the decays of the dibaryons with different masses.

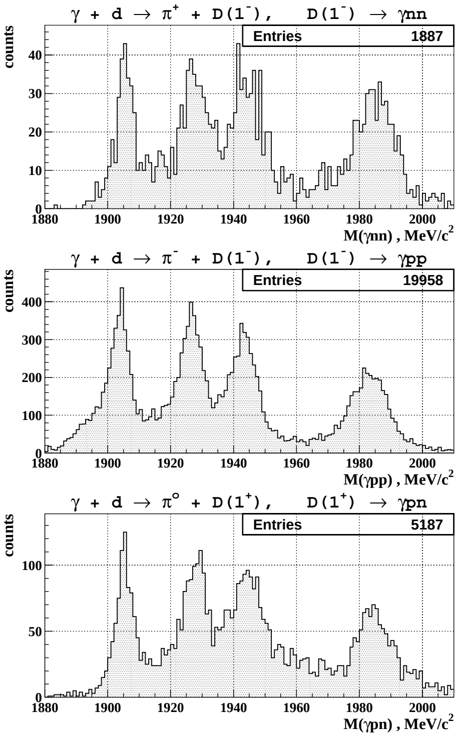

Figure 10: GEANT simulation of the SNDs with $M = 1904$, 1926, 1942, and 1982 MeV production in the processes $\gamma d \to \pi^+\gamma nn$, $\gamma d \to \pi^-\gamma pp$, and $\gamma d \to \pi^0\gamma pn$ for 500 hours of beam time.

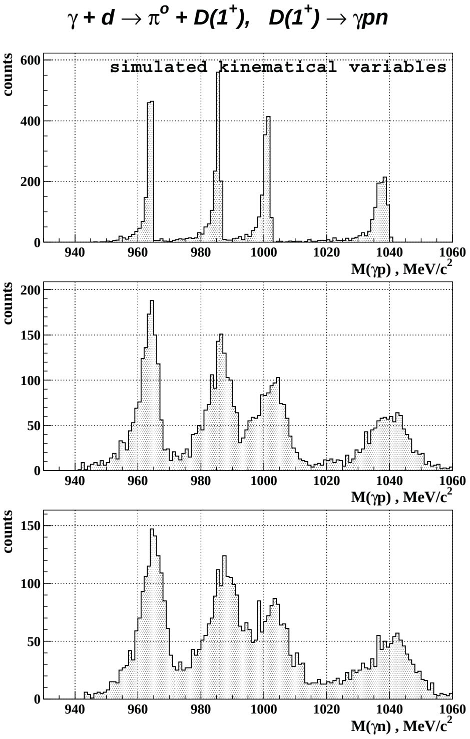

Figure 11: GEANT simulation of the invariant γp and γn mass spectra for the reaction $\gamma d \to \pi^0\gamma pn$; a– without an influence of the detectors; b and c– with an influence of the detectors

References

[1] R.L. Jaffe, Phys.Rev.Lett. **38**, 195 (1977); P.J.G. Mulders, A.T. Aerts, and J.J. de Swart, Phys.Rev.Lett. **40**, 1543 (1978); D.B. Lichtenberg, E. Predazzi, D.H. Weingarten, and J.G. Wills, Phys.Rev. **D18**, 2569 (1978); V. Matveev and P. Sorba, Lett.Nuovo Cim. **20**, 435 (1977);

[2] P.J.G. Mulders, A.T.M. Aerts, and J.J. de Swart, Phys. Rev. D **21** 2653 (1980).

[3] B. Tatischeff, J. Yonnet, M. Boivin, M.P. Comets, P. Courtat, R. Gacougnolle, Y. Le Bornec, E. Loireleux, F. Reide, and N. Willis, Phys. Rev. C **59**, 1878 (1999).

[4] L.V. Fil'kov, Sov.Physics–Lebedev Inst. Reports No.11, 49 (1986); Sov.J.Nucl.Phys. **47**, 437 (1988).

[5] D.M. Akhmedov and L.V. Fil'kov, Nucl.Phys. **A544**, 692 (1992).

[6] V.B. Kopeliovich, Phys.At.Nucl. **56**, 1084 (1993); **58**, 1237 (1995).

[7] T. Krupnovnickas, E. Norvaišas, and D.O. Riska, Lithuanian J. Phys. **41**, 13 (2001); nucl-th/0011063.

[8] L.V. Fil'kov, E.S. Konobeevski, M.V. Mordovskoy, S.I. Potashev, and V.M. Skorkin, Preprint of INR, No. 0923/96 (1996).

[9] L.V. Fil'kov, V.L. Kashevarov, E.S. Konobeevskiy, M.V. Mordovskoy, S.I. Potashev, and V.M. Skorkin, Phys. Atom. Nucl. **62**, 2021 (1999).

[10] L.V. Fil'kov, V.L. Kashevarov, E.S. Konobeevski, M.V. Mordovskoy, S.I. Potashev, and V.M. Skorkin, Phys. Rev. C **61**, 044004 (2000).

[11] L.V. Fil'kov, V.L. Kashevarov, E.S. Konobeevski, M.V. Mordovskoy, S.I. Potashev, V.A. Smirnov, V.M. Skorkin, and S.V. Zuev, Eur. Phys. J. A **12**, 369 (2001).

[12] B. Tatischeff, J. Yonnet, N. Willis, M. Boivin, M.P. Comets, P. Courtat, R. Gacougnolle, Y.Le Bornec, E. Loireleux, and F. Reide, Phys. Rev. Lett. **79**, 601 (1997).

[13] L.V. Fil'kov, Proceed. of XVI Intern. Baldin Seminar on High-Energy Physics, Dubna, Russia, 10-15 June 2002; nucl-th/0208028.

[14] Th. Walcher, hep-ph/0111279.

[15] A.I. L'vov and R.L. Workman, Phys.Rev.Lett. **81**, 1346 (1998).

[16] X. Jiang *et al.*, Phys.Rev. C **67**, 028201 (2003).

[17] M. Kohl *et al.*, Phys.Rev. C **67**, 065204 (2003).

[18] A.S. Khrykin, V.F. Boreiko, Yu.G. Budyashev, S.B. Gerasimov, N.V. Khomutov, Yu.G. Sobolev, and V.P. Zorin, Phys. Rev. C **64**, 034002 (2001).

[19] H. Calén *et al.*, Phys.Lett. **B427**, 248 (1998).

[20] H. Kuboki *et al.*, Phys. Rev. C **74**, 035203 (2006).

[21] U. Siodlaczek, P. Achenbach, J. Ahrens *et al.*, Eur. Phys. J. A **9**, 309 (2000).

[22] V.M. Alekseyev, S.N. Cherepnya, L.V. Fil'kov, and V.L. Kashevarov, Kratkie Soobscheniya po fizike, FIAN, No.1, 28 (1998); nucl-th/9812041.

[23] A. Cichocki, "Search for Super Narrow Dibaryons", PhD Dissertation, University of Virginia, (2003); B. Norum, private communication, 2012.

[24] V.L. Kashevarov, 8-th Crystal Ball and Mainz Collaboration Meeting, Glasgow, March 27–28 (2006).

[25] L.V. Fil'kov, nucl-th/0307076.

[26] Y.E. Kim and M. Orlowski, Phys.Lett. **140B**, 275 (1984); R.K. Bhadury and Y. Nogami, Phys.Lett. **152B**, 35 (1985).

[27] L.A. Kondratyuk, M.I. Krivoruchenko, and M.G. Shchepkin, Sov.J.Nucl.Phys. **43**, 899 (1986).

[28] R. Brun, *et al.*, GEANT, Cern/DD/ee/84-1, 379 1986.

POSITRON SOURCE FOR ANNIHILATION SPECTROSCOPY

R.M. Djilkibaev[a,b]

[a] Institute for Nuclear Research, Russian Academy of Sciences, Moscow, Russia
[b] Moscow Institute of Physics and Technology, State University, Moscow, Russia

Abstract

A short review of the possible applications of positron sources in the field of applied and fundamental physics is presented. An overview of current methods to get slow positrons is considered. A new scheme of positron source with a magnetic trap, increasing positron yield per primary electron for one order of magnitude, is proposed.

In the past there has been a rapid development of a relatively new method to study the structure of matter - positron annihilation spectroscopy (PAS) which complements such well-known methods: X-ray diffraction analysis on the basis of synchrotron radiation, neutron scattering, optical, electron and scanning tunneling microscopy.

Methods of analysis, diagnosis and control the level of impurity defects in materials are fundamental in the study of matter. Positron spectroscopy has a unique sensitivity in the measurement of impurity defects and size in the range of a few nanometers.

Positron spectroscopy allows us to study the electronic structure of matter, impurity and size of defects in a wide range near the surface of the material. Currently experimental measurements based on positron annihilation spectroscopy have been accomplished in metals, alloys, condensed media, semiconductors, polymers, etc.

There is a need to have an intense 10^7 e^+/sec slow positron source for positron spectroscopy. Currently, there are two main methods to get slow positrons. The first method involves the use of radioactive elements ^{22}Na, which is the reaction undergoes beta decay with the emission of a positron and gamma ray. The main disadvantage of this method involves the use of radioactive sources of high intensity of a few Curie, to create a source of slow positrons with intensity of 10^7 e^+/sec and a relatively short source half-life time - 2.6 years. The second method uses electron accelerators with energies of 15 to 200 MeV, which can significantly increase the intensity of the positron source and mostly used in practice. At the present time there are a few of research centers for positron spectroscopy of materials [1-9], using slow positron beams with intensity ~ 10^7 - 10^8 e^+/sec based on electron accelerators with energy 15-100 MeV and current 50-200 μA.

In the standard scheme of the source, yield of slow positrons is small amount – 10^{-7} e^+ /e per primary electron. Probability of production of slow positrons is product of two small factors: the efficiency of positrons conversion from electron is equal to 10^{-3} e^+ /e and the moderator efficiency to get slow positrons in a thin polycrystalline tungsten foil is equal to 10^{-4} [10-13].

A new scheme of positron source based on the use of magnetic trap [14,15], which will greatly increase passage of positrons through a thin foil moderator, and thus increase the efficiency of slow positrons yield, is proposed. Contrary to the standard scheme of the positron source, where the positrons pass through the moderator foil once.

New development of low-energy ~10 MeV, compact electron accelerators with low cost [16-19] open up new possibilities in the creation of intense slow positron source for materials research.

Positrons are generated due to interaction of electrons in a high Z material target through the pair production process. These positrons are then slowed (moderated) to thermal energies via interaction with a suitable material such as thin polycrystalline tungsten foil.

The cross-section of positron annihilation on a free electron into two gamma rays [20], in non-relativistic approximation, is given by $\sigma_{2\gamma} = \pi r_0^2 c/v$, where v is a positron velocity, c is the speed of light, r_0 is the classical electron radius. Positron annihilation cross-section tends to infinity, provided that the positron velocity tends to 0. However, positron annihilation rate (λ) tends to finite limit is equal to $\lambda = \sigma_{2\gamma} v n_e = \pi r_0^2 c n_e$, where n_e is an electron concentration. According to law of momentum conservation annihilation of e^+e^- - pair into 2 gamma rays, provided that the pair velocity is equal to zero, result in the two rays would be emitted in exactly opposite directions (180 degrees apart) with energy of 0.511 MeV. However, non zero the pair velocity, causes the direction of the gamma rays to deviate from the nominal value of 180 degrees. Likewise, the energy of the annihilation gamma rays deviates slightly from 0.511 MeV due to the Doppler effect.

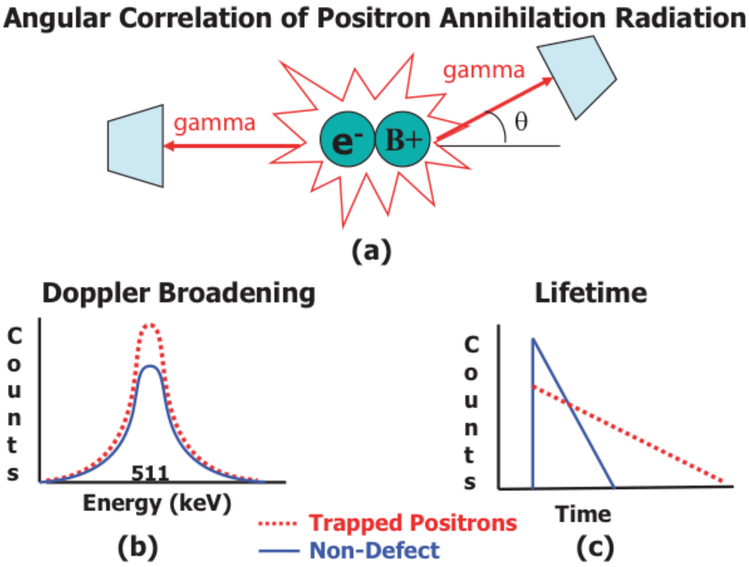

Figure 1. The three most common experimental positron techniques for measuring electron momentum are (a) angular correlation of annihilation radiation, (b) Doppler broadening, and (c) positronium lifetime. When positrons become trapped in defects, there is a reduced overlap with energetic core electrons, leading to less angular deviation (a), more counts at or near the 0.511 MeV peak (b), and longer positronium lifetimes (c) [21,22]

There are three most common positron spectroscopy techniques: first - measurement of the gamma ray angles (angular correlation), second - energy spectrum (Doppler broadened line-shape), and third - positronium lifetime will determine whether the positrons are interacting with free electrons at defects or core electrons in the bulk material. Those measurements are illustrated [21,22] in Figure 1 (a,b,c). The measurement of the distribution of angles between two annihilation gamma rays about the nominal value of 180 degrees is illustrated on Figure 1 (a). This deviation from collinearity between two 0.511 MeV annihilation gamma rays is a product of the momentum of the annihilating electron. Less deviation from collinearity indicates the presence of defects. The electron momentum also produces a Doppler shift in the 0.511 MeV gamma annihilation radiation, and this shift can be seen in an accurate energy measurement of one of the two gamma rays emitted by an individual annihilation, as illustrated in Figure 1 (b). With a Doppler broadened line- shape measurement, the distribution of the annihilation gamma ray energies about the nominal energy of 0.511 MeV is measured. Less deviation from the nominal 0.511 MeV energy value (more gamma rays detected) in a given period of time or very near 0.511 MeV and fewer detected at other energy levels indicates the presence of defects. With a positronium lifetime measurement, Figure 1 (c), the distribution of time between a time when the positron is ejected and the annihilation gamma rays observed is measured and provides information not only on the quantity of defects, but due to variations in the lifetime, on the type of defects present.

A comparison of regions accessible to various standard techniques and positron spectroscopy for defect resolution and defect concentration measurements are shown in Figure 2 [22].

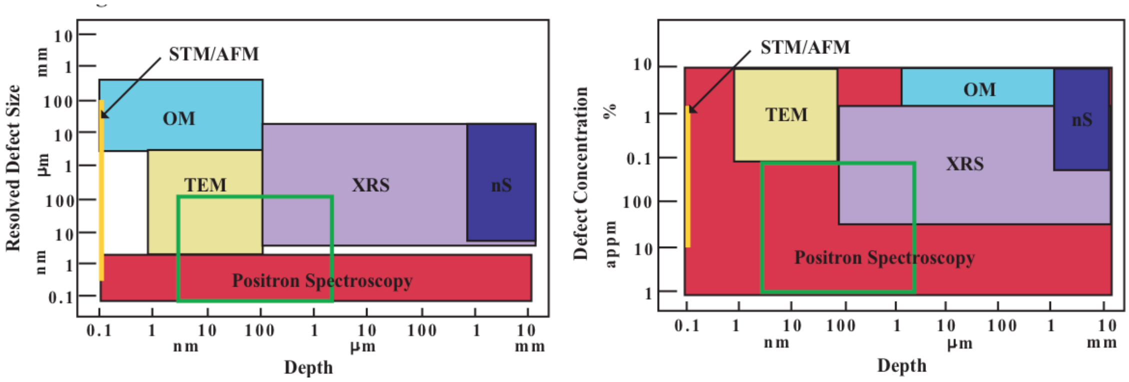

Figure 2. Defect resolution methods (left) and defect concentration methods (right). Next notations are used: optical microscopy (OM), neutron scattering (nS), transmission electron microscopy (TEM), scanning tunneling microscopy (STM), atomic force microscopy (AFM), and x-ray scattering (XRS). The solid green line outlines the range of interest for studies of fine lines used as electronic interconnects on semiconductor chips. (Figures provided by Lawrence Livermore National Laboratory)

Positronium (e+ e-) is a simplest atom and an ideal system to probe a new physics beyond the Standard model (SM). Positronium is also good for testing the accuracy of quantum electrodynamics (QED) calculations for bound states, in particular, for the triplet (1^3 S_1) state of Ps (orthopositronium, o-Ps. A precision of QED calculation is higher of two orders of magnitude then current experimental accuracy. Positronium has charge conjugation parity is equal to $(-1)^{L+S}$, where L is an orbital momentum and S is a total spin of the Ps [23]. Orthopositronium (*L*=0, *S*=1) has odd charge conjugation parity and parapositronium (p-Ps, *L=0, S=0*) has even charge conjugation parity. A system of n photons have a charge conjugation parity of $(-1)^n$. Since charge conjugation is conserved in electromagnetic interactions and thus o-Ps must decay into an odd number of photons. Decay into a single photon cannot conserve momentum, thus a three photon decay is the most probable with a lifetime in vacuum of 142 ns [24] . Parapositronium must decay into an even number of photons, two being the most probable with a lifetime in vacuum of 125 ps [25].

A new effects might be observed in rare decays of the positronium (Ps) as an example o-Ps decays into invisible mode. Invisible mode means that decays are not accompanied by release of energy in the surrounding calorimeter. The positronium decay into a neutrino- antineutrino pair has a branching ratio of $6.6 \mathrm{x} 10^{-18}$ in the SM [26]. There are a few models beyond SM have predictions for branching ratio of o-Ps decays into invisible mode, much higher then SM: 1) extra-dimensions [27,28], 2) fractionally charged particles [29,20], 3) mirror particles, which could be candidates for dark matter [31,36]. The last model is one of the possible extensions of SM of particle physics. Mirror matter could be a relevant dark matter candidate. Currently, there are two main versions of mirror matter model: symmetrical [37] and asymmetrical [38] model. For positronium the relevant coupling to its mirror twin is due to photon-paraphoton mixing describing by the interaction Lagrangian $L= \varepsilon F^{\mu\nu} F'_{\mu\nu}$, where ε is a mixing parameter, $F^{\mu\nu}$ and $F'_{\mu\nu}$ are electromagnetic and para-electromagnetic field strength tensor, respectively. The current upper limit on the branching ratio of orthopositronium o-Ps decays into invisible mode is equal to Br(o_Ps-> invisible) $< 4.2\ 10^{-7}$ (90% c.l.) [39]. Non-observation of positronium oPs → invisible places a direct limit on the mixing parameter $\varepsilon < 1.5\ 10^{-7}$ [39]. A new poroposed experiment [40] is going to improve the limit of Br(o_Ps-> invisible) $< 10^{-8}$ and sensitivity to $\varepsilon \approx 10^{-9}$.

Electron accelerators with low energy (below 10 MeV) have an important feature related with radiation safety. The cross-sections of photonuclear reactions in the high Z material target, such as tungsten, tantalum, have the maximum values when energy reaches ~15 MeV and drop rapidly with decreasing electron energy below 10 MeV. The dependence of the photon and neutron dose produced by electrons on energy of electron has been studied in [41], provided that the electrons interact with the 4mm thick tungsten target. The simulated photon and neutron dose at the isocenter (100 cm away from the target along the beam direction) are shown in Table 1. Neutron dose equivalent ratio (DER) to electromagnetic dose for 4 mm tungsten target decrease from 0.147 to 0.006 mSv/Gy X-ray for 15 and 9 MeV electron energy, respectively.

Table 1. Photon and neutron dose at the isocenter produced by electrons [41]

Electron energy (MeV)	Photon dose (Gy X-ray/e)	Neutron dose (mSv/e)	Dose Equivalent Ratio (mSv/Gy X-ray)
9	$8.5\ x10^{-16}$	$5.4\ x10^{-18}$	0.006
10	$1.2\ x10^{-15}$	$1.8\ x10^{-17}$	0.016
15	$3.7\ x10^{-15}$	$5.5\ x10^{-16}$	0.147

The basic scheme of the slow positrons production has converter and moderator. Tungsten or tantalum converter is using for positrons production through pair (e+,e-) production process induced by electrons. A schematic diagram of the converter and moderator assembly currently in use at the AIST LINAC [a1] is show in Figure 3. Electrons at 70 MeV are directed on to a 6 mm thick, water-cooled tantalum block in air. Positrons emerging in the forward direction pass through a thin titanium film into vacuum and are incident on an array of 50 μm tungsten films arranged in a rectangular mesh. Moderated positrons at low energy (several eV) are extracted from the moderator assembly by the applied positive potential (≈10 V) and magnetically guided into a transport beam line.

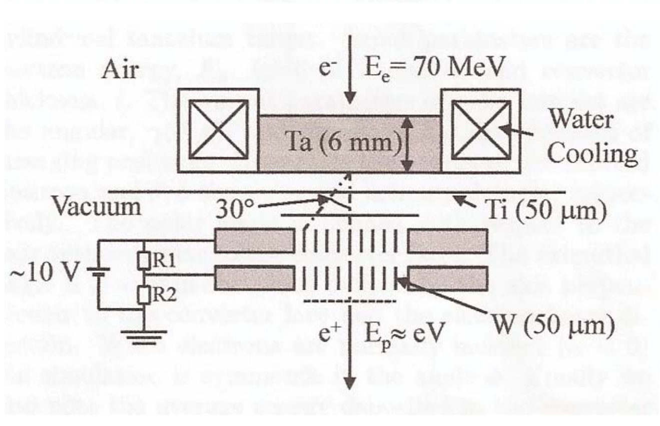

Figure 3. The design of slow positron source currently in use at the AIST (National Institute of Advanced Industrial Science and Technology) LINAC

The results of simulation for slow positron yield γ_S and moderator efficiency ε versus of electron energy E_e for the AIST positron source are shown in Figure 4 [42]. Also is shown fit results for data points of positron yield by function $a+b(E_e+c)^n$. The slow positron yield is a product of the moderator efficiency and positron production efficiency in the converter with the optimal thickness. A linear interpolation for optimal Ta converter thickness versus of electron energy based on measurements at various laboratories [43] is equal to l_{opt} [mm] = 0.67+0.0953 E_e [MeV]. Significant limitation for maximum intensity of positron source is determined by maximum of heat transfer from the converter. As the electron beam current increases the energy deposited will be sufficient to melt the converter material. An estimate for the cooling power Pw of a water cooled converter is given by the following equation [44] ,

$$Pw = 2\,\pi\,\lambda\,l\,(Tb - Tw)\,/\,(0.5 + \ln(R_c/R_b))$$

where R_c and R_b are the radius of the converter and electron beam respectively, λ is the thermal conductivity and l the converter thickness. Tb is the maximum temperature of the target material on the beam axis, while Tw is the temperature of the copper block in contact with the water coolant. For tantalum λ = 57.6 or 61.5 W/(m K) at 300 K or 1800 K, respectively. The melting point of tantalum (T = 3300 K) determines the maximum of heat transfer for a water-cooled converter, dimensions R_c = 2 cm, R_b = 1 cm, l = 0.02 cm, is equal to 23.4 kW.

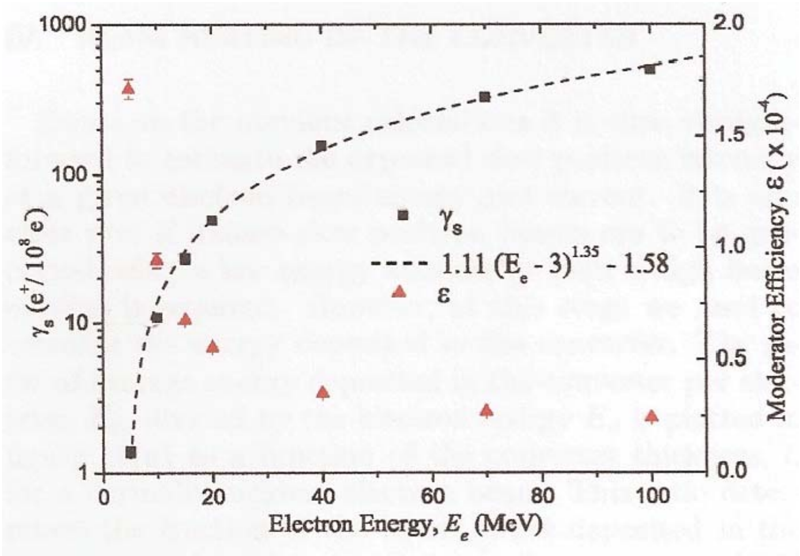

Figure 4. Slow positron yield (γ_s) per primary electron and moderator efficiency (ε) versus of electron energy E_e for the AIST source

The design for both converter and moderator in one piece of tungsten has been proposed [45], because tungsten can be used both as a converter and a moderator and any distance between the two will reduce the amount of positrons available for moderation. Tungsten vanes (0.4 mm thick) have been used as a converter for many slow positron beams [46–48]. They can also be used as a moderator. The converter/moderator design [45] for 10 tungsten vanes of 0.4 mm thick, 1 mm apart and 10 mm long is shown in Figure 5, the reflected and transmitted electrons can still have enough energy to generate more positrons. At the same time, the positrons produced will slow down in the vanes, which serve as a moderator. When the incident electrons hit a tungsten vane for the first time some positrons are generated, and after several times hitting the vanes, more positrons will be produced from the multiple steps of conversion within the tungsten. The positron production yield from the design [45] is about one order of magnitude better than that from the single-layer converter.

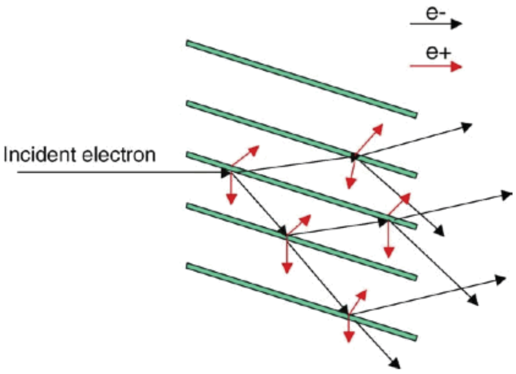

Figure 5. The design for a combined tungsten converter/moderator for the positron source at the 15 MeV LINAC at Argonne National Laboratory

A new scheme of positron source with a magnetic trap, consisting of tantalum converter and cone tungsten moderator made of 4 μm polycrystalline tungsten foils, is shown in Figure 6. The converter has a diameter of 0.5 cm and a thickness of 1.5 mm. The thickness of converter is optimized for electron beam with energy of 8-10 MeV. The magnetic trap of positron source is formed by two permanent NdFeB magnets with axial field located on the beam axis (± 7cm) from the center of the moderator (Fig. 6). The cone moderator has diameter 1 cm and length 4 cm. The magnetic trap captures low-energy positrons that repeatedly cross the foil and thus increases the probability of the positron in the moderator to slow down to thermal velocities. Typically the moderation process is considered on the basis of a diffusion length L_+ and re-emission branching ratio η_0 for the moderator material. The probability that positron can diffuse back to the surface from a given depth z is equal to $\exp(-z/L_+)$.

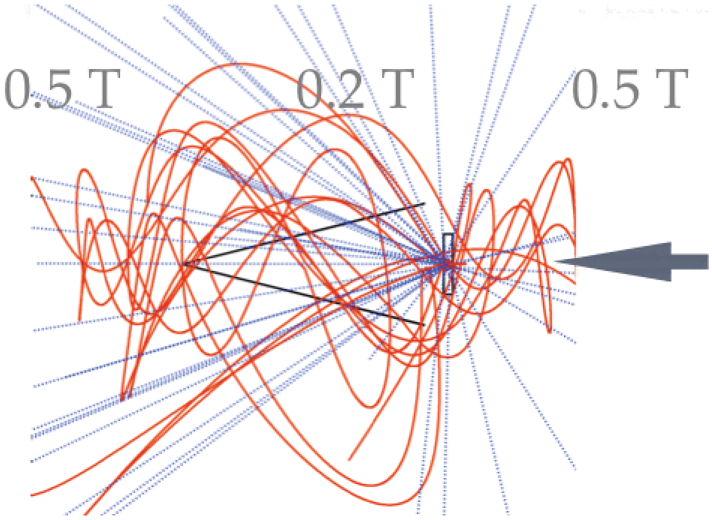

Figure 6. A scheme of positron source with a magnetic trap consisting of tantalum converter and thin tungsten foil cone moderator. The arrow shows an electron beam direction

The probability of re-emission of low energy positron from the moderator surface is given by [49]

$$\eta = \eta_0 \int_0^{\infty} f(z)\exp(-z/L_+)dz$$

where f(z) is the positron deposition depth profile. It was assumed that f(z) is a uniform function. For polycrystalline tungsten a measured diffusion length L_+ is typically in the range of 50-100 nm [50,51] and re-emission branching ratio η_0 is equal to 0.3 [52]. Thus the probability of the positron re-emission from the moderator foil (d=4μm) is equal ($\eta_0 L_+/d$) to $3.8\text{x}10^{-3}$ and $7.5\text{x}10^{-3}$ for the diffusion length of 50 and 100 nm, respectively. It is assumed that re-emitted positron has an energy 2.8 eV, the positron work function of tungsten [53]. Processes of production and slow positrons in the material are simulated using GEANT3 code[54] with cut-off energy is equal to 10 keV. The positron GEANT simulation stopped when positron energy in the moderator reaches the cut-off energy. The average penetration depth of positrons with an energy of 10 keV in tungsten foil amounts to 0.1μm. A simulated positron production yield per primary electron with energy 10 MeV in the Ta (1.5 mm) converter is in a good agreement with [42] and amounts to $1.8\text{x}10^{-3}$. A probability to slow produced positrons in the cone moderator (P_{cone}) with a magnetic trap (0.5-0.2-0.5 T) to the cut-off energy is equal to 10%. Thus combined efficiency for slow positron production by 10 MeV electron for the cone moderator with a magnetic trap (0.5-0.2-0.5 T) is equal to $0.7\text{x}10^{-6}$ and $1.4\text{x}10^{-6}$ for the diffusion length of 50 and 100 nm, respectively. The probability P_{cone} is decreased drastically by an order for the positron source (Fig. 6) without a magnetic field. In this case, the slow positron yield is equal to 10^{-7} e^+/e and comparable with the AIST result for 10 MeV electron energy is shown in Figure 4.

Preliminary simulations show that the collection efficiency of slow positrons for the cone moderator (Fig. 7) is equal to 80%. Thus the overall efficiency for slow positron production by 10 MeV electron for the cone moderator with a magnetic trap (0.5-0.2-0.5 T) is equal to $0.6\text{x}10^{-6}$ and $1.1\text{x}10^{-6}$ for the diffusion length of 50 and 100 nm, respectively. Slow positrons will be electro-magnetically filtered from fast positrons and then directly transported magnetically (100-200 G) at energies of 50-100 eV to the experimental area.

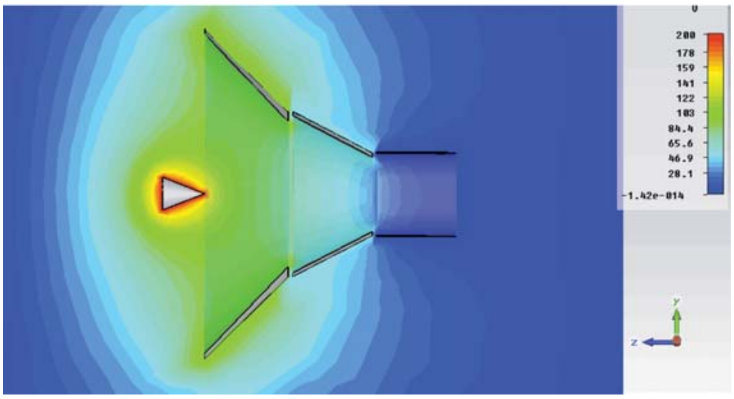

Figure 7. An electric field map for the cone moderator assembly: cone + extraction lenses

To suppress γ background in the positron beam, the transport system is commonly used curved solenoid. The motion of positrons in a curved solenoid leads to a drift in the direction perpendicular to the plane of the bend at a speed of v_d [55]

$$\beta_d = v_d / c = \frac{2}{3} 10^{-4} \frac{T_e[eV]}{R[m] \times B[G]}$$

where T_e is a kinetic positron energy, R is a radius of solenoid curvature and B is a solenoid magnetic filed. The amount of displacement of the positron beam with an energy of 100 eV in a curved solenoid with a bend angle of 180^0 , curvature radius of 1 m and magnetic field of 100 G due to the drift is equal to the value of $\pi/3$ $R10^{-2} \approx 1$cm. Additional external magnetic coils or internal electrostatic plates can then be used to compensate for the drift.

The intensity of the positron source with a magnetic trap, based on electron accelerator with an energy of 10 MeV and an average current of 10 μA can reach values to $5x10^7$ e^+/sec

Acknowledgements

I wish to thank S.N. Gninenko, R.K. Konoplich, V.G. Nedorezov, I.I. Tkachev for fruitful discussions and helpful remarks.

[1] Positron Annihilation, ed. by P.G. Coleman, S.C. Sharma, L.M. Diana, North- Holland, Amsterdam (1982)
[2] Positron Annihilation, ed. by P.C. Jain, R.M. Singuri, K.P. Gopinathan, World Scientific, Singapore (1985)
[3] P.G. Coleman, ed., Positron Beams and their Applications, World Scientific, Singapore (2000)
[4] R. Ley, Hyper. Int. 109, 167 (1997)
[5] O. Sueoka, Y. Ito, T. Azuma et al., Jpn. J. App. Phys., 24, 222 (1985)
[6] R.H. Howel, I.J. Rosenberg, M.J. Fluss, App. Phys. A 43, 247 (1987)
[7] T. Akahane, T. Chiba, N. Shiotani et al., App. Phys. A 51, 146 (1990)
[8] R. Suzuki, T. Ohdaira, T. Mikado et al., App. Surf. Sci., 116, 187 (1997)
[9] H.M. Chen, Y.C. Jean, C.D. Johan et al., App. Surf, Sci., 252, 3159 (2006)
[10] R.H. Howell, R.A. Alvarez, M. Stanek, App. Phys. Lett., 40, 751 (1982)
[11] M. Begemann, G. Graff et al. Nucl. Instr. Methods, 201, 287 (1982)
[12] K.F. Canter, Ap.P. Mills Jr., Ca. J. Phus. ,60, 551 (1982)
[13] O. Sueoka, Y. Ito, T. Azuma et al., Jpn. J. App. Phys., 24, 114 (1985)
[14] R. Djilkibaev, V.M. Lobashev, Sov. J. Nucl. Phys., 49 (2), 384 (1989)
[15] M. Shi, W.B. Waeber, D. Gerola, U. Zimmerman, D. Taqqu, NIM A 349, 8 (1994)
[16] P. Perez, L. Liszkay, J.-M. Rey at al., Phys. Status Solidi C 6, 2462 (2009)
[17] T. Muranaka, P. Debu, P. Dupre at al., J. Phys. Conf. Sers. 255, 012039 (2010)
[18] Б.С. Ишханов, В.И. Шведунов, Исследования и разработка ускорителей электронов в НИИЯФ МГУ, Вестник МГУ (2012)
[19] http://www.iba-industrial.com
[20] P.A. Dirac, Proc. Camb. Phil. Soc., 26, 361 (1930)
[21] Schultz, P. J., and C. L. Snead, Jr., "Positron Spectroscopy for Materials Characterization, " Metallurgical Transactions, 21, 4, pp. 1121 (1990)
[22] http://www.positronsystems.com

[23] M.D. Harpen, Med. Phys. 31, 57 (2004).
[24] S. Karshenboim, Int. J. Mod. Phys. A **19**, 3879 (2004)
[25] A. Czarnecki, K. Melnikov, and A. Yelkhowsky, Phys. Rev. Lett. **83**, 1135 (1999)
[26] J.Govaerts and M. Van Caille, Phys. Lett. B **381**, 451 (1996)
[27] S. Dubovsky, V. Rubakov, P. G. Tinyakov, Phys. Rev. D **62**, 105011 (2000)
[28] S. Gninenko, N. Krasnikov, A. Rubbia, Rev. D **67**, 075012 (2003)
[29] B. Holdom, Phys. Lett. **166B**, 196 (1986)
[30] S. Davidson *et al.*, J. High Energy Phys. 02, 37 (2002)
[31] T. D. Lee and C. N. Yang, Phys. Rev. **104**, 254 (1956)
[32] S. L. Glashow, Phys. Lett. **167B**, 35 (1986)
[33] R. Foot and S. N. Gninenko, Phys. Lett. B **480**, 171 (2000)
[34] Z. Berezhiani, Int. J. Mod. Phys. A **19**, 3775 (2004)
[35] L. Okun,hep-ph/0606202; [g14]
[36] M. Yu. Khlopov, *Cosmoparticle Physics* (World Scientific, Singapore, 1999)
[37] R. Foot, H. Lew, R. R. Volkas, Phys. Lett. B272, 67 (1991)
[38] Z.Berezhiani,R.Mohapatra, Phys. Rev. D62, 6607 (1995), S E. Akhmedov, Z.Berezhiani and G. Senjanović, Phys. Rev. Lett. 69, 3013 (1992); Z. Berezhiani, A. Dolgov and R.N. Mohapatra, Phys. Lett. B375, 26 (1996); Z. Berezhiani, Acta Phys. Pol. B27, 1503 (1996)
[39] A. Badertscher, P. Crivelli, W. Fetscher at al., Phys. Rev. D75, 032004 (2007)
[40] P. Crivelli, A. Belov, U. Gendotti, S. Gninenko, A. Rubbia, arXiv:1005.4802v4 (2010)
[41] W.L. Huang, Q.F. Li, Y.Z. Lin, Nucl. Instr. Meth. B 229, 339 (2005)
[42] B.E. O`Rourke, N. Hayashizaki, A. Kinomura et al., arXiv:1102.1220v2 (2011)
[43] R. Ley, FZR Report FZR-225, Forschungzentrum Rossendorf (2000)
[44] R. Andreani, A. Cattoni, Nucl. Intsr. Meth., 129, 365 (1975)
[45] H.M. Chen, Y.C. Jean, C.D. Jonag et al., Applied Surface Science 252, 3159 (2006)
[46] R.H. Howel, in P.G. Coleman, ed., Positron Beams and their Applications, World Scientific, Singapore, p. 307 (2000)
[47] R.H. Howel, L.J. Resenberg, M.J. Fluss, Appl. Phys. A43, 247 (1987)
[48] R. Suzuki, T. Ohdaira, T. Mikado et al., Material Sci. Forum 255, 114 (1997)
[49] M. Carlton, J.W. Humberston Positron Physics, Camb. Univ. Press, (2001)
[50] Weng et al., Appl. Surf. Sci., 194, 24 (2002)
[51] Van Veen et al., Mater. Sci. For., 363, 415 (2001)
[52] R. Suzuki, T. Ohdaira, A. Uedono et al., Jpn. J. App. Phys., 37, 4636 (1998)
[53] F.M. Jacobson, M. Charlton, J. Chevallier et al., J. App. Phys. 67, 575 (1990)
[54] GEANT3, Detector description and simulation tool , CERN, Geneva (1994)
[55] J.D. Jackson, Classical Electrodynamics, John Willy & Sons, New York (1975)

SOURCE OF MONOCHROMATIC PHOTONS DRIVEN BY POSITRON IN-FLIGHT ANNIHILATION USING INTERNAL TARGET OF THE STORAGE RING VEPP-3

L.Z. Dzhilavyan[1], *S.I. Mishnev*[2], *V.G. Nedorezov*[1], *D.M. Nikolenko*[2],
I.A. Rachek[2], *D.K. Toporkov*[2, 3]

[1] Institute for Nuclear Research RAS, Moscow, Russia
[2] Budker Institute of Nuclear Physics SB RAS, Novosibirsk, Russia
[3] Novosibirsk State University, Novosibirsk, Russia

The present project for a source of quasimonochromatic photons with the energies 500÷750 MeV combines the following two main methodical components:

A. The method of production quasimonochromatic photons using for positron beams with narrow energy spreads and small transverse emittances annihilation in flight in relatively thin external targets with low atomic numbers Z. Method "A" was proposed in [1] and successfully realized on the extracted beams of accelerators in a number of scientific centers [2-15], including the INR RAS (Moscow) [8].

B. The method of usage in positron (electron) storage rings internal super-thin targets with possibility to achieve their effective thicknesses up to (0.1÷0.2) radiation lengths and with keeping very high qualities of beams, circulated through these targets. Method "B" is under systematical development and successful realization in the INP SB RAS (Novosibirsk) [16, 17].

In a collision in flight of an ultra-relativistic positron with an electron of matter (here it is possible to consider the latter at rest and as free one) their photon annihilation can happen. For our purposes, basically it is sufficient to consider only the two-photon annihilation, the main features of which can be found, in particular, in [18] and for which, according to [19], we have the differential cross section in the Laboratory System (LS):

$$(d\sigma_a/d\omega_a)=[(r_0)^2/2][(\gamma+1)/(\gamma-1)]^{0.5}\{-[2/(\gamma+1-(\gamma^2-1)^{0.5}\cos\theta_a)^2]+[(3+\gamma)/((\gamma+1)(\gamma-(\gamma^2-1)^{0.5}\cos\theta_a))]-$$
$$-[(\gamma+1-(\gamma^2-1)^{0.5}\cos\theta_a)/((\gamma+1)(\gamma-(\gamma^2-1)^{0.5}\cos\theta_a))]^2\}, \qquad (1)$$

or approximately at $\theta_a \leq \sim (1/\gamma)$ and at $(1/\gamma) << \theta_a << (2/\gamma)^{0.5}$, respectively, we have:

$$(d\sigma_a/d\omega_a) \approx (r_0)^2\gamma/(1+\gamma^2(\theta_a)^2), \qquad (1')$$

$$(d\sigma_a/d\omega_a) \approx [(r_0)^2/\gamma(\theta_a)^2)], \qquad (1'')$$

where: r_0 и μ – “the classical radius" and the total rest energy of an electron; γ – a total energy of an incident positron in LS in μ-units; k_a, θ_a, and $d\omega_a$ – an energy in μ-units, an angle of emission with respect to the motion direction of an incident positron, and an element of a solid angle, for which the photon emission is considered in LS for one from the pair of annihilation photons.

It follows from (1′): $(d\sigma_a/d\omega_a)$ at $\theta_a=0$ with growth of γ tends to $(r_0)^2\gamma$, whereas for bremsstrahlung of a positron in the field of a nucleus the differential as in the angle θ_b, as in the energy of bremsstrahlung photons k_b cross section $[d^2\sigma_b/(dk_b d\omega_b)]\{\theta_b=0\}$ at some fixed k_b, according to [20], increases with growth of γ steeper than γ^2. This relationship between the very important features of these two processes makes the problem with background from bremsstrahlung generated by positrons in the annihilation target itself very serious at the growth of γ. However off-axial collimation can help to improve for annihilation conditions of competition with bremsstrahlung. For both processes the characteristic angles, at which $(d\sigma/d\theta)$ decreases by half, are about $1/\gamma$. But at $(1/\gamma) << \theta << (2/\gamma)^{0.5}$ with increasing of θ, if for the annihilation radiation $(d\sigma/d\theta)$ decreases as $\sim 1/(\theta)^2$, for bremsstrahlung $(d\sigma/d\theta)$ decreases much steeper, namely, as $\sim 1/(\theta)^4$ (see, for example, Fig. 1, which is connected with that).

In LS θ_a and k_a are connected with each other**:**

$$k_a=(\gamma+1)/[\gamma+1-(\gamma^2-1)^{0.5}\cos\theta_a]. \tag{2}$$

Hence:

$$(d\sigma_a/dk_a) = [(\pi(r_0)^2)/(\gamma^2-1)]\{-2+[((3+\gamma)(\gamma+1))/(k_a(\gamma+1-k_a))]-[(\gamma+1)/(k_a(\gamma+1-k_a))]^2\}, \tag{3}$$

and: $k_{a\,max}=1/\{1-[(\gamma-1)/(\gamma+1)]^{0.5}\}\cong\gamma+0.5\cong k_{b\,max}+1.5$; $k_{a\,min}=1/\{1+[(\gamma-1)/(\gamma+1)]^{0.5}\}\cong 0.5$.

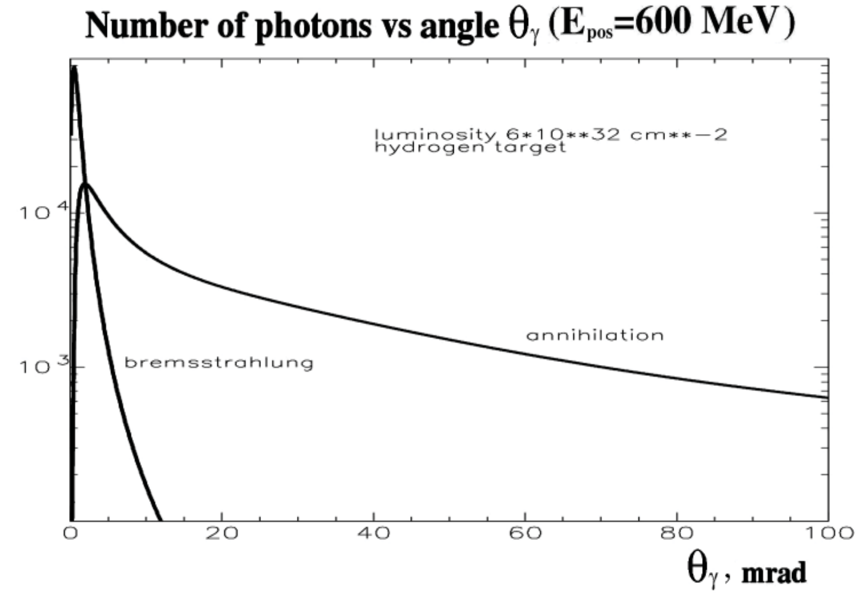

Fig. 1. Number of annihilation and bremsstrahlung photons in dependence on θ_γ *for hydrogen target at positron energy 600 MeV and luminosity* $L=6\cdot10^{32}$ cm^{-2}

In (2) and (3) there is no difference between the designations in LS for two photons emitted in the same act of two-photon annihilation, but it is convenient to separate these photons in names and symbols for values connected with them: "hard" photon (with energy k_{a1} and emission angle θ_{a1}) and "soft" photon (with energy k_{a2} and emission angle θ_{a2}). Here: $k_{a1}\geq k_{a2}$; $|\theta_{a1}|\leq|\theta_{a2}|$ and $(k_{a1}+k_{a2})=(\gamma+1)$.

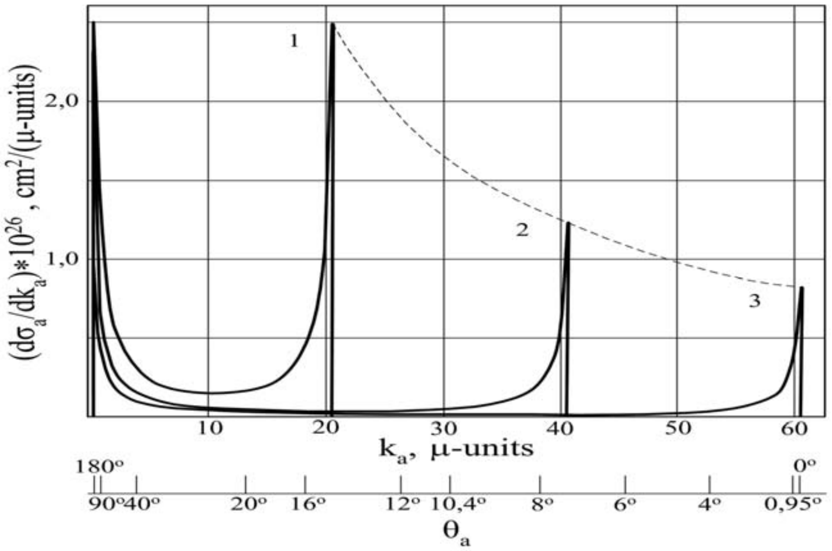

Fig. 2. $(d\sigma_a/dk_a)\{k_a\}$ *– solid lines. For curves 1; 2 and 3, respectively,* $\gamma=20$*; 40 and 60. For* $\gamma=60$ *it is shown also non-uniform horizontal axis– the axis* θ_a*. Dashed curve –* $(d\sigma_a/dk_a)\{k_{a\,max}\}\approx 2\pi(r_0)^2/k_{a\,max}$

Distributions $(d\sigma_a/dk_a)$ for $\gamma = 20$; 40 and 60 are shown in Fig. 2. Each of these distributions is symmetric with respect to its own value $k_{a\,symm}=(k_{a\,max}+k_{a\,min})/2$. Photons with $k_a\cong k_{a\,max}-0.5$ are emitted at $\theta_a\cong 1/\gamma$, when $(d\sigma_a/dk_a)\{k_a\cong k_{a\,max}-0.5\}\cong 0.5(d\sigma_a/dk_a)\{k_{a\,max}\}$ and this features set the level of “monochromaticity” without much loss of attainable intensity, which can be expected with such a "monochromatization", and the conditions for achieving this level (the allowable energy spread and the transverse emittance in the incident beam of positrons, the thickness of the annihilation target, the chosen angle for the produced photons).

For various estimations, except for the differential cross sections $(d\sigma_a/dk_a)$, the integral cross sections are also necessary, for which in LS at $k_{a\,symm}\leq k'\leq k_{a1}\leq k''\leq k_{a\,max}$, we have:

$$\sigma_a(\gamma,k',k'') = [(\pi(r_0)^2)/(\gamma^2-1)]\{-(k''-k')[2+(1/k'k'')+(1/((\gamma+1-k')(\gamma+1-k'')))]+ \\ +((\gamma^2+4\gamma+1)/(\gamma+1))\ln[(k''(\gamma+1-k'))/(k'(\gamma+1-k''))]\}; \qquad (4)$$

at axial collimation, i.e. if $k''=k_{a\,max}$ and $k'=k_{a\,max}-\Delta k$, we have**:**

$$\sigma_a(\gamma,k'=k_{a\,max}-\Delta k,k''=k_{a\,max}) = [(\pi(r_0)^2)/(\gamma^2-1)] \times \\ \times\{-2\cdot\Delta k[1+[(\gamma-(\gamma^2-1)^{0.5})/(\gamma+1-\Delta k(\gamma+1-(\gamma^2-1)^{0.5}))]+[(\gamma+(\gamma^2-1)^{0.5})/(\gamma+1+\Delta k(\gamma+1+(\gamma^2-1)^{0.5}))]]+ \\ +((\gamma^2+4\gamma+1)/(\gamma+1))\ln[(\gamma+1+\Delta k(\gamma+1+(\gamma^2-1)^{0.5}))/(\gamma+1-\Delta k(\gamma+1-(\gamma^2-1)^{0.5}))]\}; \qquad (4')$$

at $\gamma>>1$ and $\Delta k\leq(\sim 1)$**:** $\sigma_a(\gamma,k'=k_{a\,max}-\Delta k,k''=k_{a\,max})\cong[(\pi(r_0)^2)/k_{a\,max}]\ln[1+2(k_{a\,max}-k')]; \qquad (4'')$

at $\Delta k=(1/2)$**:** $\sigma_a(\gamma,k'=k_{a\,max}-(1/2),k''=k_{a\,max}) \cong [(\pi(r_0)^2\ln 2)/\gamma]. \qquad (4''')$

Interdependence of k_a and θ_a gives possibility for a "needle-like" beam of monochromatic positrons, bombarding a very thin target, to pick out at some θ_a annihilation photons with a certain k_a. And it is also possible for a case to change continuously a value of k_a, changing γ (or θ_a). This possibility holds to some extent for a non-idealized case when there are energy, angle and position deviations in a positron beam at both an entrance and an exit of a target and (with some growths of these deviations in a target of some real thickness). These conclusions were successfully confirmed at axial collimation in the region of the giant resonances (GR) in atomic nuclei. On the installations with the quasimonochromatic annihilation photons at k_a significantly higher GR-region to reduce the background of bremsstrahlung photons from the target there was used off-axial collimation alone [6, 14, 15] or in combination with tagging by registering the "soft" photon emitted in the same act of two-photon annihilation [5, 9, 11, 13]. The latter may meet strong competition from the other methods of photon tagging (tagging of bremsstrahlung photons and tagging of laser photons, suffered Compton back scattering on an electron beam). For us it is important that at any energy E of ultra-relativistic positrons E_γ-distribution of annihilation photons has peak with the intrinsic width (FWHM) ~ 250 keV, and, for example, for photon energies of ~600 MeV, this width is narrower in about an order of magnitude than the energy spreads in these other methods of "photon monochromatization".

The presented cross sections of the positron annihilation correspond to a single electron, which is suffering collision with a positron. For the annihilation cross sections per atom one must consider all electrons of an atom. This means that such cross sections are proportional to the atomic number Z, while the cross sections of positron bremsstrahlung per atom are roughly proportional to Z(Z+1) [20]. Bremsstrahlung of positrons in annihilation target is an unwanted background process. To improve the ratio effect/background in annihilation targets it is more profitable to use substance with low Z as a target material. The best element for the annihilation targets is hydrogen. The use of hydrogen targets took place in [5, 14, 15] on the external accelerator targets, but the necessity in some foils for exit window of a beam vacuum chamber and for walls of a hydrogen target increases bremsstrahlung contribution in resulting photon flux.

The second main component of this proposal is the method, using in storage rings for positrons super-thin internal targets.

Positrons (electrons), captured in a storage ring, move near some closed central orbit with a perimeter Π, determined by bending magnets. Typically, there are some straight sections in a central orbit between sections with bending magnetic field. At the considered energies of positrons (electrons) their velocity $v \cong c$, where c is the velocity of light in vacuum. So in this case a time T_0 and a frequency f_0 for circulation of positrons (electrons) on a central orbit are respectively $T_0 \cong \Pi/c$ and $f_0 = 1/T_0 \cong c/\Pi$. Some reference particle with its energy supposed to move on this central orbit. To hold near central orbit positrons (electrons) with energy, equal to the energy of a reference particle, but with transverse linear and/or angular coordinates, deviated from those for a reference particle, there is used focusing.

Changes in velocity vector of positrons (electrons) lead to the emission of photons. In particular, this type of radiation is emitted in magnetic fields of bending magnets (synchrotron radiation, leading to a loss of total particle energy E, proportional to E^4/r if to count for motion along one entire circumference of radius r, where r is the radius of the orbit of a particle in some orbit's point under consideration). Therefore, strictly speaking, a reference positron (electron) is hypothetical one, for which synchrotron radiation is "switched off". Radiation losses can be also in focusing magnetic fields of a storage ring and in magnetic fields of various other devices, installed in storage ring, as long as they change velocity vector of positrons (electrons). To compensate radiation energy losses and (if necessary) to accelerate additionally positrons (electrons) the High Frequency (HF) resonator, operating at a frequency $f_R = k_R f_0$ (k_R – integer), is installed in a storage ring.

One of the essential characteristics of a storage ring is a positron (electron) beam lifetime T_L. Usually, the desired values of T_L are rather high, so particles in a storage ring should be able to perform a large number of turns, going a long way in a residual gas inside a vacuum chamber of a storage ring and repeatedly crossing an internal target in a storage ring, if the latter is introduced into the beam. To make it possible, it is necessary to have relatively high vacuum in the chamber of storage ring, and to use a sufficiently thin internal target. In addition, the requirements for vacuum may be exacerbated because of necessity that effects of beam interaction with gas atoms to be small in comparison with effects of beam interaction with target atoms. Here we consider such cases, in which currents of positrons (electrons) are not too large, so that we can disregard during T_L interaction between particles in storage ring, and does not take into account excitation by beam parasitic HF oscillations that could also additionally reduce the T_L.

Positrons (electrons) in a storage ring can perform damped oscillations of as their transverse linear and angular coordinates as their energy and phase in an electric field of a HF resonator with respect to those for a reference particle. At certain conditions (first of all: target should be thin enough (so-called super-thin target)), these oscillations take place due to the action of different magnetic fields in a storage ring and connected with each magnetic field radiation losses, and due to the action of an electric field in a HF resonator. Damping of these oscillations goes with their times T_D and leads to contraction of a beam in a region of six-dimensional trajectory space, the sizes of which are determined by the quantum fluctuations of radiation and ionization losses of positrons (electrons), as well as their multiple scattering in the target and in the residual gas in the chamber of storage ring. When the values of T_D are unacceptably high it is possible to reduce them by introducing additional magnetic devices for increasing particles' "wobbling" and respectively for growth of "radiation friction." As such a device there can be used undulator or wiggler.

Typically, $T_D \gg T_0$. On the other hand, for the real work it should be that $T_D \ll T_L$. A beam of positrons (electrons) in the storage ring has quasi-continuous time structure: through any cross-section of its vacuum chamber phase bunches of beam pass with the frequency of HF resonator f_R (or with frequency (f_R/n), where n – integer). For many experiments in nuclear physics it is possible taking into account time-resolution of used "electronics" to consider such a beam as continuous one. The portion of such cases can be increased by increasing the frequency of the HF resonator f_R by increasing k_R.

For high-precision studies of nuclear reactions, induced by positrons, electrons themselves or by annihilation quasimonochromatic photons and bremsstrahlung photons, there are requirements of high energy and angular resolutions for these positrons and electrons. Because of energy losses and multiple scattering in physical and annihilation targets and in radiators it is necessary to use for all of them small thicknesses (typically about $10^{-3}X_0$, where X_0 – radiation lengths of targets and radiators). In storage rings with super-thin internal targets the effective thickness of the target due to multiple crossings of the target by the circulating beam with suppression of produced changes and spreads of energies and angles of the beam particles may be as high as tenths of X_0 (i.e. two orders of magnitude greater than for external targets), while quality of parameters for the beam passing through the target is maintained very high. This is the main advantage of storage rings with super-thin targets in comparison with accelerators with the extracted beams. At decreasing of the yield for the studied process because of decreasing in its cross section (in particular, with the growth of the energy of incident particles, as for a case of positron annihilation in flight) this advantage permits to □have compensation due to pointed out growth of the effective thickness of the used target. At the same time, in researches with super-thin internal targets in storage rings for positrons (electrons) it is possible to have significantly higher levels of ratio effect/background than it used to be with external targets.

Now it is known about studies of electron scattering on atomic nuclei with inclusive (e,e') and exclusive (e,e'X) reactions carried out at storage rings with internal super-thin targets. These types of experiments were permanently in the spotlight of the Seminar EMIN [16, 17]. At storage rings with internal super-thin targets it is possible also to research electronuclear reactions, in which undergone inelastic scattering electrons or positrons themselves are not registered, but only emitted in such reactions particles X are registered. And in these cases it is possible to use differences of "working" in these reactions virtual photon spectra caused by either positrons or electrons as from each other as from the spectra of real photons. It is important also that internal super-thin targets are very "transparent" for low-energy charged particles X if it is necessary to detect these particles in electronuclear or (e,e'X) reactions. A set of experiments of these types including those with the use of polarized targets has been performed (and is still in progress) in INP SB RAS (Novosibirsk).

Moreover, on the electron beam in storage ring ADONE in Frascati with the internal argon-jet target there has been realized one of additional directions of internal super-thin target application, namely, production of tagged bremsstrahlung photons with usage of nearest to internal target one of the bending magnets of this storage ring [15].

However, until now the use of internal super-thin targets in storage rings for production of annihilation photons was not carried out, although it is very interesting to examine the possibilities of such direction of their usage. In principle, for this direction there are expected the following advantages:

1. If the transverse and energy acceptances of the used circular accelerator-injector for a storage ring are sufficiently large, then due to "radiative cooling", providing growth of the positron density in the trajectory space, the current of injected positrons with the desired geometrical

and energy parameters, can be significantly increased in comparison with the current from the injector, where there is no such a growth.

2. Due to the "radiative cooling" in the storage ring itself the effective thickness of the annihilation target and coefficient of conversion from positrons to quasimonochromatic annihilation photons increase significantly.
3. The produced beam of annihilation photons acquires a quasicontinuous character, which can facilitate the work of the used "electronics" in many cases.
4. Strongly improved background conditions are provided.
5. The most "attractive" targets for the best relationship between annihilation and bremsstrahlung, namely, pure hydrogen targets become possible.

In this method expected profits are several orders of magnitude in intensity of the quasimonochromatic photons and several times in ratio of the intensities of annihilation and bremsstrahlung photons produced in the same target.

In this report the project for source of the quasimonochromatic annihilation photons with energies (500÷750) MeV on the basis of the internal super-thin hydrogen target at storage ring VEPP-3 of Institute of Nuclear Physics (Novosibirsk, about the VEPP-3 see, for example, in [21]) is presented.

According to estimations the VEPP-3 answers in a great extent to demands for such a source. The table lists some important parameters for this project.

Table. Parameters of VEPP-3, target and beams

central orbit perimeter Π, m	74.39
frequency of beam revolution f_0, MHz	4.03
period of beam revolution T_0, ns	248.14
frequency of HF resonator f_{R1}, MHz	8.06
frequency of HF resonator f_{R2}, MHz	72.54
time of injection, s	12
stored positron current I, mA	~60
energy of positrons E, MeV	~600
damping time of beam oscillations T_D, s for vertical betatron oscillations; for radial betatron oscillations; for phase oscillations	 0.161; 0.175; 0.077
H_2-target thickness X_H, atoms/cm^2	10^{16}
positron beam lifetime T_L, s	~30
average luminosity L, cm^{-2}	$\sim 6 \cdot 10^{32}$
flux of annihilation photons N_γ at $\theta_\gamma \leq 3$ mrad , s^{-1}	$\sim 2 \cdot 10^5$
flux of annihilation photons N_γ at $5 \leq \theta_\gamma \leq 10$ mrad , s^{-1}	$\sim 2 \cdot 10^5$

In one sub-cycle of injection with duration ~2 s there will be injected in VEPP-3 $\sim 2 \cdot 10^{10}$ positrons with energy ~500 MeV [22], what will give current ~10 mA in VEPP-3. So it will take 12 s for the full cycle of injection to reach the positron current I~60 mA. Positrons will be additionally accelerated up to energies (500-750) MeV during time about 10 s. The positron lifetime in the VEPP-3 with H_2-target, having the thickness 10^{16} atoms/cm^2, is T_L ~30 s. In these conditions the optimal time for the data measurement is ~33 s, taking into account also the time ~5 s for returning to the injection energy. After that the total cycle of operation starts again. But even in these conditions “macroscopic” duty factor is on the level of tens percents. At injection of positrons, which already have necessary energies, this duty factor can be essentially increased. In pointed out conditions the average over the total cycle of operation positron current will be ~13.3 mA, and the average luminosity $L \approx 8 \cdot 10^{32}$ cm^{-2}. In the table the values of N_γ are given for the positron energy E=600 MeV.

The complex of the internal super-thin target on the base of the H_2- gas storage cell (see, for example, [17]) is situated in the region of the changed central orbit (see fig. 3). The equipment, included in this complex, except for the target itself, consists of: the dipole (D1-D3) and quadrupole (Q1-Q3) magnets; the elements of the vacuum chamber; several turbo-molecular pumps with pumping speed (1-2)·10^3 l/s; the elements of beam diagnostics; two high-vacuum valves; etc. The hatched area may be used for targets and detectors in carried out physics researches. At off-axial collimation targets for physics researches having central holes may be useful to exclude main part of background from bremsstrahlung, produced by positrons in internal target itself.

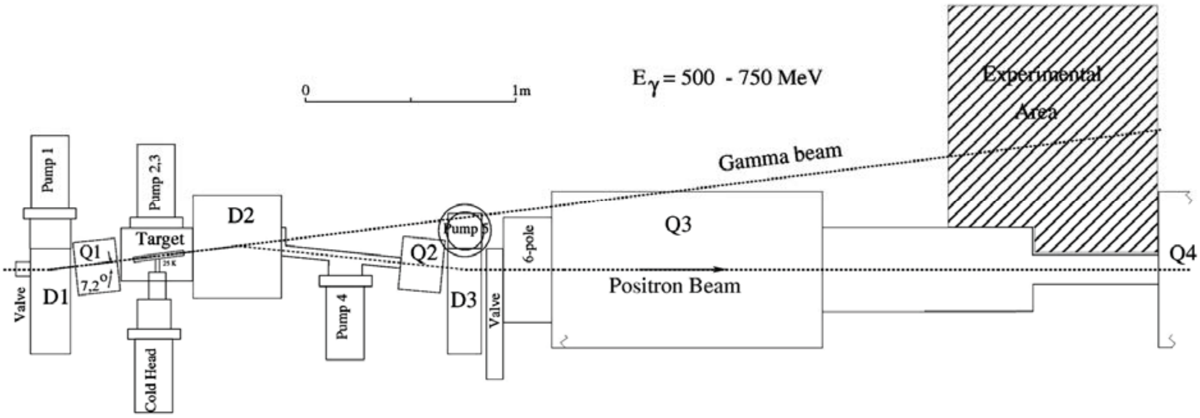

Fig. 3. Arrangement of equipment for production of quasimonochromatic annihilation photons at VEPP-3

In fig. 4a for a case of the positron energy E ≅ 600 MeV it is shown in the photon spectrum the narrow peak at the photon energy $E_\gamma \cong 600$ MeV. Such a spectrum may be essential for tasks, connected with searches of narrow resonances in photonuclear processes (see, for example, report [23] in the present Seminar). At estimations of energy spreads of real annihilation photon beams, except for the pointed out above intrinsic spread ~μ/2, it is necessary from different possible spreads for super-thin target to take into account first of all energy ($\sim 3\cdot 10^{-4}$E) and angular (horizontal – $\sim 7\cdot 10^{-4}$ rad and vertical – $\sim 1.5\cdot 10^{-4}$ rad) spreads of circulating in VEPP-3 positron beams. Taking into account expression of interdependence (2) (from which at $\Delta\theta \leq \sim(1/\gamma)$ we have $\Delta k \approx [\gamma^2(\Delta\theta)^2/2]$) we receive in these estimations instead of the intrinsic spread ~250 keV at E=600 MeV the resulting characteristic energy spread of real annihilation photon beam in VEPP-3 ~350 keV.

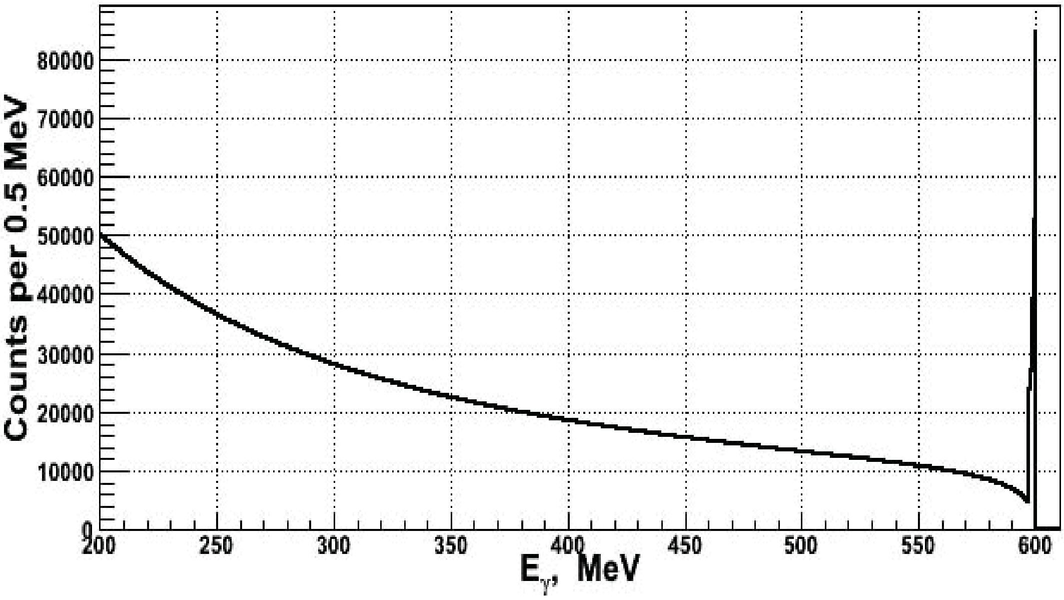

Fig. 4a. Estimated spectrum of bremsstrahlung and annihilation photons at θ_γ<3 mrad for: positron energy E=600 MeV; luminosity L=6·10^{32} $cm^{-2}s^{-1}$; binning width - 500 keV

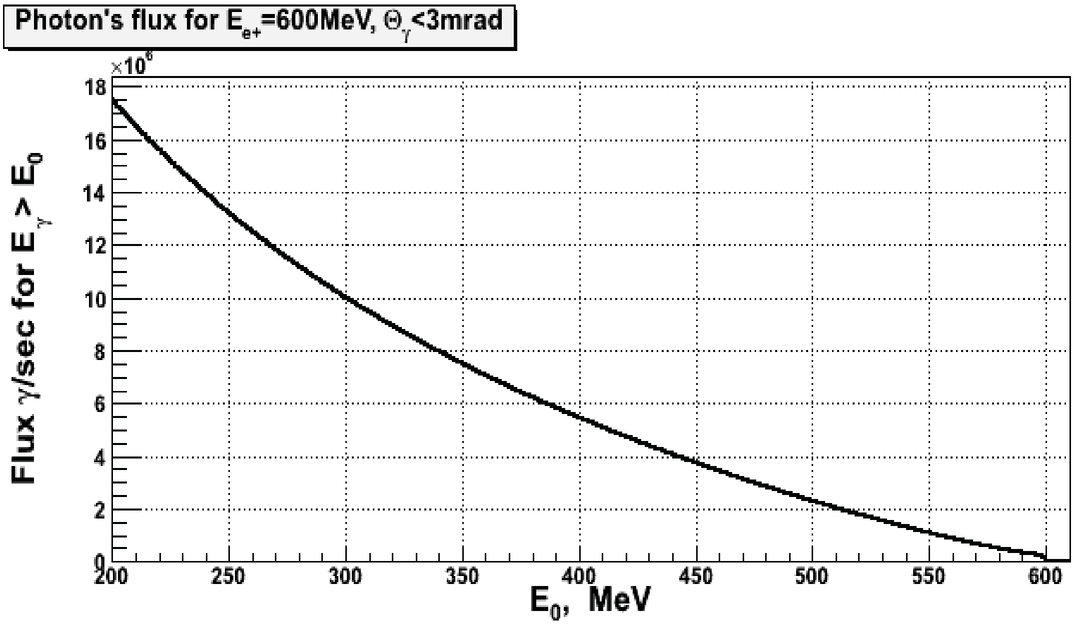

Fig.4b. Estimated flux of bremsstrahlung and annihilation photons at $\theta_\gamma<3$ mrad for: positron energy $E=600$ MeV; luminosity $L=6\cdot10^{32}$ $cm^{-2}s^{-1}$

The grave shortcomings of the shown in fig. 4a and 4b respectively the spectrum and the flux of the expected photons are connected with the relatively high level of bremsstrahlung background. However, as it was pointed out above, influence of this background may be essentially decreased at off-axial collimation. For example, at the same positron energy and luminosity as for a case of fig. 4a and 4b there are shown in fig. 5a and 5b respectively the spectrum and the flux of the expected photons , when the photon polar angle θ_γ is restricted from 5 to 10 mrad. It is seen that annihilation peak becomes wider and its height decreases approximately an order of magnitude, but number of annihilation photons in their peak is approximately the same as in the first case with $\theta_\gamma<3$ mrad, namely $\sim2\cdot10^5$ s^{-1}, and the flux of bremsstrahlung photons in the second case is less approximately one and a half order of magnitude in comparison with that in the first case.

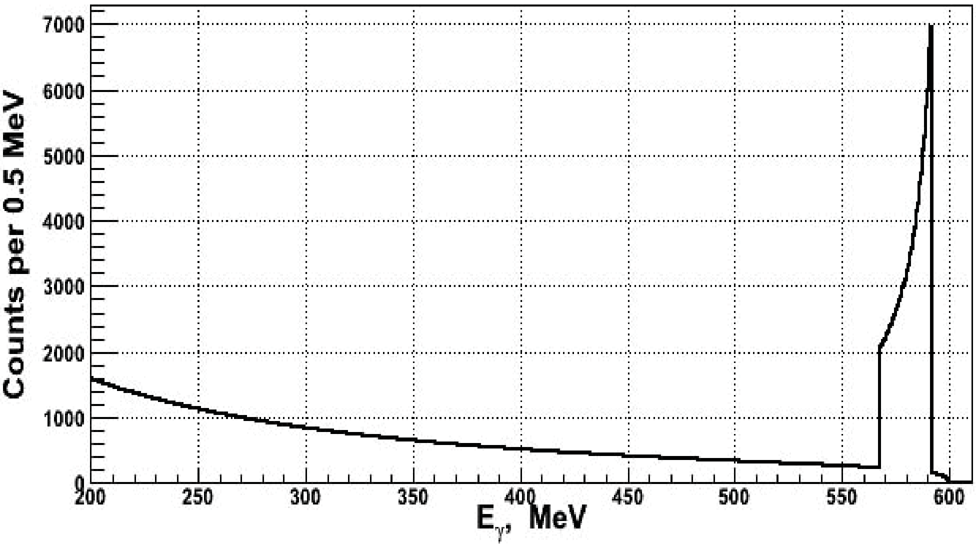

Fig. 5a. Estimated spectrum of bremsstrahlung and annihilation photons for: off-axal collimation with θ_γ from 5 to 10 mrad; positron energy $E=600$ MeV; luminosity $L=6\cdot10^{32}$ $cm^{-2}s^{-1}$; binning width - 500 keV

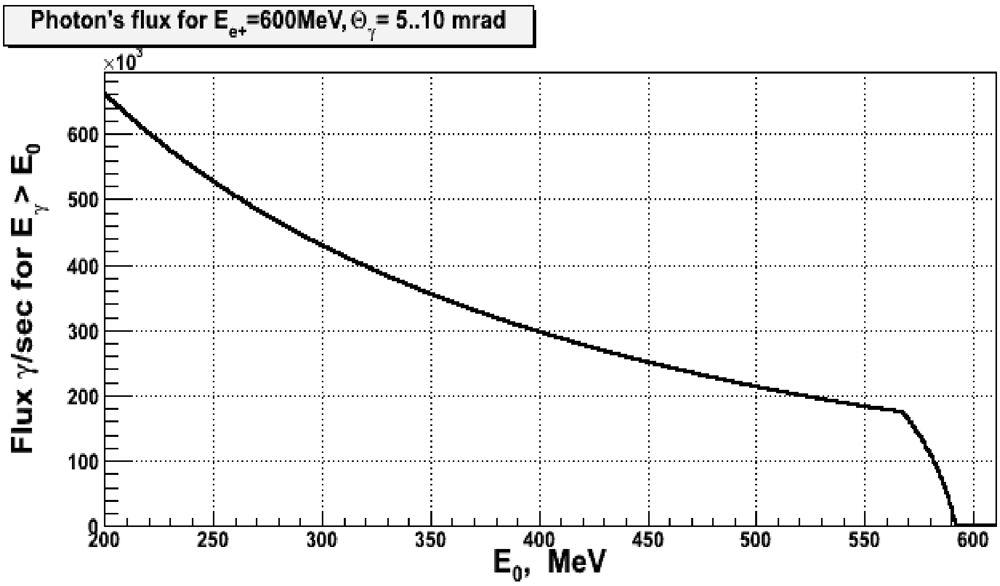

Fig. 5b. Estimated flux of bremsstrahlung and annihilation photons for: off-axial collimation with θ_γ *from 5 to 10 mrad; positron energy E=600 MeV; luminosity* $L=6\cdot10^{32}$ $cm^{-2}s^{-1}$

Beam characteristics, presented in fig. 4a, 4b, 5a, 5b and in table, are suitable for solving different problems. It is so, for example, for researches of eta-mesic nuclei, described, in particular, in one report of the present Seminar [24]. Also it is so for studying of the virtual photon spectra [25], produced in processes with relatively small transfers of energy and impulse and accompanied by reactions of photofission, for example, ^{238}U(γ,F), at energies of incident photons in the region of hundreds MeV, where for fission of nuclei-actinides there was found that total cross sections are essentially higher than, what are predicted by so-called “universal curve” [26], in result, as it is supposed, of influence of unlinear effects of quantum electrodynamics in photonuclear processes, what promises good perspectives for interesting investigations [27]. In such investigations acts of fission in relatively thin detector of fission fragments are registered in coincidence with signals from spectrometer of total absorption from photons (or, maybe, together with electrons and/or positrons), emitted in the forward direction. For detector of fission fragments it is suggested to use parallel-plate gas detectors, similar to those, used in [28], or to low pressure proportional cameras, used in [26]. It is necessary also to note that with such an annihilation photon beam measurements of total photofission cross sections of nuclei-actinides, for example, ^{238}U, are very interesting. In the last cases it is possible to use described in [25] detectors of fission fragments on the base of thin polycarbonate films with usage of data about cross sections of reaction ^{238}U(γ, *F*) as in the region of giant resonance, presented and analyzed in [25], as at higher energies (see, for example, [29]).

It is important to point out that the proposed scheme for a photon source is almost completely identical to the scheme of installation for search of a new vector boson A' in the experiment, which was also proposed for the VEPP-3 [30].

References

1. C.Tzara. Compt. Rend. Acad. Sci. 1957. V. 245. P. 56.
2. J.Miller, C.Schuhl, C.Tzara. Nucl. Phys. 1962. V. 32. P. 236; R.Bergere. In “Lecture Notes in Physics”. V. 61. Springer-Verlag. Berlin-Heidelberg-New York. 1977. P. 1.

3. S.C.Fultz *et al*. Phys. Rev. 1962. V. 127. P. 1273; B.L.Berman, S.C.Fultz. Rev. Mod. Phys. 1975. V. 47. P. 713.
4. R.E.Sund *et al*. Phys. Rev. 1968. V. 176. P. 1366.
5. J.Ballam *et al*. Nucl. Instr. and Meth. 1969. V. 73. P. 53.
6. D.Blum *et al*. Nucl. Instr. and Meth. 1974. V. 115. P. 553.
7. U.Kneissl *et al*. Nucl. Instr. and Meth. 1975. V. 127. P. 1.
8. L.Z.Dzhilavyan, N.P.Kucher. Yadernaya Fizika 1979. V. 30. P. 294 {Sov. J. Nucl. Phys. 1979. V. 30. P. 2}; L.Z.Dzhilavyan, V.L.Kuznetsov, N.P.Kucher, V.G.Nedorezov *et al.* Preprint INR P-0121, M. 1979 (in Russian).
9. A.Veyssiere, H.Beil, R.Bergère *et al*. Nucl. Instr. and Meth. 1979. V. 165. P. 417.
10. R.Leicht *et al*. Nucl. Instr. and Meth. 1981. V. 179. P. 131.
11. W.R.Dodge, E.Hayward *et al*. Phys. Rev. C. 1983. V. 28. P. 8.
12. P.Berkvens, R.Van de Vyver *et al*. Nucl. Instr. and Meth. 1984. V. 227. P. 395.
13. P.Argan *et al*. Nucl. Instr. and Meth. 1984. V. 228. P. 20.
14. G.P.Capitani *et al*. Nucl. Instr. and Meth. 1983. V. 216. P. 307.
15. G.Ricco. 1988 EMIN Proc., P. 114; M.Anghinolfi, P.Corvisiero, L.Z.Dzhilavyan, G.Ricco, M.Sanzone, M.Taiuti, A.Zucchiatti. 1988 Gordon Conference on Photonuclear Reactions.
16. S.G.Popov. EMIN Proc.: 1981 (P. 127); 1984 (P. 214); 1988 (P. 32); 1991 (P. 174); Yad. Fiz. 1999. V. 62. P. 291 {Phys. At. Nucl. 1999. V. 62. P. 256}.
17. D.M.Nikolenko. 2000 EMIN Proc. (P. 263); D.M.Nikolenko, I.A.Rachek, D.K.Toporkov, *et al*.: EMIN Proc.: 2003 (P. 109) and 2006 (P. 104); Yadernaya Fizika. 2010. V. 73. P. 1365 {Phys. At. Nucl. 2010. V. 73. P. 1322}.
18. L.Z.Dzhilavyan, N.P.Kucher, V.S.Yurchenko. Preprint INR P-0152, M. 1980 (in Russian).
19. H.W.Kendall, Martin Deutsch. Phys. Rev. 1956. V. 101. P. 20.
20. L.I.Schiff. Phys. Rev. 1951. V. 83. P. 252; H.W.Koch, J.W.Motz. Rev. Mod. Phys. 1959. V. 31. P. 920.
21. A.N.Aleshaev *et al*. Preprint INR 2011-20, Novosibirsk. 2011 (in Russian).
22. K.V.Astrelina *et al.* ZhETF. 2008. V. 133. P. 94 {JETP. 2008. V. 106. P. 77}.
23. L.V. Fil'kov. Search for super-narrow six-quark states. EMIN-2012.
24. V.V.Polyanski (for the LPI-JINR-INR collaboration). On photoproduction of eta-mesic nuclei at the LPI synchrotron. EMIN-2012.
25. L.Z.Dzhilavyan, V.G.Nedorezov. LXII Intern. Conf. “Nucleus 2012”. Book of abstracts. Saint Petersburg. 2012. P. 99.
26. A.A.Kazakov, G.Ya.Kezerashvili, L.E.Lazareva, V.G.Nedorezov, A.N.Skrinsky, *et al.* Pis’ma v ZhETF 1984. V. 40. P. 445 {JETP Lett. 1984. V. 40. P. 1271}.
27. S.T.Belyaev, D.F.Zaretzkiy, N.S.Dudina, D.I.Ivanov, V.L.Kuznetzov, V.G.Nedorezov *et al.* Preprint IAE- 5726/2. M. 1994 (in Russian).
28. H. Ries, G. Mank, J. Drexler, et al. Phys. Rev. C. 1984. V. 29. P. 2346.
29. V.G.Nedorezov, Yu.N.Ranyuk. Fotodelenie yader za gigantskim rezonansom. Kiev: Naukova dumka. 1989 (inRussian).
30. B. Wojtsekhowski, D. Nikolenko and I. Rachek, arXiv:1207.5089 [hep-ex].

ELECTRON LINEAR ACCELERATOR LUE-8-5 WITH W-Be PHOTONEUTRON TARGET AS A NEUTRON SOURCE

A.V.Andreev[1], Yu.M.Burmistrov[1], A.M.Gromov[1], E.S.Konobeevski[1], M.V.Mordovskoy[1], G.V.Solodukhov[1], S.V.Zuyev[1], V.I.Firsov[2], Yu.M.Zipenyuk[2]

[1] Institute for Nuclear Research, Russian Academy of Sciences, Moscow, Russia;

[2] State Scientific-Research and Design Institute of Rare-Metal Industry "Giredmet" JSC, Moscow, Russia

We describe a neutron source based on electron linear accelerator LUE-8-5 of the Institute for Nuclear Research and neutron-producing target consisting of tungsten bremsstrahlung converter and beryllium photoneutron target. The estimates performed show that for average electron current of 30 μA, using a W-converter with thickness of 3-5 mm and Be photoneutron target (~ 20 cm), the neutron yield will be ~ $3\text{-}5\cdot10^{10}$ n/s. The use of polyethylene moderator around the Be-target will lead to the thermal neutron flux near the target ~ $10^8\text{-}10^9$ n/(cm^2·s). Such a flux will ensure the metrological characteristics of neutron-activation determination of the content of most rare and precious metal.

Linear electron accelerators with energies of 8-10 MeV are widely used in practice in many fields of science, engineering and technology. Their attractive properties compared with reactor neutron sources and neutron generators are relatively low cost, compactness, reliability, industrial availability and safety.

Lower, in comparison with the reactor, neutron fluxes (especially of thermal energies) restrict the use of these facilities for the analysis of pure substances and materials. However, for the analysis of geological samples (ores, products of their processing and enrichment, breed, waste products of the ore enrichment enterprises, etc), these methods can be applied successfully and compete with other activation methods, not yielding and often exceeding their limits of content determination. The advantages of this approach include high performance, the ability to simultaneously determine the content of several elements during a single irradiation and representativeness of the results of the analysis. It is important also that, irradiating the samples by neutron fluxes of 10^8 - 10^9 n/(cm^2·s) during up to several hours, most of the samples can be returned in 3-4 weeks to the customer in unmodified form for the further research. Especially, it is important for the unique or expensive samples.

Main characteristics of electron accelerator LUE-8-5 are presented in Table 1.

Table 1.

Energy of accelerated electrons	8 MeV
Repetition r ate	Up to 600 Hz
Power in beam	Up to 5 kW
Pulse duration	3 μs
Average current at 50 Hz	30 μA

The neutron flux at electron accelerators can be obtained or by direct photofission reaction or by photoproduction of neutrons in a material with low atomic number. In view of that the effective energy of the bremsstrahlung gamma from tungsten converter is about 2-3 MeV, the choice of the target material is limited by ^{9}Be ((γ, n) threshold = 1.67 MeV) or deuterium (the threshold of 2.26 MeV.

Despite the fact that the (γ, n) cross section for deuterium is twice higher than for beryllium, the use of beryllium is preferable by the criteria of accessibility, good thermal conductivity and relative cheapness. Thus, for W-convertor and Be-target using 8 MeV electrons with average current of 30 μA, fast neutron yield of (3-5)·10^{10} neutrons/s can be obtained (Fig.1).

The use of moderators (Fig.2) will greatly extend the application of neutrons for analytical purposes. This applies particularly to the development of non-destructive methods for determining the elements that are poorly analyzed by fast-neutron activation These elements include some precious metals, a number of refractory metals and rare earth elements. In addition, the source of slow neutrons gives the opportunity to develop methods for determining the macro-content of elements (from 5 to 100% by weight). The use of a pneumatic transport system allows to develop techniques using short-lived isotopes with half-life $T_{1/2}$ <10 min, which are very rarely used in the reactor variant of analysis.

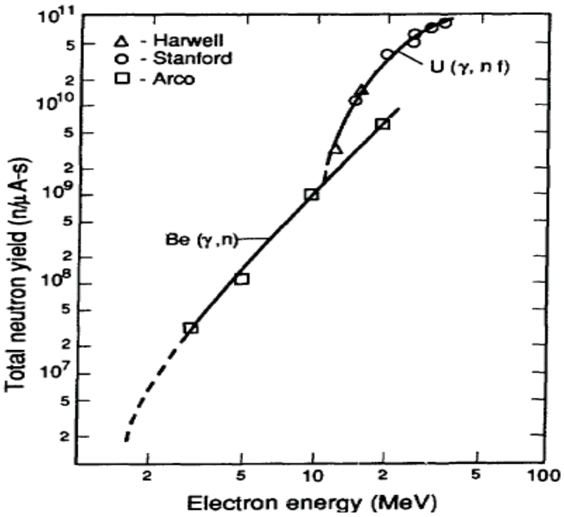

Fig.1. Total neutron yield for Be and U targets

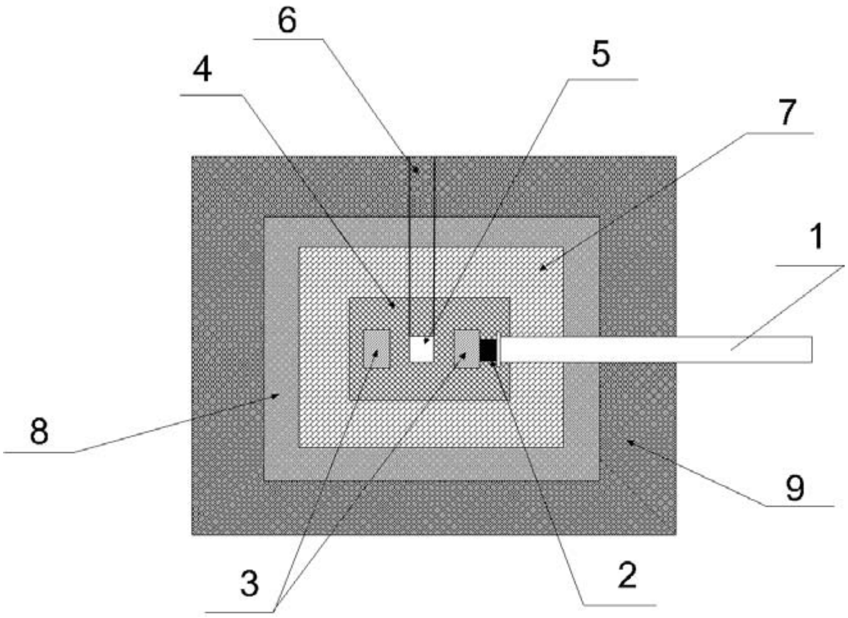

Fig.2. Photoneutron source of thermal neutrons: 1 - electron source, 2 - tungsten converter of bremsstrahlung gamma rays, 3 - berillium photoneutron target, 4 - polyethylene moderator, 5 - cavity for irradiated samples, 6 - inlet for placing irradiated samples, 7 - converter-reflector, 8 – heavy metal shielding, 9 – borated polyethylene neutron shielding.

Electrons from the accelerator LUE-8-5 (1) with a maximum energy of 8 MeV hit the tungsten converter (2) with thickness of 0.5 radiation length and form the flux of bremsstrahlung gamma rays with maximum energy of 8 MeV. These gamma rays incident on the beryllium target (material with low photoneutron threshold) form the fast neutrons with average energy of ~2 MeV. Fast neutrons in the polyethylene moderator (4) undergo collisions with hydrogen nuclei, resulting in diminishing of energy to 0.07 eV, which is close to the energy of thermal neutrons. Thermal neutrons permeate the cavity (5), in which the studied samples are irradiated. The size of the cavity depends on the required number of irradiated samples and range from $1\cdot1\cdot1$ cm^3 to $10\cdot10\cdot10$ cm^3), while the position of its center inside the moderator should coincide with a maximum of thermal neutron flux in the moderator. The imposition of samples for irradiation is performed through the hole (6). During the irradiation this hole is closed with a stopper made from the same materials as the walls of the block-moderator. Neutrons emitted outward the moderator, are collided with the material of converter (7) and some of them have reflected back into the moderator. Additionally, the converter-reflector multiplicates the not yet slowed-down fast neutrons by the reaction (n,2n). The most effective materials for use as converter are Be, W, Pb and U.

For the LUE-8-5 Neutron Source this yields the maximum thermal neutron flux of ~ $2\cdot10^8$-10^9 n/(cm^2·s) at fast-neutron yield of $1\text{-}5\cdot10^{10}$ n/s.

On the basis of numerous analyzes of hundreds of types of geological samples (10 - 50 g each) – ores and products of their processing and enrichment, the lower limits of content determination (η,% mass) of Au, U, Th, rare-earth elements, rare and refractory metals were estimated (see Table 2) [1,2].

Table 2. Lower limits of content determination of some elements in ores

Elements	η,% mass
Cr, Zn, Mo, Ce, Hg, Ta, Te	$(1\text{-}3)\cdot10^{-2}$
Sc, Co, Cu, As, Ga, Hf, U, Th	$(1\text{-}3)\cdot10^{-3}$
REE (La, Eu, Dy, Sm, Yb, Lu), Sb, Re, W, Ir	$(2\text{-}4)\cdot10^{-4}$

In conclusion it should be mentioned that the experimental values of the lower limit of content determination clearly demonstrates the capabilities of the NAA, which can be implemented on a modernized electron linac LUE-8, completed by the moderator with relevant characteristics and low-background germanium gamma spectrometer.

[1]. Andreev A.V., Burmistrov Yu.M., Firsov V.I. Estimation of possibilities of thermalized neutrons on the basis of neutron generator for activation analysis // Zavodskaya laboratoriya. V. 65 (2010) 1283-1289

[2]. J. Stokes, *et al.*, IRT 46110-019, IRT Corp. (1981)

PHOTOFISSION OF URANIUM

A.A.Kuznetsov

Skobeltsyn Institute of Nuclear Physics, Lomonosov Moscow State University, Moscow, Russia
E-mail: kuznets@depni.sinp.msu.ru

In this work we study ^{238}U photofission product yields with bremsstrahlung endpoint energy of 19.5, 29.1, 48.3 and 67.7 MeV. The experiment was carried out on an electron racetrack microtron RTM-70 at SINP MSU [1]. A sample was a natural mix of uranium isotopes coating on the aluminum disc. Identification of photofission products and the determination of their quantitative characteristics carried out by gamma spectroscopy. Gamma spectra of the residual activity of the irradiated sample were measured with high - pure germanium detector.

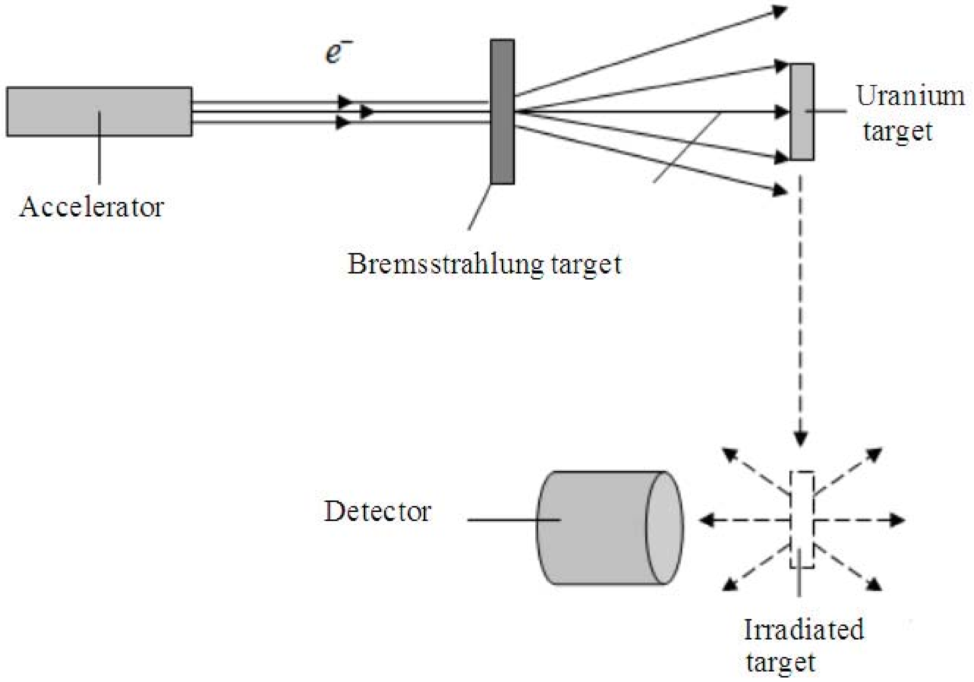

Figure 1. Experimental scheme

In this work were obtained independent and cumulative postneutron yields of fission products. From independent and cumulative yields were obtained the photofission mass distributions. In Fig. 2, the photofission chain yield is normalized to the yield of ^{238}U(γ, n)^{237}U reaction. From the mass distribution was obtained by peak to valley ratio (the ratio of asymmetric and symmetric fission components). In Fig. 3 shows the peak to valley ratio, obtained in our experiment and other experimental papers.

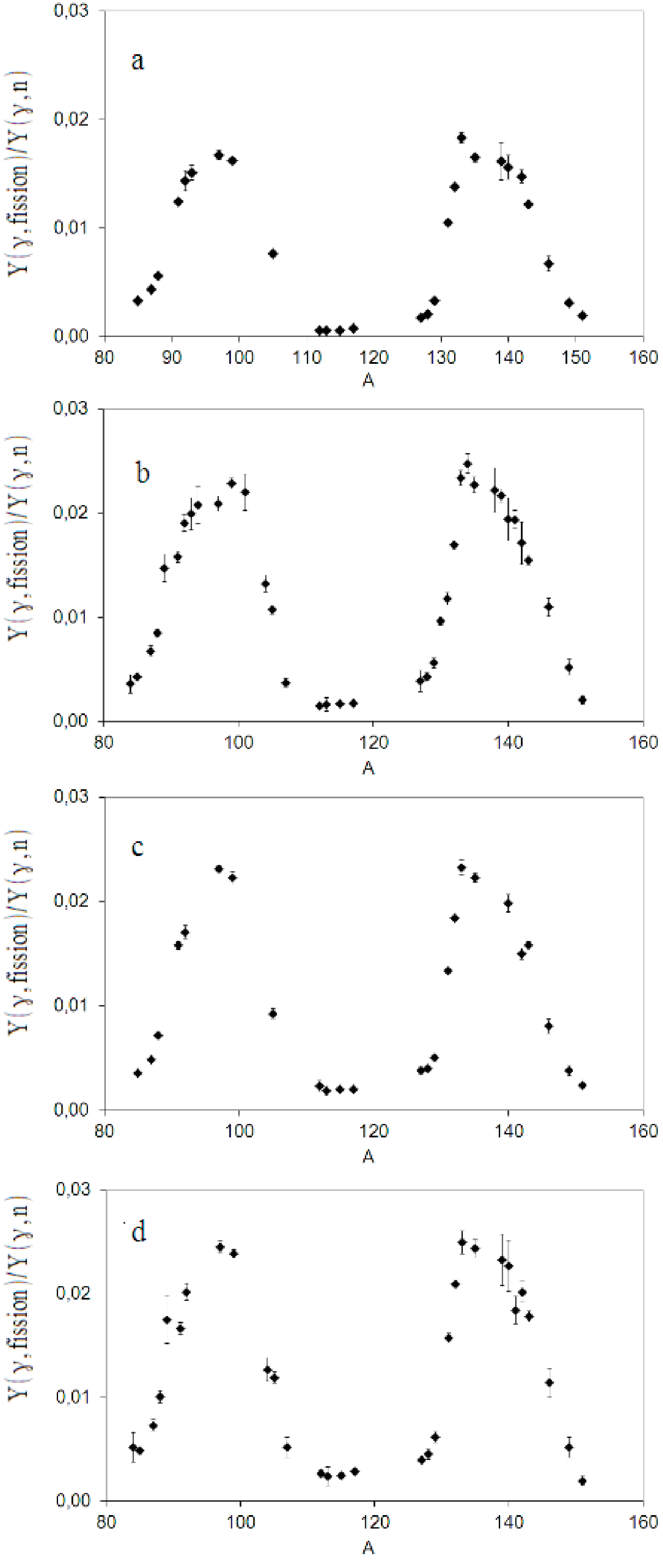

Figure 2. Mass distribution of ^{238}U photofission with bremsstrahlung endpoint energy a)19.5, b) 29.1, c) 48.3 and d) 67.7 MeV

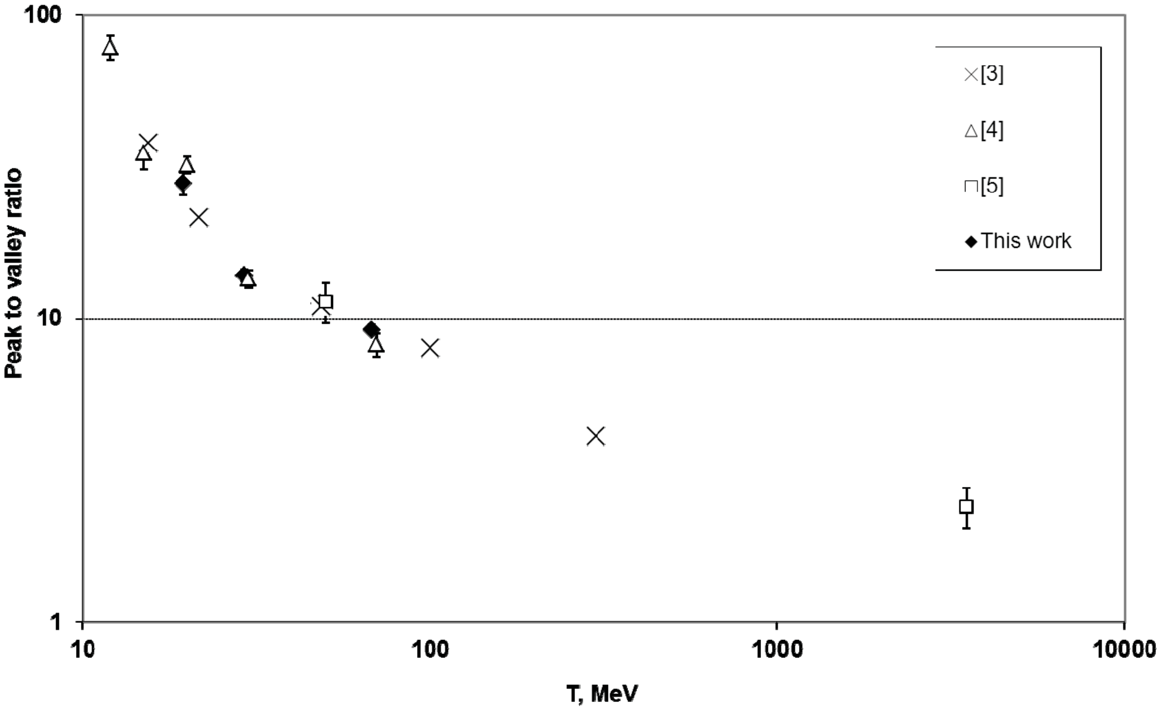

Figure 3. Peak to valley ratio in the photofission of ^{238}U as a function of bremsstrahlung endpoint energy

The total chain yield with the mass number A is the sum of symmetric and asymmetric fission modes. For each mode of fission yields is described as a Gaussian. The total yield of the fragments with the mass number A is defined as [2]:

$$Y(A) = Y_{SL}(A) + Y_{ST1}(A) + Y_{ST2}(A)$$

$$Y(A) = K_{ST1} \cdot \exp\left[-\frac{(A-\overline{A_{SL}}-D_{ST1})^2}{2\sigma_{ST1}{}^2}\right] + K_{ST1} \cdot \exp\left[-\frac{(A-\overline{A_{SL}}+D_{ST1})^2}{2\sigma_{ST1}{}^2}\right] +$$

$$+K_{ST2} \cdot \exp\left[-\frac{(A-\overline{A_{SL}}-D_{ST2})^2}{2\sigma_{ST2}{}^2}\right] + K_{ST2} \cdot \exp\left[-\frac{(A-\overline{A_{SL}}+D_{ST2})^2}{2\sigma_{ST2}{}^2}\right] + K_{SL} \cdot \exp\left[-\frac{(A-\overline{A_{SL}})^2}{2\sigma_{SL}{}^2}\right]$$

To compare the experimental data performed on the bremsstrahlung was estimated average excitation energy of the nucleus.

We obtained the mode contributions of photofission in the mass distribution depending on the average excitation energy of the fissioning nucleus. Experimental data for the analysis were obtained from our work and other experimental papers [3, 4, 6, and 7]. The contribution of the symmetric (SL) fission mode is growing. Contribution of asymmetric mode (ST1), related to the neutron shell N = 82, decreases. Contribution to the mass distribution of the asymmetric mode ST2, associated with the deformed neutron shell N = 86 - 88, in the studied energy range doesn't change.

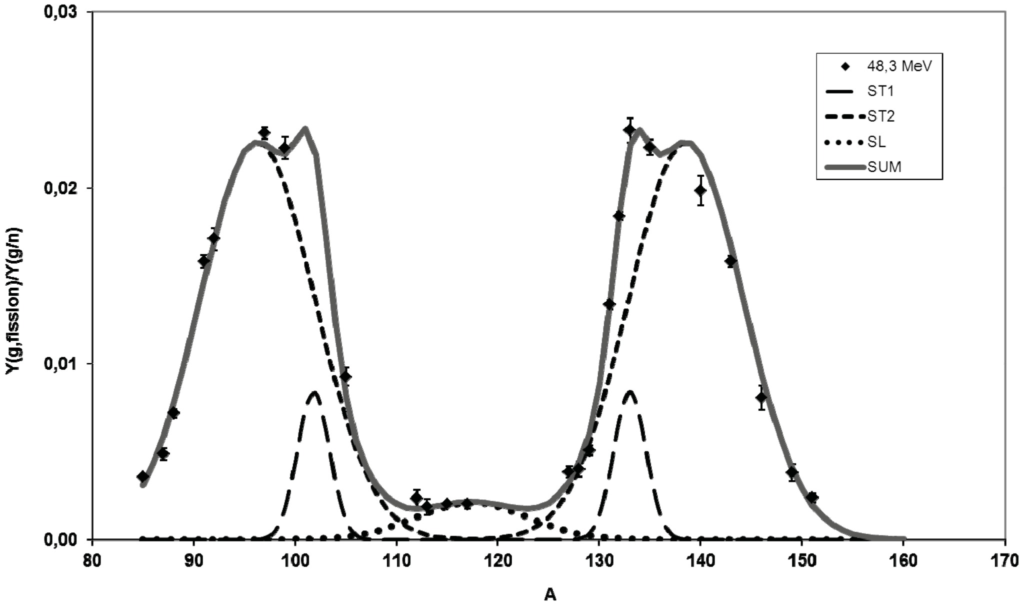

Figure 4. Plot of the five-Gaussian model of the chain yield as a function of mass *A*. The dashed curves represent individual Gaussian functions and the solid curve is their total sum. Approximation was performed for the accelerator energy of 48.3 MeV

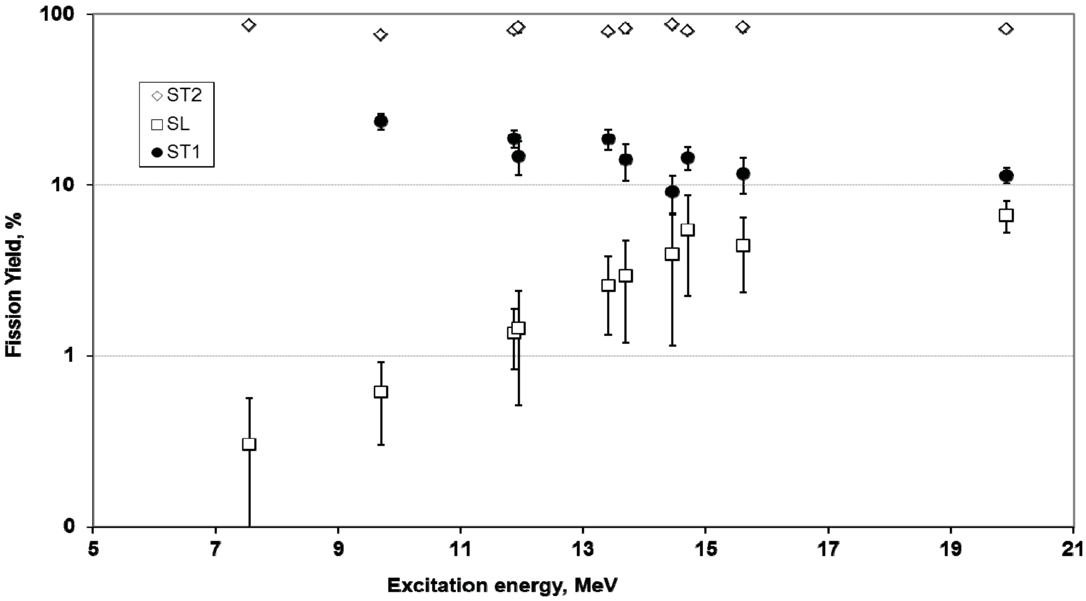

Figure 5. The dependence of the photofission chain yield for different modes of fission as a function of the average excitation energy

[1] Shvedunov V.I., Ermakov A.N., Gribov I.V. et al.//Nuclear Instruments and Methods in Physics Research A, 2005, 550, 1, P. 39.
[2] Wahl A.C.// Systematics of Fission-Product Yields, LA-13928
[3] Schmitt R.A. and Sugarman N. //Phys. Rev., 1954, 95, P. 1260.
[4] Jacobs E. et al.//Phys. Rev. C, 1980, 21, P. 237
[5] Demekhina N. A. and Karapetyan G. S. // Yad. Fiz. 2008. V.71 P.28
[6] Pomme S. et al. Nuclear Physics A572 (1994) 237-266
[7] Naik H. et al. / Nuclear Physics A853 (2011) 1–25

LOW BACKGROUND GAMMA-SPECTROMETER WITH COSMIC RAY ANTICOINCIDENCE SHIELDING

*A.V.Andreev, Yu.M.Burmistrov, E.S.Konobeevski, M.V.Mordovskoy,
S.V.Zuyev, V.I.Firsov*

Institute for Nuclear Research of Russian Academy of Sciences, Moscow, Russia
E-mail: ava@sci.lebedev.ru

The gamma ray spectrometer protected by passive shield (15 cm of Pb, 2 cm of W, 2 cm of Cu, and 1 cm of Sn) and active shield of one 50 x 50 x 5 cm^3 plastic anticoincidence scintillator is described. Various variants of external and internal passive shielding were studied. At the moment the achieved background count rate (100-3000 keV) is ~ 3 cps. The achieved level of background suppression, when using active protection, compared with the version of only passive protection is 0.78, while for 511 keV gamma line this factor is about of 0.5.

Low-background measurements using germanium detectors are performed in underground or above-ground laboratories. The background levels in underground laboratories are generally much lower than in the above-ground ones. However, measurements of the activity of samples containing short-lived isotopes, irradiated at accelerators and neutron generators, should be carried out near the irradiating apparatus (i.e. at above-ground laboratories).

In the present work as the detector of low background gamma-spectrometer we used a high purity germanium crystal with volume of 130 cm^3 and relative efficiency of 30% (compared to efficiency of 3'·3' NaJ detector for 1332 keV γ-line). For comparison with other spectrometers all data were converted to 100% relative efficiency.

As the passive shielding we tested two versions of chambers with different configurations and sizes (see Fig.1). We have different Pb shielding materials with their own activity. Some results obtained for three types of materials used are presented in Table 1.

Defined element, % by weight	Analyzed material		
	Pb-1*	Pb-2**	Cu***
U	$3.5\cdot10^{-5}$	$<3\cdot10^{-5}$	$<5\cdot10^{-5}$
Th	$1.0\cdot10^{-4}$	$4\cdot10^{-5}$	$7\cdot10^{-5}$

Table 1. *version #1.1980, ** version #2.1970,
*** Oxygen-free electrolytic copper

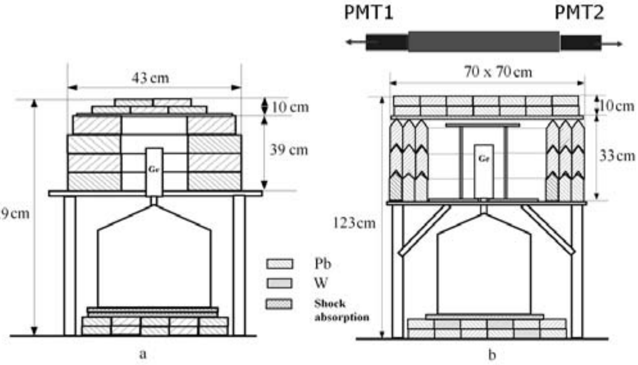

Fig. 1. Low-background chamber
a) Pb – ring; b) Pb - curly bricks

The detector was placed on a concrete platform with thick (20 cm) Pb plate with the detector's dewar underneath. This plate was used to reduce high contribution of ^{40}K 1460 keV gamma-line. Sealing and flushing the chamber with nitrogen to remove radon near the detector is the next step of the work. Monte-Carlo calculations have been performed in order to select the most appropriate material and the optimal thickness for the inner lining. It is found that some set of materials (W, Cu and finally Sn) can significantly reduce the total background. The optimal thickness of these materials (2 cm W, 2 cm Cu, and 1 cm Sn) was used in the final setup. It was observed that X-rays of Sn are reduced using 0.5 mm Cu near the detector. The internal volume of the chamber was 15*20*30 cm^3. In Fig. 2 one can see the background spectra depending on different sets of materials used. The small insertion on Fig. 2 shows the 185.7 keV peak of ^{235}U. Final total background count rate was 3.8 cps.

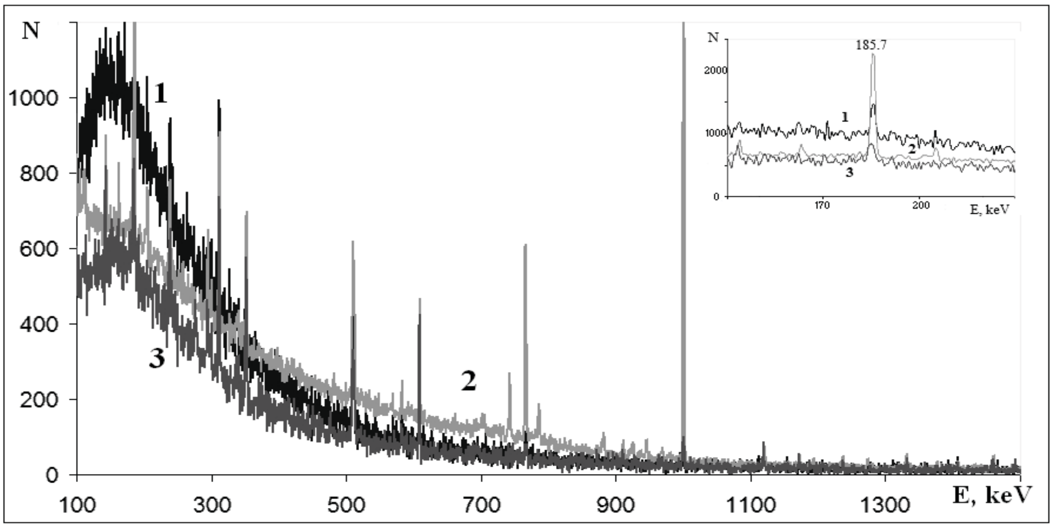

Fig. 2. Gamma spectrum of the natural background depending on different sets of materials: Pb (1), Pb + W (2), Pb+Cu+Sn+Cu (3). Acquisition time 24 hours

Then we try to use an active shielding consisting of only one 50x50x5 cm^3 plastic veto scintillator, located above the upper side of the passive shielding of the camera. The main aim of an active shielding system is to eliminate the cosmic-ray background (mainly induced by cosmic muons) without count rate loss from the examined samples. It is supposed to use scintillation detectors located outside the lead shielding, and working in anticoincidence mode with the Ge-detector. Energy loss of cosmic muons in the scintillator and detected secondary gamma radiation in the Ge-detector generate the coincident pulses. These pulses enable the rejection of the cosmic induced background events by analyzing the time distribution of these signals.

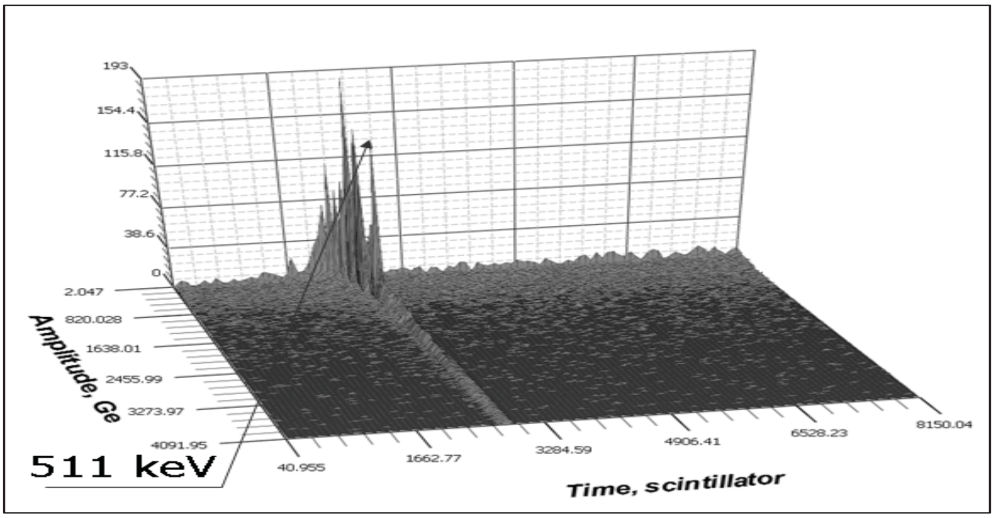

Fig.3. Two dimensional diagram – amplitude of Ge-detector vs time difference T_{Ge}-T_{Pl}, where T_{Ge} and T_{Pl} are times of signals of Ge and Plastic detectors

Many researchers have described their active shield techniques [1, 2]. The most of them used analog time-amplitude reduction. Our measurements were taken by means of the digital pulse processing module CAEN DT5720C [3]. The waveforms of the Ge-detector signals and those of signals from the two ends of the scintillator were recorded. The time range corresponded to the 50 microseconds scan and allows one to see the entire time picture of the forming of coincident events. Then, from the data array the loci of coincident events were selected (for example see Fig.3). After that we calculated the corresponding spectra (for example see Fig.4).

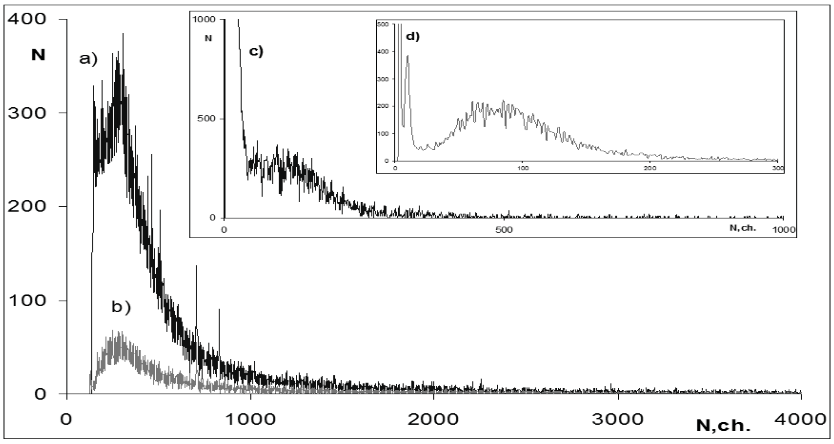

Fig.4. Single and coincidence amplitude spectra: a) single Ge-detector, b) coincidence Ge-detector, c) single plastic detector, d) coincidence plastic detector

The achieved level of background suppression when using active protection compared with the version of only passive one is 0.78, while for 511 keV gamma line this factor is about of 0.5. We tested the loss in the counting rate of useful events by measuring spectra for low activity ^{137}Cs source in the anticoincidence and direct mode. Comparison of these spectra shows that the count loss in the anticoincidence mode is very small (~0.9%). In the near future it is proposed to surround the chamber with four additional scintillators.

The experimental results correspond to the state of the art level of researches in considered area. This is confirmed by comparing the achieved characteristics with the published data from other setups [4-6].

This work was supported by the Russian Foundation of Basic Research (grant No. 11-03-01262).

REFERENCES

1. D.Mrđa, I.Bikit et al. First tests of the active shield for a gamma ray spectrometer. Radiation Measurements. V.42 (2007) 1361–1367.
2. Hamajima Y., Komura K. Background components of Ge detectors in Ogoya underground laboratory. Appl. Radiat. Isot. V.61 (2004) 179–183.
3. CAEN. Application Note AN2506. Digital Gamma Neutron discrimination with Liquid Scintillators. http://www.caen.it.
4. Kiseleva T.T. et al. The use of a low-background underground laboratory in activation analysis of pure substances and radiometry low activity naturally radioactive. Journal of Analytical Chemistry (Russia). V. 49 (1994) 12–17.
5. Laboratory of Environmental Radioactivity «LRK-1 MEPhI» of Moscow Engineering Physics Institute. Environment samples radioactivity investigation multi-detector low-background gamma-spectrometry. http://www.radiation.ru/eng/project/laborat.htm.
6. ORTEC. Low-Background Germanium Gamma-Ray Detectors. http://www.ortec-online.com/download/Low-Background.pdf.

PHOTOPRODUCTION OF NEUTRONS IN THE HEAVY WATER IRRADIATION FACILITY AT THE SL75 LINEAR ELECTRON ACCELERATOR

S.V. Akulinichev, V.M. Skorkin

Institute for Nuclear Research RAS, Moscow, 117312, Russia,
e-mail: skorkin@inr.ru

Usually the neutron source based on an electron linear accelerator use photoneutron reactions (γ, xn) from bremsstrahlung of electrons incident on a target of heavy nuclei. A neutron intensity is about $4 \bullet 10^{13}$ $MeV^{-1}s^{-1}$ at a neutron energy of 1 MeV [1]. It is possible to use for the neutron produce low-energy photonuclear reactions of $^{9}Be(\gamma,n)^{8}Be$ and $D(\gamma,n)p$. The 1 Ci radium radioisotope source containing 100 g beryllium emits neutrons with average energy 827 keV and an intensity of 10^6 $n{\cdot}s^{-1}$. The source using 1 Ci radium and of 1 L deuterium emits neutrons with energy 197 keV and the intensity of $0.5{\cdot}10^6$ $n{\cdot}s^{-1}$.

A photonuclear neutron sources, based on medical linear electron accelerators SL75 of Complex proton therapy INR RAS is presented (Fig.1). This accelerator generates 6 MeV electron pulses, the duration of 4 μs, a frequency of about 300 Hz.

Fig. 1. The SL75 linear electron accelerator

The radiation flux from the accelerator had the average photon energy about 3 MeV (Fig.2).

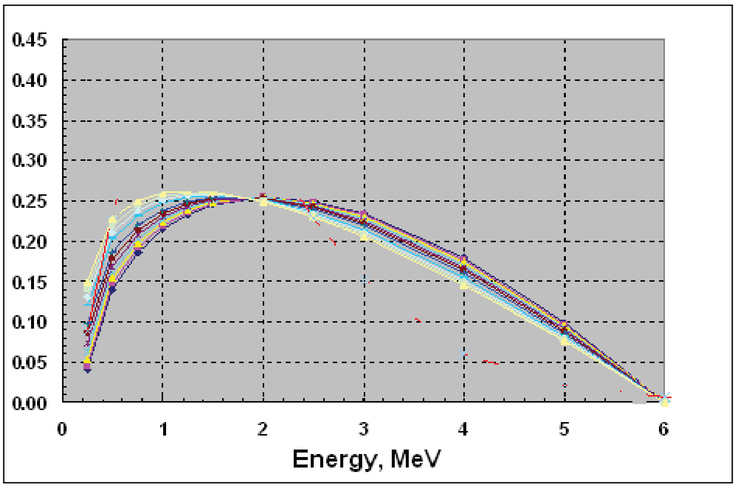

Fig. 2. The energy fluence distribution from SL75 accelerator [2-3].

There is used deuterium target for the neutrons produced in **D(γ,*n*)*p*** reactions. The cross section of **D(γ,*n*)*p*** reactions in fig. 3. About 30% of the bremsstrahlung photons have energies above the deuteron breakup threshold. As a result of photonuclear reactions in D_2O target produced fast neutrons that are slowed down and create a flow and thermal neutrons.

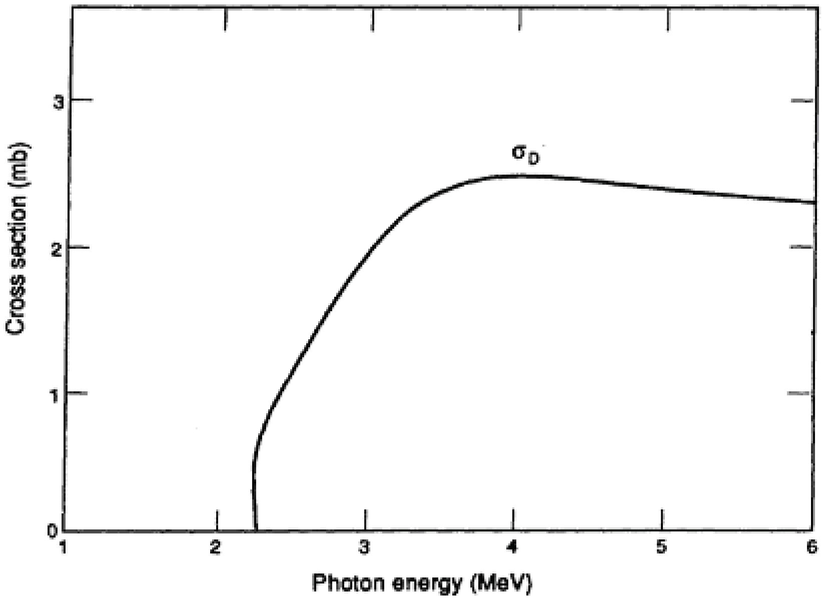

Fig. 3. The cross section of **D(γ,*n*)*p*** reactions

Gamma and neutron radiations from the photoneutron source, based on a heavy water and the SL75 linear electron accelerator were investigated. The irradiation facility consists of the heavy water target (30×30×30 cm), surrounded by a graphite reflector and lead absorber (Fig.4).

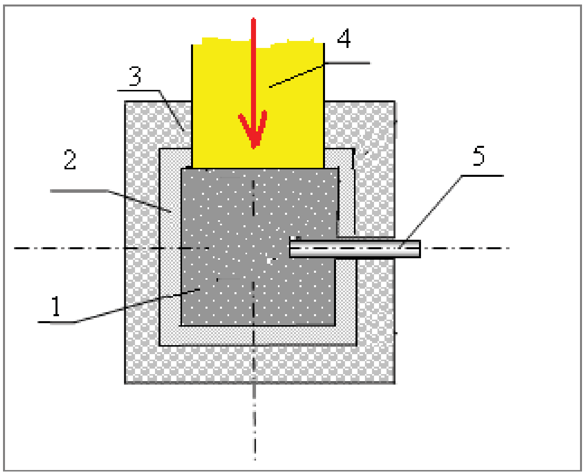

Fig.4. The heavy water neutron irradiation facility. 1 - D_2O target; 2 - a graphite reflector; 3 – and lead absorber; 4 – a gamma radiation; 5 - a neutron detector.

The neutron fluxes have been measured using neutron detectors of a system monitoring radiation. The source provides the thermal neutron flux density of 10^6 n/(cm^2·s) in a volume of about 30 liters (Fig. 5).

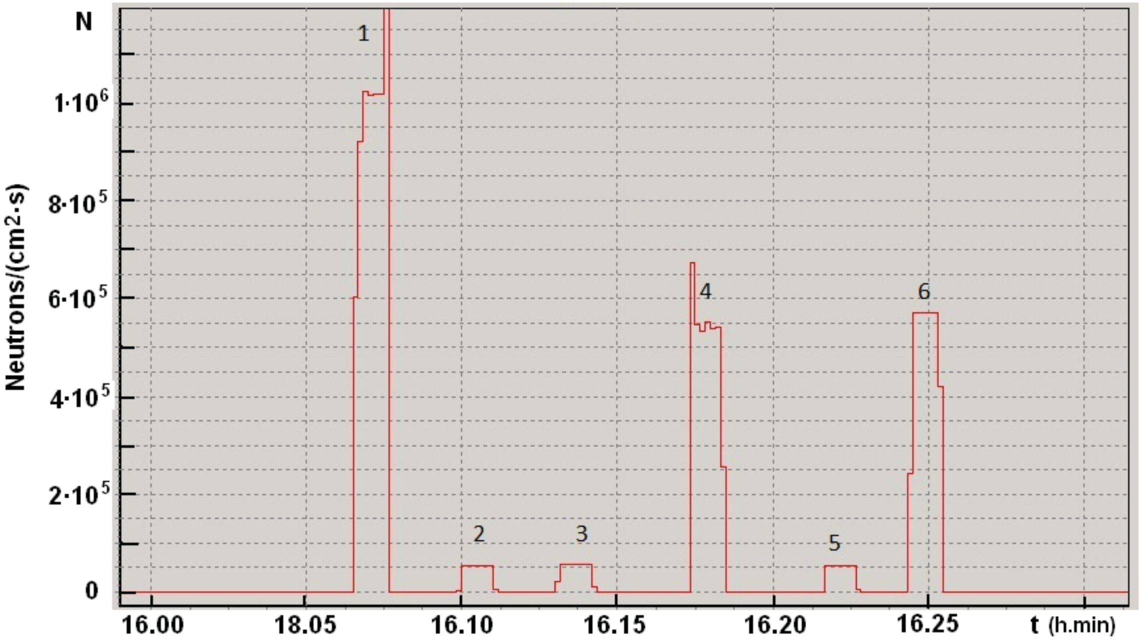

Fig.5. Diagram of the thermal neutron flux density. 1- a neutron detector into the heavy water target; 2,3- the neutron detector into a water target; 4,6- the neutron detector by the heavy water target; 5- the neutron detector by the water target.

1. The Oak Ridge Electron Linear Accelerator Pulsed Neutron Source. http://www.phy.ornl.gov/nuclear/orela/
2. G.P. Naylor/ Properties of beams from the SL75 linear accelerator// Br. J. Radiol **42**(504):951 (1969), PMID 4982657
3. G.E.Gorlachev. /Physics of electron accelerators for radiation therapy.//Institute of Neurosurgery N.N. Burdenko. 2005. 10 March.

FEYNMAN PROPAGATOR FOR PARTICLE IN HOMOGENEOUS ELECTROMAGNETIC FIELD

Yu. I. Sorokin

Institute for Nuclear Research RAS, 117312 Moscow, Russia

In development Feynman path integral ([1], [2],[3], P.78, [4]) propagator for particle with mass m and charge $e = Ze_0$ in constant homogeneous electromagnetic field $\overrightarrow{B}(0, 0, B)$, $\overrightarrow{E}(E_x, 0, E_z)$ have been gotten:

$$G(x, y, z, T, x_0, y_0, z_0, 0) = (\frac{m}{2\pi i\hbar T})^{3/2}\frac{\omega T}{2\sin(\omega T/2)}\exp(iS/\hbar), \qquad (1)$$

$$S = \frac{m}{2}\{\frac{(z - z_0)^2}{T} + \frac{FT(z + z_0)}{m^2} - \frac{F^2T^3}{12m^2} +$$
$$+\frac{\omega}{2}ctg\frac{\omega T}{2}[(x - x_0)^2 + (y - y_0)^2] + \omega(yx_0 - xy_0) +$$
$$+(x_0 + x)fT + (y_0 - y)(\frac{2f}{\omega} - fTctg\frac{\omega T}{2}) - \frac{f^2T}{\omega^2} + \frac{f^2T^2}{2\omega}ctg\frac{\omega T}{2}\}. \qquad (2)$$

$T = t - t_0 > 0$, $F = eE_z$, $f = eE_x/m$, $\omega = (eB)/(mc)$ - cyclotron frequency. As well wave function may be divided between two factors, which comfortably be considered separately. If in plane xy particle moved at first with velocity $v_x = \hbar k_x/m, v_y = \hbar k_y/m$, along x and y-axis, and its spatial indefiniteness was described with Gauss distribution with dispersion Δ and centre in $\bar{x}, \bar{y}$, it is necessary, in according to [4], [1], to bring in initial wave function data about velocity, presence magnetic field and angular momentum relatively reference point.

As result square root from initial Gaussian function got phase:

$$\Psi_0(x_0, y_0) =$$
$$= \frac{1}{\sqrt{2\pi}\Delta}\exp[-\frac{(x_0 - \bar{x})^2 + (y_0 - \bar{y})^2}{4\Delta^2} + ik_x x_0 + ik_y y_0 + \frac{im\omega}{2\hbar}(y_0\bar{x} - x_0\bar{y})],$$

that, in according to [4],[3], [1], give wave function:

$$\Psi(x, y, T) = \int G_B(x, y, T, x_0, y_0, 0)\Psi_0(x_0, y_0)dx_0dy_0 =$$
$$= \frac{m\omega\Delta}{\sqrt{2\pi}(i\hbar\sin\frac{\omega T}{2} + m\omega\Delta^2\cos\frac{\omega T}{2})}.$$

$$\cdot\exp\Big(-\frac{[x-\bar{x}-\rho_x S-(\rho_y+\frac{f}{\omega^2})C]^2+[y-\bar{y}+\frac{fT}{\omega}+\rho_x C-(\rho_y+\frac{f}{\omega^2})S]^2}{4\Delta^2\cos^2\frac{\omega T}{2}+4i\hbar\sin\frac{\omega T}{2}\cos\frac{\omega T}{2}/m\omega}+$$

$$+i(k_x+\frac{mfT}{\hbar})x+ik_y y+\frac{im\omega}{4\hbar}\{2[\bar{x}y-\bar{y}x+\frac{f^2T^2}{\omega^2}(\frac{1-C}{S}-\frac{1}{\omega T})]-$$

$$-[(x-\bar{x}+\frac{2f}{\omega^2}-\frac{fT}{\omega}ctg\frac{\omega T}{2}+2\rho_y)^2+(y-\bar{y}+\frac{fT}{\omega}+2\rho_x)^2]tg\frac{\omega T}{2}\}\Big). \quad (3)$$

$C=1-\cos\omega T, S=\sin\omega T, f=eE/m$, $\rho_x=v_x/\omega$, $\rho_y=v_y/\omega$.

It is visible, that centre of distribution move along circle of radius $\rho=\sqrt{v_x^2/\omega^2+(v_y/\omega+f/\omega^2)^2}$ with circular frequency $\omega=eB/mc$, around centre $(\bar{x}+\rho_y+f/\omega^2, \bar{y}-\rho_x-fT/\omega)$, which has velocity f/ω perpendicular electric field E_x.

Electromagnetic wave has $E=H$, from that $f/\omega=c$. It may be use illustration Compton effect: particle, in spite of sign charge, get momentum perpendicular electric field direct Pointing vector.

Wave function (3) may be use, for example, description move electrons in magnetron, move particle in conduction pump for liquid metal and Hall-effect, conform to Quantum mechanics, for example, instead of [5], P. 263.

At $\omega T \ll 1$ wave function (3) become wave function free move along y-axis with velocity v_y and uniformly accelerated motion along x-axis with beginning velocity v_x .

Three-dimensional wave function, corresponding to propagator (1,2), is formed by product (3) and it for $\omega T \ll 1$, $v_y=0$, $v_z:=v_x$, $E_z:=E_x$. Physical sense is present density function :

$$\Phi(x,y,z,T)=\mid\Psi(x,y,T)\Psi(z,T)\mid^2=$$

$$=[(2\pi)^{-3/2}(\Delta^2\cos^2\frac{\omega T}{2}+\frac{\hbar^2\sin^2\frac{\omega T}{2}}{\Delta^2m^2\omega^2})]^{-1}[\frac{\hbar^2T^2}{4m^2\Delta^3}+\Delta^2]^{-1/2}\cdot$$

$$\cdot\exp\{-\frac{[x-\bar{x}-\rho_x S-(\rho_y+\frac{f}{\omega^2})C]^2+[y-\bar{y}+\frac{fT}{\omega}+\rho_x C-(\rho_y+\frac{f}{\omega^2})S]^2}{2\Delta^2\cos^2\frac{\omega T}{2}+2\hbar^2\sin^2\frac{\omega T}{2}/(m\omega\Delta)^2}\}\cdot$$

$$\cdot\exp\{-\frac{(z-v_zT-FT^2/2m)^2}{2\Delta^2+\hbar^2T^2/2m^2\Delta^2}\}.$$

If at first spatial indefiniteness of particle was described with three-dimensional Gauss distribution with equal dispersions along axis, then further dispersion along magnetic field will gradually increase with time, as dispersion in plane perpendicular to magnetic field will periodic vary with time.

In any case, centre of distribution move according Newton mechanics path: uniformly accelerated motion along magnetic field, and two-dimensional, cycloid motion in plane perpendicular to magnetic field.

It is visible, that perpendicular dispersion focuses every odd half-turn: $\sigma = \hbar/(m\omega\Delta)) = \hbar c/(Ze_0 B\Delta)$, smoothing break of a curve in response function of mass spectrometer [6] , P. 105.

Last result may be utility for understanding properties of high-spin state, giant resonance, [7],[8], and photoproton reaction, [9].

[1] Ю.И.Сорокин. Вестник РУДН (Bulletin of Peoples' Friendship University of Russia), сер. Физика. $N^{\underline{o}}$1(13), 113(2005).

[2] Ю.И.Сорокин. Вестник РУДН, сер. Физика $N^{\underline{o}}$10, вып.1, 126(2002)

[3] Р.Фейнман, А.Хибс. *Квантовая механика и интегралы по траекториям.* (Мир, Москва, 1968), пер. с англ. *Quantum Mechanics and Path Integrals* by R.P.Feynman, A.R.Hibbs. (McCraw Hill Book Company. New York,1965).

[4] Ю.И.Сорокин. Proceedings of the XII International Seminar on Electromagnetic Interaction of Nuclei. EMIN-2009. Moscow, September 17-20, 2009. Moscow 2010. P. 146-148.

[5] Ч. Киттель. *Квантовая теория твердых тел.* (Наука, Москва, 1967), пер с англ.*Quantum Theory of Solids.* by C. Kittel. (John Wiley and Sons, Inc. New York - London. 1963)

[6] *Альфа-, бета- и гамма-спектроскопия.* Под редакцией К.Зигбана, вып.1. (Атомиздат, Москва, 1969), пер с англ. *Alpha-, Beta- and Gamma-ray spektroscopy.* Volum 1. Edited by Kai Siegbahn. (North-Holland publishing company. Amsterdam. 1965)

[7] V.A. Chetvertkova, B.S. Ishkhanov, V.N. Orlin, V.V. Varlamov. Proceedings of the XII International Seminar on Electromagnetic Interaction of Nuclei. EMIN-2009. Moscow, September 17-20, 2009. Moscow 2010. P. 56-67.

[8] Ю.И.Сорокин, Б.А.Юрьев. ЯФ(Sov.J.Nucl.Phys.), Т. 20 , 233(1974). Yu.I. Sorokin., B.A.Yuriev.// Atom. Nucl. Phys.(Sov.J. Nucl. Phys), 1975. V.20, P. 123.

[9] Ю.И.Сорокин, В.А.Хрущёв, Б.А.Юрьев. ЯФ, Т. 14 , 1118-1122 (1971). Yu.I. Sorokin, V.A.Khrushchev, B.A.Yuriev //Atom. Nucl. Phys. (Sov.J. Nucl. Phys), 1972. V.14, P. 622.

PHOTONUCLEAR REACTIONS ON PALLADIUM ISOTOPES

K. A. Stopani

Skobeltsyn institute of nuclear physics, Moscow State University, Moscow, Russia
E-mail: hatta@depni.sinp.msu.ru

Little data is available on the properties of photonuclear reactions on palladium isotopes at the energies of the giant dipole resonance and higher due to the rather complex isotopic composition of natural palladium (table 1). In previous works total photoneutron cross-sections $\sigma(\gamma,\mathrm{xn})$ and photoproton cross-sections $\sigma(\gamma,\mathrm{p})$ on ^{108}Pd, photoneutron cross-section $\sigma(\gamma,\mathrm{n})$ on ^{110}Pd, and total photoneutron cross-section on all stable isotopes were measured in the $8 \leq E_\gamma \leq 30$ MeV energy range. [1, 2]. Isomeric ratios in the reaction ^{110}Pd (γ,n) ^{109}Pd were considered in [3, 4, 5, 6, 7, 8].

Table 1: Natural abundance of stable isotopes of palladium, spins and parities J^P of nuclear ground states.

Isotope	**Abundance**	$J^P_{g.s.}$	**Isotope**	**Abundance**	$J^P_{g.s.}$
^{102}Pd	1.02%	0^+	^{106}Pd	27.33%	0^+
^{104}Pd	11.14%	0^+	^{108}Pd	26.46%	0^+
^{105}Pd	22.33%	$\frac{5}{2}^+$	^{110}Pd	11.72%	0^+

In the present work the yields of photonuclear reactions on the isotopes of natural palladium were measured using the induced activity technique at two upper energies of bremsstrahlung radiation, 29.1 and 55.5 MeV, produced using race-track microtrons. At the 29.1 MeV energy 3 mm lead bremsstrahlung target was used with an aluminum electron absorber 30 mm thick. At the 55.5 MeV energy 2.2 mm tungsten bremsstrahlung target was used. During the irradiations the beam current was recorded with a Faraday cup and an ionization chamber. Induced activity spectra were measured after the irradiations for 31 days (after the 29.1 MeV irradiation) and 45 days (after the 55.5 MeV irradiation) using an HPGe detector. 3672 γ-spectra were recorded during the measurements by an automatic web-based data acquisition and analysis system [9]. The automatic peak search and decay curve generation function of the data analysis system was used to process the measured spectra and determine the activities of the reaction products. Next the method [10] was used to obtain the yields of the reactions from the decay chains formed by their products.

Reaction yields determined from the analysis of the spectra are shown in table 2. Reactions up to $(\gamma, \mathrm{n}\alpha)$ were observed. Additionaly isomeric ratios were calculated when the yields of the final nucleus in the isomeric and ground state were available, listed in table 3. Figure 1 shows the comparison of existing values of the isomeric ratio in the reaction ^{110}Pd (γ,n) ^{109}Pd with our results.

The automated induced activity technique as used in the present work is a convenient tool that allows to measure yields of several reactions in a non-monoisotopic target simultaneously. In a combination with modern compact electron accelerators it can be used to study photonuclear reactions at the energies greater than the energy of giant dipole resonance.

Table 2: Experimental photonuclear reactions yields normalized to the reaction $^{110}\mathrm{Pd}(\gamma,n)^{109}\mathrm{Pd}$.

Irradiation at 29.1 MeV

Reaction	**Relative yield**
$^{102}\mathrm{Pd}\ (\gamma,n)\ ^{101}\mathrm{Pd}$	1.018(4)
$^{110}\mathrm{Pd}\ (\gamma,n)\ ^{109}\mathrm{Pd}$	1.000(4)
$^{102}\mathrm{Pd}\ (\gamma,p)\ ^{101}\mathrm{Rh}$	0.140(1)
$^{106}\mathrm{Pd}\ (\gamma,p)\ ^{105}\mathrm{Rh}$	0.0537(3)
$^{108}\mathrm{Pd}\ (\gamma,p)\ ^{107}\mathrm{Rh}$	0.0427(3)
$^{102}\mathrm{Pd}\ (\gamma,2n)\ ^{100}\mathrm{Pd}$	0.171(8)

Irradiation at 55.5 MeV

Reaction	**Relative yield**
(γ,n)	
$^{102}\mathrm{Pd}(\gamma,\mathrm{n})^{101}\mathrm{Pd} + 10.92\,^{104}\mathrm{Pd}(\gamma,\mathrm{3n})^{101}\mathrm{Pd}$	1.449(7)
$^{104}\mathrm{Pd}(\gamma,\mathrm{n})^{103}\mathrm{Pd} + 2.00\,^{105}\mathrm{Pd}(\gamma,\mathrm{2n})^{103}\mathrm{Pd}$	2.44(4)
$^{110}\mathrm{Pd}(\gamma,\mathrm{n})^{109\mathrm{m}}\mathrm{Pd}$	0.1091(6)
$^{110}\mathrm{Pd}(\gamma,\mathrm{n})^{109\mathrm{g.s.}}\mathrm{Pd}$	0.891(6)
(γ,p)	
$^{102}\mathrm{Pd}(\gamma,\mathrm{p})^{101\mathrm{m}}\mathrm{Rh} + 10.92\,^{104}\mathrm{Pd}(\gamma,\mathrm{2n1p})^{101\mathrm{m}}\mathrm{Rh}$	0.17(2)
$^{102}\mathrm{Pd}(\gamma,\mathrm{p})^{101\mathrm{g.s.}}\mathrm{Rh} + 10.92\,^{104}\mathrm{Pd}(\gamma,\mathrm{2n1p})^{101\mathrm{g.s.}}\mathrm{Rh}$	0.125(1)
$^{105}\mathrm{Pd}(\gamma,\mathrm{p})^{104\mathrm{m}}\mathrm{Rh} + 1.22\,^{106}\mathrm{Pd}(\gamma,\mathrm{np})^{104\mathrm{m}}\mathrm{Rh}$	0.0186(7)
$^{106}\mathrm{Pd}(\gamma,\mathrm{p})^{105\mathrm{g.s.}}\mathrm{Rh} + 0.97\,^{108}\mathrm{Pd}(\gamma,\mathrm{2n1p})^{105\mathrm{g.s.}}\mathrm{Rh}$	0.0630(3)
$^{108}\mathrm{Pd}(\gamma,\mathrm{p})^{107}\mathrm{Rh} + 0.44\,^{110}\mathrm{Pd}(\gamma,\mathrm{2n1p})^{107}\mathrm{Rh}$	0.0455(2)
$^{110}\mathrm{Pd}(\gamma,\mathrm{p})^{109}\mathrm{Rh}$	0.023(4)
(γ,np)	
$^{102}\mathrm{Pd}(\gamma,\mathrm{np})^{100}\mathrm{Rh} + 10.92\,^{104}\mathrm{Pd}(\gamma,\mathrm{3n1p})^{100}\mathrm{Rh}$	0.0408(3)
$^{104}\mathrm{Pd}(\gamma,\mathrm{np})^{102\mathrm{m}}\mathrm{Rh} + 2.00\,^{105}\mathrm{Pd}(\gamma,\mathrm{2n1p})^{102\mathrm{m}}\mathrm{Rh}$	0.0058(5)
$^{104}\mathrm{Pd}(\gamma,\mathrm{np})^{102\mathrm{g.s.}}\mathrm{Rh} + 2.00\,^{105}\mathrm{Pd}(\gamma,\mathrm{2n1p})^{102\mathrm{g.s.}}\mathrm{Rh}$	0.0219(3)
$^{108}\mathrm{Pd}(\gamma,\mathrm{np})^{106\mathrm{m}}\mathrm{Rh} + 0.44\,^{110}\mathrm{Pd}(\gamma,\mathrm{3n1p})^{106\mathrm{m}}\mathrm{Rh}$	0.00216(4)
$^{110}\mathrm{Pd}(\gamma,\mathrm{np})^{108\mathrm{m}}\mathrm{Rh}$	0.00112(4)
Other	
$^{102}\mathrm{Pd}(\gamma,\mathrm{2n})^{100}\mathrm{Pd} + 10.92\,^{104}\mathrm{Pd}(\gamma,\mathrm{4n})^{100}\mathrm{Pd}$	0.1652(8)
$^{102}\mathrm{Pd}(\gamma,\mathrm{3n})^{99}\mathrm{Pd} + 10.92\,^{104}\mathrm{Pd}(\gamma,\mathrm{5n})^{99}\mathrm{Pd}$	0.0059(1)
$^{102}\mathrm{Pd}(\gamma,\mathrm{2n1p})^{99\mathrm{m}}\mathrm{Rh} + 10.92\,^{104}\mathrm{Pd}(\gamma,\mathrm{4n1p})^{99\mathrm{m}}\mathrm{Rh}$	0.0087(2)
$^{102}\mathrm{Pd}(\gamma,\mathrm{2n1p})^{99\mathrm{g.s.}}\mathrm{Rh} + 10.92\,^{104}\mathrm{Pd}(\gamma,\mathrm{4n1p})^{99\mathrm{g.s.}}\mathrm{Rh}$	0.0064(3)
$^{102}\mathrm{Pd}(\gamma,\mathrm{na})^{97}\mathrm{Ru} + 10.92\,^{104}\mathrm{Pd}(\gamma,\mathrm{3n1}\alpha)^{97}\mathrm{Ru}$	0.0049(8)
$^{105}\mathrm{Pd}(\gamma,\mathrm{2p})^{103}\mathrm{Ru} + 1.22\,^{106}\mathrm{Pd}(\gamma,\mathrm{1n2p})^{103}\mathrm{Ru}$	$7.66(9)\times10^{-4}$
$^{108}\mathrm{Pd}(\gamma,\mathrm{1n2p})^{105}\mathrm{Ru} + 0.44\,^{110}\mathrm{Pd}(\gamma,\mathrm{3n2p})^{105}\mathrm{Ru}$	$1.5(1)\times10^{-4}$

Table 3: Isomeric ratios of reaction yields $R = y_m/y_{g.s.}$.

Reaction	$J^P_{\mathrm{g.s.}}$ (final nucleus)	Isomeric state (final nucleus)	**Isomeric ratio R**	
			29.1 MeV	**55.5 MeV**
$^{102}\mathrm{Pd}\ (\gamma,\mathrm{p})\ ^{101}\mathrm{Rh}$	$1/2^-$	157 keV, $J^P = 9/2^+$	0.49(1)	1.4(2)
$^{102}\mathrm{Pd}\ (\gamma,\mathrm{2n1p})\ ^{99}\mathrm{Rh}$	$1/2^-$	64 keV, $J^P = 9/2^+$		1.4(1)
$^{104}\mathrm{Pd}\ (\gamma,\mathrm{np})\ ^{102}\mathrm{Rh}$	$(1^-, 2^-)$	141 keV, $J^P = 6^{(+)}$		0.26(2)
$^{110}\mathrm{Pd}\ (\gamma,\mathrm{n})\ ^{109}\mathrm{Pd}$	$5/2^+$	189 keV, $J^P = 11/2^-$	0.10(2)	0.099(5)

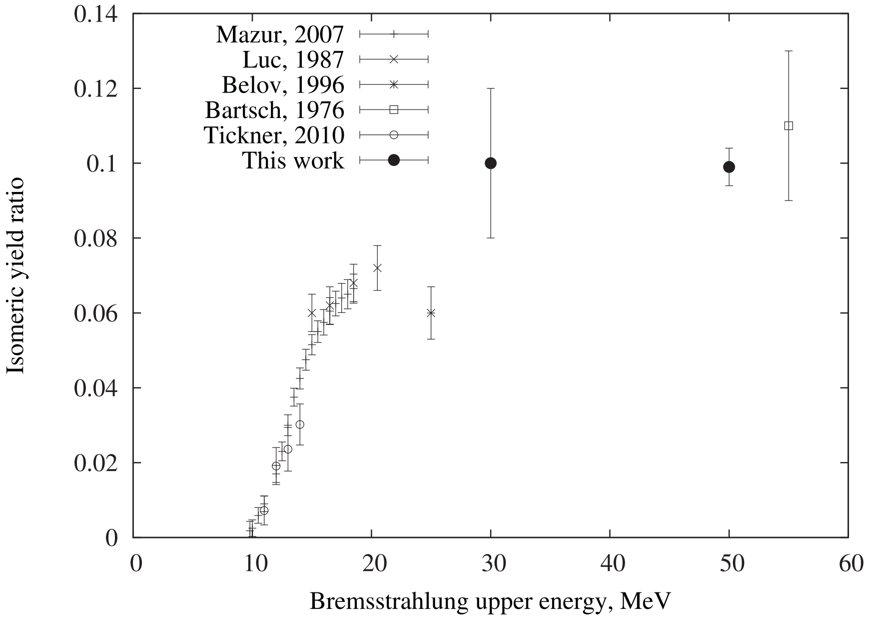

Figure 1: Comparison of isomeric ratios in the reaction ^{110}Pd (γ,n) ^{109}Pd obtained in different works.

References

[1] Deague T., Muirhead E., Spicer B. Structure in the giant resonance of ^{108}Pd and of ^{110}Pd // Nucl. Phys. A. — 1969. — Vol. 139.

[2] A study of the giant dipole resonance of vibrational nuclei in the $103 \leq A \leq 133$ mass region / A. Leprêtre, H. Beil, R. Bergère et al. // Nucl. Phys. A. — 1974. — Vol. 219, no. 1. — P. 39 – 60.

[3] Critical consideration of the statistical model analysis of photonuclear isomeric cross-section ratios / H. Bartsch, K. Huber, U. Kneissl, H. Krieger // Nucl. Phys. A. — 1976. — Vol. 256, no. 2. — P. 243 – 252.

[4] Isomeric yield ratios in the productions of Sm^{143m,g}, Nd^{141m,g}, Zr^{89m,g} and Pd^{109m,g} by 14 MeV neutrons and 15–20,5 MeV bremsstrahlung / H. D. Luc, T. D. Thiep, T. T. An, P. An // Bolg. J. of Phys. — 1987. — Vol. 14, no. 2. — P. 152 – 161.

[5] Возбуждение изомерных состояний $1h_{11/2}$ в реакциях (γ, n) / А. Г. Белов, Ю. П. Гангрский, А. П. Тончев, Н. П. Балабанов // ЯФ. — 1996. — Т. 59, № 4. — С. 585–591.

[6] Изомерные отношения в реакциях (γ,p) при энергиях гигантского дипольного резонанса / Ю. П. Гангрский, П. Зузаан, Н. П. Колесников и др. // ЯФ. — 1999. — Т. 62, № 10. — С. 1733–1739.

[7] Tickner J., Bencardino R., Roach G. // Nucl. Inst. and Meth. B. — 2010. — Vol. 268. — P. 99–105.

[8] Mazur V. M., Bigan Z. M., Symochko D. M. Excitation cross-section of the $11/2^-$ isomeric states of the ^{109}Pd and ^{111}Cd nuclei for (γ,n) reactions in the gamma-quantum energy range of 8–18 MeV // Ukr. J. Phys. — 2007. — Vol. 52. — P. 744.

[9] Belyshev S., Stopani K. Automation of measurements and data analysis in induced activity technique experiments (in print) // Moscow University Physics Bulletin. — 2012. — Vol. 67.

[10] Measuring nuclear reaction yields in a procedure based on decay chain analysis / S. Belyshev, K. Stopani, S. Troschiev et al. // Moscow University Physics Bulletin. — 2011. — Vol. 66. — P. 363–368.

SIMULATION OF BREMSSTRAHLUNG FROM INTERACTION OF A FEMTOSECOND TERAWATT LASER PULSES WITH MATTER

A.Turinge[1]*, A.Rusakov*[1]*, A.Savel'ev*[2]*, A.Brantov*[3]*, V.Bychenkov*[3]

1-INR RAN, Russia, 2-MSU, Russia, 3-LPI, Russia

The goal of the work was the simulation of the distributions of output signals of E and ΔE scintillation detectors in the experiment of interaction of the laser pulses with a subterawatt power with a lead target. The laser pulse with duration of 50 fs and maximum intensity of $2*10^{18}$ W/cm^2 propagates along the X axis and focuses onto the target surface in a hot spot with size of 4 microns. The pulse has a linear polarization along the axis Z (direction of the electric field). For such pulses, electrons are heated up due to the ponderomotive force as well as stochastic heating in the incident and reflected pulses in the pre-plasma [1]. The energy and angle distributions (the angles between the electron momentum and axes) calculated by using 3D PIC simulations are shown in fig.1.

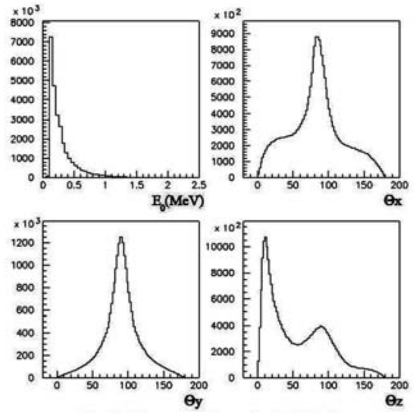

Fig.1.Energy and angle distributions of the initial electrons

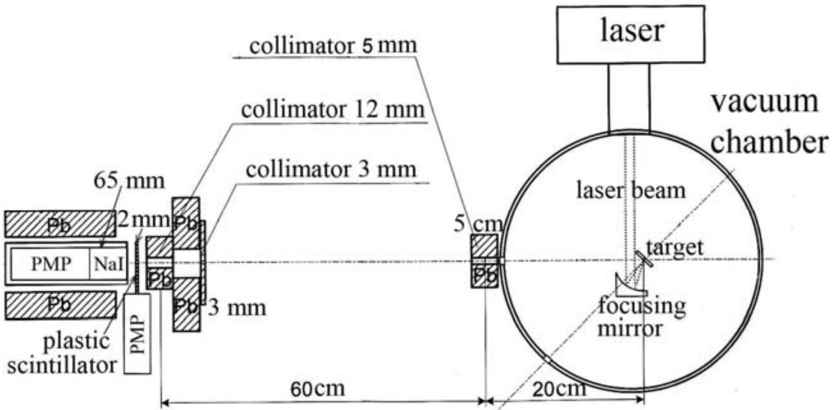

Fig.2.Scheme of the experimental facility

The scheme of the experimental facility is shown in fig.2. Due to the very small angle of collimation (~10^{-6} sr) only a small part of the initial electrons can be measured. The energy distribution of these primary electrons (solid curve), and bremsstrahlung photons (dotted curve), produced in the target by other electrons were calculated by using code GEANT3 [2] (several tens of millions events were scattered) (fig.3a). The given work was done to take into account the distortion of the spectrum for a given geometry and NaI detector response function. Signal distributions in NaI и ΔE detectors are in coincidence with each other.

One can see that number of primary bremsstrahlung photons emitted from the target is almost twice the number of primary electrons. These photons with energies of ~10 keV make predominant contribution (>99.9%) in the output signals of the detectors (fig.4).

The main part (>99%) of electrons emitted from the target (with energy of ~100keV) could not reach the detectors due to almost a meter of air between the target and detector. E and ΔE signal distributions, produced by initial electrons only and bremsstrahlung photons (without initial bremsstrahlung photons produced by other electrons in the target) are shown in fig.5.

The connections between the energy of the initial bremsstrahlung photons produced in the target and the signals in E and ΔE detectors are shown in fig.3b,c,d. Thus, the measured output signals can give us an indirect view of the momentum and energy distribution of electrons emitted from the target.

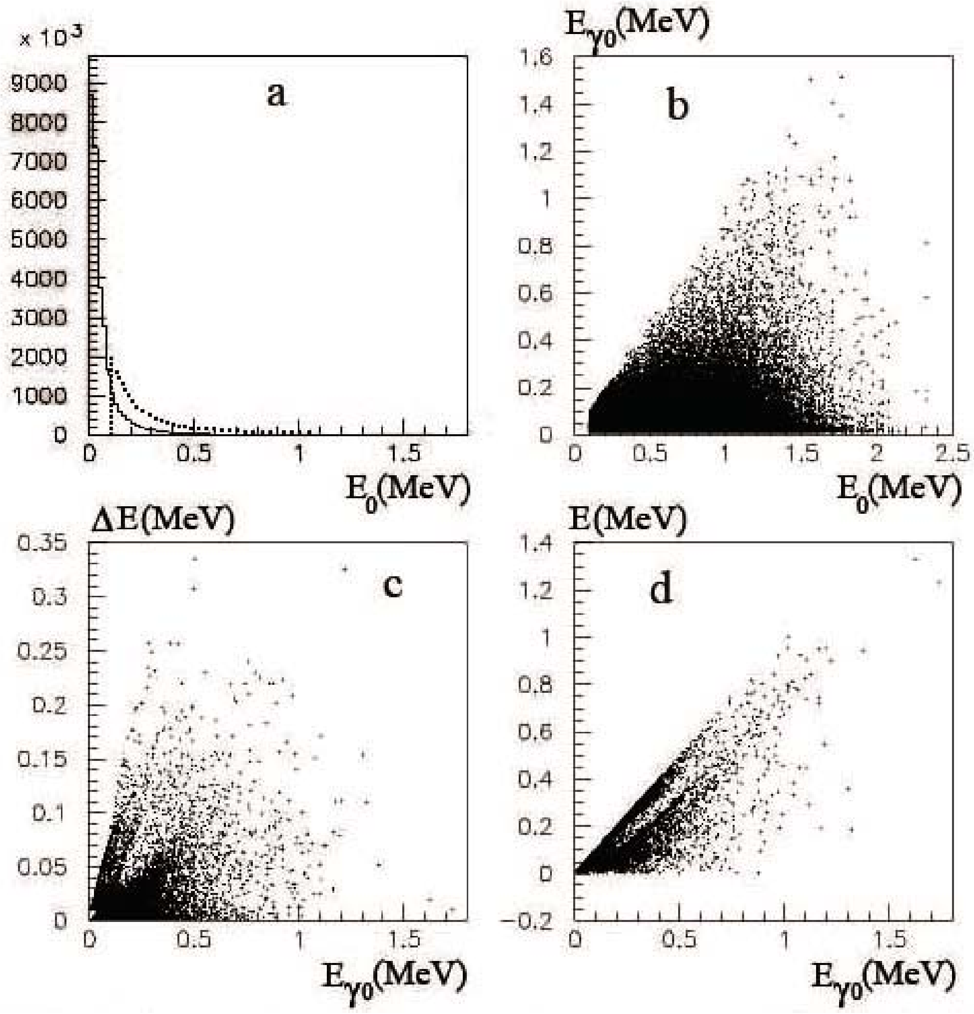

Fig.3.Connection between the energy of the initial electrons (E_0), initial bremsstrahlung photons produced in the target ($E_{\gamma 0}$) and the signals in E and ΔE detectors

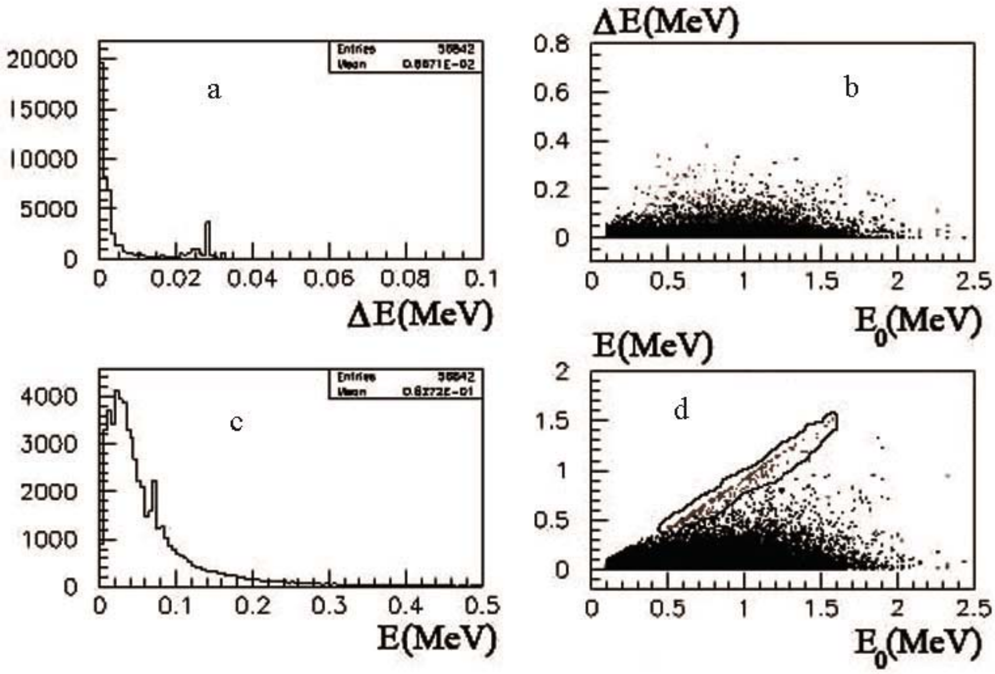

Fig.4. Connection between the energy of the initial electrons (E_0) and the signals in NaI (E) and ΔE detectors. Solid line on 4d encircles the signals produced by the electrons

Comparison of the obtained simulated data with the experimental results was done (fig.6). We can see that there is a good agreement between simulated and experimental data for NaI detector (fig.6a). The discrepancy between simulated and experimental data from ΔE detector (see fig.6b) can be explained by restricted experimental resolution of ΔE detector, that has not been taken into account during our simulation.

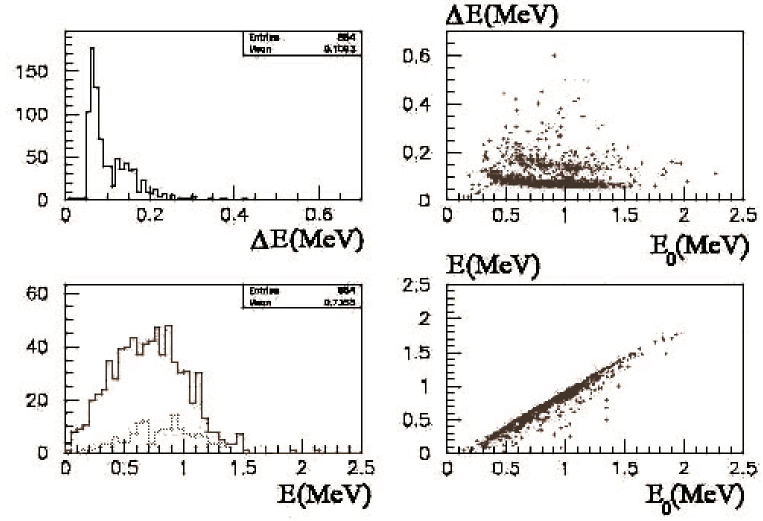

Fig.5.Connection between energy of the initial electrons and the signals in NaI & ΔE detectors without initial bremsstrahlung photons (solid curve – electrons, dotted curve – photons)

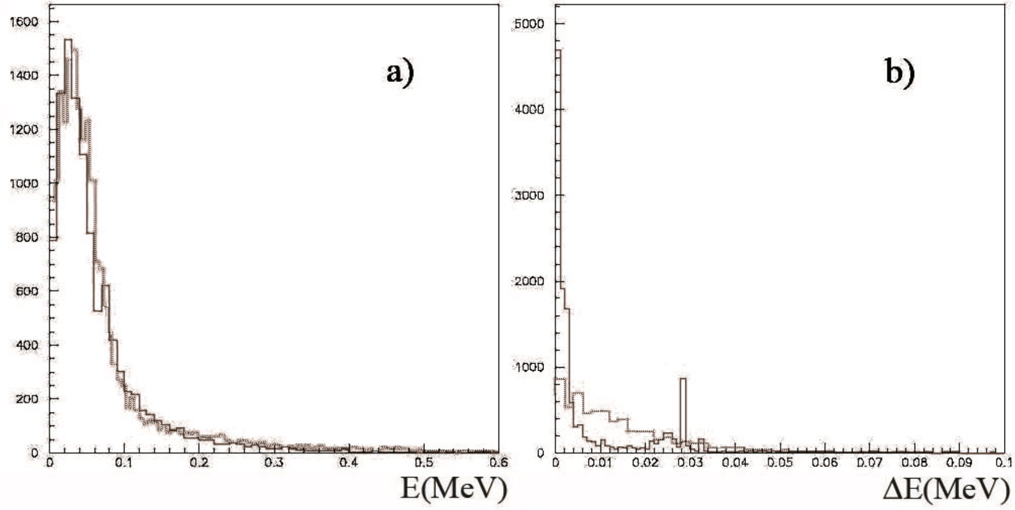

Fig.6.Covparison of the simulated data (solid curve) with experimental data (dotted curve)

Conclusion: the used experimental scheme allows us to measure the energy distribution of the bremsstrahlung photons and gives us an indirect view of the momentum and energy distribution of electrons emitted from the target only. Obviously, more perfect techniques, for example, using of magnetic spectrometers, are required for a correct experimental measurement of the energy spectra. At the same time performed modeling allows one to restore the original experimental spectra from the observed distributions, although the result is not obvious due to a so-called incorrect character of this problem. This study is of great interest as it opens up a new direction of research of photonuclear reactions and the study of nonlinear effects in quantum electrodynamics.

This work was partially supported by RFBR.

References.

1.Y.Sentoku et.al., Appl. Phys. B 74, 207-215 (2002).
2. http://geant3.cern.ch/

SCINTILLATION (ΔE - E) DETECTOR FOR EXPERIMENTS WITH FEMTOSECOND LASER

D.P. Zagorodnyuk[1], *A.V. Rusakov*[1]

[1] Institute for Nuclear Research, Russian Academy of Sciences, Moscow, Russia

The main goal of the work is the creation of the detector for the femtosecond laser experiments at ILC MSU. The physical basis and general principles of such experiments for initiating nuclear processes using femtosecond laser radiation are considered in [1, 2]. Irradiating the target, femtosecond laser pulse initiate intensive electron and gamma radiation flux. One of the methods of electrons and gamma rays discrimination is using a radiation detector of the (ΔE-E) type – a system based on thin scintillator and total absorption detector. Such system possesses high efficiency for electrons and gamma quanta identification.

The ΔE detector consists of a thin 2 mm polyvinyl-toluene POPOP plastic scintillator, with corresponding characteristics: decay time – 3 ns, self-radiation absorption length – 5 m, conversion efficiency – 48% of anthracene, maximum in radiation spectrum – 380 nm, energy release deposition – 400 keV in 2mm of plastic. It is covered by a reflective 0.02 mm aluminum foil layer and 0.12 mm black paper. The ΔE detector serves as a shoot-through layer, defines energy resolution for incoming particles and gives a short pulse flash, which is important for achieving an acceptable counting rate. The total absorption detector is based on NaI crystal (65 × 65 mm). Both detectors are viewed by PMT-143.

Calibration of NaI detector was done using ^{60}Co source, and plastic detector was calibrated with radioactive beta-source ^{90}Sr (figure 1).

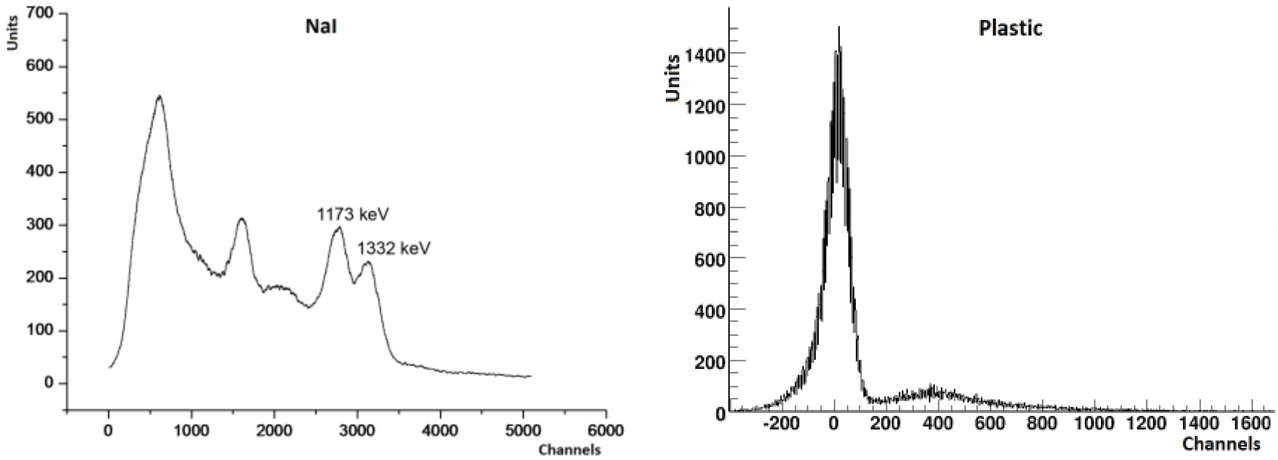

a) b)

Fig. 1. Calibration of a) NaI detector with ^{60}Co; b) ΔE plastic detector with ^{90}Sr

This detector was used in experiment carried out by the Laboratory of Photonuclear Reactions INR RAS together with Joint Laboratory of Relativistic Laser Plasma ILC MSU. It is based on femtosecond laser system with following parameters [3]: Wave Length – 800 nm, Repetition Frequency – 10 Hz, Pulse Energy 50 mJ, Diameter of Focus Spot – 4 μm, Target Intensity – 2.5×10^{18} W/cm^2. Experimental facility includes: laser, beaming system, vacuum chamber with beam optics, detection system. Laser beam is focusing on the smooth Pb 1 mm target placed in vacuum chamber, at 45 degrees to target normal. Reaction products escape through 5 mm aperture. To reduce detector counting rate, the optimal distance from vacuum chamber to detectors was chosen at 60 cm, including collimating system. Detectors were covered by lead screen to avoid scattered X-radiation. During our experiments detector counting rate indicated on average 0.36 events/pulse.

Electronic block diagram of the experimental facility, including synchronization system is shown in figure 2

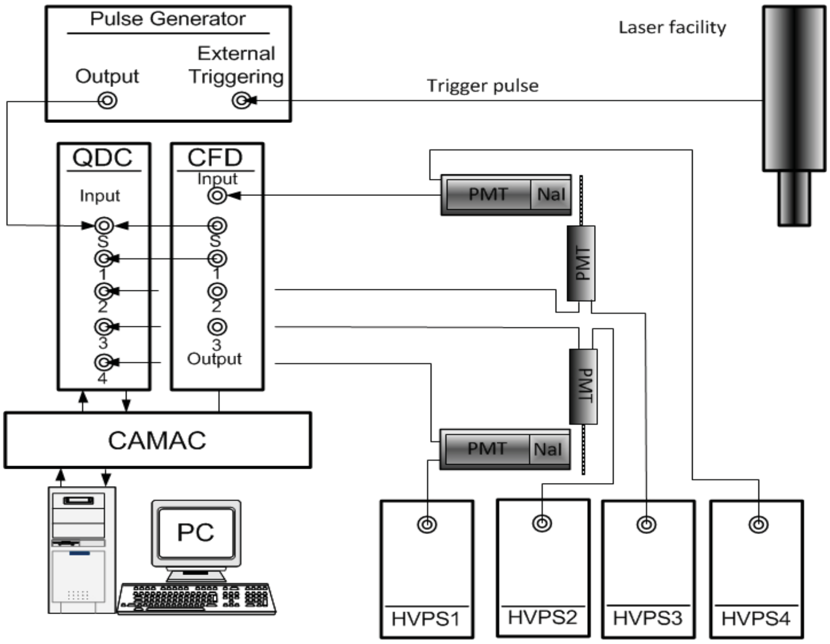

Fig. 2. Electronic block diagram of the experimental facility

Received preliminary results on measured energy spectra of photons and electrons for two pulse durations (50 fs, 400 fs) are shown in figures 3.1, 3.2. The measurements were analyzed using standard package ROOT, taking in consideration the calibration data.

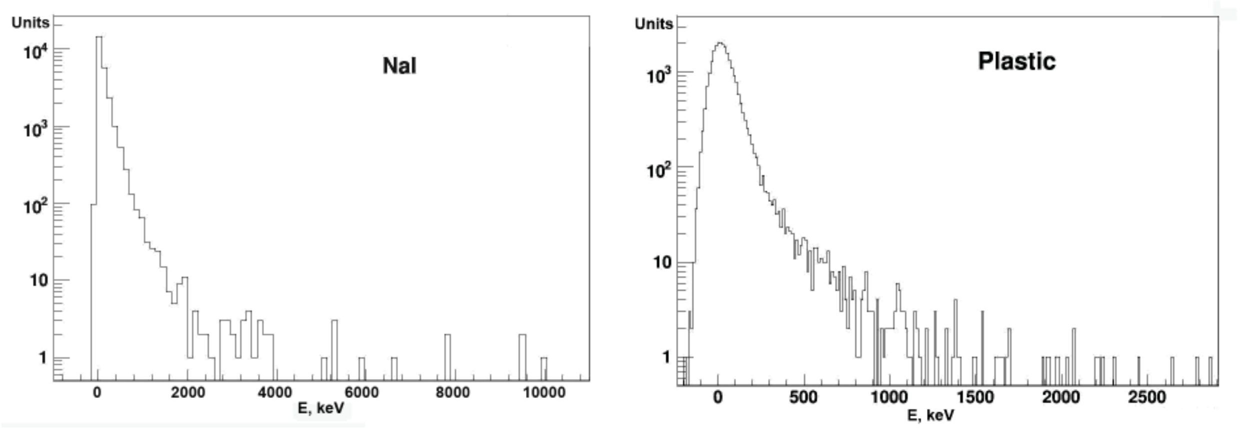

Fig. 3.1. Energy spectra of photons and electrons, for 50 fs pulse duration

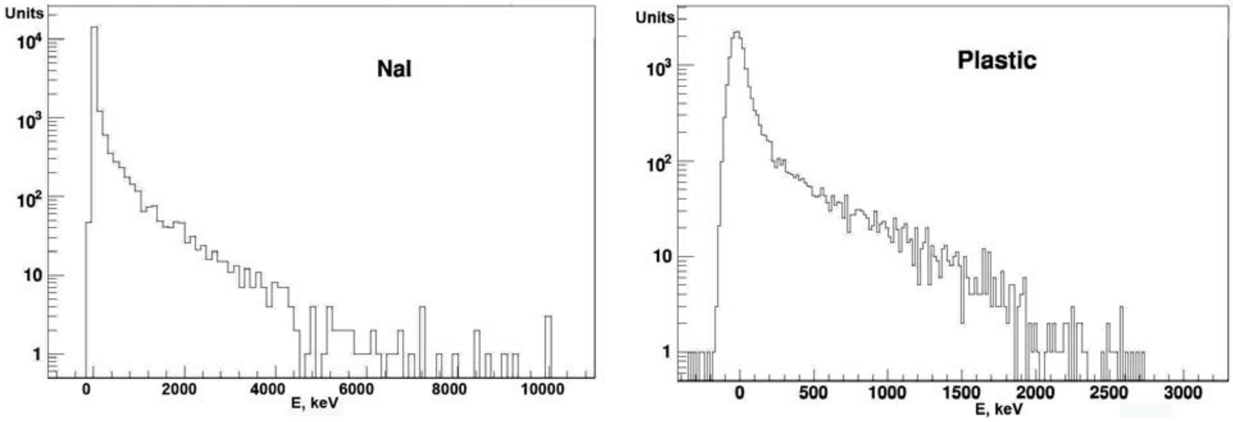

Fig. 3.2. Energy spectra of photons and electrons, for 400 fs pulse duration

During the experiments, we obtained preliminary results. They show, that (ΔE-E) type scintillation detector allows receiving suitable results on registration of gamma-rays quanta with energy over several MeV and electrons with average energy 100-200 keV. Thus, (ΔE-E) detection system could be used in femtosecond laser experiments for different nuclear-physical applications.

Authors are grateful to A. Lapik for advices provided during the detector construction. This work was supported by RFBR, grant 11-02-00286a.

References

[1] What Superpower Laser Pulses Are Needed for? "PRIRODA №4", April, 2007
[2] Andreev A.V, Gordienko V. M, Savel'ev A. B. "Nuclear processes in a high-temperature plasma produced by an ultrashort laser pulse". QUANTUM ELECTRONICS, 2001, 31 (11), 941–956.
[3] Bolshakov V. V., Vorobyev A. A., Volkov R. V., Knyazkov V. A., Savelyev A. B., Eremin N. V., Paskhalov A. A., Shevelko A. P., Kazakov E. D., Romanovsky M. Yu. Reception of relativistic intensity with use of the femtosecond radiations of Ti:Sapphire laser system with 0.2-TW peak power. APPLIED PHYSICS, No. 1, 2009.

NEUTRON-GAMMA DISCRIMINATION IN ORGANIC SCINTILLATORS USING VARIOUS PULSE-SHAPE PARAMETERS

E. S. Konobeevski, M. V. Mordovskoy, I. M. Sharapov, S. V. Zuyev

Institute for Nuclear Research of Russian Academy of Sciences, Moscow, Russia
E-mail: konobeev@inr.ru

Abstract: The possibility of using liquid scintillators and stilbene for digital n-γ discrimination using CAEN Waveform Digitizer is examined. The charge-integration and the charge-decay methods was employed to compare the pulse shape discrimination properties in four scintillators: EJ-301, EJ-315 (C_6D_6), NE-213 and Stilbene. It is proposed to use the new shape-parameters to improve the n-γ discrimination.

To obtain new data on neutron-neutron interaction in a wide energy range (20-100 MeV) a setup for study the nd-breakup reaction was installed at the Institute for Nuclear Research (INR) of Russian Academy of Sciences [1]. This setup allows one to detect the three final particles - two neutrons and protons and determine their energies. The experiment is performed at the neutron beam channel RADEX of Moscow meson factory of INR [2].

In our study of the deuteron breakup reaction we use various scintillation detectors of neutrons. As an active target-detector we used liquid deuterated (C_6D_6) EJ-315-scintillator produced by Eljen Technology Company (analog of NE-230 and BC-537 scintillators). Behind the target along the beam of primary neutrons was placed neutron beam monitor on the base of stilbene crystal.

As the monitor and the active target detectors operate in the presence of background gamma-ray, it is necessary to apply scintillators, which allow pulse-shape discrimination of neutrons and gamma rays. In our work we compared various organic scintillators based on stilbene crystals and liquid scintillators (EJ-301, EJ-315, NE-213).

The most widely used methods for neutron detection in the presence of gamma radiation background utilizes the difference in the shapes of the scintillation pulses induced by neutrons (recoil protons) and γ-rays in organic scintillators. Pulse shape discrimination (PSD) phenomena discovered and demonstrated many decades ago are based on the existence of two-decay component fluorescence, in which, in addition to the main component decaying exponentially (prompt fluorescence), there is usually a slower emission that has the same wavelength, but longer decay time (delayed emission) [3]. The short range of the energetic protons produced from neutron collisions yields a high concentration of exited molecules, compared to the longer range of the electrons from the gamma interactions, leading to the enhanced level of delayed emission with longer decay times in neutron-induced pulses in comparison to those produced by the gamma excitation. This leads to a somewhat different for m of the scintillation signal from neutrons and gamma rays. The difference in the slow decay component of the light emission induced by neutrons and gamma-rays is the basis of digital pulse-shape discrimination in the scintillating detectors.

The associated photomultiplier signals were digitized by means of the Mod. DT5720C (2 Channel, 12bit, 250MS/s) Waveform Digitizer developed by CAEN - Costruzioni Apparecchiature Elettroniche Nucleari SpA [4]. Signals with amplitude up to 2 V were digitized by 4096-channel FLASH-ADC with periodicity of 4 ns.

Based on the type (shape) of signals some parameters characterizing the shape of the pulse were considered. We used these parameters in the charge-integration and the charge-decay methods for the n-γ discrimination. The shape of pulses were fitted using the function

$$f(t) = A \cdot e^{t/TAU}, \qquad (1)$$

where *f(t)* is the digitized value of the pulse at time *t*, *A* is the maximum amplitude, *TAU* is the decay time of the slow pulse component, *QL* and *QS* are “long” and “short” parts of the integral of the pulse. We also used *QL/A*-parameter, characterizing the effective width of the pulse and therefore different for neutrons and γ-rays, and *PSD* [6] parameter defined as:

$$\boldsymbol{PSD} = \frac{\boldsymbol{QL} - \boldsymbol{QS}}{\boldsymbol{QL}} . \qquad (2)$$

The decay time *TAU*, effective width *QL/A* and *PSD* are the shape-parameters. For n-γ discrimination, usually, two-dimensional scatter-plots of the shape-parameters vs. pulse-height are used.

For quantitative comparison of the quality of separation between γ-rays and neutrons we consider the figure of merit (*FOM*) which is defined [4] as

$$\boldsymbol{FOM} = \frac{\Delta \boldsymbol{Peak}}{\boldsymbol{FWHM}_n + \boldsymbol{FWHM}_\gamma}, \qquad (3)$$

where Δ*Peak* is the separation between the neutron and gamma peaks and $FWHM_n$ and $FWHM_\gamma$ are the full widths at half maximum of the neutron and gamma peaks in the n-γ spectrum, which is the projection of the two dimensional scatter plot onto the shape parameter axis. Therefore, a larger *FOM* value means a better separation between neutron and γ-ray events.

In addition to two-dimensional scatter-plots of the shape-parameters vs. pulse-height, *QL* or *QS* may also be considered two-dimensional scatter-plots of one shape-parameter to another. Examples of such two-dimensional scatter-plots for the cases *PSD* vs. *QL/A*, *PSD* vs. *TAU* and *TAU* vs. *QL/A* are shown in fig. 1.

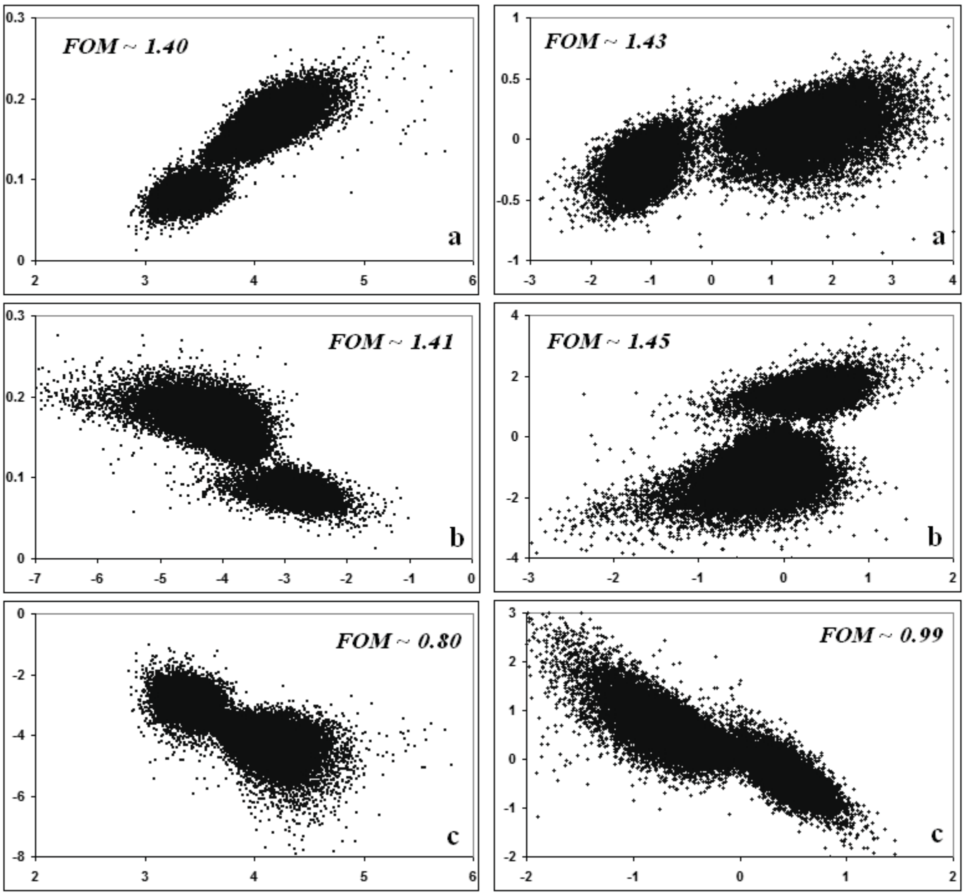

Fig. 1. The two-dimensional scatter-plots of the shape-parameters *PSD* vs. *QL/A* (a), *PSD* vs. *TAU* (b) and *TAU* vs. *QL/A* (c) before (left) and after (right) the transformation of variables are shown for the EJ-301 scintillator irradiating by PuBe source.

These diagrams show that the projections on the axes will give not very good separation. However, it is clear that the n- and γ-events are grouped symmetrically around a center of rotation. Further optimization of the separation can be achieved by a rotation around the center of rotation at an angle at which the line connecting the centers of n- and γ-spots becomes parallel to one of the axes of the two-dimensional diagram. This operation is equivalent to the rotation of primary axis at the same angle, and leads to some new variables, which are the new shape-parameters. Such coordinate transformation results in the diagram showed in Fig. 1 (right). After the projection on the shape parameter axis we obtain the new spectra and can estimate the quality of separation using *FOM*, defined as above (3).

Table shows the corresponding FOM for all compared scintillators and for different combinations of shape-parameters. We see a clear improvement of the separation, especially for stilbene and EJ-301.

Table. The best values of *FOM* for the compared scintillators

Scintillator	*FOM*			
	PSD(A)	*PSD'(QL/A')*	*PSD'(TAU')*	*TAU'(QL/A')*
Stilbene	1.35	1.41	1.41	1.10
EJ-301	1.15	1.43	1.45	0.99
EJ-315	1.55	1.60	1.60	0.86
NE-213	1.04	1.09	1.07	0.85

The data in Table suggest the possibility of improvement in n-γ separation with the introduction of the new shape-parameters with respect to the standard methods of n-γ discrimination. On the example of stilbene and liquid scintillator EJ-301 one can show that the use of new variables *PSD'* vs. *QL/A'* and the *PSD'* vs. *TAU'* improves the quality of n-γ-separation. Data obtained using PuBe source, as well as data obtained at neutron channel RADEX show a good n-γ- separation in the energy region of 0.5-30 MeV.

This work was supported by the Russian Foundation of Basic Research (grant No. 10-02-00603).

REFERENCES

1. *Burmistrov Yu. M., Zuyev S. V., Konobeevski E. S., Mordovskoy M. V. et al.* An Experimental Setup for Studying Neutron–Neutron Final State Interaction on the Neutron Channel of the Moscow Meson Factory // Instruments and Experimental Techniques. V. 52 (2009) 769 –773.
2. *Koptelov E.A. et al.* A complex of complementary pulsed neutron sources, neutron and radiographic nanodiagnostic instruments at the Institute for Nuclear Research RAS // J. Phys.: Conf. Ser. V. 291 (2011) 012012, P. 1 – 6.
3. *Zaitseva N, Glenn A, Carman L et al.* Pulse Shape Discrimination in Impure and Mixed Single-Crystal Organic Scintillators // IEEE Trans. Nucl. Sci. V. 58 (2011) 3411 – 3420.
4. *CAEN. Application Note AN2506*. Digital Gamma Neutron discrimination with Liquid Scintillators // http://www.caen.it.

Труды XIII международного семинара
по электромагнитным взаимодействиям ядер
ЭМИН-2012
Москва, 20-23 сентября 2012 г.

Подписано в печать 22.01.2013
Ф-т 60x84/8. Уч.-изд.л. 13,0 Печ.л. 22,5 Зак. 22270 Тираж 80 экз. Бесплатно
Печать цифровая с оригинала, предоставленного аторами
Издательский отдел
Федеральное государственное бюджетное учреждение науки
Институт ядерных исследований Российской академии наук
117312, Москва, проспект 60-летия Октября, 7а